

PROBING MAGNETISM AT THE NANOMETER SCALE
USING TUNNELING SPECTROSCOPY

A Dissertation

Presented to the Faculty of the Graduate School

of Cornell University

in Partial Fulfillment of the Requirements for the Degree of

Doctor of Philosophy

by

Mandar Madhukar Deshmukh

August 2002

© Mandar Madhukar Deshmukh 2002

ALL RIGHTS RESERVED

PROBING MAGNETISM AT THE NANOMETER SCALE USING
TUNNELING SPECTROSCOPY

Mandar Madhukar Deshmukh, Ph.D.

Cornell University 2002

This thesis describes experiments in which we use metallic quantum dots to explore a wide range of physical phenomena at the nanometer scale. The discrete energy levels within a metallic nanoparticle, which forms the quantum dot, reflect the interactions within it. Tunneling via the individual energy levels also provides a new means to study the physics of the electrodes.

We have studied in detail the current flow via both one and many energy levels within a non-magnetic nanoparticle. The experiments, in combination with rate-equation calculations, have allowed us to probe the role of non-equilibrium transport and electron-electron interactions in a quantitative manner.

Having explored non-magnetic systems, we have extended the experiments to magnetic systems where we measure the electron-tunneling level spectrum within nanometer-scale cobalt particles as a function of magnetic field and gate voltage, thus probing individual quantum many-body eigenstates inside ferromagnetic samples. Variations among the observed levels indicate that different quantum states

within one particle are subject to different magnetic anisotropy energies. Gate-voltage studies demonstrate that the low-energy tunneling spectrum is affected dramatically by the presence of non-equilibrium spin excitations.

By making a device with an aluminum nanoparticle and one of the electrodes in our device out of a ferromagnetic metal, we can examine spin-polarized tunneling via discrete quantum states. We also observe magnetic-field-dependent shifts in the magnetic electrode's electrochemical potential relative to the energy levels of the quantum dot. The shifts vary between samples and are generally smaller than those expected due to the magnet's spin-polarized density of states. We propose that this variation is due to field-dependent charge redistribution at the magnetic interface.

Biographical Sketch

Mandar Deshmukh was born on October 20th, 1974, in Pune, India. He grew up in military cantonments at different locations all over India, as his father worked for the Border Security Force (BSF). One of his fondest activities as a child was horse-riding for long hours during the summer. The privileged growing-up experience in cantonments had an impact on him, and until his 8th grade his dream was to join the Indian Air Force and fly the Mirages. This dream was to undergo a metamorphosis during his high school years. There he was increasingly interested in mathematics and the physical sciences. An excellent academic environment at his school Jñana Prabodhini and Fergusson College led to the drastic change in his career plans.

Instead of joining the National Defence Academy (NDA) in Pune, he chose to go to the Indian Institute of Technology (IIT) at Bombay in 1992. He graduated after four years with a B.Tech. while majoring in Engineering Physics. Encouraged by his correspondence with Professor Robert Pohl he decided to apply to Cornell for the graduate studies, and came here in the fall of 1996. He finished his graduate studies in the summer of 2002, after spending six fun-filled years in Ithaca.

He will start his post-doctoral research at Harvard in the fall of 2002.

To My Parents

*Then pray that the journey is long.
That the summer mornings are many,
that you will enter ports seen for the first time
with such pleasure, with such joy!
Stop at the Phoenician markets
and purchase fine merchandise,
mother-of-pearl and corals, amber and ebony,
and pleasurable perfumes of all kinds,
buy as many pleasurable perfumes as you can;
visit hosts of Egyptian cities,
to learn and learn from those who have knowledge.*

*Always keep Ithaca fixed in your mind.
To arrive there is your ultimate goal.
But do not hurry the voyage at all.
It is better to let it last for long years;
and to even anchor at the isle when you are old,
rich with all you have gained on the way,
not expecting that Ithaca will offer you riches.*

*Ithaca has given you a beautiful voyage.
Without her you would never have taken the road.
But she has nothing to give you now.*

*And if you have found her poor, Ithaca has not defrauded you.
With such great wisdom you have gained, with so much experience
you must surely have understood by then what Ithacas mean.*

— C.P. Cavafy, Ithaca (Translated by Rae Dalven)

Acknowledgements

I have spent an exciting and enjoyable six years at Cornell, largely due to the amazing people that I had the good fortune to associate with. The research described in this thesis is the culmination of years of hard work, and would not have been possible without the help of a number of people. I want to take this opportunity to thank them for their help and support.

I am grateful to my advisor Dan Ralph for his advice, encouragement, and support over these years. His enthusiasm for new ideas is infectious, and has helped to broaden my interest in physics. I have enjoyed learning from him.

My committee members Jeevak Parpia and Chris Henley have helped me with their advice and suggestions, and I am grateful for that. Bob Buhrman and Paul McEuen deserve special thanks for their help and advice during my job-search.

One person in the low-temp group who cannot be thanked enough is Eric Smith. His help and advice in all experimental matters is indispensable. Besides being an excellent source of technical advice Eric is a wonderful person, who is always ready to go out of his way to help people. Thanks Eric.

I was fortunate to have worked closely with two of the postdocs in our group – Sophie Guéron and Edgar Bonet. I took over one of the projects from Sophie and she patiently showed me the ropes around the lab. Edgar Bonet has helped me to

understand a great deal about the physics of tunneling spectroscopy. His ability to think laterally was very helpful and inspiring.

A significant portion of my time in the low-temp. corridor was spent in the company of Alex Corwin, Ed, and Abhay, having discussions on things ranging from the latest problem with my experiments, to the fine details of “demolition derby”. Thanks Alex for introducing me to Genplot and many other experimental tricks. Abhay’s expertise with the coffee machine often aided my attempts at beating the “sleep devil” during the long nights. Discussing physics with Ed was very useful in getting to the bottom of an issue. Not only were they helpful in my experiments, they were also around to share my frustrations and excitements, to support and to encourage. I would also like to thank Alex Champagne, Jason, Kirill, Jiwoong, Sergey, Aaron, and Preeti for their help. I wish them the very best in their endeavors.

Arunabha has been a very close friend since we were both undergrads at IIT-Bombay. Talking to him has helped me through rough times. Bindu’s caring attitude translated into regular letters which were always a joy to go through. Thanks Arunabha and Bindu for being great friends.

I thank Prita for her love, patience, and unwavering support. She has transformed my life, and made it richer in countless ways.

I also want to take this opportunity to thank my parents and sisters for their love and encouragement. This work would not have been possible without their support. My parents inculcated in me the ethic for hard work and I cannot thank them enough for that.

Table of Contents

1	Introduction	1
1.1	Quantum dots	3
1.2	Metallic vs. semiconductor quantum dots	4
1.3	Organization of this thesis	5
	Bibliography	8
2	Introduction to nanoparticle transistors	9
2.1	Motivation for the experiments using nanoparticle transistors	10
2.2	Single electron transistor	12
2.2.1	Effect of the gate electrode in a SET	15
2.3	Single electron tunneling spectroscopy	17
2.3.1	Energy diagrams	18
2.3.2	Observing the energy levels	20
2.4	Fabrication Process	24
2.4.1	Making a nano-hole	24
2.4.2	Making a transistor using a nano-hole	34
2.5	Measurement procedure	42
2.5.1	Dipping samples in liquid helium	42
2.5.2	Measurement in a dilution refrigerator	47
	Bibliography	54
3	Rate equations calculations for a nanometer scale transistor	55
3.1	Rate-equation calculations of current flow	56
3.1.1	Energy of the eigenstates	57
3.1.2	Steady-state occupation probabilities	62
3.1.3	Current	64
3.2	One spin-degenerate energy level accessible	66
3.2.1	General formula	66
3.2.2	High bias limit	67
3.2.3	Position and width of the current step	69
3.2.4	Zeeman splitting of the energy level	71

3.3	Two levels accessible	73
3.3.1	Rate equation	78
3.3.2	Current	80
3.4	Two levels accessible with variations in the interactions	84
3.5	Conclusions	85
Bibliography		88
4	Tunneling via discrete quantum states in an aluminum nanoparticle	90
4.1	Experimental details	91
4.1.1	Tunneling spectroscopy as a function of gate voltage	95
4.2	Tunneling via one energy level	98
4.3	Tunneling via many energy levels	100
4.3.1	Current amplitudes	101
4.3.2	Width of conductance peaks	107
4.3.3	Position of conductance peaks	109
4.4	Conclusions	113
Bibliography		115
5	Polarization measurements of a bulk ferromagnet using discrete electronic states in an aluminum nanoparticle	116
5.1	Polarization of electrons in ferromagnets	117
5.1.1	Stoner model with parabolic bands	119
5.1.2	Previous experiments to probe polarization	121
5.2	Device fabrication and measurement	124
5.3	Density of states polarization	126
5.3.1	Background	128
5.3.2	Measuring the change in chemical potential	135
5.3.3	Comparison of measurements and theory	141
5.4	Tunneling polarization	145
5.4.1	Measuring the current via a single spin-degenerate energy level	146
5.4.2	Current flow via excited states	153
5.5	Conclusions	155
Bibliography		157
6	Tunneling spectroscopy of ferromagnetic nanoparticles	159
6.1	Sample fabrication	160
6.2	Tunneling spectroscopy of a cobalt nanoparticle	163
6.2.1	Low-field magnetic field data	163
6.2.2	High-field magnetic field data	169
6.3	Understanding the low-field data	172

6.3.1	Phenomenological model to understand how magnetic switching affects the energy levels	174
6.4	What is the origin of the observed resonances?	182
6.4.1	Spin-wave excitations within the magnetic nanoparticle	183
6.4.2	Non-equilibrium transport via a magnetic nanoparticle	184
6.5	Experimental results using the gate electrode	187
6.5.1	Testing the non-equilibrium picture	187
6.5.2	Determining the spin type of resonances	190
6.5.3	Evolution of the degeneracy point as a function of the magnetic field	192
6.6	Amplitude of the resonances	196
6.6.1	Low magnetic field data	196
6.6.2	Data from gated devices at high magnetic fields	198
6.6.3	Cotunneling ?	204
6.7	Summary and open questions	205
Bibliography		207
7	Tunneling spectroscopy of a nanomagnet using a ferromagnetic electrode	209
7.1	Introduction	210
7.2	Fabrication	210
7.3	Experimental data	212
7.4	Outlook	217
Bibliography		218
8	Nanofabrication using a stencil mask	219
8.1	Introduction	219
8.2	Fabrication of stencil and nanostructures	220
8.2.1	Clogging of holes	225
8.2.2	Role of surface diffusion	227
8.2.3	Fabrication of micrometer-scale structures	229
8.3	Conclusion	229
Bibliography		231
9	Conclusion	232
A	Stripline cryogenic filters	233
A.1	Fabrication of miniature electronic filters	234
A.2	Result of using these filters	239
Bibliography		242

List of Tables

5.1	Change in chemical potential as a function of magnetic field for a cobalt sample.	138
5.2	Change in chemical potential as a function of magnetic field for a nickel sample.	143
8.1	Effect of thermal diffusion on fabricated structures.	228

List of Figures

1.1	Schematic of a quantum dot.	2
1.2	Variety of devices studied in this thesis.	6
2.1	Schematic of single electron transistor showing various capacitances and resistances.	14
2.2	Energy of a SET as a function of gate voltage, V_g	16
2.3	Energy diagram for a nanoparticle transistor for positive bias voltage.	19
2.4	Energy diagram for a nanoparticle transistor showing the two possible threshold transitions.	21
2.5	Cartoon depicting the principle of tunneling spectroscopy.	23
2.6	Cross-sectional schematic diagram of a nanoparticle transistor.	25
2.7	Pattern for photolithography.	27
2.8	Schematic of the steps for fabricating a nano-hole (part1).	29
2.9	Schematic of the steps for fabricating a nano-hole (part2).	32
2.10	STEM image of a nano-hole.	35
2.11	Sample holder for gate-fabrication.	36
2.12	Fabrication steps for deposition of the electrodes and the nanoparticles.	40
2.13	Sample holder for gate-fabrication.	43
2.14	Circuit diagram used for measurements.	45
2.15	Schematic of the measurement setup.	46
2.16	Example of a “good” and a “bad” device.	48
2.17	Plot of Coulomb blockade peaks in an aluminum device.	51
2.18	Plot of differential conductance vs bias voltage showing peaks due to discrete states in an aluminum nanoparticle.	52
3.1	Circuit schematic showing the different voltages applied to a SET.	58
3.2	Energy diagram showing current thresholds.	61
3.3	Different tunneling events contributing for the case of current flowing via one energy level.	65
3.4	Effect of gate voltage on the current and conductance via one energy level.	68
3.5	Energy diagram showing one energy level when large bias is applied.	70
3.6	Effect of temperature on the conductance peak width and position.	72

3.7	Zeeman field splitting of a single spin-degenerate energy level.	74
3.8	Asymmetry in the conductance of a spin-split energy level.	75
3.9	Energy diagram for a quantum dot with two energy levels.	76
3.10	Transitions for a quantum dot with two energy levels.	77
3.11	Shift in position of current step due to non-equilibrium.	81
3.12	Non-linearities in evolution of levels due to non-equilibrium.	83
3.13	Position of conductance peak as a function of interaction.	86
4.1	Schematic of an all-aluminum nanoparticle transistor.	92
4.2	High bias I-V and dI/dV-V plot	93
4.3	I-V and dI/dV plot showing structure due to discrete states.	94
4.4	Colorscale conductance plot for an aluminum nanoparticle transistor	97
4.5	Current via one energy level.	99
4.6	Energy diagram for different lines.	102
4.7	Magnitude of the tunneling current and width of dI/dV peak.	103
4.8	Current along line II.	105
4.9	Current along line II with rate-equation fit.	106
4.10	Energy diagram before and after the kink.	111
4.11	Colorscale plot of the data showing the kink.	112
5.1	Calculated density of states for nickel.	118
5.2	Density of states for Stoner model with parabolic bands.	120
5.3	Device schematic of a device with one ferromagnetic lead.	125
5.4	I-V and dI/dV-V plot for device with one ferromagnetic lead.	127
5.5	Cartoon showing the effect of the magnetic field on the electrochemical potential of a ferromagnet.	129
5.6	Change in electrochemical potential of the ferromagnetic electrode viewed as an “effective” gate action.	131
5.7	Cartoon depiction of the two linear effects contributing to the asymmetric Zeeman splitting of a spin-degenerate energy level.	133
5.8	Colorscale conductance plot of a device with a cobalt electrode.	136
5.9	Colorscale conductance plot of a device with a nickel electrode for negative V	140
5.10	Colorscale conductance plot of a device with a nickel electrode for positive V	142
5.11	Current via spin non-degenerate energy levels.	147
5.12	Energy diagrams for tunneling via spin non-degenerate energy levels.	148
5.13	Energy diagram showing different tunneling rates associated with the magnetic and non-magnetic electrodes.	150
5.14	Tunneling polarization as a function of the magnetic field.	151
5.15	Conductance plot showing the negative conductance peak.	154
6.1	Device schematic of a device with a cobalt nanoparticle and two non-magnetic leads.	162

6.2	dI/dV-V for a device with a cobalt nanoparticle and non-magnetic electrodes.	165
6.3	Colorscale conductance plot for a device with cobalt nanoparticle as a function of magnetic field -1 T to +1 T.	166
6.4	Colorscale conductance plot for a device with cobalt nanoparticle showing complex hysteretic features due to dipolar coupling.	167
6.5	Colorscale conductance plot for a device with cobalt nanoparticle as a function of magnetic field -8 T to +1 T.	170
6.6	Cartoon showing minimal ingredients necessary for describing a magnetic system.	173
6.7	Plot of the calculated magnetization and addition energy as a function of the magnetic field.	176
6.8	Plot of the addition energy exhibiting non-monotonic features when the variation in anisotropy is taken into account.	180
6.9	Cartoon showing the origin of non-equilibrium transitions.	185
6.10	Colorscale conductance plot of a gated Co nanoparticle as a function of V_g and V - evidence for non-equilibrium.	188
6.11	Magnetic field behavior of a cobalt nanoparticle device when the electron number is varied by one.	191
6.12	Gate scans for a cobalt nanoparticle at different strengths of the magnetic field.	193
6.13	Plot of the degeneracy point (V_{deg}) as a function of the magnetic field.	195
6.14	Plot of the current via an energy level as a function of the magnetic field.	197
6.15	Gate scans for a device with cobalt nanoparticle as a function of the gate voltage for a sequence of magnetic fields.	199
6.16	Cartoon diagram showing the region near the charge degeneracy point.	201
6.17	Colorscale conductance plot showing the presence of structure within the Coulomb blockade region.	203
7.1	Schematic of a device with a cobalt electrode, a cobalt nanoparticle and an aluminum lead.	211
7.2	Colorscale conductance plot of a device with a cobalt lead, a cobalt nanoparticle and an aluminum lead as a function of the magnetic field (-0.5 T - 0.5 T).	213
7.3	Cartoon showing a possible scheme for measuring the TMR effect for tunneling via a single energy level.	214
7.4	Colorscale conductance plot of a device with a cobalt lead, a cobalt nanoparticle and an aluminum lead as a function of the magnetic field (-1.5 T - 1.5 T).	216
8.1	STEM images showing the structures fabricated using the stencil mask.	221
8.2	Diagram of deposition through the stencil mask using a pinhole evaporation source.	224

8.3	Results for the clogging tests and a device fabricated using stencil masks.	226
A.1	Design of the stripline filters.	235
A.2	Schematic of the “pillbox” used for electromagnetic sheilding of the filters.	237
A.3	Electron temperature after filtering.	238
A.4	Electron temperature vs. refrigerator temperature.	240

Chapter 1

Introduction

Understanding the basic properties of solids requires a good understanding of their electronic properties, and this has proved to be a challenging task because of the complexity of electronic interactions. In the past 20 years, technological developments have led to the fabrication of electronic structures that allow us to confine a fixed number of electrons and study their interactions, providing us with a new way to probe and understand interacting electron systems in a systematic manner [1, 2, 3]. The artificially confined electrons are very similar to the electrons in atoms, and at the same time allow access to regimes that are difficult to realize in atomic systems. These confined electronic structures are referred to by various names: single-electron transistors, quantum dots (QDs), zero dimensional electron gases, and Coulomb islands. The quantum dot, in many ways, has provided us with a means to rediscover and explore – in unprecedented detail – the basic physics of many electron systems, as was the case in atomic physics, but with a greater degree of control and with many more experimental knobs. The quantum dot structure has been used to study the effects of: spatial symmetries [4], superconductivity [5], magnetism [6], Kondo interactions [7], and many other phenomena.

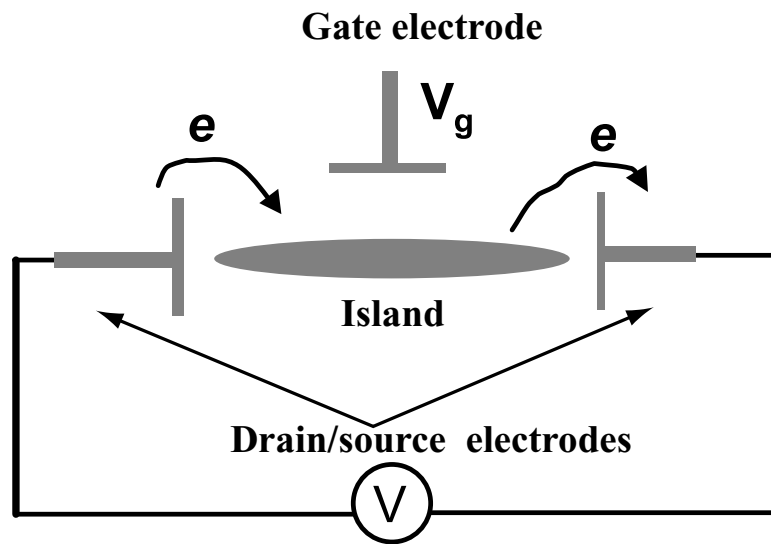


Figure 1.1: Schematic of a quantum dot showing various electrodes, and the central island where the electrons are confined.

1.1 Quantum dots

Figure 1.1 shows the schematic of a quantum dot (QD). A quantum dot consists of an island, in which the electrons are confined, and three electrodes: the source, drain and gate electrode. The island is isolated from the source and drain electrodes by tunnel barriers. Electron transport occurs due to the tunneling of an electron from the source onto the island and then onto the drain electrodes, whereas the gate electrode affects the transport by changing the electrostatic potential of the island. The central island of the QD can be thought of as a pool of electrons very weakly coupled to the other electrodes. As one begins to make this island smaller there are two energy scales that increasingly become important. The first one is the charging energy – the energy required to charge the island with one excess electron, e . This energy can be written as

$$E_C = \frac{e^2}{2C}, \quad (1.1)$$

C is the total capacitance of the system. The microscopic origin of this charging energy is the Coulomb interaction between the electrons. Simply speaking, as one makes the island smaller this energy becomes larger, reflecting the importance of electronic interactions in mesoscopic systems.¹ The second energy scale that becomes relevant is the discreteness of the energy levels in this pool of electrons. This confined puddle of electrons on the central island is similar to the electrons-in-a-box problem. One of the effects of making the island smaller is that the electronic energy levels can be resolved from each other. In the typical electrons-in-a-box problem, the average spacing between energy levels, δ , is $\sim 1/d^3$, where d is the dimension of the island. As a result, the smaller the “box” gets, the better resolved the energy

¹It should be pointed out that this is a heuristic argument, and it is the capacitance of the island relative to its environment (the electrodes), rather than the self-capacitance, that accurately reflects the cost of the charging energy.

levels become. This energy level spectrum, like the ones in atoms, reflects forces at work in the puddle of electrons. We will use these well resolved energy levels to probe an array of systems.

The central island forms the heart of a quantum dot, and its size dictates the kind of physics that can be explored using that device. It is made by confining the electrons by material boundaries, or in semiconductors by using electric field to define the dot region. Both methods require using lithography tools on the 10- to 100-nanometer scale, and this is typically achieved by electron-beam lithography. In the early 80's, this tool became available to the experimental community, and since then a variety of physics has been explored.

1.2 Metallic vs. semiconductor quantum dots

In this thesis I will describe experiments with quantum dots where electrons are confined on a metallic island. It is interesting to note the differences between semiconductor and metallic quantum dots since this will allow me to put this work in a broader context.

The main difference between the two types of quantum dots is the length scales. In semiconductor quantum dots, the puddle of electron is created by applying an electric field; this depletes the electrons in a two dimensional electron gas confined in a semiconductor heterostructure. The Fermi wavelength in these heterostructures is about 10 nm, and depends on the density of electrons. This is to be contrasted with the metallic quantum dots where the electrons are confined by the physical boundary of the metallic dot. The Fermi wavelength in metals is $\sim 5 \text{ \AA}$, the typical spacing between atoms in the lattice. As a result, the semiconductor quantum are relatively insensitive to local atomic defects which get smoothed out; however, that

is not the case for metallic quantum dots. They can be used to probe the effects of impurities or disorder or both. The semiconductor QDs have the flexibility that the geometry can be modified just by applying a voltage to an electrode, whereas this cannot be done for metallic quantum dots since the electrons screen any external potential quite effectively. The flexibility of changing the geometry in semiconductor quantum dots allows the freedom to carry out ensemble measurements and make statistical inferences. The metallic quantum dots are, however, ideal systems to study the physics of confinement, since the tunnel barriers are not affected by the voltages applied to various electrodes; this is not the case for semiconductor based systems where the height of the tunnel barrier is modified by the applied voltages. The biggest advantage of metallic quantum dots is that they allow the freedom to fabricate various electrodes and quantum dots from a variety of different materials. A number of metals have been studied: aluminum to probe the superconducting correlations, noble metals with high atomic number like gold to understand the role of spin-orbit interactions, and ferromagnets like cobalt to probe magnetism at the nanometer scale. This versatility, of using “real world” metals, allows us to explore the physics of electronic interactions and transport across interfaces.

1.3 Organization of this thesis

This thesis is written in logical order of the physics, and not in the chronological order of the experiments I have worked on for the past five years. In Chapter 2, I will introduce the basic technique of tunneling spectroscopy, which is common to all the experiments I will be discussing later. It will mainly deal with the basic idea of measuring the discrete energy levels in a metal nanoparticle by measuring the current through it as electrons tunnel in a sequential manner. Chapter 3 con-

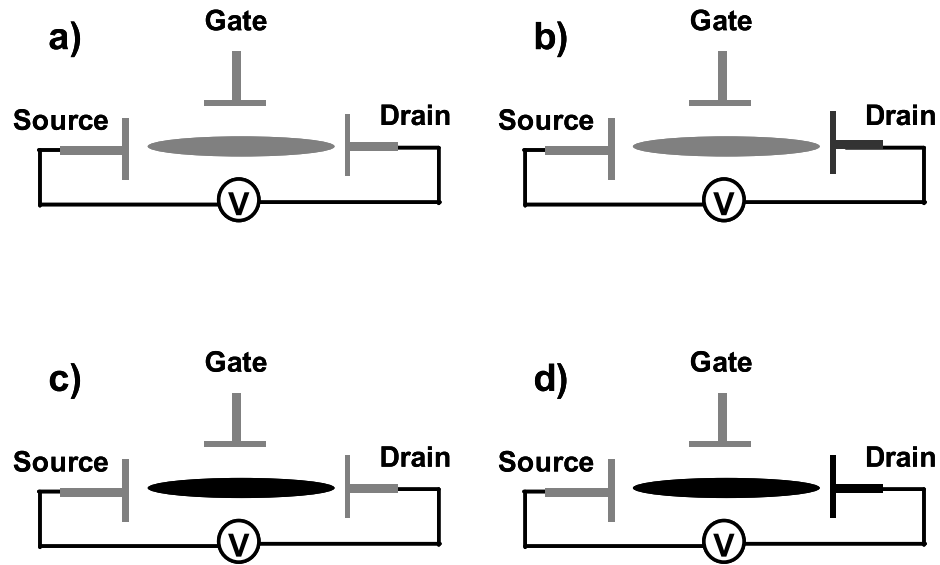


Figure 1.2: Cartoons of various devices described in this thesis. Grey colored electrodes indicate that the electrode is fabricated from a non-magnetic material, whereas, a black colored electrode is magnetic. a) Device with all the electrodes fabricated from non-magnetic material is described in Chapter 4. b) In Chapter 5, we describe the device with one electrode, either drain or source, fabricated from magnetic material. c) In Chapter 6, the central island is made from of a magnetic material. d) Experimental results from a device with the island and one of the electrodes fabricated from a magnetic material are described in Chapter 7.

tains the basic rate equation formalism which describes the sequential tunneling of electrons. This rate-equation framework allows us to simulate the experiments and extract quantitative information from the experimental data. Chapters 4-7 describe four different experiments with increasing complexity. Figure 1.2 shows cartoons of the devices that will be discussed in these four chapters. Chapter 4 describes tunneling spectroscopy measurements on an aluminum nanoparticle, where we can observe the effect of electron-electron interactions. The polarization of ferromagnets can be probed in two different ways by fabricating one of the electrodes from a ferromagnetic material; the results from this experiment are described in Chapter 5. In Chapter 6, experiments involving tunneling spectroscopy of quantum states in ferromagnetic nanoparticles are described. Another step in increasing complexity involves fabricating the metallic nanoparticle and one of the electrodes with a ferromagnetic material. This experiment was motivated by the idea of studying spin-polarized tunneling. Preliminary measurements from this experiment are described in Chapter 7.

Finally, in Chapter 8, I will describe preliminary work on a stencil-based fabrication technique, and in Chapter 9, I will summarize the work described in this thesis.

Bibliography

- [1] R. C. Ashoori, *Nature* **379**, 413 (1996).
- [2] M. A. Kastner, *Physics Today* **46**, 24 (January 1993).
- [3] L. P. Kouwenhoven, *Rep. Prog. Phys.* **64**, 701 (2001).
- [4] C. M. Marcus *et al.*, *Chaos, Solitons and Fractals* **8**, 1261 (1997).
- [5] C. T. Black, D. C. Ralph, and M. Tinkham, *Phys. Rev. Lett.* **76**, 688 (1996).
- [6] S. Guéron, M. M. Deshmukh, E. B. Myers, and D. C. Ralph, *Phys. Rev. Lett.* **83**, 4148 (1999).
- [7] D. Goldhaber-Gordon *et al.*, *Nature* **391**, 156 (1998).

Chapter 2

Introduction to nanoparticle transistors

As mentioned in Chapter 1, single electron transistors have been used to probe a variety of physical phenomena. In this chapter we introduce the nanoparticle transistor and single electron tunneling spectroscopy; this technique is used to measure the electronic spectra of a nanoparticle. The idea that electron tunneling could be used to probe properties of nanometer scale metallic clusters is several decades old, and was pioneered by Giaever and Zeller [1]. Their measurements involved measuring the I-V characteristics of metallic clusters embedded in insulating films; this allowed them to probe the charging properties. However, these measurements were *ensemble* measurements since a large number of metallic clusters were involved in the current transport. The nanoparticle transistor differs in that the single electron tunneling occurs via a *single* nanoparticle. This enables us to make quantitative comparisons to models and extract information that is not convolved with the statistics of size and number distribution of nanoparticles.

The most difficult part of fabricating nanoparticle transistors is contacting a *sin-*

gle nanoparticle with electrodes. Several techniques [2, 3, 4, 5] have been developed to overcome this difficulty. However, the technique developed by Dan Ralph, Chuck Black, and M. Tinkham [6] has been most successful for a variety of reasons, the most important being the stability of the device at low temperatures. All the devices studied in this thesis have been fabricated using this technique, and we will describe the fabrication procedure later in this chapter. Before we consider the experimental details, it is interesting to revisit various ideas that motivated the experiments.

2.1 Motivation for the experiments using nanoparticle transistors

Nanofabrication allows the investigation of devices that operate by means of physical mechanisms completely different from the underlying principle behind most electronic devices fabricated using the present technology (smallest feature size in the Pentium processor developed by Intel is ~ 130 nm). Nanometer-scale devices are characterized by the fact that electron transport occurs via discrete “electrons-in-a-box” states, instead of a continuum of states in much larger devices. Tunneling via discrete energy levels is common to a variety of systems, and there is a need to understand all the processes that affect electron transport. In addition to the interest in nanometer-scale devices for potential applications, it is essential to understand the fundamental properties of nanometer scale systems.

Dan Ralph and co-workers have successfully used nanoparticle transistors [2, 6, 7] to observe a variety of interesting physics at the nanometer scale. I will briefly mention their main results since they emphasize that this is a versatile technique. Ralph *et. al.* had originally used aluminum to fabricate the central island of the

quantum dot. Their main results were:

- They could determine the parity of the number of electrons on the quantum dot by observing the evolution of energy levels as a function of the magnetic field [6].
- Since they used aluminum for making the quantum dot, they could probe the superconductivity at nanometer scale for the first time, and correlate the effects of size and parity of the superconductor with the superconducting gap [7].
- Using the gate electrode, they could observe the effects of transport in the nonequilibrium regime. They could observe, qualitatively, the signature of electron-electron interactions in the energy level spectrum of a nanoparticle. This indicated that the independent electron picture is not correct, and interactions need to be taken into account [2].

The common theme of these experiments was to investigate the physics by observing the energy level spectrum of nanoparticles. This technique opened up the possibility of answering some other very interesting questions in mesoscopic physics. The following questions have motivated the work in this thesis.

- What is the nature of relaxation between quantum states? Under appropriate conditions, an electron can tunnel into a higher energy state in a metal nanoparticle, followed by a tunneling out of an electron in a lower energy state. This leaves the system in an excited state. Whether or not this excitation relaxes before the next tunneling event affects the current-voltage curve. It is essential to understand this process in order to understand the dephasing mechanism in nanometer scale devices. Realization of systems where ideas of

quantum computation could be applied crucially depends on our understanding of dephasing in nanometer-scale devices.

- What is the nature of spin-polarized tunneling? Tunneling electrons from a ferromagnet are known to be polarized; however, the amount of polarization is dependent on the interfacial states in the tunnel barrier. Understanding the physics of spin-polarized electron tunneling is crucial for potential applications which harness the spin degree of freedom together with the electronic degree of freedom.
- What is nature of electronic correlations in a nanometer scale magnet? Like superconductivity, magnetism is a correlated state. However, it is mostly understood in term of models which rarely capture the realistic behavior of the materials. The electronic spectra of the nanomagnet will provide new means to probe forces like exchange and anisotropy.

Having discussed the ideas behind our experiments I will next discuss the basics of single electron transistors.

2.2 Single electron transistor

The single electron transistor (SET) derives its name from the principle on which it is based – that the electronic charge is quantized [8]. A simple way of getting to the basic physics of a SET is by asking the question: what is the energy required to place an extra charge, e , on an isolated piece of metal? Using elementary electrostatics, the charging energy, E_C can be written as:

$$E_C = \frac{e^2}{2C}, \quad (2.1)$$

where e is the electronic charge, and C is the self capacitance of the isolated piece of metal.

Now consider the schematic of a SET shown in Figure 2.1, where a metallic island is weakly coupled to the electrodes via tunnel barriers. Each of the tunnel barriers is characterized by a capacitance and resistance. The island is considered to be isolated if the resistance is larger than the quantum of resistance, $R_Q = h/e^2 \approx 26 \text{ k}\Omega$. Here we will only consider devices where the island is well isolated. In this case the charging energy is not simply the self capacitance of the island, but the sum of various capacitances, ($C_\Sigma = C_1 + C_2 + C_g$), that connect it to various electrodes. The energy required to charge the island with a charge Q can be written as,

$$E_C = \frac{Q^2}{2C_\Sigma}. \quad (2.2)$$

Since the charge on the island varies only by multiples of e , the charge Q can be rewritten it as $Q = Q_0 + Ne$, where Q_0 is the background charge and N is the number of excess electrons on the island. This is minimized when N is the integer closest to $-Q_0/e$. Also, we will deal with devices where the Coulomb energy is much larger than the level spacing, so that only the two lowest energy values for N are permitted during the process of current flow. For devices that will be considered here, the typical capacitances are the order of 1 aF. The charging energy associated with a device having two junctions with \sim aF capacitance is 40 meV (400 K).

If a SET is now cooled down to a temperature where the thermal energy, $k_B T$, is less than the charging energy, E_C , the device has non-ohmic characteristics. When $k_B T > E_C$, the thermal fluctuations are able to transfer electrons and a non-zero current can be observed while applying any small bias across the sample. However, this is not the case when $k_B T < E_C$; now a finite external bias has to be applied to provide the extra charging energy required for an electron to tunnel onto the

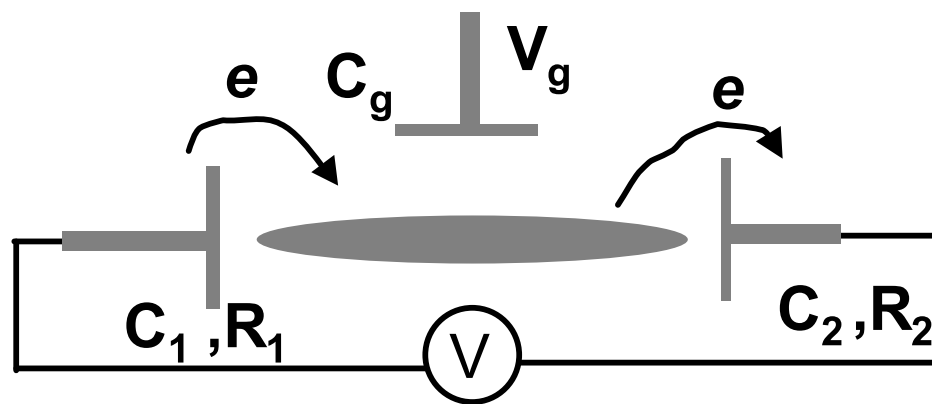


Figure 2.1: Schematic of a single electron transistor with various electrodes and capacitance of the central island associated with each one of them.

island. This produces a blockade of current at non-zero bias that is referred to as Coulomb blockade, and it is an important characteristic of a SET. The Coulomb blockade can be observed in two-terminal devices with an island weakly coupled to two electrodes. However, it is the gate electrode that modulates this blockade and makes the device a real “transistor.” We consider the role of the gate electrode next.

2.2.1 Effect of the gate electrode in a SET

The gate electrode affects the electron transport by modulating the electrostatic potential of the island. This can be understood clearly if one examines the microscopic origin of the parameter Q_0 introduced earlier. Consider the electrochemical potential of the island¹ when no voltage is applied to any of the electrodes. Under these conditions the chemical potential of the two leads will be aligned, however, the chemical potential of the island is determined solely by the residual potential that it feels because of its electrostatic environment. The magnitude of Q_0 is related to the mismatch of the chemical potential of the leads and that of the island. The relation can be written simply as:

$$|Q_0| = C_\Sigma \frac{|\Delta\mu_{island}|}{e}, \quad (2.3)$$

where $\Delta\mu_{island}$ is the mismatch in the chemical potential of the island relative to the leads. Q_0 is a continuous quantity and not quantized in units of e , and mathematically one can account for this mismatch of the chemical potential by assuming that a continuous charge Q_0 resides on the island. Now, if a non-zero gate voltage, V_g , is applied, Q_0 changes by $-C_g V_g$. This implies that a positive bias would increase the number of electrons on the island. The effect of the gate voltage is summarized in

¹Electrochemical potential is a measure of the energy required to change the electron number by one. For the case of a quantum-dot, the energy required for addition and subtraction of an electron are different, whereas, in the thermodynamic limit these two energies are the same.

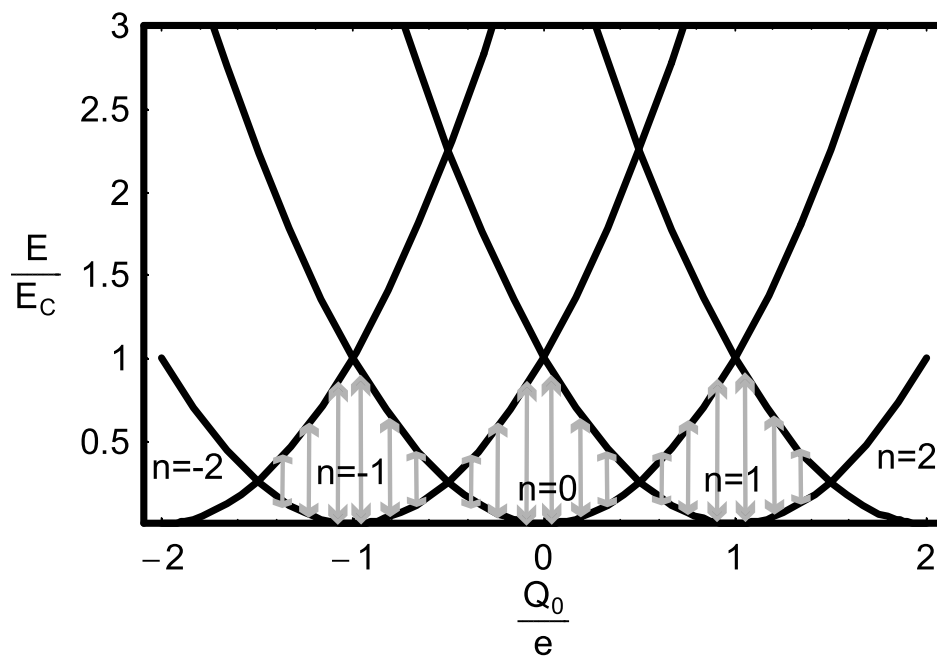


Figure 2.2: Energy of the SET as a function of Q_0/e (proportional to $-V_g$) for various values of n . The system occupies the local minima, consequently the number of electrons on the island change by discrete units. The grey arrows indicate the energy required for tunneling at a sequence of gate voltages. This variation is continuous, unlike the variation in the electron number.

Figure 2.2, which shows the energy of the island as function of Q_0 for various values of n (the number of excess electrons relative to the charge neutral state). So, as one changes the gate voltage, the charge on the island changes by 1 electron at a time so as to minimize the energy of the system. Between these discrete changes in n , the threshold voltage required for an electron to tunnel into the island changes in a continuous manner as shown by the grey arrows marked in Figure 2.2. The threshold voltage is defined as the bias voltage required to charge or discharge the island with one electron, and is simply the voltage that provides for the excess energy required for the transition. The gate electrode modulates the blockade and the current, and as a result this three terminal device is referred to as a transistor [9]. The SET is not a very useful source for providing gain as one would expect from a conventional transistor,² however, it is an extremely sensitive electrometer.

Coulomb blockade and transistor behavior can be observed in micron size islands, but in order to observe the discrete energy levels the size of the island has to be about 10 nm or less. In the next section, we look at various requirements for measuring the energy level spectra in nanometer-scale transistors.

2.3 Single electron tunneling spectroscopy

How small does an island of the single electron transistor have to be before one starts observing the energy levels? In the free electron model of a metal, the spacing between the electronic energy levels (measured at the Fermi energy) is given by:

$$\delta = \frac{4E_F}{3N}, \quad (2.4)$$

²There are a couple of reasons that make it difficult for SETs to be used as a source of gain, 1) highly non-linear transconductance (dI/dV_g), and 2) more importantly the variation in the offset charge Q_0 as a function of time. For a good discussion on comparison between field effect transistors (FETs) and single electron transistors (SETs) see ref.[10].

where E_F is the Fermi energy, and N is the number of electrons. In order to achieve a level spacing $\delta = 1K = 0.086$ meV, a spherical aluminum ($E_F = 11.7$ meV) [11] island has to have a diameter of ~ 10 nm. In the later sections, we will discuss how this seemingly arbitrary requirement of minimum level spacing arises. In the next subsection, we discuss energy diagrams which allow visualization of various tunneling events.

2.3.1 Energy diagrams

In order to extract information from the experimental data it is essential to visualize various tunneling events, and energy diagrams are a great help in that respect. We will discuss them briefly since they will be used frequently in the later chapters.

Figure 2.3 shows an energy diagram with discrete energy levels within the nanoparticle when a nonzero bias voltage is applied across the two electrodes. The two tunnel barriers labelled as 1 and 2 are intentionally shown to be asymmetric ($C_1 \neq C_2$). The cost of charging the quantum dot is indicated by the position of the energy-levels in the quantum dot relative to the Fermi energy of the electrodes at zero bias (dotted line in Figure 2.3). A positive bias applied to the right electrode lowers the chemical potential relative to the other electrode. In the diagram shown, the Coulomb blockade has not been overcome and no current flows through the device. The filled states, with electrons at energies below the Fermi energies of either leads, do not contribute to the current flow. However, the situation changes when the bias is increased further.

Figure 2.4 (a) shows one of the processes that allows the current to flow through the device. In this case, the first step or the threshold transition is the charging of the island with an extra electron after the Coulomb blockade has been overcome;

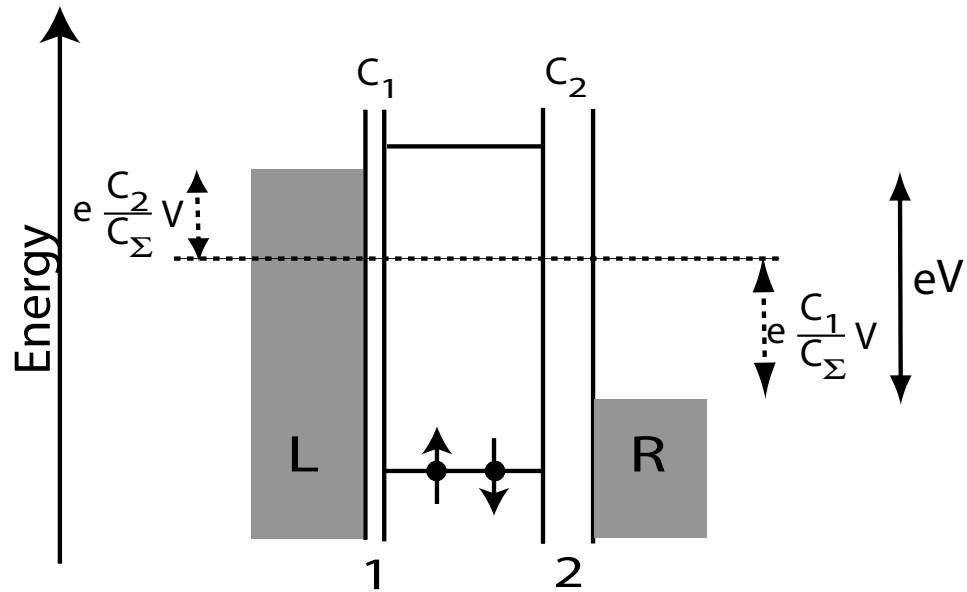


Figure 2.3: Energy level diagram for a nanoparticle SET with a positive bias applied to the right electrode ($V > 0$). The two junctions, 1 and 2, have different capacitances associated with them. The filled states are indicated by up and down arrows corresponding to the spin of the electrons.

this is indicated by a black arrow. After the dot has been charged, the next event that follows is the discharging across the second tunnel barrier. These two steps are elastic, and cause a net current to flow across the two tunnel barriers. Figure 2.4 (b) shows the other possibility for the two step process that can cause a current to flow through the device at finite bias. Here, the first step involves discharging of the nanoparticle, followed by a charging step. For the case of a symmetric quantum dot ($C_1 = C_2$), it is simple to determine which of the transitions, either $n_0 \rightarrow n_0 + 1$ or $n_0 \rightarrow n_0 - 1$, is the threshold transition, depending on the magnitude of Q_0 . If $|Q_0| < 1/2$, the first step involves tunneling off of an electron, otherwise it involves tunneling on. This can be easily visualized by looking at Figure 2.2, where the threshold transition is decided by what is the charge state of the closest neighboring parabola. In our devices where $C_1 \neq C_2$ – in fact they can be quite asymmetric – it is not possible to use the above mentioned heuristic argument.

2.3.2 Observing the energy levels

Having discussed various steps involved in tunneling of the electrons across the two junctions, we will now consider qualitatively how the energy levels are probed (this issue will be considered rigorously in the next chapter). Figure 2.5 shows schematically how the energy levels can be detected by measuring the conductance of the device. As shown in Figure 2.5 (a), when no bias voltage is applied there is no current flowing through the device (Figure 2.5 (e)) since there is no energy level available for resonant tunneling of electrons. However, as the bias is increased, the current increases gradually (Figure 2.5 (b)) because the thermal smearing ($\sim k_B T$) of the Fermi energy of the lead allows some electrons in the lead to resonantly tunnel

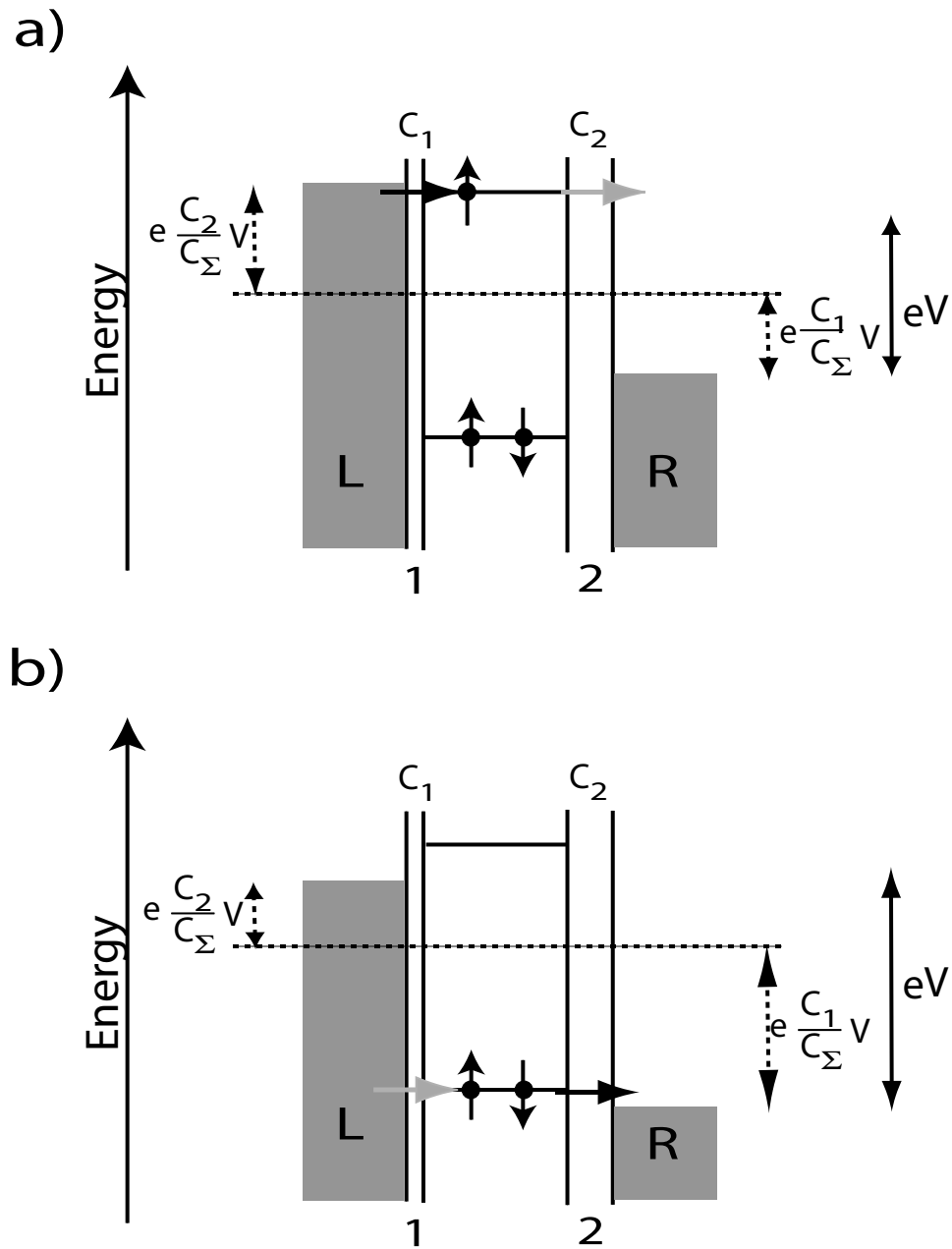


Figure 2.4: Energy level diagram depicting the two process by which the current can flow from one electrode to another. a) The first step is the charging process (black arrow), also indicated by the notation: $n_0 \rightarrow n_0 + 1$, where n_0 is the number of electrons on the nanoparticle in the uncharged state. It is followed by a discharging step as indicated by the grey arrow. b) The first step is the discharging process (black arrow), also indicated by the notation: $n_0 \rightarrow n_0 - 1$, where n_0 is the number of electrons on the nanoparticle in the uncharged state. The next step is the charging step across tunnel barrier 1.

via the energy level.³ The current saturates when the Fermi energy of the left lead is completely past the first energy level; this causes the differential conductance of the device to drop to zero. As the bias is increased further the current increases because the electron can tunnel via the second empty energy level which has now become accessible. Once the Fermi energy is past the second level, the current saturates and the differential conductance drops to zero. The position of peaks in the differential conductance corresponds to the position of the energy levels.⁴ Measuring the conductance in this way allows us to perform spectroscopy on the nanoparticle.

In the simplistic picture described above, we do not consider the possibility where more tunneling-out paths become available (or alternatively our cartoon shows peaks in conductance with the threshold transition occurring across only one barrier).⁵ This picture, however, helps to emphasize the role of another energy scale in our experimental system – the thermal energy of the electrons ($k_B T_e$), where T_e is the electron temperature. This can be measured by fitting the current steps to the Fermi function.⁶ If the average level spacing between the energy levels, δ , is comparable to the width of the conductance peak, $\sim 3k_B T_e$, then the resolution between energy levels is inadequate. In order to achieve optimum resolution, we need $\delta > 3k_B T_e$. We will revisit the issue of electron temperature in Section 2.5.2. The relationship of various energy scales discussed in this section is:

$$E_C \gg \delta > k_B T_e. \quad (2.5)$$

³In this simple analysis we are assuming that the resistance of the tunnel barriers is much larger than the quantum of resistance, as a result cotunneling may be neglected.

⁴It will become clear in Chapter 3 that the observed position of the energy level also depends on the temperature.

⁵In real data we can have conductance peaks which correspond to threshold transitions across either of the two barriers, even for the same sign of the bias.

⁶The effective electron temperature, T_e , is not the same as the lattice temperature because of the weak electron-phonon coupling. This issue will be discussed further in Section 2.5.

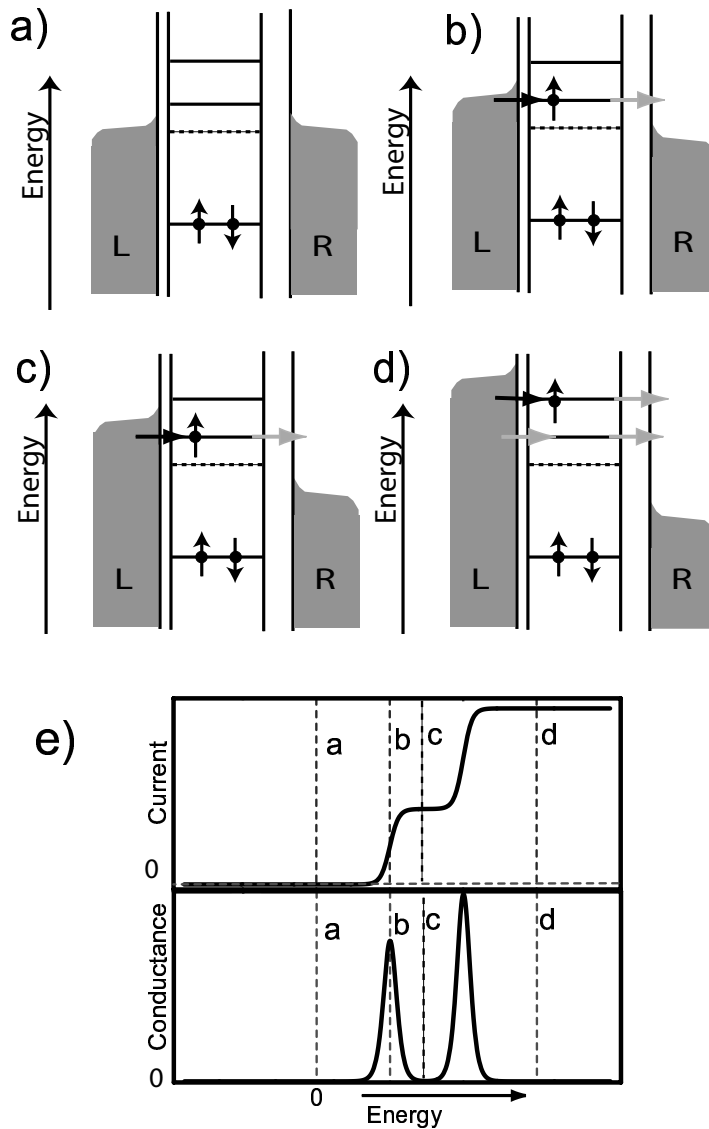


Figure 2.5: (a-d) Energy level diagrams as a positive bias voltage, V_{bias} , is gradually applied across the device and current begins to flow through the device. The dotted line indicates the position of the leads when $V_{bias} = 0$. a) Energy diagram with $V_{bias} = 0$, no current flows through the device (as shown in (e)). b) Energy diagram with $V_{bias} \neq 0$ and the electrons in the tail of the Fermi energy resonantly tunnel through the first energy level giving rise to an increase in the current and conductance (as shown in (e)). c) As the Fermi energy sweeps past the first energy level, the current saturates and the conductance drops, and d) Energy diagrams for successive increases in the bias voltage leading to tunneling via the second energy level and a second peak in conductance. e) Current and conductance measured through the device as bias voltage is increased.

Having discussed the basic principle behind our experiments, we are going to consider the experimental aspects in the following section.

2.4 Fabrication Process

One of the most challenging aspects of making a nanoparticle transistor is to fabricate electrodes to contact a nanoparticle. The nanoparticle transistor that we have used for our experiments is quite different from the planar devices that are most commonly used, and from the schematic of a SET we have used for illustration. Figure 2.6 shows the cross-sectional schematic of the device. The crucial step in the fabrication process is making a 5 – 10 nm hole in an insulating silicon nitride membrane. The fabrication technique for this geometry was invented by Dan Ralph and co-workers [6, 7, 2], by adapting a recipe invented by Kristin Ralls, Bob Buhrman, and Richard Tiberio [12, 13]. We have used the recipe developed by Dan Ralph and co-workers with slight modifications. One important piece of advice for anybody trying to fabricate devices using the recipe discussed below is – be consistent. We describe the complete fabrication next.

2.4.1 Making a nano-hole

The nano-holes are generally made in bulk (9 wafers, 81 samples on each wafer), and then the wafers are cleaved to get the required number of samples for each set of devices. In the first set of steps, a freely suspended silicon nitride membrane is fabricated; this is followed by a set of steps to define and etch a *single* nano-hole on each of the membranes. Figure 2.7 shows the pattern to be exposed on the wafer for fabricating the silicon nitride membranes, and Figures 2.8 and 2.9 show the cartoons

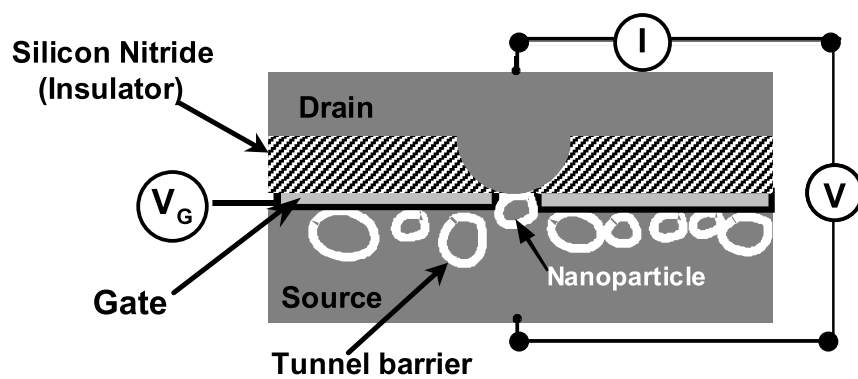


Figure 2.6: Cross-sectional device schematic of the nanoparticle transistor used in our experiments.

of the various processes. The recipe described here for making the nano-holes was invented by Kristin Ralls [12, 13].

1. Start with double-side-polished $\langle 100 \rangle$ oriented silicon wafer (flip polished wafers can be used). The $\langle 111 \rangle$ planes are at 54.74° from the plane of the wafer (35.26° from the normal). It is essential to know the thickness of the wafer in order to predict the final membrane sizes for a given mask. I have mostly used 20 mil ($\sim 500 \mu\text{m}$) wafers since they are not as fragile as the 15 mil ones, however folks in the Buhrman group mostly use 15 mil, so it should work as well. Note that there is about $40 \mu\text{m}$ of undercut during the etch, so the mask opening should be $40 \mu\text{m}$ smaller than the etch angle and wafer thickness suggest. The amount of this undercut will depend on the temperature of the wet etch (KOH) – the higher the temperature, the more undercut. Depending on the availability one can get the wafers in a week to one month after ordering. 20 mil wafers are difficult to find and this may require more time.
2. Phil Infante, at CNF, has performed the MOS-area processing needed in this work. The MOS process involves depositing 100 nm low pressure chemical vapor deposition (LPCVD) low stress nitride. It is essential to deposit 100 nm now – even though we eventually want 50 nm of silicon nitride – because there is thinning of the membrane during the wet etch that follows. Phil Infante needs one month's notice to grow silicon nitride, so that should be factored in if one wants the wafers for making devices. The CNF staff can also train people to do this step on their own.
3. The wafers are then cleaned with acetone and isopropanol, followed by blow-drying. It is essential to clean the wafer with isopropanol after using acetone

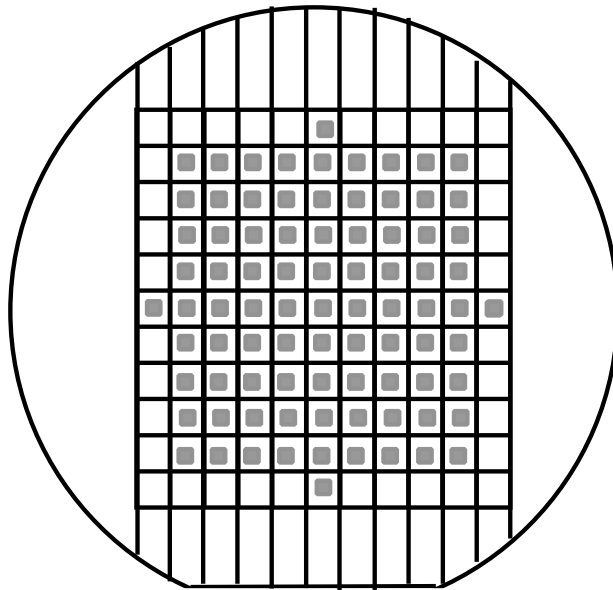


Figure 2.7: Pattern for the freely suspended nitride membranes on a 3 inch wafer. Membranes are indicated in grey color and the etch lines are indicated in black. (Not to scale)

since acetone has a tendency to leave a residue.

4. Spin S-1813 photoresist on the front (membrane) side of the wafer. Bake on clean aluminum foil at 90°C for 10 minutes. This layer is to protect the silicon nitride from scratching.
5. Spin S-1813 photoresist on the back side for 1 min at 4000 rpm. Then bake at 90°C for 30 minutes. (Approximate time required for spinning resist on both sides of nine wafers and various bakes – 2 hours.)
6. Align the long break lines on the mask so that they are perpendicular to the primary wafer flat. Expose on the HTG contact aligner, 405 nm channel B (the usual settings) for 6 sec (the pattern to be exposed is shown in Figure 2.7). Develop in MF312 diluted 1:1 with DI water, 60 s or until the pattern is clear over the entire wafer. (Figure 2.7 shows the schematic of the pattern to be exposed onto the wafer.) The folks at CNF frequently change the developers in stock, and suggest alternate developing schemes. However, the minimum feature size in our pattern is $\sim 100 \mu\text{m}$ so these changes do not affect this process. From now on the fabrication steps will be shown for only one element of the 9×9 array of freely suspended silicon nitride windows. (Approximate time required for nine wafers to perform the exposure and the development – 1 hour. Schematic shown in Figure 2.8 (b).)
7. Use any photoresist and a Q-tip to patch any tweezer damage to the patterned side, then hardbake the resist at 90°C for 20 minutes. (Approximate time required for nine wafers – 45 min.)
8. Clean the Applied Materials reactive ion etcher (RIE) by running an O₂ plasma (30 sccm, 30 mTorr is fine) for 5 minutes. Load the wafers and etch the nitride

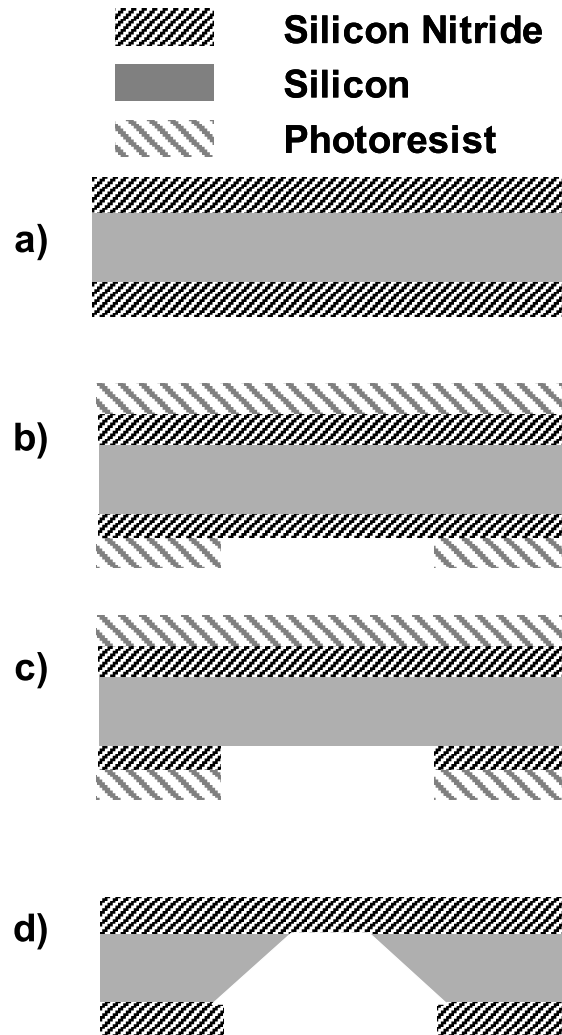


Figure 2.8: (Not to scale) Cross-sectional device schematic of the device during various stages of the fabrication of the freely suspended silicon nitride window: a) shows the starting wafer (20 mil thick) with 100 nm of low-stress silicon nitride, b) photolithography to define the square pattern on the wafer, c) RIE to remove the silicon nitride and expose the silicon, and d) removal of the photoresist, followed by an anisotropic wet etch using hot KOH, forms the freely suspended silicon nitride.

in CHF_3/O_2 30/0.7 sccm, 30 mTorr, power = 100%. For one wafer, the etch takes 12 minutes, for three, 15 minutes. Wafers must be supported on small chips so that they do not slide off the electrode when the chamber is roughed out. Without breaking vacuum, do an O_2 etch at 40 sccm 40 mT, power = 100% (10 minutes for three wafers) to remove the patterning photoresist. (Schematic shown in Figure 2.8 (c). Approximate time required for nine wafers – 1.5 hours.)

9. Clean off the remaining photoresist from both sides of the wafers with acetone, isopropyl, and deionized (DI) water.
10. Mix KOH (potassium hydroxide) with DI water in the ratio of 125 gm of KOH per 500 ml of solution. Make enough to comfortably cover the wafers. With the current wafer holders, I use 1500 ml solution. Maintain the temperature of the etching solution at 98°C . The higher the temperature, the faster the etch, but higher temperatures will also degrade the degree of anisotropy, and lead to larger window sizes. Place the wafers in the KOH solution and etch approximately 15 minutes beyond the time that the windows are first visible when looking through the wafer to a light source. The etching time takes about 3.25 hours for a 20 mil wafer in 95°C solution. When the etch is done, boil the wafers in DI water for at least 10 minutes, and then boil them again in a second (very clean) beaker of DI water in an effort to remove all residual KOH. Then remove each wafer, one at a time, from the beaker, rinse thoroughly with DI water spray (both sides), and drip dry the wafers being sure that runoff from the tweezers does not flow across the window area. (Schematic shown in Figure 2.8 (d). Approximate time required for nine wafers – 4.5 hours including setup time and cleanup.)

11. Inspect the wafers in the optical microscope, recording window size, cleanliness, and any unplanned through holes. Scribe the wafer name on the back side of the wafer.
12. Remove the back side nitride overhang using a physical mask in the reactive ion etcher, CHF_3/O_2 30/0.7 sccm, 30 mTorr, power = 100 %, for 7 minutes. (Approximate time required for nine wafers – 2.5 hours.)
13. Thin the front side nitride to a final thickness of 50 nm in the RIE, doing many short etches and checking the thickness with the Leitz microscope equipped with an interferometer. Note that initially the nitride is thick enough so that the thick film algorithm must be used on the Leitz. The etch rate is normally about 1 nm/s, so measure the initial thickness of the nitride, etch about halfway to 50 nm, check the thickness to calibrate the etch rate, and then etch to a final thickness of about 50 ± 1 nm. (Approximate time required for nine wafers – 4.0 hours.)
14. Spin 5.5% 495 PMMA, at 3500 rpm for 1 minute, using a mask chuck and the spring-loaded wafer holder. Bake at 170 C for one hour. (Schematic shown in Figure 2.9 (e). Approximate time required for nine wafers – 2.0 hours.)
15. Expose using the electron beam on the VB6. This is a very crucial step as things can go horribly wrong if they are not done with due care. I recommend doing a dose test on a wafer; one wafer sacrificed for this test is better than wasting the whole lot of wafers. Follow the procedure for this one wafer and see what distribution of hole sizes one gets. Then adjust the dose to get what is needed. The other important thing to think about is: what size of holes are needed for whatever you plan on doing? For the gated devices, I always

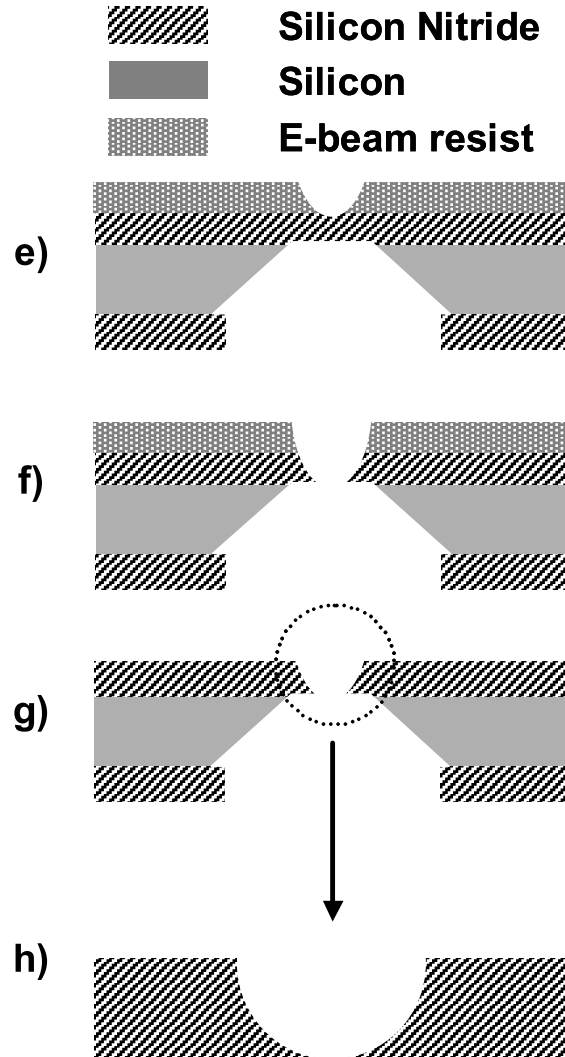


Figure 2.9: Cross-sectional device schematic of the device at various stages of fabrication after the fabrication of the suspended silicon nitride window: e) e-beam lithography and development, f) RIE using the Applied Materials etcher to form the nano-hole, g) removal of the e-beam resist using the RIE, and h) close-up cartoon view of the nano-hole to emphasize the bowl shaped cross-section of the hole.

used the 4 pixel exposure since I needed slightly bigger holes to begin with than for devices without gates. There are several executable files with suffix `gated.com` that can be used for exposing wafers for making gated samples.⁷ (Approximate time required for e-beam exposure for two wafers – 1.0 hours.)

16. Develop in 1:1 MIBK:IPA for 90 seconds. Lately I have used 60 seconds, and things have turned out OK. There is a need to look at this parameter since people at CNF think that the 90 seconds developing time is sure to overdevelop the features we expose. After developing, rinse in IPA (Iso-propyl alcohol/propanol) and then drip dry. (Figure 2.9 (e))

17. The final step is the nonlinear etch. This step is **the** crucial step, and several man-hours have been sacrificed at the altar of this step. The keyword is consistency for all the fabrication steps, but especially for this step. To get any good results one has to be consistent. The first thing to do is to clean the chamber thoroughly before using the Applied Materials reactive ion etcher (RIE). This has become important since in the last 2 years people have been etching all sorts of stuff in the Applied Materials etcher. My cleaning procedure is to O₂ clean for 5 min, then a CHF₃/O₂ etch for 5 min, and then follow it up with a O₂ clean for 5 min. I believe these 15 minutes are well spent, and I recommend them strongly. Now the chamber is ready for an etch. RIE the developed wafers in the Applied Materials RIE; the non-linear configuration is required for this step. The parameters of the etch are CHF₃/O₂: 30/0.7 sccm, 30 mTorr pressure, Power =100% for 1 min and 30 seconds, then remove the sample and do an oxygen clean, replace the sample again, etch

⁷These files are located on the main computer controlling the VB6, and are located in the Ralph group directory. The best way to reach these files is to ask CNF staff members, or ask someone from Ralph group.

for 1 min 30 sec. This total etch time is sensitive to a number of factors and one wafer from a lot should be used to try things out. It is important that the wafer be removed between intermediate O₂ cleans since such a clean will remove the e-beam resist before making the nano-hole in the silicon nitride membrane. Also, check that the system is balanced by doing a “dummy” etch after every O₂ clean, and before actually putting the wafer in for the etch. After the etching has been done, follow this with a 3 min O₂ clean without breaking the vacuum (40 mTorr and 40 sccm of O₂). This step removes the e-beam resist. (Approximate time required for etching a set of holes is – 1.5 hours including the conditioning of the chamber; this does not scale with the number of samples.)

These steps allow fabrication of a nano-hole (Figure 2.9 (h)). Figure 2.10 [14] shows a nano-hole imaged using a scanning transmission electron microscope (STEM). As mentioned earlier, the final size is a function of various parameters, and they can be adjusted to achieve the required hole size. For making the nanoparticle transistors the hole size required is ~ 10 nm. Next we consider how the nano-hole is used to fabricate a nanoparticle transistor.

2.4.2 Making a transistor using a nano-hole

Once the holes are fabricated at the CNF all the remaining steps are carried out in the Ralph group’s Sharon evaporator. One requires an overnight pump-down for every step described below; which means that one needs to use the evaporator for 4 continuous nights if one is making the gated devices. For two terminal devices (devices with no gate), it only takes one night to fabricate the samples. The first step is to fabricate the gate. I include the recipe that I have used.

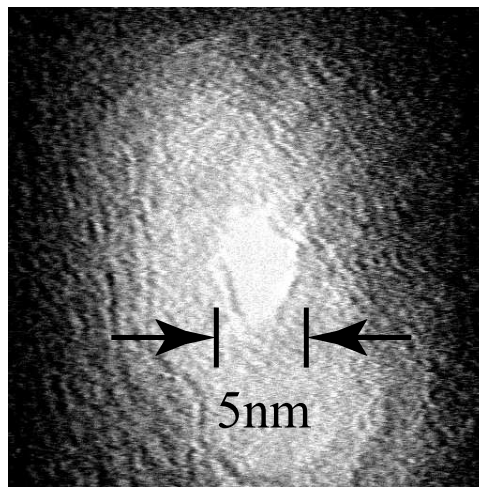


Figure 2.10: Nano-hole imaged using a scanning transmission electron microscope (STEM). The dark areas correspond to the electron opaque region of the silicon nitride membrane, whereas lighter regions correspond to thinner regions. The nano-hole is completely electron transparent.

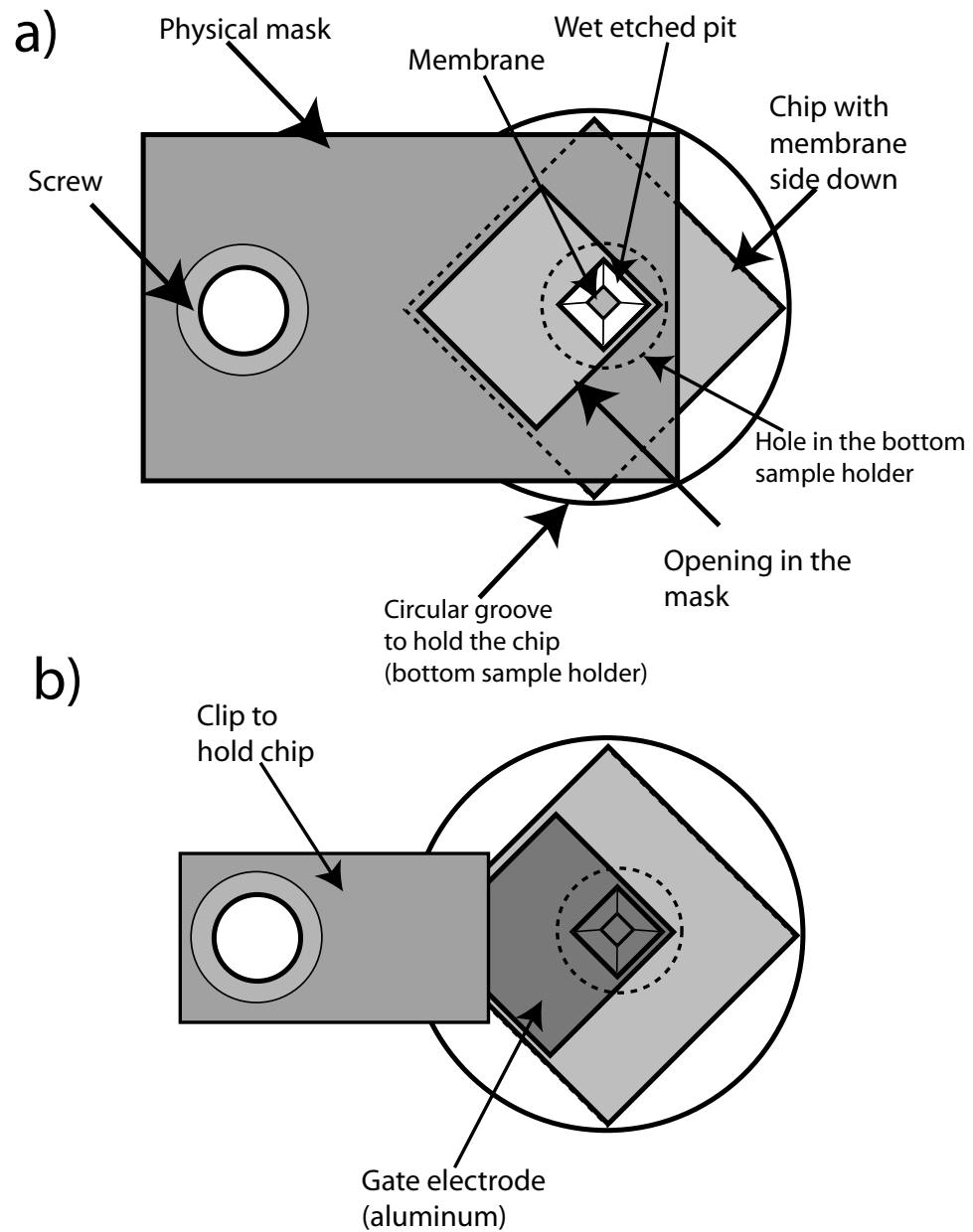


Figure 2.11: a) Schematic of the sample loading arrangement for the deposition of the gate electrode. b) Sample loading arrangement for anodization and deposition of SiO_x .

1. The samples are cleaved along the etch lines and loaded one-by-one in the gated sample holder (schematic shown in Figure 2.11 (a)). The samples are screwed onto the fixed stage. Two pellets of aluminum are used in a thermal boat to deposit the gate electrode. After loading the samples and the evaporation source, the chamber is pumped down; the stage is baked at 100°C for an hour. Towards the end of this hour, when the stage is hot, a dummy evaporation of the aluminum is done to get rid of the water vapor adsorbed on the evaporation source. The shutter is closed during this part, to avoid depositing aluminum onto the samples. After an overnight pump-down, 180 \AA of aluminum is deposited at $3 - 4 \text{ \AA/s}$ to define the gate electrode (Figure 2.12 (i)). Following the cooling of the source, the chamber is vented. The next step is anodizing, which forms the oxide layer to isolate the gate from the drain [15, 16].
2. The physical mask used for defining the gate is removed and a clip is used to contact the gate electrode and to hold the chip down (schematic shown in Figure 2.11 (b)). The sample holder is then attached to the fixed stage using teflon screws and a spacer, which are used to ensure that the gate electrode is floating with respect to the evaporation-chamber ground. Once the samples are loaded, an aluminum wire is used to contact the stage and is connected to a feed-through so that a bias voltage can be applied to the gate electrode. Following this, the chamber is pumped down, and the stage is baked, using a stage heater, for an hour. After an overnight pump-down, the samples are ready to be anodized. Before the anodization is started it is important to close the shutter to avoid occasional sputtering from the high voltage source. The first step in the anodization process is to let in O_2 gas into the chamber and to start a plasma using the high voltage source. The voltage setting for the

high voltage source is 1000 V. It is essential to let the samples first float with respect to the plasma to form good oxide layer without pinholes [15, 16]; this is done for 15 minutes. After that the O_2 gas is pumped out and replenished. The samples are anodized in a floating state for another 15 minutes after which they are connected in a circuit where the samples can be biased relative to the chamber ground. An ammeter is used to monitor the current flowing in the circuit, and a voltmeter measures the voltage drop between the samples and ground. At 0 V bias voltage the anodization is carried out for 15 minutes. After this the bias voltage is increased in steps of 0.5 V until it reaches 3.5 V, and at each step the bias voltage is maintained for 15 minutes. The O_2 gas is replenished every 30 minutes. When the bias voltage reaches 3.5 V the gas is replenished, and the anodization is continued for 2 hours. At the end of that period, the anodization is complete and the samples can be vented. This forms the first layer of oxide. This step is followed by deposition of silicon oxide (SiOx) to make sure there are no pinholes that will short the gate and the drain electrode.

3. After the chamber is vented following anodization, the sample holder is now reattached to the fixed stage without the teflon screws and spacers. The SiOx evaporation boat is loaded and the chamber is pumped down. The stage is baked for an hour and a dummy evaporation is done. The dummy evaporation is quite important before the SiOx deposition since it is porous and adsorbs a large quantity of moisture and outgasses a lot. After the overnight pump-down, the stage is cooled to liquid nitrogen temperature, and the temperature of the stage is monitored during the cooldown. It takes about 30 minutes of flowing liquid nitrogen to cool the sample to a temperature of ~ 100 K.

The evaporation is conducted at a rate of $3 - 4 \text{ \AA/s}$, and a total of 80 \AA is deposited. After the deposition, the stage is allowed to warm up without heating the stage; the warmup time can be shortened significantly by flowing warm air (from the utility outlets) through the space where liquid nitrogen was introduced. The amount of oxide deposited here is not enough to clog the holes if one starts with holes $\sim 10 \text{ nm}$ diameter. A cartoon view of the device after the deposition of the oxide is shown in Figure 2.12 (j).

4. Following the deposition of the oxide over the gate electrode, the last step in the fabrication process can be carried out. This involves deposition of the electrodes and the nanoparticles. The clips attached for anodization, as shown in Figure 2.11 (b), are removed, and the chips are rotated by 180° . Then the physical masks used in the gate process are attached again, as shown in Figure 2.13. In this way the gate electrode and the drain electrode are diagonally located on the chip, and can be contacted individually during the measurement. After the samples are loaded in the sample holder, they are attached to the rotating stage. Metals to be used for deposition are placed in an e-beam hearth, or in the thermal boats. I have mostly used e-beam evaporation for this last step. The first electrode of all the devices I have fabricated is made of aluminum; as a result, the first tunnel barrier is easily formed by oxidizing the aluminum by letting in oxygen into the chamber. For this reason it is important to pump-out the lines connecting the chamber and the oxygen gas bottle while the chamber is pumping down. Once the lines and the chamber are pumped-out using the roughing pump, the cryo-pump can be engaged. As is the case for all the previous depositions – the stage is baked, however, for the rotating stage the bake time is 1 hour 40 min since it takes

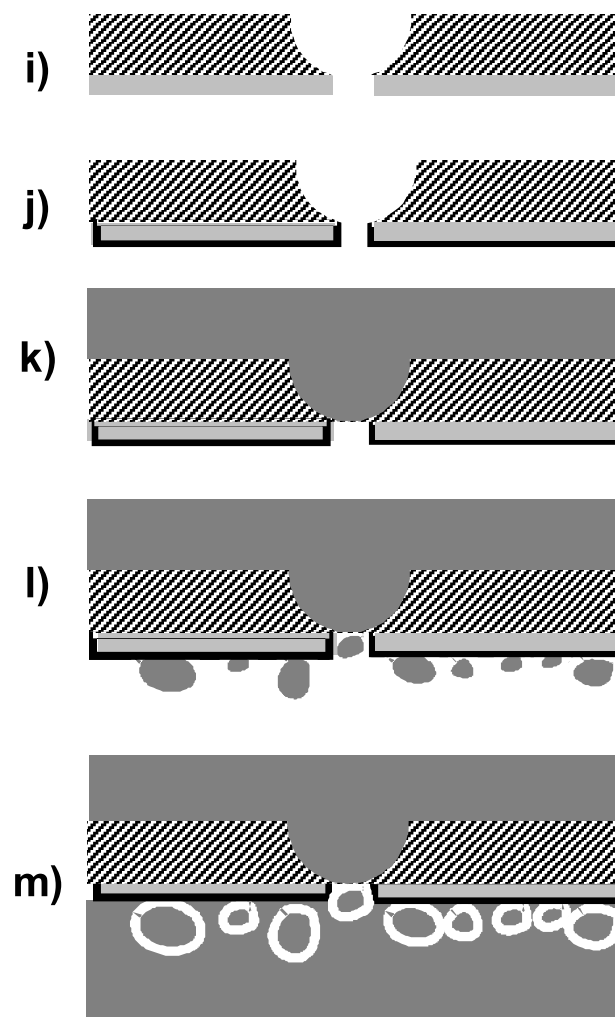


Figure 2.12: These diagrams show the final steps of deposition to form the electrodes and the nanoparticle; i) deposition of the gate electrode, j) formation of gate oxide from anodization, and deposition of SiO_x at liquid nitrogen temperature, k) deposition of the first electrode in the bowl shaped hole; followed by oxidation to fabricate the first tunnel barrier, l) deposition of nanoparticles and fabrication of the second tunnel barrier, and m) deposition of the second electrode.

longer for stage temperature to reach 100°C. The purpose behind a stage bake is to get rid of any water vapor that may be adhering to substrate, and clogging the nano-hole. When the stage is hot, dummy evaporation of all the metals is done (taking care to remember that the shutter should be closed). After an overnight pump-down, the samples are ready for evaporation. The first electrode to be deposited is the one on the flat side of the wafer, also referred to as the bowl-shaped hole side, with 1500 Å of aluminum at a rate of 7 – 10 Å/s. Al is deposited on the bottom side⁸ of the schematic shown in Figure 2.13. Once this is done, the stage is rotated so that the side with pit, formed due to the KOH etch, faces the evaporation sources. The gate valve is then closed, and O₂ gas is introduced in the chamber to a pressure of 50 mTorr for 3 minutes. This forms the first tunnel barrier. After this, the chamber is pumped out and particles are deposited. If the particles are being made out of aluminum then 22 Å of metal is deposited at a rate of 2 Å/s, or if they are being made out of cobalt 5 Å of cobalt is deposited at 1 Å/s. Evaporated metal tends to ball-up due to surface tension, and form discrete islands. Following this evaporation, if the nanoparticle is made of aluminum then the second tunnel barrier is formed in same way as the first one – by oxidizing in O₂ at 50 mTorr for 3 minutes. However, if it is a cobalt nanoparticle, then oxidation is not a viable option,⁹ and in that case 11 Å of aluminum oxide (AlO_x) is deposited using e-beam evaporation at a rate of 1.5 Å/s. After the formation of the oxide the second electrode is deposited. If it is to be made of aluminum, then 1500 Å is deposited at 7 – 10 Å/s; in case

⁸Backside of the plane of the paper on which the schematic is drawn.

⁹Oxidation of cobalt forms cobalt-oxide, an antiferromagnet. In general oxidation of ferromagnetic materials is not desirable since the magnetic oxide can cause spin-flip scattering. The mechanism for such scattering events is not well understood as of now.

the second electrode is to be made of either cobalt, or nickel, then 800 Å of the metal is deposited at 3 – 4 Å/s. This deposition completes the fabrication process.

The samples are removed from the chamber and unloaded carefully to avoid scratching the top electrodes. Care should also be taken to store these samples since the samples are extremely susceptible to electrostatic damage. I have normally not measured the samples for a week after fabrication. There is empirical evidence to suggest that the resistance between the top two electrodes, drain and gate, improves substantially during this time; this increases the isolation and reduces the leakage between the electrodes.

2.5 Measurement procedure

The measurements of the devices are carried out in two stages: the first one is called “dipping”, and the second one is cooling down the “good samples” in a dilution refrigerator.

2.5.1 Dipping samples in liquid helium

During this step the samples are checked quickly to see if they worth cooling down in the refrigerator. Since a significant fraction of samples, around 75%, are not worth investigating further – for a variety of reasons described later – it is quite essential to do the dipping carefully. The circuit used for the dipping is shown in Figure 2.14. The schematic of the dipping setup is shown in Figure 2.15, with the slight modification that the magnetic field is not used at this stage. As mentioned earlier, the samples are extremely sensitive to electrostatic discharge, so it is crucial

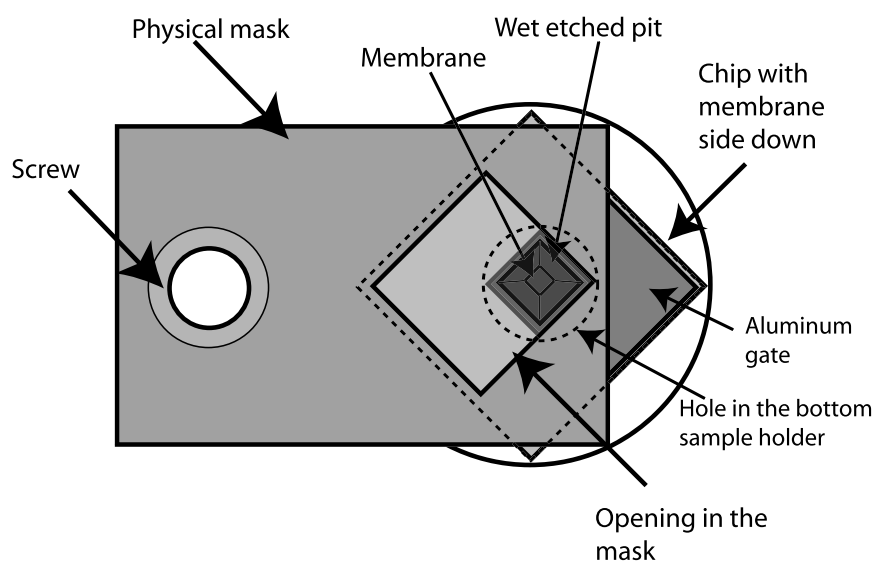


Figure 2.13: This cartoon shows the sample loading arrangement for the final step of depositing the electrodes and the nanoparticles.

that one grounds oneself with a grounding strap, and the sample-holder's terminals are shorted to each other. This ensures that some voltage is not accidentally applied across the device. Once the samples are loaded onto a dipstick they are pre-cooled to liquid nitrogen temperature. As soon as the boiling stops, the dipstick can be removed and inserted into a helium dewar; this cools the samples immediately to 4 K. Once the samples have cooled they can be connected into the circuit using the make-before-break switch. The computer acquisition program will acquire an I-V curve as the bias is swept at a frequency 10 mHz. It is also useful to look at the current through the device on an oscilloscope since bad devices can be detected quickly. A good device will exhibit a Coulomb blockade, and display sharp features in the I-V curve. We will define a good device by eliminating the devices which have "bad" characteristics. A device can be "bad" in a couple of different ways:

Capacitive device

It is easy to detect a device that is purely a capacitor, without a nanoparticle present in the junction, if one observes the current on the oscilloscope. In this case the trace will indicate either a positive or a negative displacement current most of the time. If one increases the frequency at which the voltage is swept the amplitude of the current will increase. A similar increase in current amplitude is seen if the amplitude of the bias voltage sweep is increased. These two characteristics uniquely identify this device as a capacitive device. Note that the displacement current is proportional to the rate of change of the bias voltage; consequently the current has a linear dependence on the frequency, and the amplitude. This device does not have any nanoparticle between the two electrodes; this is quite likely in a significant number of our devices considering that require on a nanoparticle to form directly

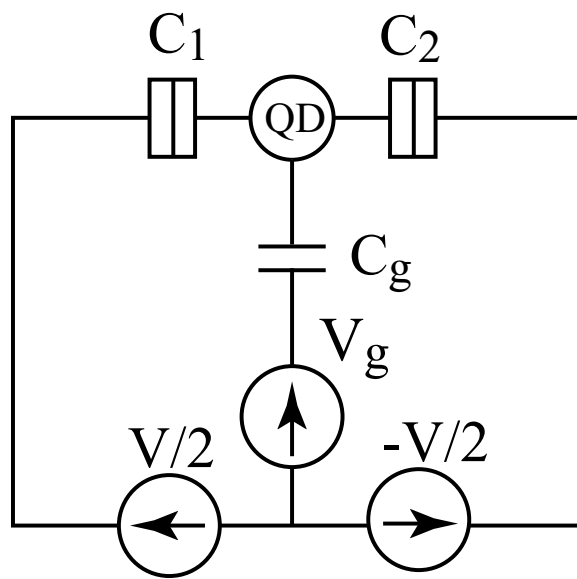


Figure 2.14: Circuit diagram for the measurement setup used for tunneling spectroscopy.

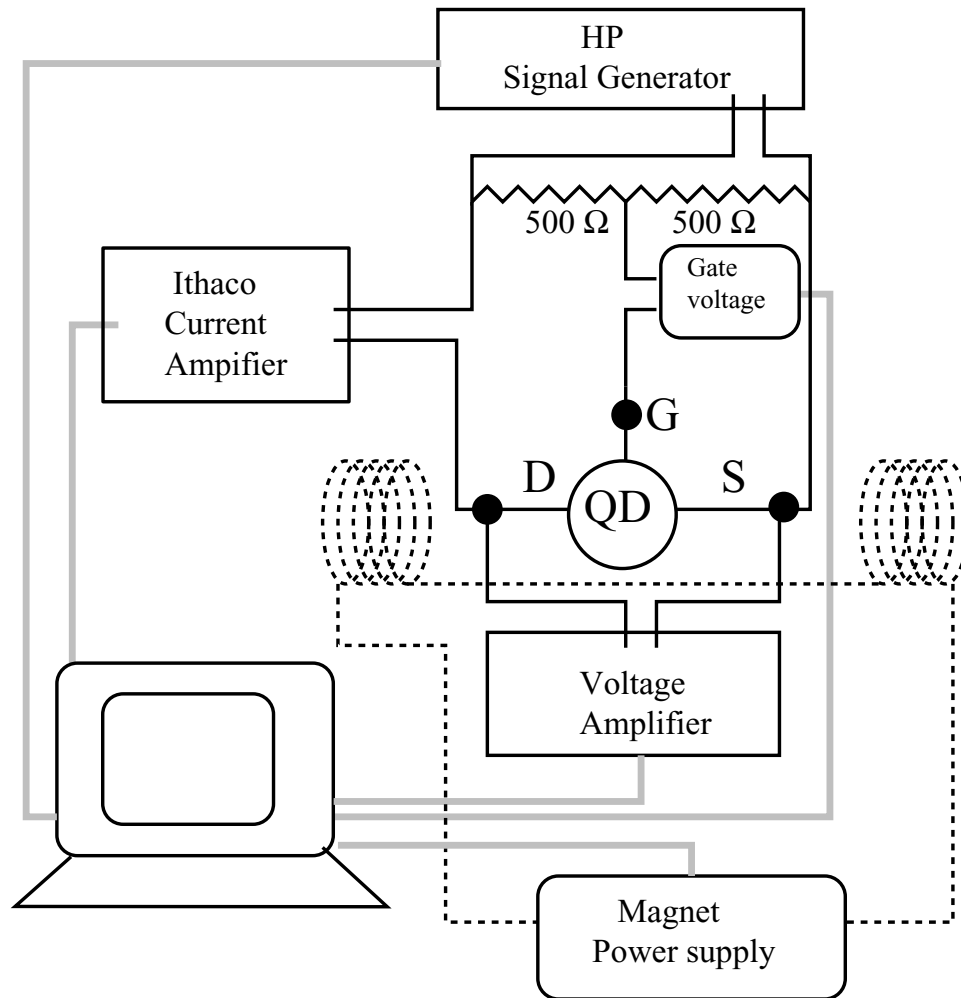


Figure 2.15: Schematic diagram of the measurement setup with the data acquisition system. Black lines indicate electrical connections, whereas grey lines indicate lines of communication between the data-acquisition computer and various equipments. QD is the quantum dot with three electrodes drain (D), source (S), and gate (G).

on a nano-hole. A large number of such devices in one set of samples indicates that the hole may be very small, and may be getting clogged during the gate process.

Resistive device

In this case the I-V curve looks like that for a resistor. The resistance varies quite a bit depending on the size of the hole. A large number of such samples in a set of samples may suggest that the holes are too large.

Incomplete Coulomb blockade

This category of bad devices is closely related to the devices of the resistive kind. In this case the blockade is smooth and the I-V curve lacks sharp features. This occurs mostly due to multiple particles in parallel connecting the two electrodes. Figure 2.16 (a) shows a device with these features.

A good device will exhibit none of the abovementioned characteristics, and have complete Coulomb blockade, together with sharp features in the I-V curve. Figure 2.16 (b) shows an example of a good device. When a good device is found a gate voltage should be applied to check if the blockade is modified. After a good device is identified, it is warmed up gradually to room temperature and is ready to be cooled in the dilution refrigerator.

2.5.2 Measurement in a dilution refrigerator

Measuring the device in the dilution refrigerator is very similar to the measurement during the dipping stage, and the experimental setup is as shown in Figure 2.15. After cooling down the sample to the base temperature of the dilution refrigerator (20 mK), the computer-controlled acquisition system allows measurement as a func-

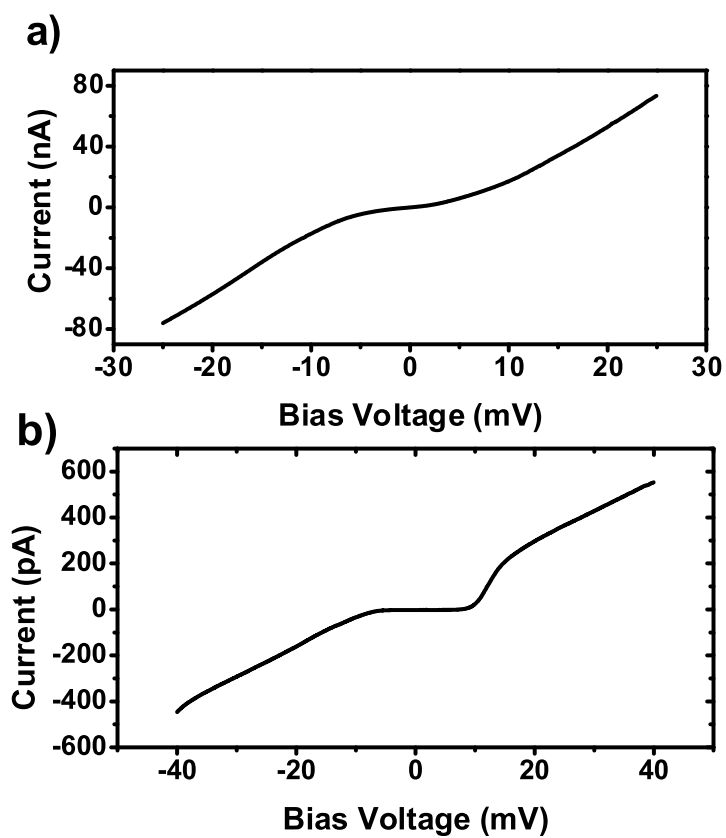


Figure 2.16: (a) I-V curve from a “bad” device, measured at 4 K, with multiple particles in parallel connected to the two electrodes. Trace of several Coulomb blockades in parallel is reflected in the non-linearity of the device. (b) I-V curve from a “good” device, at 4 K, shows a sharp Coulomb blockade.

tion of bias voltage, magnetic field, and gate voltage. The bias and gate voltage generator is controlled by the computer via the GPIB protocol, and the magnet power-supply is controlled via the RS-232 protocol. The current amplifier and the voltage amplifier operate on an internal battery, and the output of the amplifiers is connected via coaxial cables into a National Instruments DAQ card. Before the measurements are started, it is important to measure the noise in the setup, and to minimize it since it can affect the quality of the acquired data. The best way to measure the noise is to connect a triax splitter instead of a device; then turn the gain of the current amplifier to highest setting (10^{-11} A/V), and turn off the filtering on the current amplifier. Observing the output of the current amplifier on an oscilloscope allows monitoring of the noise. In the best case scenario, the noise level is 0.5 pA in the absence of any filtering. If this is not the case then there is a problem, and it has to be fixed before the measurements can be started. I will go over the various sources of noise briefly, and the procedure for minimizing them:

Noise reduction

The following sources of noise should be checked before connecting the samples in the dilution refrigerator to the external circuit.

Ground loops

Ground loops are a prominent source of noise, and are caused by the presence of two grounds in the circuit [17]. The best way to check for them is by looking over the circuit and ensuring that the only ground that you use to connect to the outer shields of a coaxial, or a triaxial, cable is the one connected to the refrigerator's support structure – the only ground used in the measurement setup.

Amplifiers and the voltage generators

The amplifiers used in the measurement have internal batteries (which last up to 17 hours), and I strongly recommend using this feature since connecting them to the mains causes the output to be more noisy. The signal generators used should be floating, and this can be checked by using an ohmmeter; if they are not floating then one is sure to run into problems with the ground loops. One way to make doubly sure that there are no ground loops is to connect the signal generators to the mains via isolation transformers.

Bad cables

Bad triaxial cables can create extra noise in the system by inadequately shielding the cables. This should be the last resort in terms of minimizing the noise and requires replacing the cables one at a time to find the bad one.

Once the noise is reduced to a level of 0.5 pA the setup is ready for acquisition. Note that the sources of noise that have been addressed above are mainly due to the external circuit. However, there is always the high frequency noise that travels from the equipment down to the samples. Reducing this noise is important for achieving lower electron temperatures, which in turn improves the resolution in energy (as discussed in Section 2.3.2). In order to achieve lower electronic temperatures I have fabricated a cryogenic filter; I will briefly discuss the construction of this filter in Appendix A. Once the noise in the circuit is minimized, the samples can be measured.

Example of data acquired from a dilution refrigerator

Figure 2.17 shows the conductance plot as a function of applied bias voltage. Discrete states in the nanoparticle can be observed at bias voltages immediately after

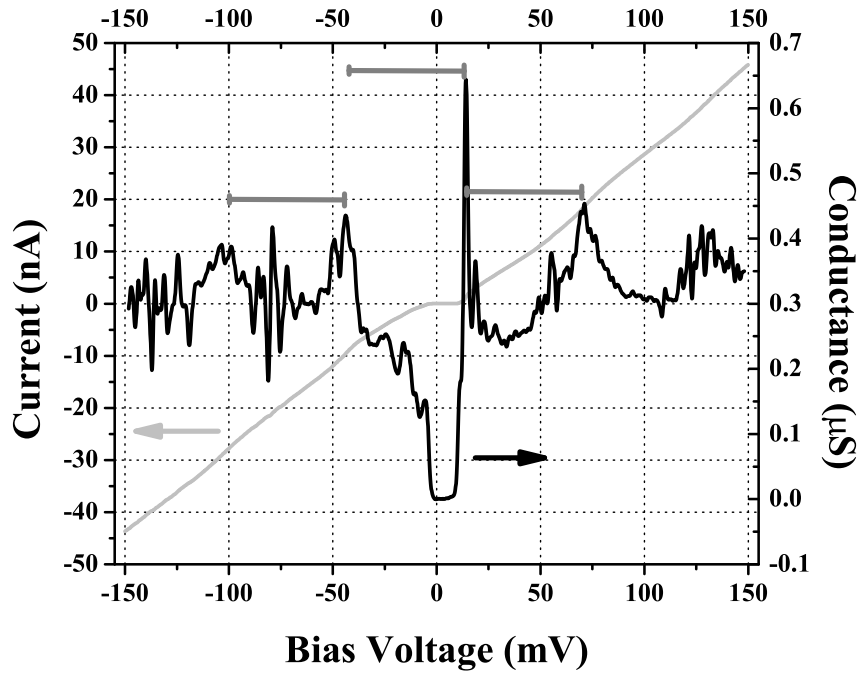


Figure 2.17: Plot of differential conductance vs. bias voltage and current vs. bias voltage for a device for high bias voltages. The data shown here was acquired at 20 mK, and is from a device with all the electrodes and the nanoparticle fabricated using aluminum. Here we clearly see the periodicity of the Coulomb charging energy in the plot of conductance. Peaks other than those closest to the Coulomb blockade region correspond to simultaneous tunneling of more than one electron. The gray bars mark the charging energy for this device. We measure the discrete energy levels in our device close to the blockade region, where only sequential tunneling of electrons can take place.

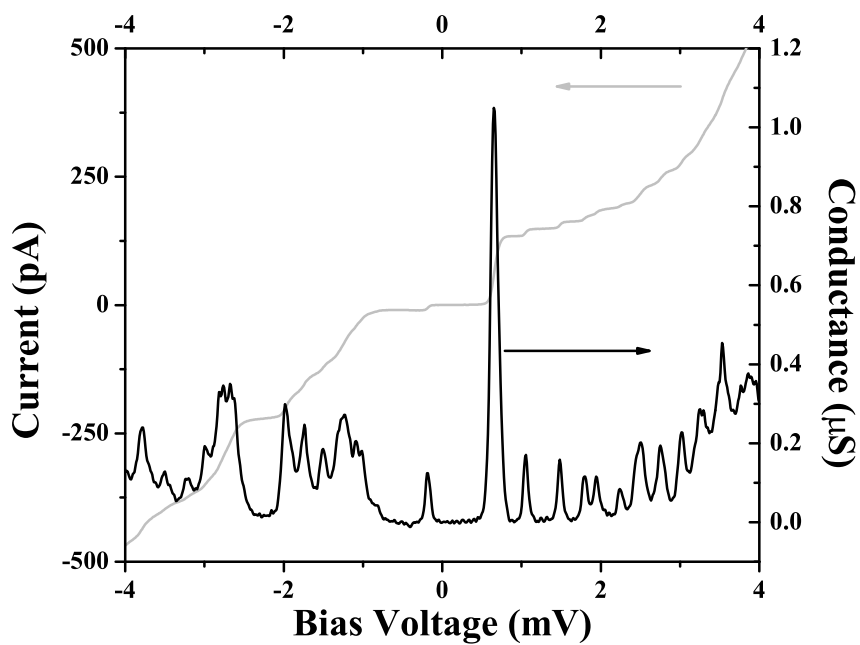


Figure 2.18: Plot of differential conductance vs. bias voltage and current vs. bias voltage for a device. The data shown here was acquired at a refrigerator temperature of 20 mK, and is from a device with all the electrodes and the nanoparticle fabricated using aluminum. Here only sequential single electron tunneling events take place. Discrete states give rise to steps in the measured current, and peaks in differential conductance. The region of Coulomb blockade near 0 mV is clearly seen.

the Coulomb blockade is overcome. Higher order peaks correspond to charging events where multiple electrons tunnel onto the island, and we do not measure our devices at such bias voltages. Figure 2.18 shows the I-V and dI/dV -V plot for a smaller bias voltage range. The steps in current correspond to threshold transitions, where one more energy level becomes available for current transport. The peaks in conductance correspond to the position of the energy levels within the nanoparticle. Measuring similar spectrum for a series of magnetic fields or gate voltage or both allows us to probe a variety of phenomena.

In the next chapter, we discuss the formalism of rate-equation which will allow us to extract quantitative information from the experimental data to be discussed in Chapter 4-8.

Bibliography

- [1] I. Giaever and H. R. Zeller, Phys. Rev. Lett. **20**, 1504, (1968).
- [2] D. C. Ralph, C. T. Black, and M. Tinkham, Phys. Rev. Lett. **78**, 4087, (1997).
- [3] D. Davidović and M. Tinkham, Phys. Rev. Lett. **83**, 1644, (1999).
- [4] H. Park *et al.*, Appl. Phys. Lett. **75**, 301 (1999).
- [5] D. Porath and P. Millo, J. Appl. Phys. **81**, 2241 (1997).
- [6] D. C. Ralph, C. T. Black, and M. Tinkham, Phys. Rev. Lett. **74**, 3241 (1995).
- [7] C. T. Black, D. C. Ralph, and M. Tinkham, Phys. Rev. Lett. **76**, 688 (1996).
- [8] D. V. Averin, A. N. Kotorov, and K. K. Likharev, Phys. Rev. B **44**, 6199 (1991).
- [9] T. A. Fulton and G. J. Dolan, Phys. Rev. Lett. **59**, 109 (1987).
- [10] M. H. Devoret and R. J. Schoelkopf, Nature **406**, 1039 (2000).
- [11] N. W. Ashcroft and N. D. Mermin, in *Solid State Physics* (W.P. Saunders Company).
- [12] K. S. Ralls, R. A. Buhrman, and R. C. Tiberio, Appl. Phys. Lett. **55**, 2459 (1989).
- [13] K. S. Ralls, Ph.D. thesis, Cornell University (1990).
- [14] M. M. Deshmukh, D. C. Ralph, M. Thomas, and J. Silcox, Appl. Phys. Lett. **75**, 1631 (1999).
- [15] J. L. Miles and P. H. Smith, J. Electrochem. Soc. **110**, 1241 (1963).
- [16] J. F. O'Hanlon, J. Vac. Sci. Tech. **7**, 330 (1969).
- [17] R. C. Richardson and E. N. Smith (ed.), in *Experimental Techniques in Condensed Matter Physics at Low Temperatures* (Addison Wesley).

Chapter 3

Rate equations calculations for a nanometer scale transistor

As described in the previous chapter, nanometer-scale single-electron transistors can now be fabricated in which electron flow occurs through a discrete spectrum of well-resolved quantum states on a metallic island [1]. A discrete energy spectrum has also been observed in devices incorporating semiconducting quantum dots and molecules [2, 3, 4]. In a transistor geometry, the source-drain voltage V and the gate voltage V_g , can be adjusted to achieve the simplest case that electron flow occurs just through a single quantum state. As V and V_g are changed, additional excited electronic states may also become energetically accessible for tunneling, providing alternative channels for current flow. In this regime, the tunneling processes can become quite complicated, due to the many combinations of non-equilibrium states that may be excited during tunneling, and the possibility of relaxation between these states.

As long as the tunnel-barrier resistances are much greater than h/e^2 and internal relaxation is negligible, the currents travelling via any number of energetically-

accessible states can be analyzed in a sequential-tunneling picture using a rate-equation approach. The general procedure for completing this type of analysis has been outlined previously, for example in Ref. [5, 6, 7]. This chapter is a revised version of a paper [8]. Edgar Bonet and I [8, 9] were motivated to model simple cases of sequential tunneling to explain and understand some of experimental results that I will discuss in the later chapters. We developed a way to implement the rate-equation approach together, and eventually used different platforms for implementation. Edgar wrote a C code to solve the problem numerically, whereas I used MATHEMATICA to solve the model analytically. Both these methods have their advantages and disadvantages, and I will point them out during the course of this chapter.

In the following section we consider the basic formalism of the rate-equation approach used to model sequential tunneling in a general manner. Later in the chapter we consider specific examples.

3.1 Rate-equation calculations of current flow

We are interested in calculating the tunneling current via a non-magnetic single-electron transistor in the regime where the discrete quantum states in the transistor island are well resolved. The circuit under consideration is shown in Fig. 3.1, which illustrates the definitions of the bias voltage V and the gate voltage V_g . We will limit our discussion to the conditions under which the energy levels are best resolved: (a) $k_B T$ is smaller than the level spacing, (b) the level spacing is much smaller than the Coulomb charging energy of the transistor island $e^2/(2C_\Sigma)$, where C_Σ is the total capacitance of the island, (c) the tunnel barriers have resistances $\gg h/e^2$, so that cotunneling processes may be neglected and the tunneling current is accurately

described by lowest-order perturbation theory [10], and (d) $k_B T$ is larger than the intrinsic lifetime broadening of the quantum states. In parts of the discussion, in order to simplify the notation, we will also assume that electron interactions are sufficiently weak that many-body eigenstates are well-approximated as single Slater-determinants specified by the occupation of a set of single-electron states. We neglect many-body effects associated with Fermi-edge singularities in electrodes with low-electron densities [11] and effects of coupling to phonons or local degrees of freedom, which can produce additional features in tunneling characteristics [12, 13, 14]. Under these approximations, the temperature enters our calculation only through the Fermi functions in the electrodes.

Our primary goals are to study the effects on current flow of non-equilibrium electronic excitations and electron-electron interactions. Non-equilibrium excitations can be suppressed when excited electronic states return back to the ground state at a rate that is fast compared to the electron tunneling rate. However, measurements on metal nanoparticles indicate that the relaxation rate is usually comparable to, or slower than, the tunneling rate in realistic samples [15, 9]. Therefore we will generally neglect internal relaxation effects entirely, limiting ourselves to noting the ways in which internal relaxation will produce qualitative changes to the results.

3.1.1 Energy of the eigenstates

In general, the quantum-mechanical electronic states within the transistor island can be complicated correlated many-electron eigenstates. The energy of any state can be written as a sum of three terms:

$$E = E_C + E_K + E_J, \quad (3.1)$$

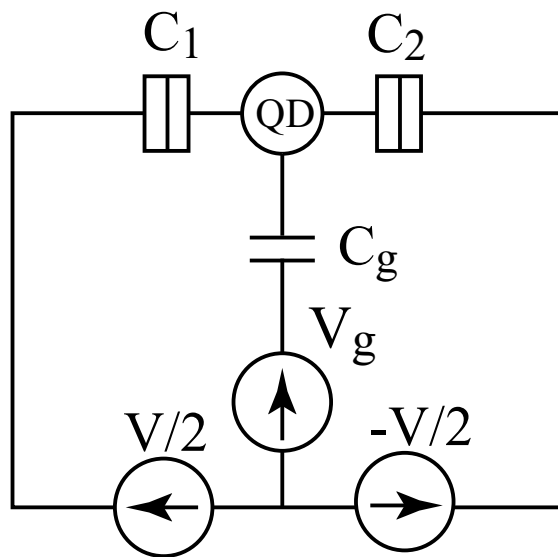


Figure 3.1: Circuit schematic defining the bias voltage V , the gate voltage V_g and the capacitances C_l , C_r and C_g . QD indicates the quantum dot.

the terms being respectively the electrostatic or “Coulomb” energy, the kinetic energy, and the fluctuations in the electron-electron interactions which vary as the many body state of the quantum dot changes. Notice that the mean-field contribution of the electron-electron interactions is the same as the electrostatic energy E_C [10]. Therefore E_J accounts only for the level-to-level fluctuations in these interactions.

Electrostatic energy

As discussed in section 2.2, the electrostatic energy is the largest energy-scale associated with nanoparticle transistor, and its microscopic origin lies in the mean-field approximation of the electron-electron interactions. The electrostatic energy of an island with N electrons can be written as

$$E_C = \frac{1}{2C_\Sigma}(Q_0 + Ne)^2, \quad (3.2)$$

where C_Σ is the total capacitance associated with the system and Q_0 is the background charge (related to the chemical potential of the system as discussed in section 2.2.1). Depending on the value of Q_0 , the number of electrons in the system can either increase or decrease by one during tunneling. These two charge states allow sequential transfer of charge from one electrode to another, once the threshold energy is provided by the applied bias. For the purpose of the discussion in this chapter we will consider the two charge states as N_0 and $N_1 = N_0 + 1$.

Kinetic energy

The kinetic energy of the electrons in the island can be written

$$E_K = \sum_i \epsilon_i^K n_i \quad (3.3)$$

where ϵ_i^K is the energy, relative to the Fermi level, of spin-degenerate single-electron quantum state i , and n_i is the occupancy of this level (either 0, 1, or 2).

In the absence of variations in electron-electron interactions between electrons in different energy levels, the energy of the island is just $E_C + E_K$. With our conventions, the threshold voltages required for the onset of a tunneling process can be pictured with simple energy diagrams, as illustrated in Fig. 3.2. For example, at $T = 0$, electrons can tunnel from lead k into the island if the island is a N_0 -electron state and Fermi energy E_k^F of lead k is above the energy ϵ_i of a non-fully occupied level. In the same way, electrons can tunnel out of the island into lead k if the island is in a N_1 -electron state and E_k^F is below the energy of a non-empty state. The onset of the current is associated with the first level available for tunneling, i.e. the lowest-energy non-full level in the N_0 -electrons ground state or the highest-energy non-empty level in the N_1 -electrons ground state. As V is ramped for a fixed value of V_g , the Fermi energy in a lead can sweep past the energy required to initiate tunneling via an eigenstate, producing a stepwise change in current.

The voltage-position, width, and current-amplitude of this step are the quantities that we will analyze. It is important to note that as V is increased, more than one spin-degenerate quantum level can contribute to tunneling even at the initial onset of current flow. One example of this case is illustrated by Fig. 3.2(b). The first allowed tunneling transition is for an electron to enter the level with energy ϵ_d from the right electrode. However, after this electron has tunneled in to give a total of N_1 electrons on the island, transitions to the left electrode can occur either from the state with energy ϵ_d , or from the lower-energy occupied state depicted in Fig. 3.2(b). If an electron tunnels out of the lower-energy state, subsequent tunneling transitions from the right electrode can involve either quantum level. Therefore, calculations of current for this situation must include tunneling processes occurring via both levels.

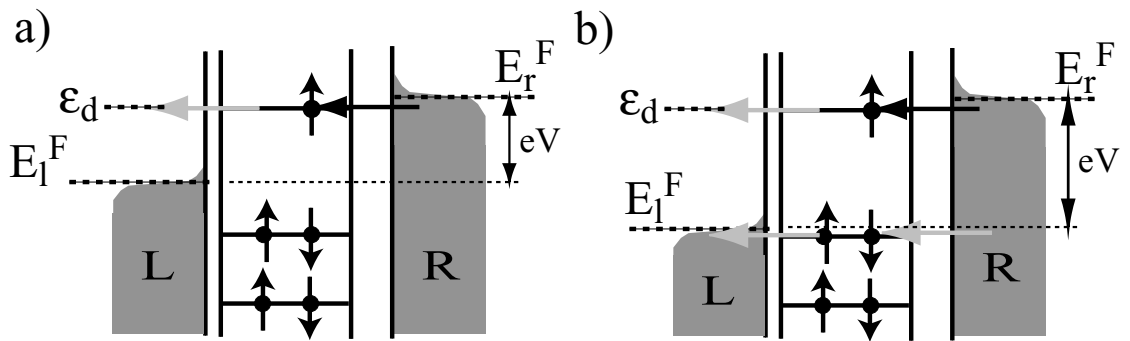


Figure 3.2: Energy diagrams for the single electron transistor. The island is represented by a set of discrete energy levels and the leads by continua of levels. Filled dots in the island stand for electrons present in an N_0 -electron ground state. The transition marked with a black arrow is the one which determines the initial threshold for starting current flow. The transitions marked by grey arrows then also contribute to the total current. (a) When the Fermi energy of the right lead is swept past the first level available for tunneling at energy ϵ_d , current can tunnel through this level. (b) For a slightly lower gate voltage and higher bias voltage, two levels contribute to tunneling even at the initial onset of current flow. The onset of current can occur as a function of the gate voltage or bias voltage or both.

It is possible to have current flow at vanishing V if the Fermi energy of both leads is aligned with the first level available for tunneling. The gate voltage that realizes this condition is called *degeneracy point* and is defined by

$$V_g^0 = -\frac{C_\Sigma}{eC_g}\epsilon_d \quad (3.4)$$

where ϵ_d is the energy of this particular level.

Variations in electron-electron interactions

In the presence of variations in electron-electron interactions between electrons in different energy levels [15], the energy of the island has the extra term

$$E_J = J(\{n_i\}) \quad (3.5)$$

Eq. (3.1) can be interpreted as an expansion of the energy of the system around the ground state: the second term is the part of E that is linear in $\{n_i\}$, the first term is the mean-field contribution of the quadratic part and $J(\{n_i\})$ is defined to be the rest. The net effect of the $J(\{n_i\})$ term is to produce shifts in the energy thresholds for tunneling that depend on the actual state of the particle. For instance, the effective energy level ϵ'_i for adding an electron to level i starting with the N_0 -electron state $\{n_j\}$ is

$$\epsilon'_i = \epsilon_i + J(\{n_j + \delta_{ij}\}) - J(\{n_j\}). \quad (3.6)$$

Notice that this is only defined if $n_i < 2$. In the same way, the energy of a non-empty energy level in a N_1 state can be defined as *minus* the energy required to remove an electron from that level.

3.1.2 Steady-state occupation probabilities

Because of the influence of the Coulomb charging energy, even in the simplest cases that we will consider, the occupation probability for a given many-body state $|\alpha\rangle =$

$\{n_i\}$ of the particle *cannot* be factorized as the product of occupancy probabilities for each single-electron level. Therefore we have to solve the full rate-equation problem where the occupation probability of each many-body state is treated as an independent variable.

The evolution of the occupation probability of state $|\alpha\rangle$ is given by[5, 6]

$$\frac{dP_\alpha}{dt} = \sum_{\beta} (\Gamma_{\beta \rightarrow \alpha} P_\beta - \Gamma_{\alpha \rightarrow \beta} P_\alpha) \quad (3.7)$$

where $\Gamma_{\alpha \rightarrow \beta}$ is the transition rate from state $|\alpha\rangle$ to state $|\beta\rangle$.

This can be written in matrix form as

$$\frac{d\mathbf{P}}{dt} = \mathbf{\Gamma} \cdot \mathbf{P} \quad (3.8)$$

with the following coefficients for the matrix $\mathbf{\Gamma}$:

$$\Gamma_{\alpha\beta} = \Gamma_{\beta \rightarrow \alpha} \quad \text{if} \quad \alpha \neq \beta \quad (3.9a)$$

$$\Gamma_{\alpha\alpha} = - \sum_{\beta \neq \alpha} \Gamma_{\alpha \rightarrow \beta}. \quad (3.9b)$$

We do not consider cotunneling or internal relaxation in the particle. Therefore, the possible transitions are those that have the same occupancy for all the levels, except one electron difference in one level. Let's assume that states $|\alpha\rangle$ and $|\beta\rangle$ differ only by $|\beta\rangle$ having one extra electron in level i . Then

$$\begin{aligned} \Gamma_{\alpha \rightarrow \beta} &= \gamma_i^l f(\epsilon_i' - E_i^F)(2 - n_i) \\ &\quad + \gamma_i^r f(\epsilon_i' - E_r^F)(2 - n_i) \end{aligned} \quad (3.10a)$$

$$\begin{aligned} \Gamma_{\beta \rightarrow \alpha} &= \gamma_i^l (1 - f(\epsilon_i' - E_i^F))n_i \\ &\quad + \gamma_i^r (1 - f(\epsilon_i' - E_r^F))n_i \end{aligned} \quad (3.10b)$$

where

$$f(x) = 1/(1 + \exp(x/k_B T)) \quad (3.11)$$

is the Fermi function corresponding to the temperature in the leads and γ_i^l and γ_i^r are the bare tunneling rates between level i and each of the leads. Here ϵ_i' is the energy needed to add an electron to state $|\alpha\rangle$ in level i . It includes the contribution of the interaction term.

The steady-state occupation probabilities can be found by finding the eigenvector \mathbf{P}_0 of $\mathbf{\Gamma}$ associated with the eigenvalue zero.

3.1.3 Current

Once the occupation probabilities for each state $|\alpha\rangle$ are determined at given values of V and V_g , then the current can be calculated either through the right tunnel barrier or through the left barrier. In the steady state these two currents are equal. The current through the left barrier is [5, 6]

$$I_l = |e| \sum_{\alpha} \sum_{\beta} \Gamma_{\alpha \rightarrow \beta}^l P_{\alpha} \quad (3.12)$$

where $\Gamma_{\alpha \rightarrow \beta}^l$ is the contribution of the left lead to $\Gamma_{\alpha \rightarrow \beta}$, multiplied by $+1$ or -1 depending on whether the $\alpha \rightarrow \beta$ transition gives a positive or negative contribution to the current.

In order to get a feeling of the physics that will come out of this rate-equation model, in the rest of the chapter we will consider selected examples that are simple enough to be solved by hand, yet have the basic ingredients of the complete problem.

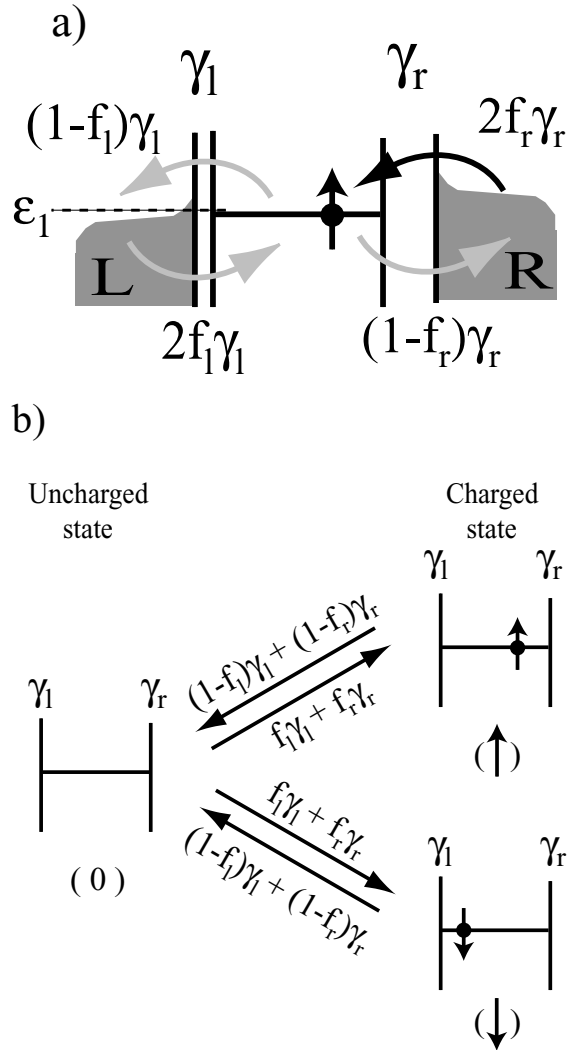


Figure 3.3: a) The figure shows the energy level diagram for calculating the current when only one energy level is involved in the transport. The uncharged state has 0 electron, and the charged state has 1 electron. b) Possible steps for the charging and discharging of the dot; this allows the current to be transported from one lead to another.

3.2 One spin-degenerate energy level accessible

3.2.1 General formula

Consider the situation represented in Fig. 3.3(a) where only one spin-degenerate energy level, with energy ϵ_1 , is accessible for tunneling and (on account of the large Coulomb energy) it can be occupied by either zero or one electron, but not two. If we call

$$f_r = f(\epsilon_1 - E_r^F) \quad (3.13a)$$

$$f_l = f(\epsilon_1 - E_l^F) \quad (3.13b)$$

and the various states being $0, \uparrow, \downarrow$, as shown in Figure 3.3(b), the transition rates are

$$\Gamma_{0 \rightarrow \uparrow} = \gamma_r f_r + \gamma_l f_l \quad (3.14a)$$

$$\Gamma_{0 \rightarrow \downarrow} = \gamma_r f_r + \gamma_l f_l \quad (3.14b)$$

$$\Gamma_{\uparrow \rightarrow 0} = \gamma_r (1 - f_r) + \gamma_l (1 - f_l) \quad (3.14c)$$

$$\Gamma_{\downarrow \rightarrow 0} = \gamma_r (1 - f_r) + \gamma_l (1 - f_l) \quad (3.14d)$$

for the tunneling-in and tunneling-out transitions. Then, the occupation probabilities can be calculated in using the method described in the previous section. They can be written as

$$P_{\uparrow} = \frac{\gamma_r f_r + \gamma_l f_l}{\gamma_r (1 + f_r) + \gamma_l (1 + f_l)} \quad (3.15a)$$

$$P_{\downarrow} = \frac{\gamma_r f_r + \gamma_l f_l}{\gamma_r (1 + f_r) + \gamma_l (1 + f_l)} \quad (3.15b)$$

$$P_0 = \frac{\gamma_r (1 - f_r) + \gamma_l (1 - f_l)}{\gamma_r (1 + f_r) + \gamma_l (1 + f_l)} \quad (3.15c)$$

and the current through the left lead in the steady state is

$$\begin{aligned} I &= |e| (\gamma_l(1 - f_l)(P_\uparrow + P_\downarrow) - 2\gamma_l f_l P_0) \\ &= 2|e| \frac{\gamma_r \gamma_l (f_r - f_l)}{\gamma_r(1 + f_r) + \gamma_l(1 + f_l)}. \end{aligned} \quad (3.16)$$

This expression differs from an approximate form used in Ref. [16] to analyze tunneling data.

We can plot the current as a function of the applied voltages by replacing f_k by their definitions in Eqs. (3.13). Figure 3.4(a) and (b) shows the current steps, and the conductance peaks respectively, as a function of the bias voltage when the gate voltage is first equal to the degeneracy point, then is tuned away from it.

The case in which one spin-degenerate level is accessible for tunneling, and the Coulomb energy permits an occupation of either 1 or 2 electrons (rather than 0 or 1) can be solved by exactly the same methods:¹

$$I = 2e \frac{\gamma_r \gamma_l (f_l - f_r)}{\gamma_r(2 - f_r) + \gamma_l(2 - f_l)}. \quad (3.17)$$

3.2.2 High bias limit

If the level spacing is very large compared to $k_B T$, there is an interesting regime in which V is substantially bigger than $k_B T/|e|$ yet only one level is involved in the current transport. The limiting current, in this case, is bias-independent and can be obtained from Eq. (3.16) by setting $f_r = 1$ and $f_l = 0$ (positive bias) or $f_l = 1$ and $f_r = 0$ (negative bias). For these two cases we have respectively:[17]

$$I_+ = 2|e| \frac{\gamma_r \gamma_l}{2\gamma_r + \gamma_l} \quad (3.18a)$$

$$I_- = -2|e| \frac{\gamma_r \gamma_l}{\gamma_r + 2\gamma_l}. \quad (3.18b)$$

¹Note that the results in Equations 3.16 and 3.17 are very natural, in that current must be zero if any of the three factors in the numerator are zero.

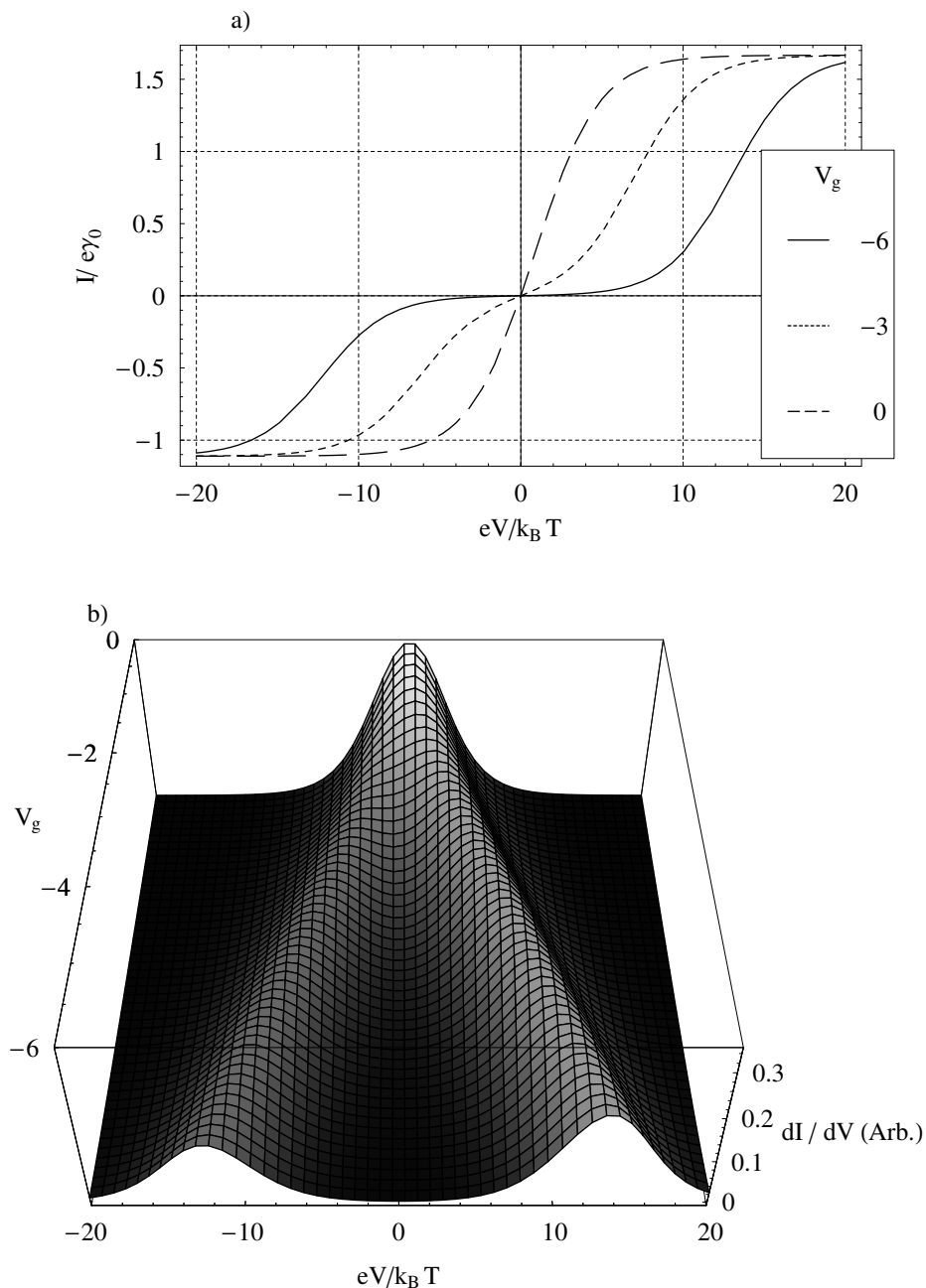


Figure 3.4: a) Current profiles as a function of the bias voltage for the case of a single spin-degenerate level accessible for tunneling, for three different gate voltages. We assume $C_r = C_l$ and $\gamma_l = 4\gamma_r$. The bias voltage is plotted in units of $k_B T/|e|$. The current is in units of $|e|\gamma_0$ where $\gamma_0 = \gamma_l\gamma_r/(\gamma_l + \gamma_r)$. The reduced gate voltage $v_g = |e|C_g(V_g - V_g^0)/C_\Sigma k_B T$ is 0, -3 or -6. b) Differential conductance plot shown as a function of the gate voltage V_g for the device with $C_r = C_l$ and $\gamma_l = 4\gamma_r$.

These expressions give different heights for the positive and negative current steps. Measuring these heights can, therefore, allow an experimental determination of both γ_r and γ_l . Note that this is in contrast with the case in which tunneling occurs through a single level that is not spin degenerate. In that case, the currents at high bias are

$$I_1^\pm = \pm |e| \frac{\gamma_r \gamma_l}{\gamma_r + \gamma_l} \quad (3.19)$$

for both bias direction [17], so that γ_r and γ_l cannot be determined separately.

In the limit of two barriers with very different tunneling rates for the same device (which can be experimentally relevant if the barrier thickness is not well controlled), the current depends only on the smaller γ . For example, if $\gamma_l \gg \gamma_r$, then $I_+ = 2|e|\gamma_r$ and $I_- = -|e|\gamma_r$. The factor of 2 in I_+/I_- arises from the difference in the number of spin states accessible for tunneling during the rate-limiting transition across the right barrier.

3.2.3 Position and width of the current step

Next, we consider the case depicted in Fig. 3.5, in which V_g is adjusted away from the degeneracy point, so that at the threshold V for tunneling only the effective Fermi energy in the right electrode is close to ϵ_1 , while the Fermi energy of the left electrode is at a much lower energy. That is, we will assume $f_l = 0$. Using this assumption, after some algebra Equation (3.16) becomes

$$I = I_+ f \left(\epsilon_1 - E_r^F - k_B T \ln \frac{2\gamma_r + \gamma_l}{\gamma_r + \gamma_l} \right). \quad (3.20)$$

Even though both spin-states of the quantum level contribute to tunneling, we can see in this expression that the current step has the shape of a simple Fermi function whose width is given by the electron temperature of the leads. However, at non-zero temperature, the center of the step is shifted relative to its position at zero

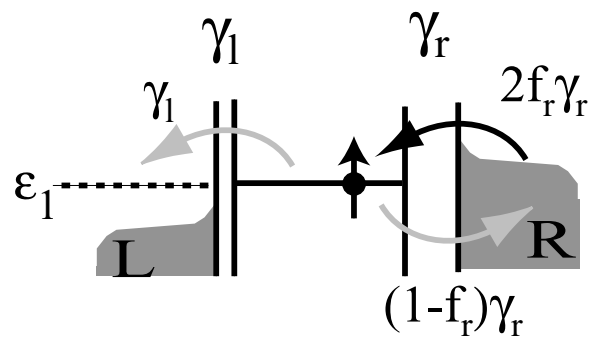


Figure 3.5: Energy diagram with one level available for tunneling and $V_g < V_G^0$. Since E_i^F is substantially below ϵ_1 , electrons can tunnel into the island only from the right lead.

temperature. The shift is proportional to the temperature, vanishes if $\gamma_l \gg \gamma_r$, and has a maximum value of $k_B T \ln 2$ when $\gamma_r \gg \gamma_l$. Fig. 3.6(a) shows the shape of the conductance peak dI/dV in the latter limit for three different temperatures, and Fig. 3.6(b) shows the greyscale plot of TdI/dV as a function of the temperature. The plot of TdI/dV compensates for the decrease in the peak conductance as a function of temperature. Linear dependence of the peak position on the temperature is evident from this graph, where the position of the peak is indicated by white color.

3.2.4 Zeeman splitting of the energy level

In the presence of an applied magnetic field, the two spin states associated with a given orbital level are no longer degenerate, but split to give the energies $\epsilon^{\downarrow,\uparrow} = \epsilon_1 \pm g\mu_B\mu_0 H/2$. We use the notation $f_k^{\downarrow,\uparrow} \equiv f(\epsilon_1^{\downarrow,\uparrow} - E_k^F)$, then the transition rates are

$$\Gamma_{0 \rightarrow \downarrow, \uparrow} = \gamma_r f_r^{\downarrow, \uparrow} + \gamma_l f_l^{\downarrow, \uparrow} \quad (3.21a)$$

$$\Gamma_{\downarrow, \uparrow \rightarrow 0} = \gamma_r (1 - f_r^{\downarrow, \uparrow}) + \gamma_l (1 - f_l^{\downarrow, \uparrow}). \quad (3.21b)$$

The occupation probabilities are

$$P_0 = \frac{1}{1 + \frac{\Gamma_{0 \rightarrow \downarrow}}{\Gamma_{\downarrow \rightarrow 0}} + \frac{\Gamma_{0 \rightarrow \uparrow}}{\Gamma_{\uparrow \rightarrow 0}}} \quad (3.22a)$$

$$P_{\downarrow, \uparrow} = \frac{\Gamma_{0 \rightarrow \downarrow, \uparrow}}{\Gamma_{\downarrow, \uparrow \rightarrow 0}} P_0 \quad (3.22b)$$

and the current through the left lead is

$$I = |e|\gamma_l ((1 - f_l^\downarrow)P_\downarrow + (1 - f_l^\uparrow)P_\uparrow - (f_l^\downarrow + f_l^\uparrow)P_0) \quad (3.23)$$

Figure 3.7 shows the effect of the magnetic field on the conductance peak at positive bias for a gate voltage below the degeneracy point. The peak – that was observed

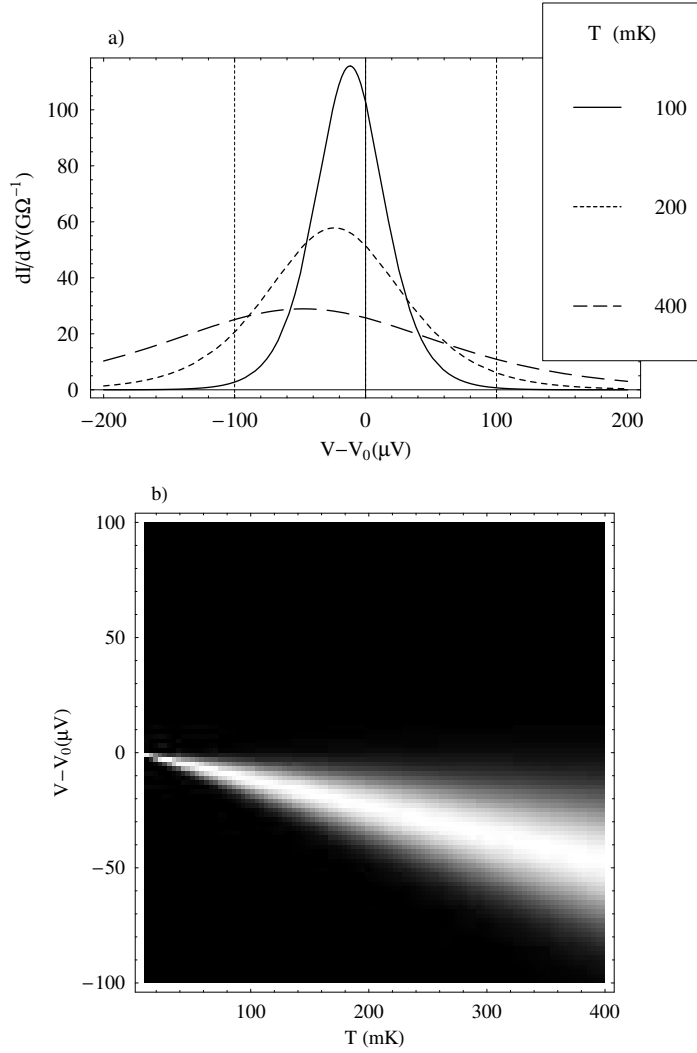


Figure 3.6: (a) Conductance peak at positive bias and negative gate voltage for three different temperatures. We assume $C_r = C_l$, $\gamma_l = 50$ MHz[9] and $\gamma_r \gg \gamma_l$. The peak occurs at $V_0 = 2C_g(V_g - V_g^0)/C_\Sigma$ at zero temperature and shifts from this position by an amount $2k_B T \ln 2/|e|$ at non-zero temperature. b) The effect of temperature on the position of this peak can be seen here. Shown here is greyscale plot of TdI/dV as a function of temperature (peak conductance $\propto 1/T$, therefore by plotting TdI/dV we compensate for the loss of peak amplitude). The peak in conductance is indicated by the white colored region while regions of zero conductance are indicated by the black areas. The broadening of the peaks can also be seen as a function of temperature.

before any magnetic field was applied – splits into two subpeaks of different weight. This asymmetry can be understood by noticing that the first subpeak² carries a current given by Eq. (3.19) and the two peaks together give a total current given by Eq. (3.18). Then the fraction of the total current carried by the first subpeak is just

$$\frac{I_1^+}{I_+} = \frac{2\gamma_r + \gamma_l}{2\gamma_r + 2\gamma_l}. \quad (3.24)$$

If the resistance of the right barrier is much smaller than that of the left barrier we have $\gamma_r \gg \gamma_l$, and this ratio of current steps ($\frac{I_1^+}{I_+}$) is one and the second peak vanishes [17].³ On the other hand, if $\gamma_l \gg \gamma_r$, the peak splits into two subpeaks carrying the same current. These two cases of asymmetry can be clearly seen in Figure 3.8.⁴

3.3 Two levels accessible

Next consider the situation pictured in Fig. 3.9 where two spin-degenerate levels are accessible for tunneling and the number of electrons in these levels is $N = 2$ or 3. Because of Coulomb blockade, no current flow is possible until an electron can tunnel from the right electrode to state 2; however after this happens both states 1 and 2 can contribute to the current even at the initial current onset. Any particular charge state of the two energy level system is indicated by showing the occupation, with appropriate spins, in level 1 followed by those in level 2; this convention is clearly noted in Figures 3.9 and 3.10. For example the state with two electrons in

²The first subpeak corresponds to the one that contributes to the current at lower bias voltage. In this particular case where $N_0 \rightarrow N_0 + 1$ is the threshold transition; the first subpeak is due to tunneling via energy level with “spin-up” character. Here “up” is the direction of the applied magnetic field. The second subpeak – which occurs at higher bias – is due to tunneling via energy level with “spin-down” character.

³In the energy diagrams used in this thesis we indicate the higher resistance barrier by drawing it to be thicker than the other.

⁴I think that many people mistakenly attribute absence of Zeeman splitting to the more exotic case of higher spin states of a quantum dot without ruling out this simple scenario [20].

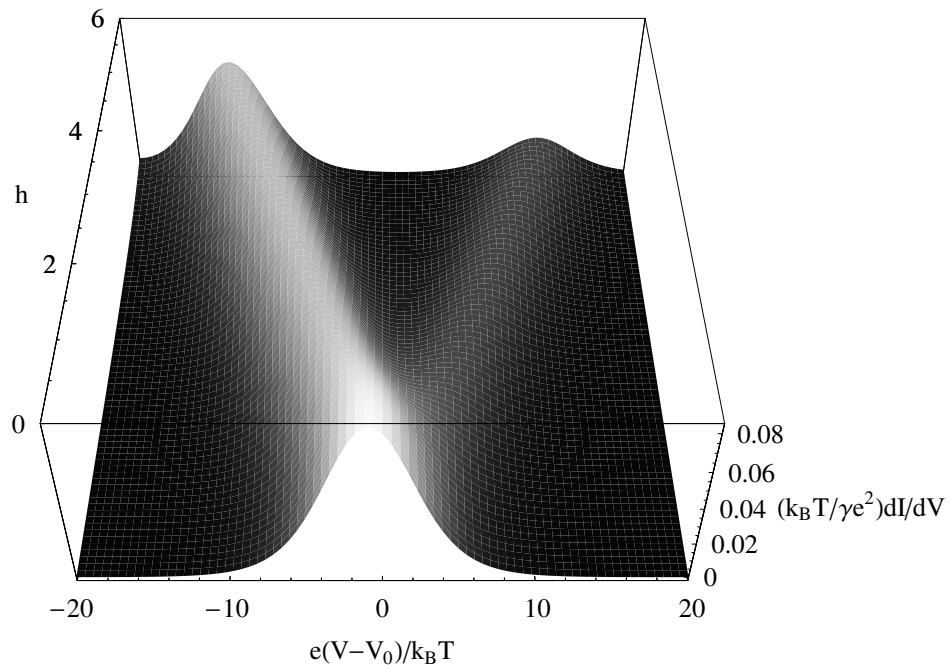


Figure 3.7: (a) Splitting of a conductance peak in a magnetic field. We assume $f_l^\pm = 0$, $C_r = C_l$, and $\gamma_r = \gamma_l = \gamma$. At zero temperature and zero field the peak occurs at $V_0 = 2C_g(V_g - V_g^0)/C_\Sigma$. The reduced field is defined as $h = g\mu_B\mu_0 H/(2k_B T)$. Notice the unequal heights of the two conductance peaks.

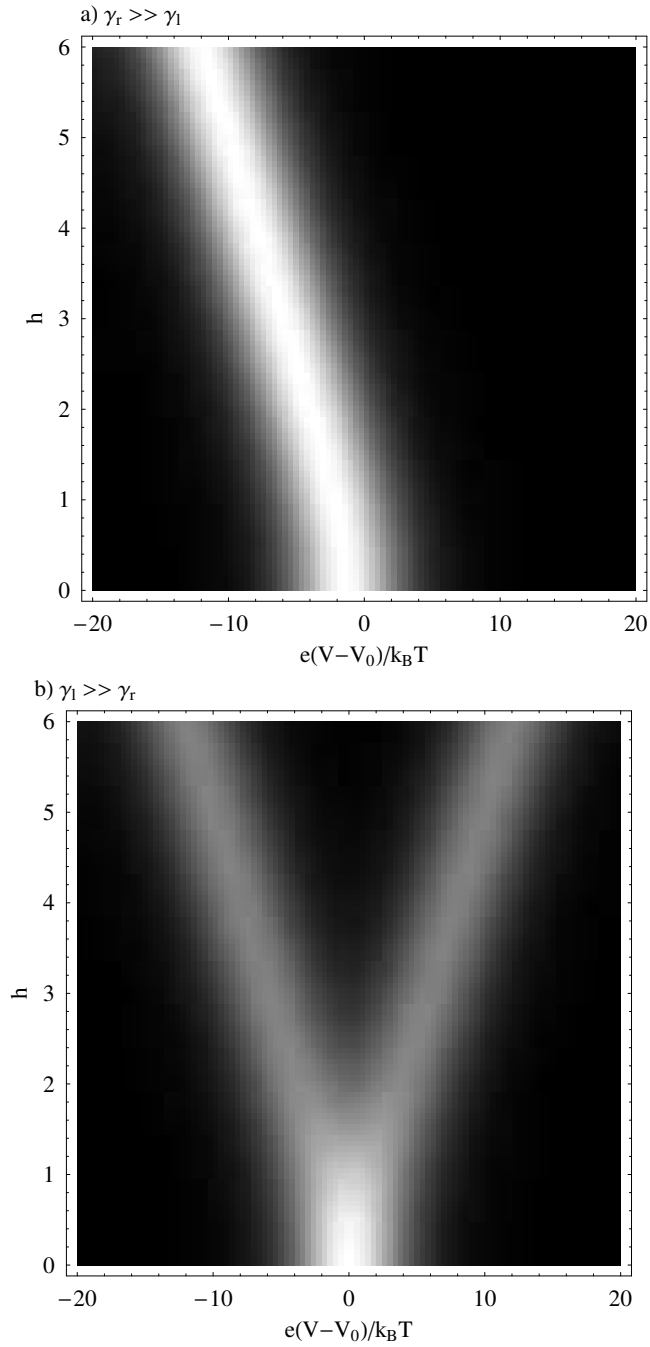


Figure 3.8: Calculated greyscale conductance plot for two cases: (a) $\gamma_r \gg \gamma_l$, the rate limiting step occurs across the left barrier, and the weight of the second Zeeman-split pair is negligibly small. (b) $\gamma_l \gg \gamma_r$, the rate limiting step occurs across the right tunnel barrier, and the peak splits into two subpeaks carrying the same current.

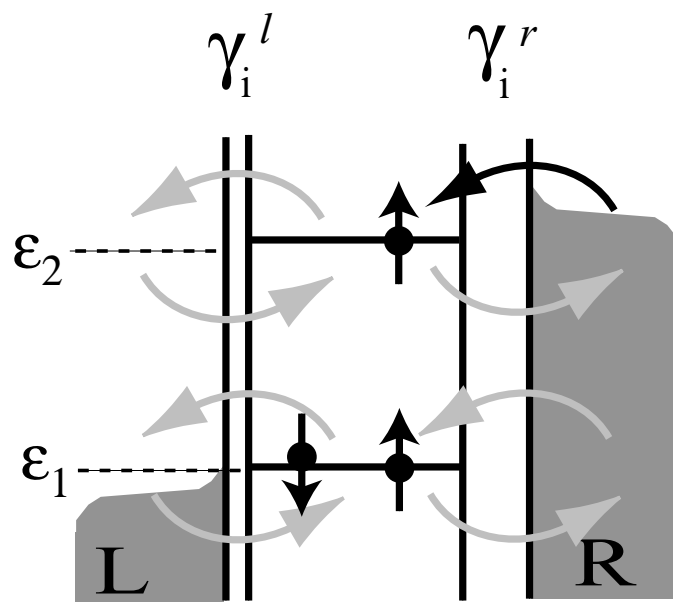
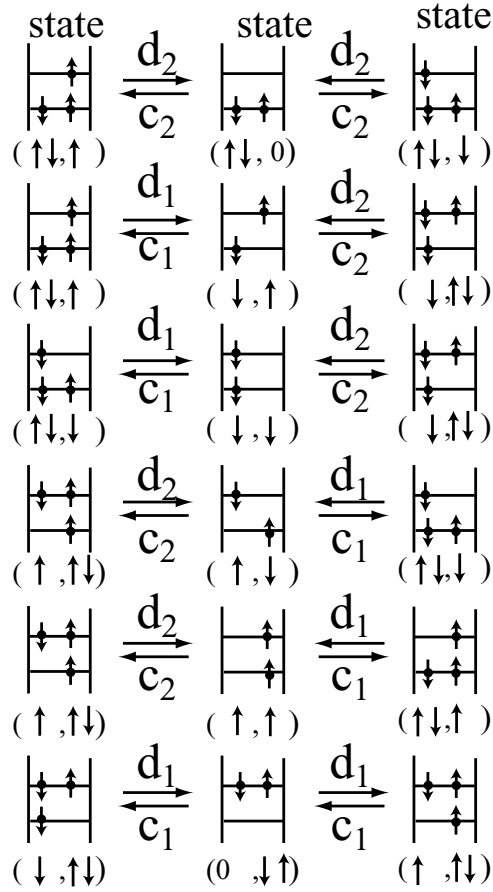


Figure 3.9: Energy diagram for a case with two levels available for tunneling. Also indicated at all the possible paths for the electron to tunnel-in and tunnel-out.

Charged Uncharged Charged



$$c_i = \gamma_i^l f_i^l + \gamma_i^r f_i^r$$

$$d_i = \gamma_i^l (1-f_i^l) + \gamma_i^r (1-f_i^r)$$

Figure 3.10: Available transitions for a quantum dot with two energy levels available with 2 electrons in the uncharged states. There are $6 = \binom{4}{2}$ possible uncharged states, and $4 = \binom{4}{3}$ charged states. These transitions represent all the possible states as the bias voltage is gradually increased to the eventual position shown in Figure 3.9.

level 1 and a spin-up electron in level 2 is represented by $(\uparrow\downarrow, \uparrow)$, and let $P(\uparrow\downarrow, \uparrow)$ be the steady state probability of finding the system in the state $(\uparrow\downarrow, \uparrow)$. γ_i^k denotes the bare tunneling rate of level i across barrier k . Figure 3.10 shows the available transitions together with the corresponding transition rates.

3.3.1 Rate equation

The rate equation, in this case, has to describe twelve possible transitions between ten different states. It is, therefore, convenient to use the matrix notation of Eq. (3.8), which gives

$$\frac{d}{dt} \begin{pmatrix} P(\uparrow\downarrow, 00) \\ P(\uparrow 0, \uparrow 0) \\ P(\uparrow 0, 0 \downarrow) \\ P(0 \downarrow, \uparrow 0) \\ P(0 \downarrow, 0 \downarrow) \\ P(00, \uparrow\downarrow) \\ P(\uparrow\downarrow, \uparrow 0) \\ P(\uparrow\downarrow, 0 \downarrow) \\ P(\uparrow 0, \uparrow\downarrow) \\ P(0 \downarrow, \uparrow\downarrow) \end{pmatrix} = \mathbf{\Gamma} \begin{pmatrix} P(\uparrow\downarrow, 00) \\ P(\uparrow 0, \uparrow 0) \\ P(\uparrow 0, 0 \downarrow) \\ P(0 \downarrow, \uparrow 0) \\ P(0 \downarrow, 0 \downarrow) \\ P(00, \uparrow\downarrow) \\ P(\uparrow\downarrow, \uparrow 0) \\ P(\uparrow\downarrow, 0 \downarrow) \\ P(\uparrow 0, \uparrow\downarrow) \\ P(0 \downarrow, \uparrow\downarrow) \end{pmatrix} \quad (3.25)$$

with

$$\mathbf{\Gamma} = \left(\begin{array}{cccccc|cccc} -2c_2 & 0 & 0 & 0 & 0 & 0 & d_2 & d_2 & 0 & 0 \\ 0 & -c_1 - c_2 & 0 & 0 & 0 & 0 & d_1 & 0 & d_2 & 0 \\ 0 & 0 & -c_1 - c_2 & 0 & 0 & 0 & 0 & d_1 & d_2 & 0 \\ 0 & 0 & 0 & -c_1 - c_2 & 0 & 0 & d_1 & 0 & 0 & d_2 \\ 0 & 0 & 0 & 0 & -c_1 - c_2 & 0 & 0 & d_1 & 0 & d_2 \\ 0 & 0 & 0 & 0 & 0 & -2c_1 & 0 & 0 & d_1 & d_1 \\ \hline c_2 & c_1 & 0 & c_1 & 0 & 0 & -2d_1 - d_2 & 0 & 0 & 0 \\ c_2 & 0 & c_1 & 0 & c_1 & 0 & 0 & -2d_1 - d_2 & 0 & 0 \\ 0 & c_2 & c_2 & 0 & 0 & c_1 & 0 & 0 & -2d_2 - d_1 & 0 \\ 0 & 0 & 0 & c_2 & c_2 & c_1 & 0 & 0 & 0 & -2d_2 - d_1 \end{array} \right),$$

where $c_i = \gamma_i^l f_i^l + \gamma_i^r f_i^r$, and $d_i = \gamma_i^l(1 - f_i^l) + \gamma_i^r(1 - f_i^r)$. This matrix has the structure

$$\mathbf{\Gamma} = \left(\begin{array}{c|c} \mathbf{\Gamma}_{uu} & \mathbf{\Gamma}_{uc} \\ \hline \mathbf{\Gamma}_{cu} & \mathbf{\Gamma}_{cc} \end{array} \right) \quad (3.26)$$

where $\mathbf{\Gamma}_{uu}$ and $\mathbf{\Gamma}_{cc}$ are diagonal blocks associated respectively with the N_0 -electron (*uncharged*) and N_1 -electron (*charged*) states. The cross-diagonal blocks are associated with the tunneling-out ($\mathbf{\Gamma}_{uc}$) and tunneling-in ($\mathbf{\Gamma}_{cu}$) events. This structure is preserved for whatever number of levels are available for tunneling.

MATHEMATICA can then be used to find the *analytical* form for the steady state probabilities in terms of the tunneling rates for the barriers (γ_i^k ; $k = l, r$; $i = 1, 2$), and the Fermi functions in the leads evaluated at the energy of each of the levels (f_i^k ; $k = l, r$; $i = 1, 2$). Solving for the steady state probabilities essentially means solving for the eigenvectors corresponding to the eigenvalue 0 for the matrix $\mathbf{\Gamma}$.⁵

⁵This works quite well for matrices with dimension up to 35. The advantage of this method

3.3.2 Current

Once the steady state probabilities are evaluated, the current can be calculated by evaluating the *net* tunneling rate across one barrier as described by Equation 3.12. In Fig. 3.11 we compare this current expression to the current we would have in the presence of infinitely fast relaxation in the island (states $(\uparrow 0, \uparrow 0), (\uparrow 0, 0 \downarrow), (0 \downarrow, 0 \downarrow)$, and $(\uparrow 0, \uparrow 0)$ relaxing instantaneously to $(\uparrow \downarrow, 00)$). In such a case, electrons can only tunnel into the higher energy level in the island. Since the tunneling-in of electrons is the rate-limiting process, this situation is equivalent to the case of Eq. (3.16) when only one level is accessible for tunneling, and the current would just be

$$I_{\text{equilibrium}} = 2|e|\gamma_2^r f(\epsilon_2 - E_r^F). \quad (3.27)$$

The main effect of non-equilibrium states as illustrated in Fig. 3.11 is therefore to shift the current step to lower voltage. Although not exactly a Fermi function, the shape of the current step is very close to a Fermi function, shifted by $-1.79k_B T$ and widened by 8.5%. The shift can be understood as follows: When $E_r^F = \epsilon_2$, electrons tunneling to the upper level come from half-full states in the right lead. If the island is in a non-equilibrium state ($(\uparrow 0, \uparrow 0)$ or $(00, \uparrow \downarrow)$), electrons can also tunnel to the lower level. Since these electrons come from full states in the lead, the current at $E_r^F = \epsilon_2$ is higher when these states are allowed, hence the shift.

The shift in the position of the peak due to non-equilibrium can be examined from another perspective. As shown in Figure 3.12(a) equilibrium and non-equilibrium scenarios can be seen in the same device with different gate and bias voltages. As one sweeps the gate voltage, the threshold bias voltage required for initiating the

over the C program written by Edgar Bonet, is that one can find analytical expressions for various quantities. For example, analytical expressions for a sub-space of parameters helps to understand the role of a particular parameter. Also, once the expression for current is found for the largest bias condition, the current for all the intermediate conditions does not need to be calculated separately.

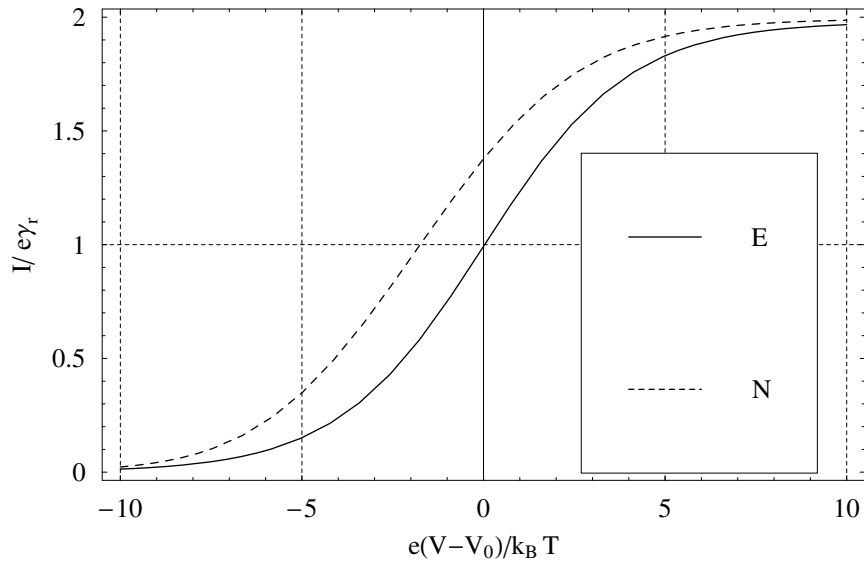


Figure 3.11: Two curves indicated are: E - equilibrium curve, and N - non-equilibrium curve; they show the shift of the current step by non-equilibrium in the 2-levels-accessible case. We assume $\gamma_1^l = \gamma_2^l = \gamma_l$ and $\gamma_1^r = \gamma_2^r = \gamma_r$, with $\gamma_l \gg \gamma_r$. The step occurs at $V_0 = 2C_g(V_g - V_g^0)/C_\Sigma$ at zero temperature. The “equilibrium” curve assumes infinitely fast relaxation in the island. The “non-equilibrium” curve assumes no relaxation.

current transport changes, as a result one can go from having a single energy level to having two levels involved in current transport. The transition from these two situations results in a “kink” in the linear evolution of the energy level. A simple way to visualize this is to look at differential conductance as a function of bias voltage and gate voltage. This “kink” in the position of the peak can be clearly seen for positive bias voltage in the Figure 3.12(b), where another level becomes available for tunneling out. Although having another energy level does not cause any substantial increase in the current, it changes the position of the peak in a noticeable manner. We will look at the experimental observation of such a feature in the next chapter. The T -dependent shift for the case of current flowing via two levels looks very similar to the result for one level displayed in Fig. 3.6, however it is of a different nature since it originates from non-equilibrium states. This shift is proportional to $k_B T$, but depends on the exact relative magnitudes of all the tunneling-in and tunneling-out rates.

The discussion until this point assumes that the electrostatic contribution to the energy of all the energy levels is the same irrespective of the occupancy of energy levels. This mean-field picture of the interaction between the electrons is not accurate, and it is essential to take into account the variation in interaction between electrons depending on the occupancy of various energy levels. Next we consider how these interactions change the position of various energy levels for a simple case with two energy levels involved in the transport. We will consider only variation in the electrostatic energy, ignoring the contribution of the exchange interactions.

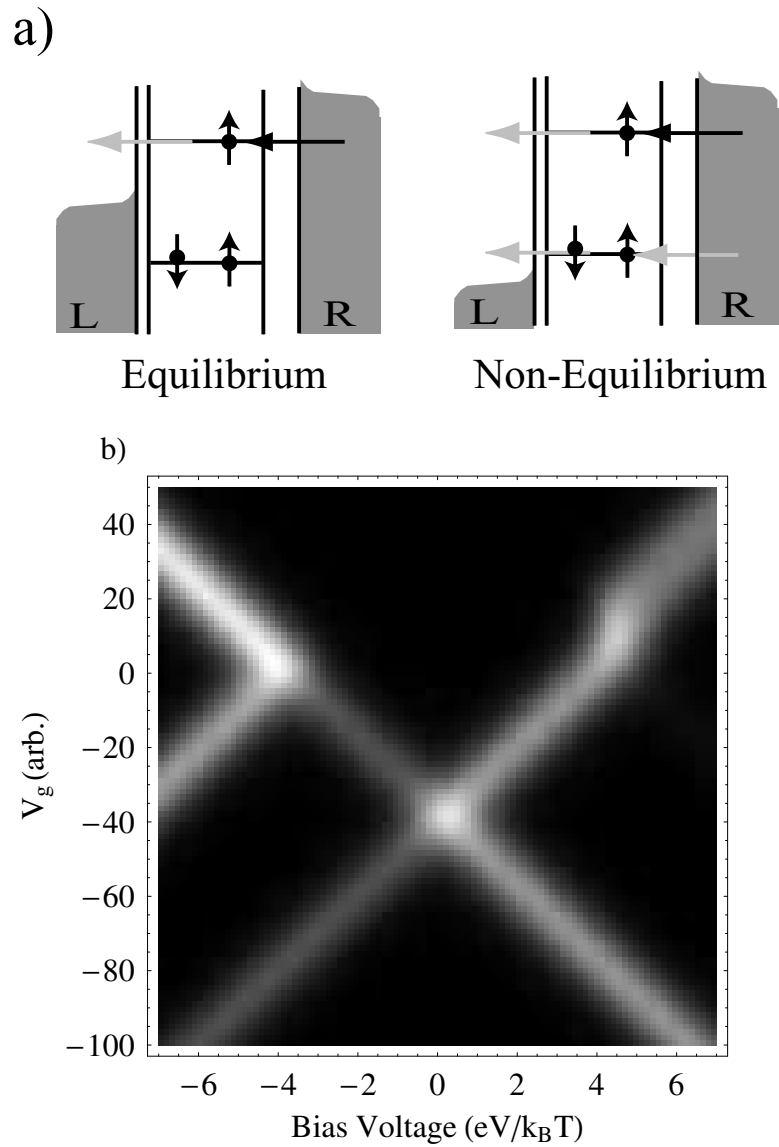


Figure 3.12: a) These energy level diagrams show the position of the two energy levels relative to the Fermi energy of the leads for the two cases: equilibrium tunneling and non-equilibrium tunneling. b) Greyscale conductance plot as a function of bias and gate voltage. We assume $\gamma_1^l = \gamma_2^l = \gamma_l$ and $\gamma_1^r \approx \gamma_2^r = \gamma_r$, with $\gamma_l \gg \gamma_r$. For $V_{deg} < V_g < 0$ and $V > 0$, the current flows via only one energy level. However, for $V_g > 0$, the current starts flowing with a second energy level available for discharging. Since this new channel for discharging is not the rate limiting step there is no increase in current, consequently no increase in conductance height. The “kink” in the evolution of the conductance peak, as a function of V_g , can be clearly seen at $V_g \approx 0$ and $eV/k_B T \approx 4$.

3.4 Two levels accessible with variations in the interactions

In the presence of variations in electron-electron interactions, the energy thresholds for tunneling are different depending on whether the island is initially in a ground state or in an excited state. For example, in the case described in the previous section, this effect can make the energy required for the $(\uparrow 0, \uparrow 0) \rightarrow (\uparrow 0, \uparrow \downarrow)$ transition different than the $(\uparrow \downarrow, 00) \rightarrow (\uparrow \downarrow, \uparrow 0)$ transition. We can account for such variations by assigning a different energy to the upper level in the presence or absence of an excitation in the island. Namely, the energy of the upper level will be ϵ_2 for the $(\uparrow \downarrow, 00) \rightarrow (\uparrow \downarrow, \uparrow 0)$ and $(\uparrow \downarrow, 00) \rightarrow (\uparrow \downarrow, 0 \downarrow)$ transition and $\epsilon'_2 = \epsilon_2 + \delta$ for the $(\uparrow 0, \uparrow 0) \rightarrow (\uparrow 0, \uparrow \downarrow)$, $(0 \downarrow, \uparrow 0) \rightarrow (0 \downarrow, \uparrow \downarrow)$, $(0 \downarrow, 0 \downarrow) \rightarrow (0 \downarrow, \uparrow \downarrow)$, and $(\uparrow 0, 0 \downarrow) \rightarrow (\uparrow 0, \uparrow \downarrow)$ transitions. Here δ is a measure of the strength of the variations. The possible transitions are still described by Fig. 3.10 and the corresponding rate equations are the same as Eqs. (3.25). We can solve for the rate equation problem analytically to solve for the current as a function of the interaction parameter δ .

Figure 3.13 shows the differential conductance (dI/dV) for a range of the interaction strength δ . For $\delta < 0$ the energy required for the tunneling transition is decreased by non-equilibrium in the presence of electron-electron interactions. The result of this is to produce an additional shift in the voltage-position of the current step, on top of the shift already described due to non-equilibrium states in the absence of electron-electron interactions (see Section 3.3.2). This additional shift is proportional to $|\delta|$ if $|\delta| \ll k_B T$ and becomes a constant on the order of $k_B T$ if $|\delta| \gg k_B T$. We will discuss, in the next chapter, how this is experimentally

observed. For positive δ , the effect of non-equilibrium is to produce an extra step in the I - V curve at voltages larger than the position of the $\delta = 0$ current step. This analysis indicates that the position of the conductance peak is affected by the presence of electron-electron interactions as well as non-equilibrium occupation of energy levels.

As V is increased so that more than two levels become energetically-accessible for tunneling, the ensemble of possible non-equilibrium excitations grows combinatorially, and each combination of excitations can produce a different shift for the tunneling resonance energies. Interactions which depend on the spin state of the island (neglected thus far) can produce further complications. The non-equilibrium excitations can produce a variety of effects depending on the ratio γ_l/γ_r and on the magnitude of variations in electron-electron interactions. When the interaction-induced shifts are comparable to $k_B T$, they have been observed to produce an effective broadening of the observed conductance peaks; we will consider this again in the context of the experiments during the next chapter. For larger interactions, shifts due to non-equilibrium excitations have been resolved individually [15, 19].

3.5 Conclusions

We have solved the rate equations describing electron tunneling via discrete quantum states on a nanoscale island, for selected simple cases, under the assumption that the rate for internal relaxation of excited electronic states is slower than the electron tunneling rate. Even the simplest case of tunneling via a single spin-degenerate energy level has some initially-surprising features. The magnitude of the maximum tunneling current can depend on the sign of the applied bias V , and the voltage-position of the resonance is temperature-dependent. When two spin-degenerate

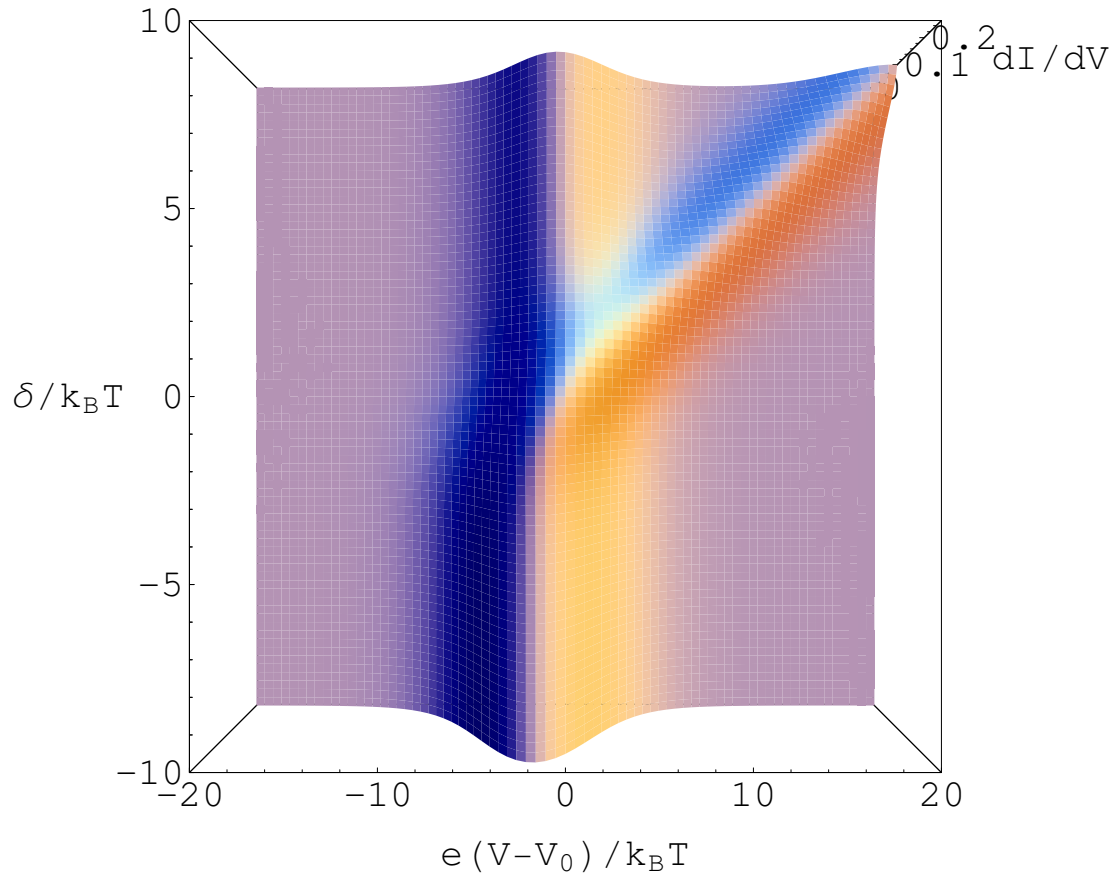


Figure 3.13: (color)a) Colorscale differential conductance plot (in units of $k_B T/\gamma e^2$) for a range of interaction strengths. We assume $C_l = C_r$, $\gamma_1^l = \gamma_2^l = \gamma_l$, and $\gamma_1^r = \gamma_2^r = \gamma_r$, with $\gamma_l \gg \gamma_r$. For positive δ we notice that another energy level appears at higher bias voltages for $\delta > k_B T$.

quantum levels are accessible for tunneling, the behavior is even richer because of the influence of non-equilibrium excitations on the island. The voltage-position of the resonance can undergo strong temperature-dependent shifts even in regimes (*e.g.*, positive bias and $\gamma_l \gg \gamma_r$ noted above) where the one-level resonance positions do not depend on temperature. Understanding the variations in the strength of electron-electron interactions is critical in the non-equilibrium regime with two or more levels accessible. Such variations can produce additional shifts of resonance curves on top of the shifts noted previously, and they can also introduce extra steps into the current-voltage curves.

In the next chapter, we will see how the results of these rate equation calculations can be applied to experiments to extract useful parameters, like the various tunneling rates associated with energy levels.

Bibliography

- [1] D. C. Ralph, C. T. Black, and M. Tinkham, Phys. Rev. Lett. **74**, 4087 (1995).
- [2] R. C. Ashoori, Nature **379**, 413 (1996).
- [3] D. H. Cobden, M. Bockrath, P. L. McEuen, A. G. Rinzler, and R. E. Smalley, Phys. Rev. Lett. **81**, 681 (1998).
- [4] J. Park *et al.*, Nature **417**, 722 (2002).
- [5] D. V. Averin, A. N. Kotorov, and K. K. Likharev, Phys. Rev. B. **44**, 6199 (1991).
- [6] C. W. J. Beenakker, Phys. Rev. B. **44**, 1646 (1991).
- [7] J. von Delft and D. C. Ralph, Phys. Rep. **345**, 61 (2001).
- [8] E. Bonet, M. M. Deshmukh, and D. C. Ralph, Phys. Rev. B. **65**, 045317 (2002).
- [9] M. M. Deshmukh, E. Bonet, A. N. Pasupathy, and D. C. Ralph, Phys. Rev. B **65**, 073301 (2002).
- [10] D. V. Averin and Yu. V. Nazarov, in *Single Charge Tunneling: Coulomb Blockade Phenomena in Nanostructures*, edited by H. Grabert and M. H. Devoret (Plenum Press and NATO Scientific Affairs Division, New York, 1992), p.217.
- [11] A. K. Geim, P. C. Main, N. La. Scala, Jr., L. Eaves, T. J. Foster, P. H. Beton, J. W. Sakai, F. W. Sheard, M. Henini, G. Hill, and M. A. Pate, Phys. Rev. Lett. **72**, 2061 (1994).
- [12] N. S. Wingreen, K. W. Jacobsen, and J. W. Wilkins, Phys. Rev. Lett. **61**, 396 (1988).
- [13] H. Park, J. Park, A. K. Lim, E. H. Anderson, A. P. Alivisatos, and P. L. McEuen, Nature (London) **407**, 57 (2000).
- [14] M. DiVentra, S.-G. Kim, S. T. Pantelides, and N. D. Lang, Phys. Rev. Lett. **86**, 288 (2001).

- [15] O. Agam, N. S. Wingreen, B. L. Altshuler, D. C. Ralph, Phys. Rev. B. **78**, 1956 (1997).
- [16] M. R. Deshpande, J. W. Sleight, M. A. Reed, R. G. Wheeler, and R. J. Matyi, Phys. Rev. Lett. **76**, 1328 (1996).
- [17] L. I. Glazman and K. A. Matveev, Pis'ma Zh. Eksp. Teor. Fiz. **48**, 403 (1988).[JETP Lett. **48**, 445 (1988)].
- [18] M. R. Deshpande, J. W. Sleight, M. A. Reed, and R. G. Wheeler, Phys. Rev. B **62**, 8240 (2000).
- [19] M. M. Deshmukh, S. Kleff, S. Guéron, E. Bonet, A. N. Pasupathy, J. von Delft, and D. C. Ralph, Phys. Rev. Lett. **87**, 226801 (2001).
- [20] D. Davidović and M. Tinkham, Phys. Rev. B **61**, R16359 (2000).

Chapter 4

Tunneling via discrete quantum states in an aluminum nanoparticle

In nanometer-scale devices, electron tunneling can be used to probe the spectrum of discrete quantum states. By varying gate and source-drain voltages (V_g, V) in a transistor geometry, energy levels have been measured inside semiconductor quantum dots [1], metal nanoparticles [2], and molecules [3]. Despite the popularity of this technique, little attention has been paid to the detailed quantitative form of the tunneling resonances, particularly when measured as a function of increasing source-drain bias. Here we analyze the energies, conductance amplitudes, and widths of the individual tunneling resonances for an Al nanoparticle. By varying V_g and V , we can manipulate electron flow controllably through one state, or through many, and we can extract tunneling rates for each level. When only one state participates in tunneling, the resonance properties are in accord with expectations for simple sequential tunneling. However, for larger voltages, the resonance energies, widths,

and currents can all be modified by the population of excited quantum states. For an understanding of the high- V regime, non-equilibrium transitions must be taken into account. Although there are many experiments that have probed the equilibrium transport, there are few that have looked at non-equilibrium transport [4, 5]. Here, we consider a detailed quantitative analysis.

The discussion in this chapter is along the lines of a paper [6] we wrote. The fabrication procedure and the measurement procedure is the same as described in Chapter 2. However, I briefly describe the experimental procedure in the next section.

4.1 Experimental details

A cross-sectional device schematic is shown in Figure 4.1. The use of an aluminum particle with aluminum oxide tunnel barriers provides mechanical and charge stability, and allows V and V_g to be varied without significantly altering barrier resistances. Fabrication [4] is done using electron-beam lithography and reactive ion etching to create a bowl-shaped hole in a silicon-nitride membrane, with a minimum diameter ~ 10 nm. A gate electrode is formed by depositing 18.5 nm Al, followed by anodization to 3.5 V in an oxygen plasma, and then deposition of 8.5 nm of SiO_x . The rest of the device is made by depositing a thick Al electrode onto the bowl-shaped side of the membrane, oxidizing for 3 min in 50 mTorr of O_2 , depositing 1.5 nm Al onto the other side of the device to make a layer of Al nanoparticles, oxidizing, and then depositing the lower Al electrode.

Device parameters are determined from the large- V structure of the 4.2 K Coulomb staircase curve [7]. The capacitance associated with the barrier with higher

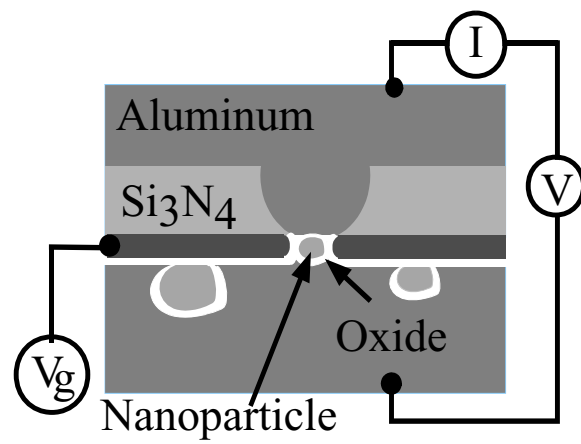


Figure 4.1: Schematic of an aluminum nanoparticle transistor.

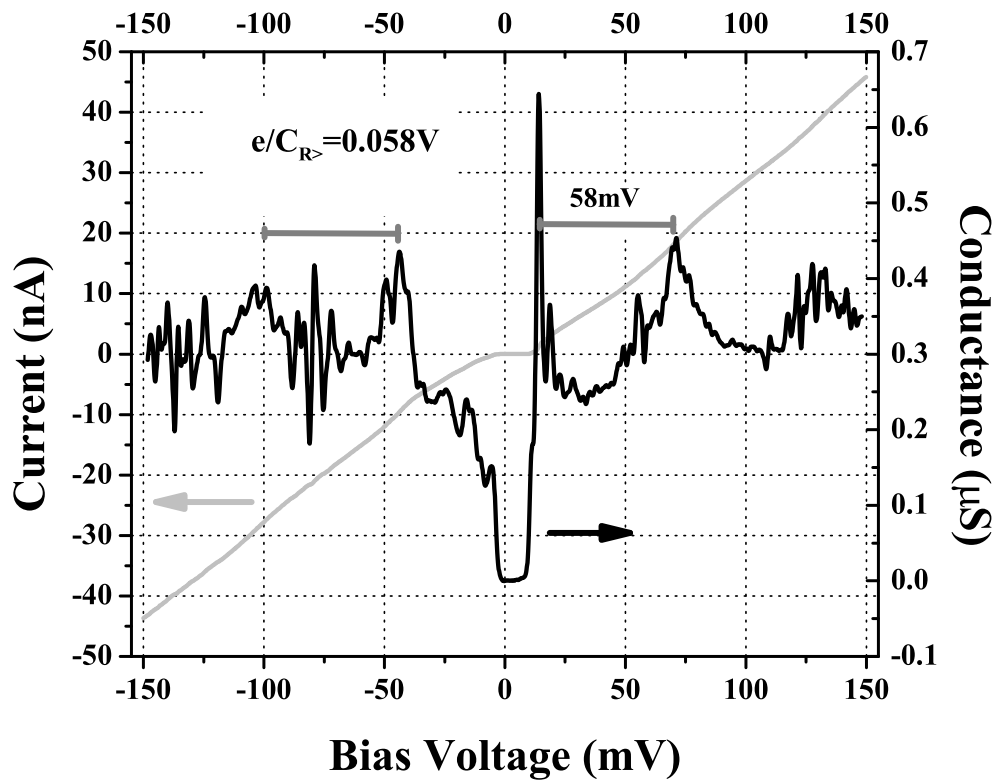


Figure 4.2: High bias current vs. voltage and dI/dV as a function of bias voltage for the device considered in this chapter. The periodicity of the Coulomb staircase is clearly seen in the differential conductance plot. The periodicity is due to the capacitance associated with the rate limiting tunnel barrier.

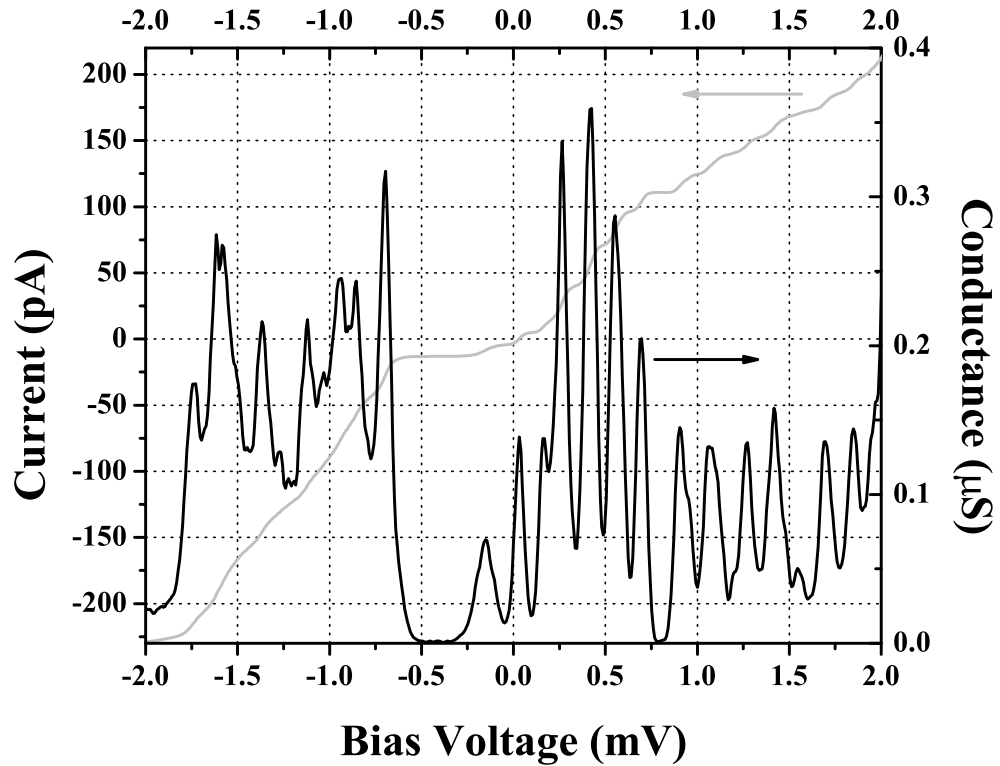


Figure 4.3: Plots showing the current measured as a function of the applied bias voltage ($I - V$), at a fixed gate voltage ($V_g = -663$ mV), and magnetic field ($\mu_0 H = 1$ T). Also shown is the differential conductance (dI/dV) plot, which is calculated by evaluating the numerical derivative of the current as a function of the bias voltage. The peaks in conductance coincide with the steps in the current. An electron temperature of ~ 90 mK is estimated from the width of the peaks in the conductance plot. The threshold for tunneling-in has decreased to zero due to the applied gate-voltage and magnetic field, and as a result the Coulomb blockade is not seen at zero bias.

resistance,¹ $C_{R>}$, is associated with the periodicity in the $I - V$ and $dI/dV - I$ plots. $C_{R>}$ is the smaller of the two capacitances due to each of the tunnel barriers. The ratio of the capacitances of the two tunnel barriers can be calculated from the ratio of the voltages required for tunneling via the same state for different signs of the bias. This allows us to calculate the capacitance for the two tunnel barriers. The gate capacitance C_g is calculated from the slope of the states as a function of gate voltage (as shown in Figure 4.4). The capacitance of nanoparticle to the top electrode is $C_L = 7.9 \pm 0.9$ aF, to the bottom electrode $C_R = 2.7 \pm 0.3$ aF, and the gate capacitance is $C_g = 0.06 \pm 0.009$ aF. The sum of the resistances of the two tunnel junctions is $R_\Sigma \approx 3M\Omega$, with individual resistances sufficiently large so that the intrinsic widths of the quantum states are smaller than $k_B T$. Assuming a roughly hemispherical particle shape [7], and a capacitance per unit area of 0.05 aF/nm² [8], we estimate a nanoparticle diameter ~ 10 nm.²

4.1.1 Tunneling spectroscopy as a function of gate voltage

We saw in Chapters 2 and 3 how tunneling spectroscopy allows us to probe the discrete energy-levels in a nanoparticle. Now, we will consider experimental data where tunneling spectroscopy is carried out as a function of gate voltage, V_g ; this allows us to probe transport in regimes where we can controllably tune the number of energy levels involved in the transport.

Figure 4.3 shows the current and conductance of the device as a function of the

¹The higher resistance tunnel barrier is the rate limiting barrier among the two barriers. We discuss later in this section how this barrier can be identified from the conductance plot as a function of gate voltage. Ralph *et al.* [4] used orthodox Coulomb-blockade theory to fit an $I - V$ curve to extract the parameters – like resistance and capacitance – for a device. Details of their fitting procedure are available in Chuck Black’s thesis [7].

²The junction capacitance of the nanoparticle with the different electrodes is relevant for the calculation rather than the self-capacitance of the nanoparticle which is much smaller.

bias voltage. The steps in current correspond to the availability of another energy level for the electrons to tunnel on, or off the nanoparticle; these steps are observed after the Coulomb blockade threshold is overcome by the applied bias. The differential conductance plot shows peaks corresponding to the steps in current. In Figure 4.4, we plot the differential conductance dI/dV as a function of V_g and V , when the sample is cooled in a dilution refrigerator with copper-powder filters on the electrical leads. The lines in the figure are due to tunneling resonances through discrete quantum states in the nanoparticle. Lines having a positive slope correspond to tunneling thresholds across the lower-resistance junction L, and negative slopes are thresholds across junction R [2]. The discontinuity evident in the figure, near $V_g = -557$ mV, is due to a V_g -driven change in the charge on another nanoparticle adjacent to the one through which tunneling occurs. This merely shifts the electrostatic potential of the current-carrying particle. The intrinsic energies, current levels, and widths of the resonances are not otherwise altered, so that the full dI/dV -spectrum can be constructed.

From the absence of spin-Zeeman splitting in a magnetic field for resonance lines I and II, we can identify these transitions with tunneling from an odd number of electrons n_0 on the particle to an even number [7, 9]. Since these resonances require increased $|V|$ as a function of V_g , they are $n_0 \rightarrow n_0 - 1$ transitions (see Figure 4.6). Resonances III and IV correspond to even $(n_0 - 1) \rightarrow$ odd n_0 transitions. The large gaps in V between each of resonances I and II and the next parallel lines are due to the energy difference $\sim 2\Delta$ between a fully paired superconducting state in the Al particle and the next lowest-energy tunneling state with 2 quasiparticles [4].

Having discussed the basic features of the data we next consider how it can be used to understand the physics in two different regimes: tunneling via one energy

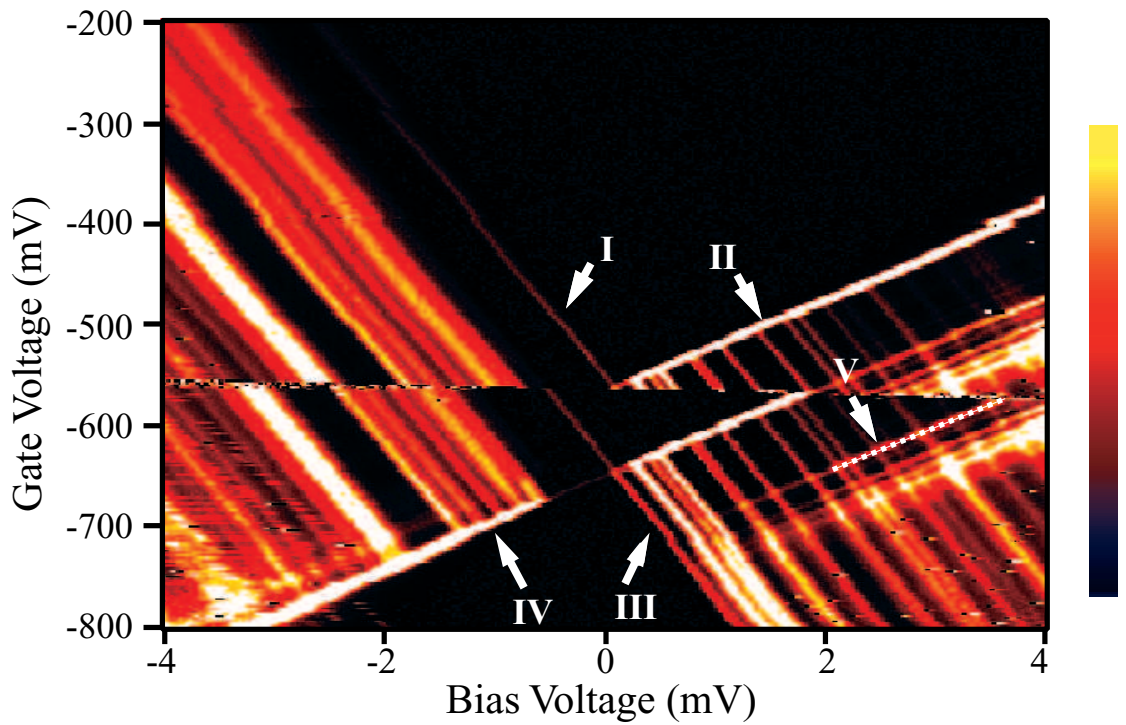


Figure 4.4: Colorscale differential conductance as a function of gate voltage, V_g , and bias voltage, V . A 0.06 Tesla field is applied to drive the Al leads normal. The conductance scale maximum is $3 \times 10^{-7} \Omega^{-1}$.

level and tunneling via many energy levels.

4.2 Tunneling via one energy level

We first consider the region of V_g near -650 mV, where V_g and V can be adjusted so that a single spin-degenerate quantum state (state 0) is accessible for tunneling (in Figure 4.5 we show both a zoomed-in view of Figure 4.4 and selected I - V curves). For the case under consideration, in which the quantum level is either empty or singly occupied, the current predicted for sequential tunneling is (as discussed in Section 3.2) [10, 11]

$$I = e \frac{2\gamma_{0L}\gamma_{0R}(f_L - f_R)}{(1 + f_L)\gamma_{0L} + (1 + f_R)\gamma_{0R}} \quad (4.1)$$

where γ_{0L} (γ_{0R}) is the bare rate for an electron to tunnel from the quantum state 0 to an unoccupied density of states in electrode L (R) and f_i is the occupation probability for states in electrode i with energy equal to the resonance state (for a thermal distribution $f_i = [1 + \exp[(\epsilon_0 - \mu_i)/kT]]^{-1}$, with ϵ_0 the energy to occupy the quantum state, and μ_i the chemical potential in electrode i).³ Our observations are in excellent accord with this model. For instance, the tunneling current through the quantum state is not the same for both bias directions, being $I_+ = 16.6 \pm 0.1$ pA for $V > 0$ (*i.e.* crossing lines II or III) and $I_- = -8.4 \pm 0.1$ pA for $V < 0$ (crossing lines I or IV). This has been observed previously [3, 12] and is a consequence of spin-degeneracy. For $V > 0$, electrons tunnel across the high-resistance rate-limiting tunnel barrier into an empty state, so that either spin-up or spin-down electrons can tunnel. For $V < 0$, the rate-limiting step is for an electron of a given spin on the particle to tunnel through the high-resistance barrier, and the current level is

³Equation 4.1 differs from an incorrect analysis done by Deshpande *et al.* in ref. [12, 13].

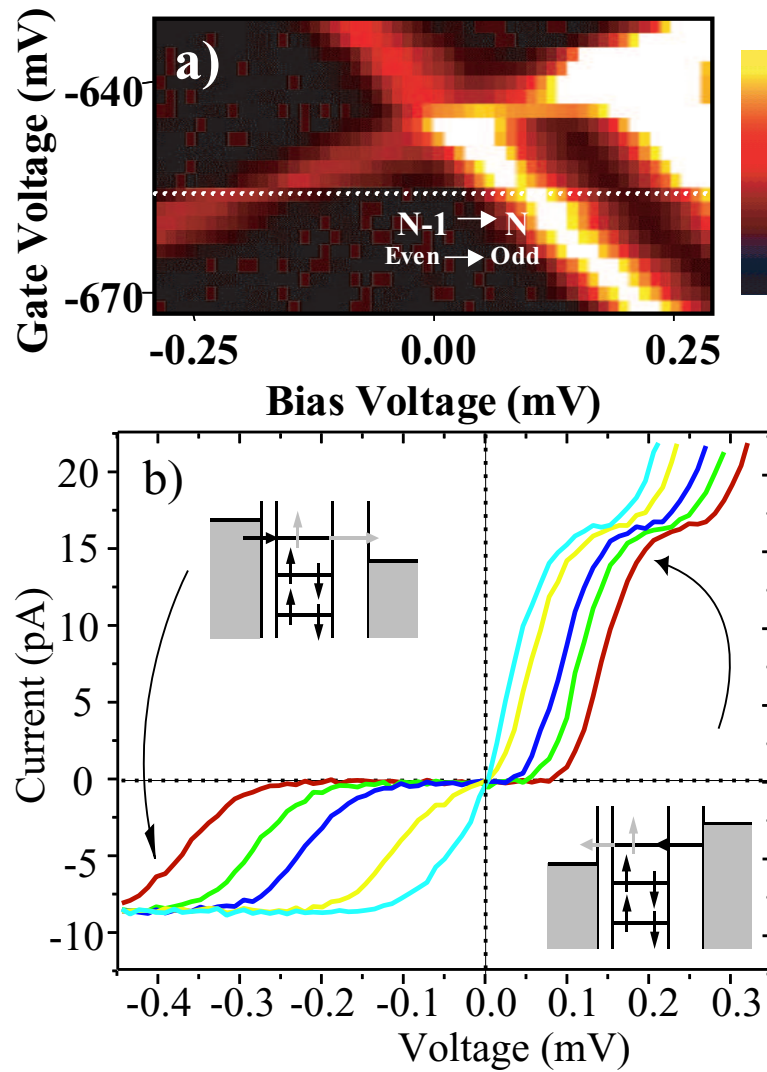


Figure 4.5: a) Zoomed in view of the colorscale conductance plot shown in Figure 4.4. This shows the region where only one energy level is involved in the current transport. The two lines (marked III-IV in Figure 4.4) correspond to the conductance peaks from tunneling via the same level for two different directions of current transport. b) I-V plots for a sequence of gate voltages around the dotted-line marked in a). The line scans are from V_g -650 mV to -658 mV in 2 mV steps. The two steps in current correspond to the two lines III-IV. The inset shows the energy diagram corresponding to the two current steps.

approximately cut in half.⁴ By equating the measured currents to Equation 4.1, we determine $\gamma_{0R} = (5.3 \pm 0.1) \times 10^7 s^{-1}$ for the high-resistance junction and $\gamma_{0L} \sim 7 \times 10^9 s^{-1}$. In addition, for resonances (*e.g.*, III, IV) in which the spin-degeneracy of the state is split by a magnetic field, the currents through the two Zeeman states for a given bias direction are not equal [9, 13], in agreement with the simple tunneling theory (see Section 3.2.4). The maximum current through the lower-energy Zeeman state is $e\gamma_{0L}\gamma_{0R}/(\gamma_{0L} + \gamma_{0R})$ for either bias direction, and the second state then adds current to produce the maximum allowed by Equation 4.1. This asymmetry in the splitting of the Zeeman split levels was discussed in the Section 3.2.4.

As the gate voltage is increased or decreased, many energy levels are involved in the transport and we will consider that next.

4.3 Tunneling via many energy levels

We can controllably tune the device so that more than one quantum state can participate in tunneling. This is illustrated by following line II in Figure 4.4. This line corresponds to processes which are initiated by an electron tunneling off the nanoparticle from the quantum state 0 to electrode L. However, as one follows line II to higher V, past negative-sloping resonance lines which intersect line II, these lines indicate that the subsequent tunneling of an electron from electrode R back onto the nanoparticle can proceed via many different energy levels other than state 0. The total current under these conditions can be modelled by a master equation which takes into account all allowed transitions between the energetically-accessible n_0 - and $(n_0 - 1)$ -electron states [11]. In Figure 4.6, we show tunneling diagrams

⁴In the limit when the tunneling rates are very asymmetric ($\gamma_{0L} \gg \gamma_{0R}$) the ratio of the currents is exactly $\frac{1}{2}$.

depicting representative accessible states for resonances I-IV in a non-equilibrium regime.

There are several aspects of the measured data that we will analyze, namely, the amplitude of the current, width of the conductance peaks, and the position of the peaks. In the next subsection, we consider the amplitude of the current which will allow us to calculate tunneling rates associated with different energy levels.

4.3.1 Current amplitudes

In Figure 4.7(a) we plot the step height in current associated with resonance lines I-IV, as V_g and V are tuned to follow the lines in the $|V|-V_g$ plane. Peaks I and III have approximately constant amplitude, while the currents for peaks II and IV grow quickly as $|V|$ enters the non-equilibrium regime. This can be understood trivially. For peaks I and III, the tunneling threshold is across the higher-resistance tunnel junction R. This junction is always rate-limiting and it matters little how many transport channels are available across junction L. For peaks II and IV, the tunneling threshold is across the low-resistance barrier L, but the rate-limiting process occurs across the other barrier R. As $|V|$ is increased, more quantum levels contribute to this process, and the current grows. The amplitude of the tunneling current along line II can be used to extract the tunneling rates of the two tunnel barriers. First, we calculate the average tunneling rates for the left ($\bar{\gamma}_L$), and right ($\bar{\gamma}_R$).⁵ If we assume that the tunneling rates associated with each of the levels is the same for the same side ($\gamma_{iR} = \bar{\gamma}_R$ and $\gamma_{iL} = \bar{\gamma}_L$), and the number of energy levels involved in the transport is n , then the current for each of the steps along line II can be written

⁵This way of calculating the average tunneling rates is due to Edgar Bonet.

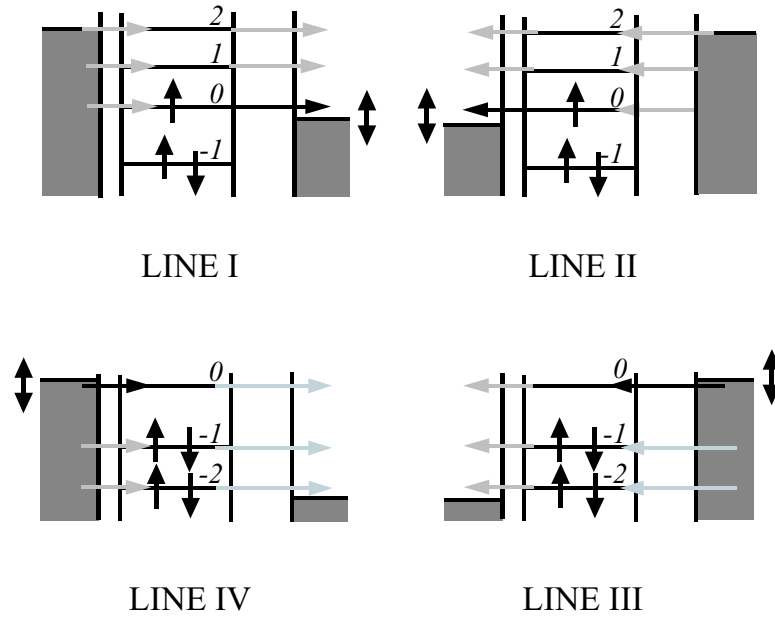


Figure 4.6: Tunneling diagrams depicting tunneling transitions active for resonance lines I-IV in a non-equilibrium regime. Black spins represent the ground-state electron configuration. Black arrows indicate the threshold tunneling transition, and gray arrows denote other transitions that contribute to the current for the value of V depicted.

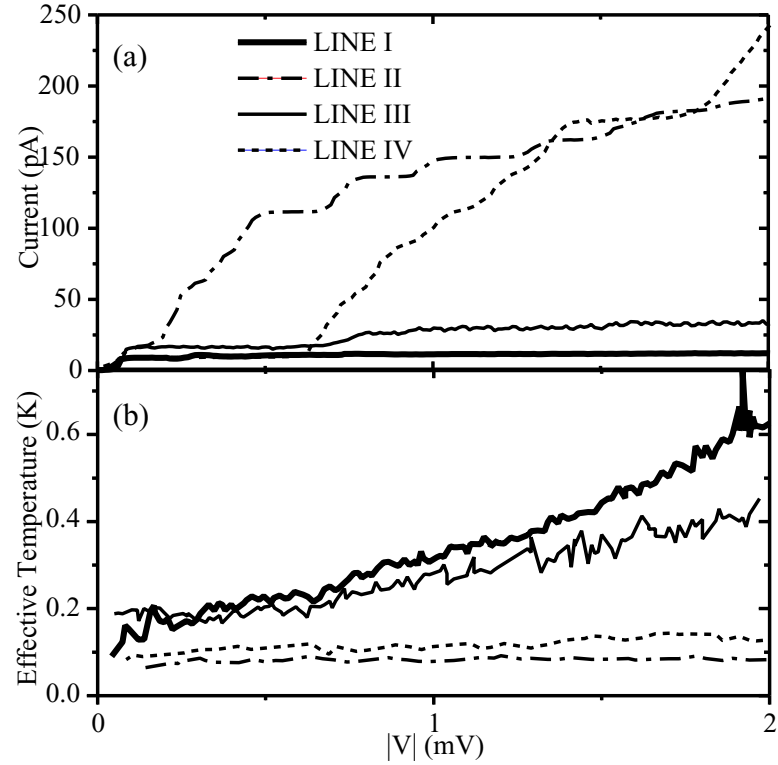


Figure 4.7: Properties of the resonance lines as V_g is varied to change the value of the V at which the resonances appear. The second tunneling states become energetically accessible for $|V| > 0.18$ mV for resonance line I, 0.19 mV for line II, 0.50 mV for line III, and 0.64 mV for line IV. (a) Magnitude of tunneling current. (b) Width of the dI/dV peak as a function of V , expressed as an effective temperature.

as:⁶

$$I_{II} = e \frac{2n\bar{\gamma}_R\bar{\gamma}_L}{2n\bar{\gamma}_R + \bar{\gamma}_L}. \quad (4.2)$$

Figure 4.8(a) shows the measured current steps along line II as a function of the bias voltage. Each of the steps in the current corresponds to one of ten energy levels ($i = 0$ to 10) that are involved in the current transport as the bias and the gate voltage are changed. The current will asymptotically saturate (as a function of n) when $n \approx \bar{\gamma}_L/\bar{\gamma}_R$; using this rule of thumb, an order of magnitude estimate of ratio of tunneling rates for the two barriers indicates that $\bar{\gamma}_L/\bar{\gamma}_R \sim 10$. A better way to estimate average tunneling rates is shown in Figure 4.8(b). Here, we essentially fit the plot of inverse of current steps vs. the inverse of step number, using the inverse of Equation 4.2. From the slope and intercept of this fit we get $\bar{\gamma}_R = (0.11 \pm 0.01) \times 10^9 s^{-1}$ and $\bar{\gamma}_L = (2.9 \pm 0.3) \times 10^9 s^{-1}$.

By measuring the current along peaks II and IV as levels are added one by one, and then fitting to the master-equation results described in the previous chapter, we can measure rate-limiting tunneling rates for each quantum state in a more rigorous way: the γ_{iR} , for $i = 0$ to 5, are $(5.3, 15.7, 8.0, 16, 15, 9) \times 10^7 s^{-1}$, $\bar{\gamma}_L \approx 3 \times 10^9 s^{-1}$, and (assuming relaxation effects are negligible) $\gamma_{-1R} \approx 17 \times 10^7 s^{-1}$. The result of fitting is shown in Figure 4.9.

Having discussed the amplitude of the current as a function of bias voltage, and the procedure of calculating the tunneling rates, we next consider the width of the conductance peaks.

⁶For line II: when n doubly degenerate levels are available, the number of ways for an electron to tunnel in from the left tunnel barrier is $2n$, and the number of ways for it to tunnel out of the right barrier is just 1.

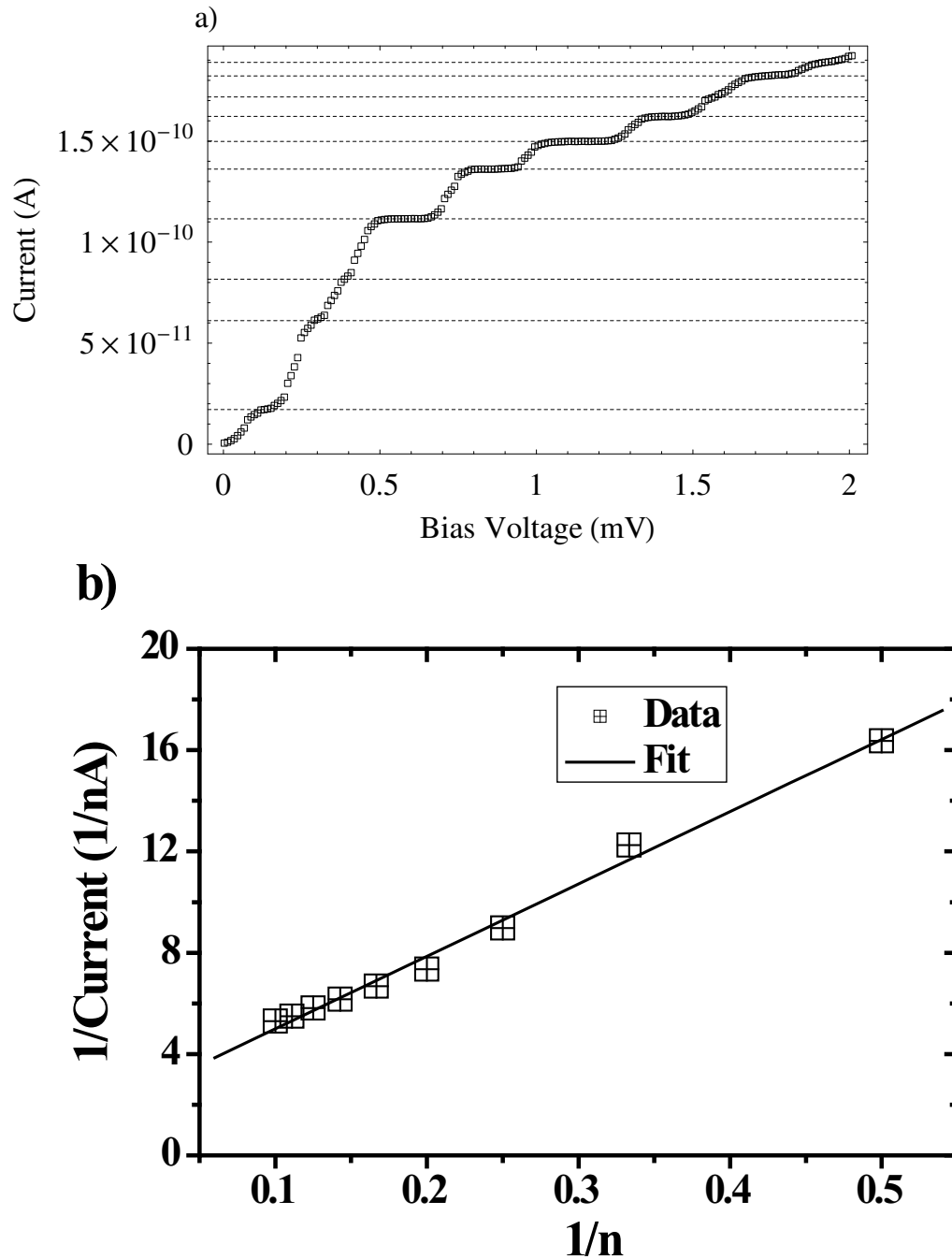


Figure 4.8: a) Shows the current along line II (marked in Figure 4.4) as a function of the bias voltage. The dotted lines indicate various current steps corresponding to the ten levels ($i = 0$ to 9). The dotted lines are guides to the eye which indicate the different current steps. b) Plot of inverse of current steps marked in (a), vs. the inverse of step number ($1/n$). The fitting function is the inverse of Equation 4.2. The fit parameters: slope and intercept, are used to calculate $\bar{\gamma}_R$ and $\bar{\gamma}_L$.

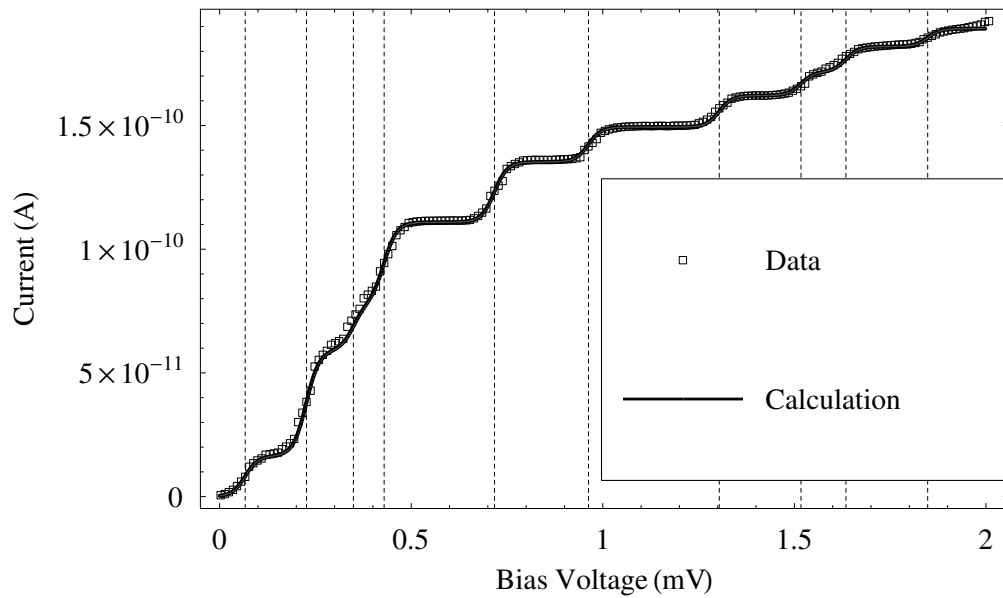


Figure 4.9: The result of fitting the current along line II as function of bias voltage, using the rate-equation approach discussed in Chapter 3. The vertical lines indicate the bias voltage at which another energy level becomes available for the current transport, giving rise to an increase in the current. The data shown here is the same as the Line II shown in Figure 4.7(a).

4.3.2 Width of conductance peaks

Figure 4.7(b) shows the widths of the tunneling resonance lines I-IV. These were determined by fitting the V dependence of each conductance peak to the derivative of a Fermi function, and then converting the voltage width to an effective temperature by multiplying by the capacitance ratio $(e/k_B)C_L/(C_L + C_R)$ for peaks I and III or $(e/k_B)C_R/(C_L + C_R)$ for peaks II and IV [7, 9]. In either the equilibrium or non-equilibrium regimes, the prediction of the simplest master equation, discussed in Chapter 3, is that the peak shape should be a derivative of the Fermi function with a width approximately equal to the electronic temperature in the electrodes. Our measurements agree with this model within the equilibrium regime, with a constant electron temperature $T \approx 90$ mK.⁷ Line III is broader than the others at low V because the magnetic field of 60 mT applied to drive the Al electrodes normal produces an unresolved Zeeman splitting ($\Delta E/k_B = 2\mu_B H/k_B = 80$ mK).

As $|V|$ is increased into the non-equilibrium regime, peaks I and III undergo large increases in width and peak IV broadens slightly, while peak II shows no measurable change. The differences are not merely an effect of heating in the electrodes, because peaks II and IV have the largest magnitudes of current and power. We suggest that these measurements can be explained as a consequence of electronic interactions in the non-equilibrium regime, by a mechanism due to Agam *et al.* [5]. Consider resonance line III, for which the tunneling threshold corresponds to an electron entering quantum state 0. For $V > 0.50$ mV the next tunneling event, which discharges the particle, may occur out of different, lower energy states (see Figure 4.6), leaving an electron-hole excitation on the nanoparticle. Agam *et al.* suggested that if this non-

⁷This experiment was done before the addition of the micofabricated stripline filters to our setup. The electron temperature is higher than for devices without, most likely due to some leakage current. With the stripline filters, the electron temperature was reduced to ~ 40 mK (Appendix A).

equilibrium state does not relax before the next electron tunnels onto the particle, it can shift the energy of the tunneling resonances on account of an alteration of the electron-electron interaction energy.⁸ In past work on smaller aluminum particles, shifted transitions were resolved individually [5]; however the relative shift is expected to decrease with increasing nanoparticle size [5], so it is reasonable that the shifts would produce only broadened resonances for the 10 nm particle under investigation here. Because a growing ensemble of different non-equilibrium states can be excited with increasing $|V|$, this mechanism can explain the increase in width of line III as a function of $|V|$. The same non-equilibrium mechanisms should also come into play for line IV, for $V < -0.64$ mV, but the broadening there is reduced because the threshold tunneling event is across the lower-resistance junction, L. Barrier R quickly becomes rate limiting as line IV is crossed, so that higher-energy non-equilibrium resonances do not add significant additional current. In order for the non-equilibrium mechanism to apply for line III, the relaxation rate of some non-equilibrium excitations to the ground state must be comparable to or slower than $\gamma_{0R} = 5.3 \times 10^7 s^{-1}$. The rate predicted by Agam *et al.* for *spin-preserving* energy relaxation in aluminum particles is $\sim 10^8 s^{-1}$ [5].

Resonances I and II are a different case, because the tunneling threshold corresponds to an electron leaving quantum state 0. The subsequent tunneling event, adding an electron back to the nanoparticle, may for large V occur into higher-energy states (see Figure 4.6), but nevertheless this excitation alone cannot produce a non-equilibrium shift in the energy of subsequent discharging transitions. The reason is that only this electron is free to tunnel off the nanoparticle; there is no electron in quantum state 0 whose transition energy might be shifted. Therefore

⁸A statement in ref.[5] that the first tunneling resonance should be unaffected by non-equilibrium is incorrect in some cases when spin is taken into account.

within the picture of Agam *et al.* [5], no non-equilibrium broadening should be expected for levels I and II, in conflict with the data for level I. This discrepancy can be explained if non-equilibrium excitations on the nanoparticle can be generated not only by the tunneling transitions on or off the particle that have been considered previously [5], but also by transitions in which a high-energy electron relaxes within the nanoparticle and produces an electron-hole excitation. Broadening would then be generated by the Agam mechanism. Within this scenario, the difference between the broadening visible for resonance line I and the lack of broadening of line II would follow from the fact that for peak II a high-energy electron on the particle can quickly exit through the low-resistance tunnel junction L, while for peak I the high-energy particle must exit through the high-resistance junction R, giving a much longer residence time during which relaxation transitions can occur. In order for line I to be broadened, the fastest relaxation rates must become comparable to $\gamma_{0R} = 5.3 \times 10^7 s^{-1}$ as $|V|$ increases.

In this section we have argued that the widths of the conductance peaks are affected by the non-equilibrium states that are involved in the current transport, together with electron-electron interactions. In the next section we consider how the position of peaks can also be modified as a result of these two factors – non-equilibrium and electron-electron interactions.

4.3.3 Position of conductance peaks

By tuning V_g and V into the non-equilibrium regime, the apparent *energies* of the dI/dV peaks can also be changed. This is clearest for line III (Figure 4.11), which undergoes a shift of $33 \mu\text{V}$ to lower voltage when the threshold for non-equilibrium tunneling via state -1 (line V in Figures 4.4 and 4.11(a)) is crossed. Because we

have measured rate-limiting tunneling rates for the energetically-accessible states from the current amplitudes, we can test whether this shift can be explained by the simplest master equation approach discussed in Chapter 3, which assumes that the underlying energies of the quantum states are not changed by non-equilibrium interactions. Figure 4.10(a) and (b) show the energy diagrams corresponding to situations before and after the kink respectively. Using the rate equation approach described in Chapter 3 we can calculate the current through the device after the kink. The current can then be written in a simplified form with an assumption ($\bar{\gamma}_R \ll \bar{\gamma}_L$) as,

$$I_{kink} = e \frac{2f_R\gamma_{0R}\gamma_{-1R}((f_R + 2f_Rx)\gamma_{0R} + x(x+2)\gamma_{-1R})}{f_R^2\gamma_{0R}^2 + 4f_Rx\gamma_{0R}\gamma_{-1R} + x^2\gamma_{-1R}^2}, \quad (4.3)$$

where f_R – a function of bias voltage V – is the Fermi function of right lead, and $x = \gamma_{0L}/\gamma_{-1L}$. Only one relevant parameter was not determined previously: x . The reason this parameter was difficult to determine is that the left side is never the rate-limiting side, and hence one can only determine the average tunneling rate associated with this barrier – not individual tunneling rates. This solution of the master equation does predict a voltage shift ($\propto T$) for the conductance peak compared to the equilibrium case, and for $x < 0.15$ it can explain the full value of the experimental shift in the position of the conductance peak corresponding to line III. However, we judge $x < 0.15$ to be improbable, because the measured values of γ_{iR} fall within a more narrow distribution, and one would expect the distribution of γ_{iL} to fall within the similar range. For $x \sim 1$ in Equation 4.3, the predicted shift is $15 \mu\text{V}$ – much smaller than we measure.

We can more naturally explain the full value of the shift in the position of line III by again taking into account that the presence of a non-equilibrium excitation can change the energy of a tunneling transition. In the equilibrium regime,

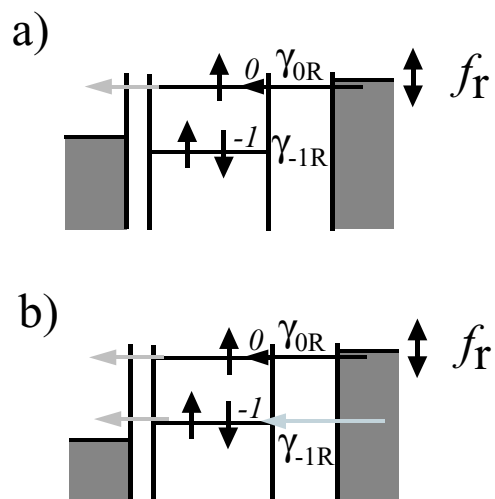


Figure 4.10: (a) Energy diagram corresponding to the situation before the kink (before line V “intersects” line III). (b) Energy diagram corresponding to the situation after the kink (after line V “intersects” line III).

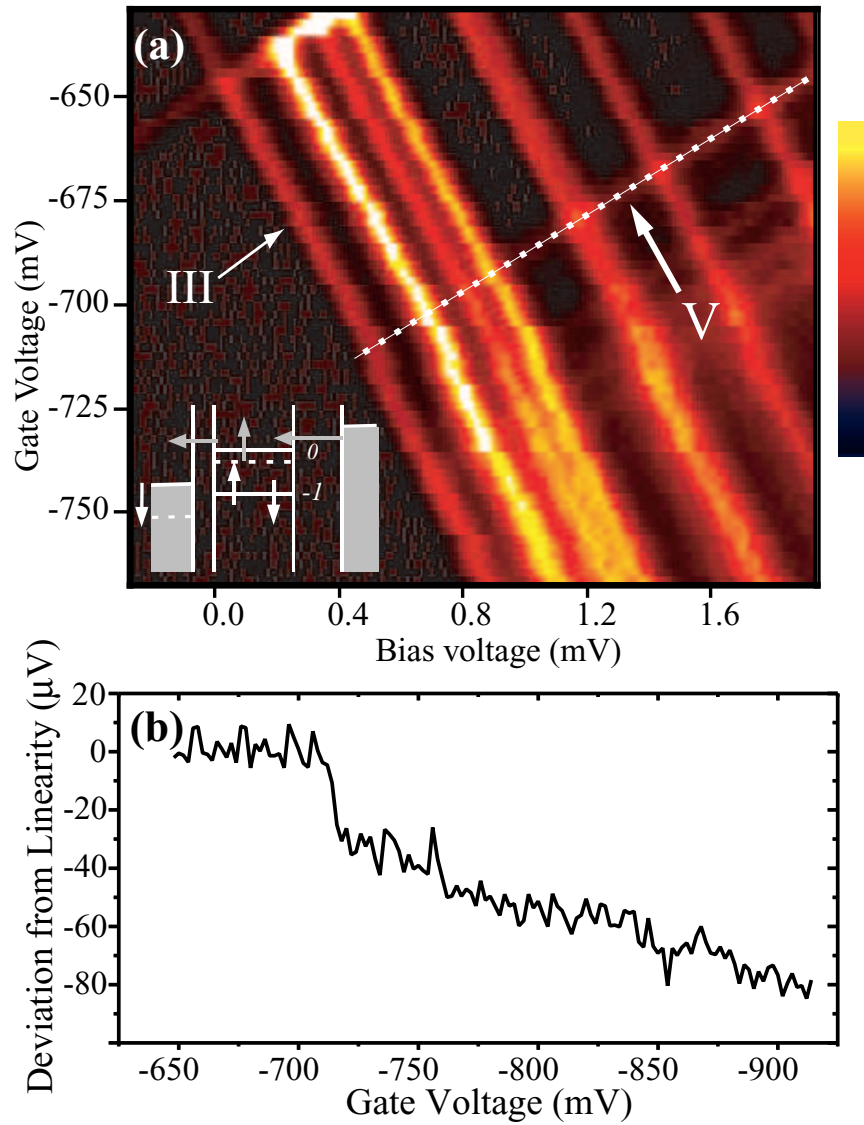


Figure 4.11: (a) Zoomed in view of the colorscale conductance plot shown in Figure 4.4. A kink in the evolution of line III is seen as line V “intersects” with it. The inset shows the energy diagram for the before and after the “intersection” of the lines (dotted lines correspond to the situation afterwards). (b) Deviation from linearity for the V -position of peak III as a function of V_g . A line was fitted to the peak position in the equilibrium regime between $V_g = -650$ mV and -701 mV, and this was subtracted from the measured positions.

the occupation of quantum state 0 corresponds to a transition from a fully-paired superconducting state on the aluminum particle to a state with one high-energy quasiparticle; in the non-equilibrium case, the transition can be from a state with two quasiparticles to one, with a transition energy lowered by $\sim 2\Delta \approx 0.35$ meV [14]. This is much bigger than $k_B T \sim 10$ μ eV, and in this case, the observed resonance is shifted to lower $|V|$ by an amount $\propto T$ because electrons in the tail of the Fermi distribution, of the leads, can excite the non-equilibrium state and open the lower-energy current channel. This is clearly seen in Figure 3.13, where the interactions were included during the rate-equation calculation.⁹ For $x=1$ and $T \sim 90$ mK the master-equation result is that the measured shift, in the position of the conductance peak corresponding to line III, can be produced by a non-equilibrium lowering of the transition energy by any amount greater than 20 μ eV $\sim 2k_B T$.

4.4 Conclusions

In this chapter we used the rate equation approach described in Chapter 3 to extract tunneling rates for different energy levels. When transport occurs through a single quantum level, our results are in agreement with the expectations of sequential tunneling. At large values of $|V|$, the non-equilibrium population of excited electronic states, together with electron-electron interactions, modifies the widths of the tunneling resonances and causes their apparent energies to shift as a function of temperature. This is the first detailed study where rate equation approach has been used extensively to extract the tunneling parameters of a quantum dot.

I want to emphasize that these experimental results are very generic, in the

⁹This would correspond to the case of $\delta/k_B T < -10$ shown in Figure 3.13. In this case the shift saturates, and is proportional to the temperature.

sense that they can be observed in a variety of systems where a sequential tunneling picture is valid. In the next chapter we consider how the physics of spin dependent tunneling can be explored by fabricating one of the electrodes out of a magnetic material.

Bibliography

- [1] R. C. Ashoori, Nature (London) **379**, 413 (1996).
- [2] J. von Delft and D. C. Ralph, Phys. Rep. **345**, 61 (2001).
- [3] D. H. Cobden *et al.*, Phys. Rev. Lett. **81**, 681 (1998).
- [4] D. C. Ralph, C. T. Black, and M. Tinkham, Phys. Rev. Lett. **78**, 4087 (1997).
- [5] O. Agam *et al.*, Phys. Rev. Lett. **78**, 1956 (1997).
- [6] M. M. Deshmukh, E. Bonet, A. N. Pasupathy, and D. C. Ralph, Phys. Rev. B **65**, 073301-1 (2002).
- [7] C. T. Black, Ph.D. thesis, Harvard University, 1996.
- [8] J. G. Lu, J. M. Hergenrother, and M. Tinkham, Phys. Rev. B **57**, 4591 (1998).
- [9] D. C. Ralph, C. T. Black, and M. Tinkham, Phys. Rev. Lett. **74**, 3241 (1995).
- [10] L. I. Glazman and K. A. Matveev, JETP Lett. **48**, 445 (1988); C. W. J. Beenakker, Phys. Rev. B. **44**, 1646, (1991).
- [11] E. Bonet, M. M. Deshmukh, and D. C. Ralph, Phys. Rev. B **65**, 045317 (2002).
- [12] M. R. Deshpande, J. W. Sleight, M. A. Reed, and R. G. Wheeler, Phys. Rev. B **62**, 8240 (2000).
- [13] M. R. Deshpande *et al.*, Phys. Rev. Lett. **76**, 1328 (1996).
- [14] M. Schechter and J. von Delft, communication.

Chapter 5

Polarization measurements of a bulk ferromagnet using discrete electronic states in an aluminum nanoparticle

There has been an increasing interest in manipulating the spin of electrons, with the primary motivation being to use this degree of freedom for potential device applications [1, 2]. In order to use the spin degree of freedom it is required that a unequal number of spin-up and spin-down electrons be created in a controllable manner. There are several strategies being pursued to create an unequal number of spins, with two prominent approaches being the use of circularly polarized light to generate spin-polarization [3] in a non-magnetic semiconductor, and the use of a ferromagnet as a source of spin-polarized currents [4]. As of now the use of ferromagnet as a source of spins seems to be most promising for devices from a practical standpoint [2]. This makes it imperative to understand the polarization of

electrons – the asymmetry in the number of spin-up and spin-down electrons – in a ferromagnet and the nature of spin polarized current flow. Spin polarization in a ferromagnet has been probed in a number of ways: by using electron tunneling from a ferromagnet into a spin-split quasiparticle states in a superconductor [5], by using a ferromagnetic scanning tunneling microscope (STM) tip [6], by using Andreev reflection from a ferromagnet-superconductor interface [7], and by using a SET with ferromagnetic leads [8]. In many ways the experiments we describe in this chapter will combine the ideas used in some of the experiments [5, 8] mentioned above.

In the previous chapter we saw how the discrete electronic states can be probed using the flow of electrons. This flow of electrons also revealed information about the nature of electronic interactions *on* the metallic nanoparticle. However, in this chapter, we will see how the discrete electronic states can be used to probe *one of the electrodes* of the device. More specifically, we will probe the magnetic polarization of the ferromagnet, and the polarization of the electrons that tunnel from the ferromagnet. Before we dive into the details of polarization we will briefly discuss the ideas behind some previous polarization measurements in the next section. This will also help to provide a broader context for our measurements, and bring out the differences between our measurements and those carried out by others.

5.1 Polarization of electrons in ferromagnets

The asymmetry in the number of spin-up and spin-down electrons in a ferromagnet is a result of the competition between the exchange energy, which tends to align spins of electrons, and the kinetic energy of electrons. A material is a ferromagnet when the

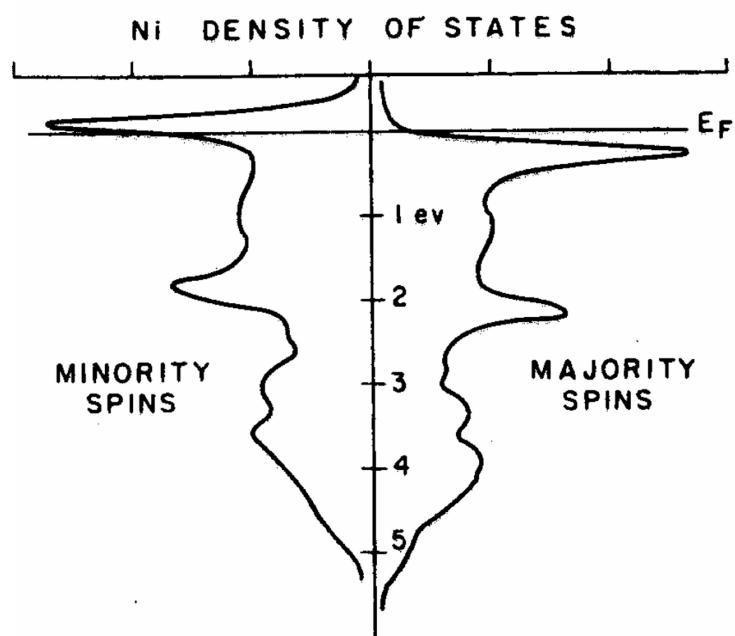


Figure 5.1: Calculated density of states of Ni (from Ref [9]).

exchange energy dominates the kinetic energy.¹ As mentioned earlier, polarization simply measures asymmetry in the number of spins in a ferromagnet. Figure 5.1 shows the density of states plot for nickel, here one can observe the asymmetry in the total number of spins, and the asymmetry in the density of states at the Fermi energy. Note that although the total number of spins for spin-up (majority spins) is larger than that of spin-down (minority spins), the density of states at the Fermi energy has the opposite distribution – more states of the minority-spin than the majority spin. As far as the transport properties are concerned, the states near the Fermi energy are the only relevant states. This simple picture exemplifies the complicated band structure of ferromagnets. For simplicity, the bands of a ferromagnet are often approximated with parabolic, free electron-like, bands. This free-electron like approximation together with the Stoner model is used in most descriptions of a ferromagnet and captures some of the qualitative features.

5.1.1 Stoner model with parabolic bands

In order to capture some of the features of ferromagnetism in a simple model, one can assume free-electron like bands together with a constant exchange interaction.² The Hamiltonian for this simple model can be written as

$$H_{Stoner} = \sum_i \frac{\vec{p}_i^2}{2m} - \vec{\sigma}_i \cdot \vec{\Delta}_{Stoner}, \quad (5.1)$$

where \vec{p}_i is the momentum of the i^{th} electron, m is the effective mass, $\vec{\sigma}_i$ is the spin of the electron, and $\vec{\Delta}_{Stoner}$ is the exchange field. This says that the energy of electrons with the same momentum and opposite spin differs by $2\Delta_{Stoner}$.³ The in-

¹We will come back to the basics of ferromagnetism in the next chapter (Chapter 6) where we consider this in greater detail.

²We will consider in greater detail, during the next chapter, how this description is inadequate for realistic ferromagnets.

³The exact magnitude of Δ_{Stoner} is not important for the discussion in this chapter.

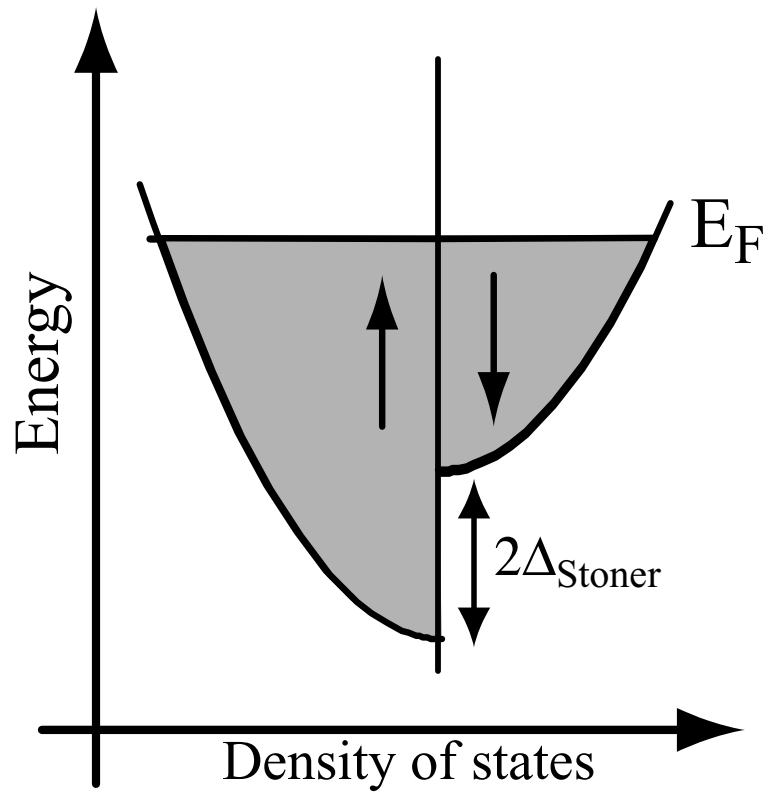


Figure 5.2: Density of states for a ferromagnet within the Stoner model with parabolic bands.

herent assumptions are that the detailed structure of the bands is irrelevant and the exchange can be described using a mean-field description. It should be emphasized that these assumptions are very crude, but they do make the problem tractable. The density of states for a ferromagnet within such a model is shown in Figure 5.2. Next we discuss previous experiments probing the polarization of ferromagnets.

5.1.2 Previous experiments to probe polarization

The pioneering experiments of Meservey and Tedrow [5, 9] used a ferromagnetic-insulator-superconductor (FIS) junction to probe the polarization of the ferromagnet. The basic idea was to use the spin-split quasiparticle states of a BCS superconductor as a way of measuring the relative proportion of the spins tunneling from the ferromagnet. The differential conductance of the FIS device, as a function of bias voltage, reflects the convolution of the spin-split quasiparticle states of the superconductor and the density of states of the ferromagnet. Meservey and Tedrow measured minimal spin-flip scattering during the tunneling; this allowed them to deconvolve the tunneling density of states for the spin-up and spin down electrons in the ferromagnet. The polarization of the electrons tunneling from the ferromagnet was found it to be positive, implying that more spin-up electrons tunnel compared to spin-down. Meservey and Tedrow measured the polarization of nickel to be $+23 \pm 3\%$. The positive sign of the measured polarization was something that was difficult to reconcile with the realistic density of states (shown in Figure 5.1) since there are more states of the spin-down character at the Fermi energy. This was explained by considering that although the density of states is dominated by *d*-like electrons, it is primarily the *s*-like, itinerant, electrons that dominate the tunneling. This picture of having mostly itinerant electrons tunneling from a Stoner ferromag-

net (shown in Figure 5.2) is commonly used to explain the results from tunneling measurements of polarization. According to a model developed by Stearns [10], the quantity that Meservey and Tedrow [5, 9] measured was the polarization of the itinerant electrons

$$P_{tunnel} = \frac{k_F^\uparrow - k_F^\downarrow}{k_F^\uparrow + k_F^\downarrow}, \quad (5.2)$$

where $|k_F^\uparrow|^2 = (2m/\hbar^2)E_F$ and $|k_F^\downarrow|^2 = (2m/\hbar^2)(E_F - \Delta_{Stoner})$ are the wave-vectors at the Fermi energy for the spin-up and spin-down itinerant electrons, respectively.

Another set of experiments, based on the tunnel magnetoresistance (TMR) effect, measure the magnitude – but not the sign – of the tunneling polarization using the ferromagnet-insulator-ferromagnet (FIF) geometry [11, 12, 13]. One can make the two ferromagnetic electrodes so that they have different switching fields, and as a result one can measure the resistance of such a device both when the two magnetic layers are parallel and antiparallel. The relative change in the resistance between the parallel and antiparallel states ($\Delta R/R$) is related to the two polarizations via a simple model due to Julliere [11],

$$\frac{\Delta R}{R} = \frac{2P_1P_2}{1 + P_1P_2}, \quad (5.3)$$

where P_1 and P_2 are the polarizations associated with the two ferromagnetic layers, and depend on the materials used to fabricating the device. These measurements also measure the polarization of the s-like electrons in the ferromagnets, like the measurement of Meservey and Tedrow [5, 9].

Upadhyay *et al.* and Soulen *et al.* [7] used Andreev reflection from a ferromagnet [14] to probe the magnitude of the polarization of the transmitted current. The idea of these experiments is to measure the conductance of a ferromagnet-superconductor interface formed at a point contact. The conductance below the

gap of the superconductor is enhanced to a degree that depends on the polarization of the ferromagnet [14]. These experiments probe the polarization of the spin current in the limit of complete transparency; this is in contrast to the tunneling polarization measurements, which rely on the opaqueness of the tunnel barrier. A polarization measurement using Andreev reflection cannot determine the sign of polarization, only the magnitude. Using the Stoner model with parabolic bands for the ferromagnet the current polarization measured in Andreev reflection can be written as

$$P_{current} = \left| \frac{(k_F^\uparrow)^2 - (k_F^\downarrow)^2}{(k_F^\uparrow)^2 + (k_F^\downarrow)^2} \right|, \quad (5.4)$$

where $|k_F^\uparrow|^2 = (2m/\hbar^2)E_F$ and $|k_F^\downarrow|^2 = (2m/\hbar^2)(E_F - \Delta_{Stoner})$ are the Fermi wavevectors at the Fermi energy for the spin-up and spin-down electrons [15]. Physically this quantity measures the excess number of channels available for one spin over the other, where the number of channels is $\sim (dk_F)^2$; d is diameter of the point-contact and k_F is the Fermi wavevector. As a result, the polarization measured using Andreev reflection is quite a different quantity, both numerically and physically from the tunneling polarization.

Ono *et al.* [8] used a single electron transistor (SET) with a magnetic island or magnetic leads or both, and they fabricated their devices so that the charging energy, $E_C = e^2/2C_\Sigma$, was of the same order of magnitude as the change in the chemical potential for a magnetic system in an applied magnetic field ($\Delta\mu \propto P_{DOS}$), where $\Delta\mu$ is the change in the chemical potential and P_{DOS} is the density of states polarization.⁴ As a result, they observed Coulomb-blockade oscillations as a function of magnetic field as well as gate voltage. Knowing the device parameters, they argued that they could estimate the density of states polarization (P_{DOS}). The sign

⁴This concept will be considered in greater detail in Section 5.3.2.

of the polarization measured in the experiments of Ono *et al.* [8] was negative – more density of states of spin down character at the Fermi energy – a result that was different from the measurements of Meservey and Tedrow [5, 9], who measured positive tunneling polarization. We will discuss this measurement later in the context of our experiments.

The four techniques discussed above measure different aspects of polarization. The measurements that we will discuss in this chapter borrow on the ideas from some of the experiments discussed above, in particular the experiments of Meservey and Tedrow [5], and Ono *et al.* [8]. I want to emphasize that our experiments are different since they allow the determination of two different measures of polarization *in the same device*, and with greater accuracy than the work by Ono *et al.* [8]. Next we consider briefly the device fabrication and the experimental details.

5.2 Device fabrication and measurement

The fabrication procedure for the devices is the same as described in Section 2.4. However, we will describe it here briefly for the sake of completeness. Figure 5.3 shows the schematic of the device used in these experiments. All the devices measured in this project are two terminal devices (without a gate electrode). The fabrication process starts with a series of steps to create a freely suspended silicon nitride membrane, followed by e-beam lithography and reactive ion etching to create a 5-10 nm hole in the nitride membrane (this is described in detail in Section 2.4.1). Fabrication of the nano-hole is followed by deposition of electrodes in an evaporator with a base pressure of low 10^{-7} Torr. The samples are attached to a stage which can be rotated *in situ*. The first electrode is fabricated by depositing 1500 Å of aluminum at a rate of 5 – 9 Å/s on the side with the bowl shaped hole. Following

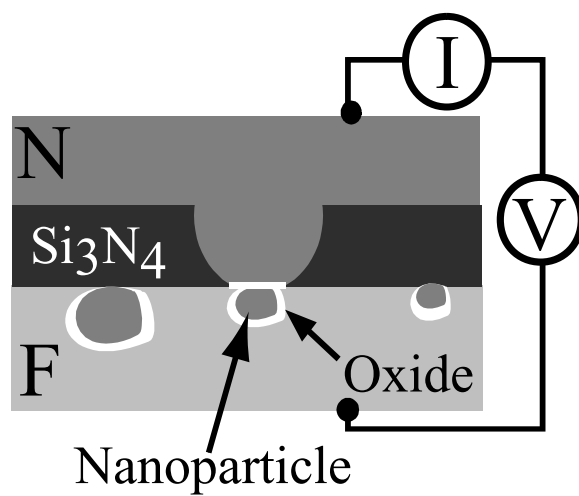


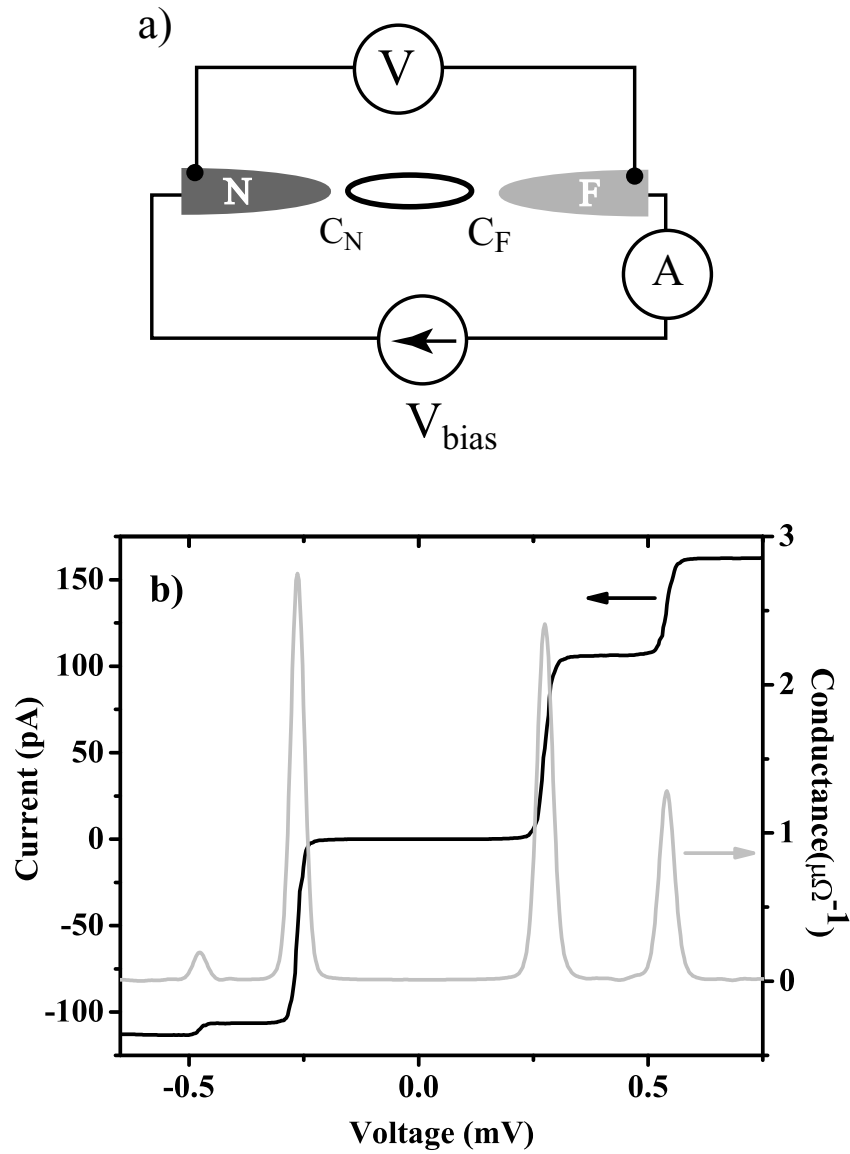
Figure 5.3: Device schematic with the non-magnetic electrode (indicated by N), and the ferromagnetic electrode (indicated by F).

this, the first tunnel barrier for the two terminal device is fabricated by oxidizing the sample with 50 mTorr of O_2 for 3 minutes. The next step is to deposit the nanoparticles by evaporating 20 Å of aluminum, and oxidizing it – in the same way as described for the first tunnel barrier – to form the second barrier. The last step involves fabrication of the ferromagnetic electrode by depositing 800 Å of either cobalt or nickel. After the completion of the fabrication, the devices are measured at 4.2 K to select the good ones (as described in Section 2.5.1), following which, the good devices are cooled in the dilution refrigerator.

The samples are measured using a similar setup as described in Section 2.5.1. Figure 5.4(a) shows the schematic of the circuit used for the four probe measurements. The stripline filters described in Appendix A are used for all the measurements and the difference in the electronic temperature is seen in the narrow width of the Fermi function (as shown in Figure 5.4(b)). This reduced width, and consequently reduced electronic temperature (~ 40 mK), is to be compared with the data shown in the previous chapter (~ 90 mK).

5.3 Density of states polarization

One of the consequences of applying a magnetic field to a magnet is that its chemical potential changes due to the unequal density of states for spin-up and spin-down electrons. Measuring this chemical potential shift can ideally provide information about the density of states at the Fermi energy [8]. In this section we will see how this change in the chemical potential affects our experiments.



5.3.1 Background

The origin of the change in the chemical potential of the system as a function of magnetic field can be understood by asking the question: what happens to the distribution of spins as a function of magnetic field? For starters, let us consider a very simple model [8], and later we will see how this model is improved by Allan MacDonald [16]. The inherent assumption, in the simple model, is that there are two collinear spin bands. At zero magnetic field the Fermi energy of the spin-up band (majority spins) and spin-down band (minority spins) are aligned since the two bands are in thermodynamic equilibrium (as shown in Figure 5.5(a)). However, as a magnetic field is applied, the energy of states in the two bands will shift in opposite directions on account of the Zeeman energy, as shown in Figure 5.5(b). Eventually the electrons will equilibrate by having some spin-down electrons flip to spin-up. Because of the different densities of states at the Fermi level for spin-up and spin-down electrons, the chemical potential of the system changes by an amount,

$$\Delta\mu = -\frac{1}{2}g\mu_B H \frac{(D_{\uparrow}(E_F) - D_{\downarrow}(E_F))}{(D_{\uparrow}(E_F) + D_{\downarrow}(E_F))}, \quad (5.5)$$

where $\Delta\mu$ is the change in the chemical potential, g the g-factor for the ferromagnet, μ_B is the Bohr magneton, H is the applied magnetic field, and $D_{\uparrow,\downarrow}(E_F)$ is the density of states for the spin-up, \uparrow , and spin-down, \downarrow , bands respectively. This change in chemical potential can be rewritten in terms of the polarization of the density of states (P_{DOS}) as,

$$\Delta\mu = -\frac{1}{2}g\mu_B H P_{DOS}, \quad (5.6)$$

where,

$$P_{DOS} = \frac{D_{\uparrow}(E_F) - D_{\downarrow}(E_F)}{D_{\uparrow}(E_F) + D_{\downarrow}(E_F)}. \quad (5.7)$$

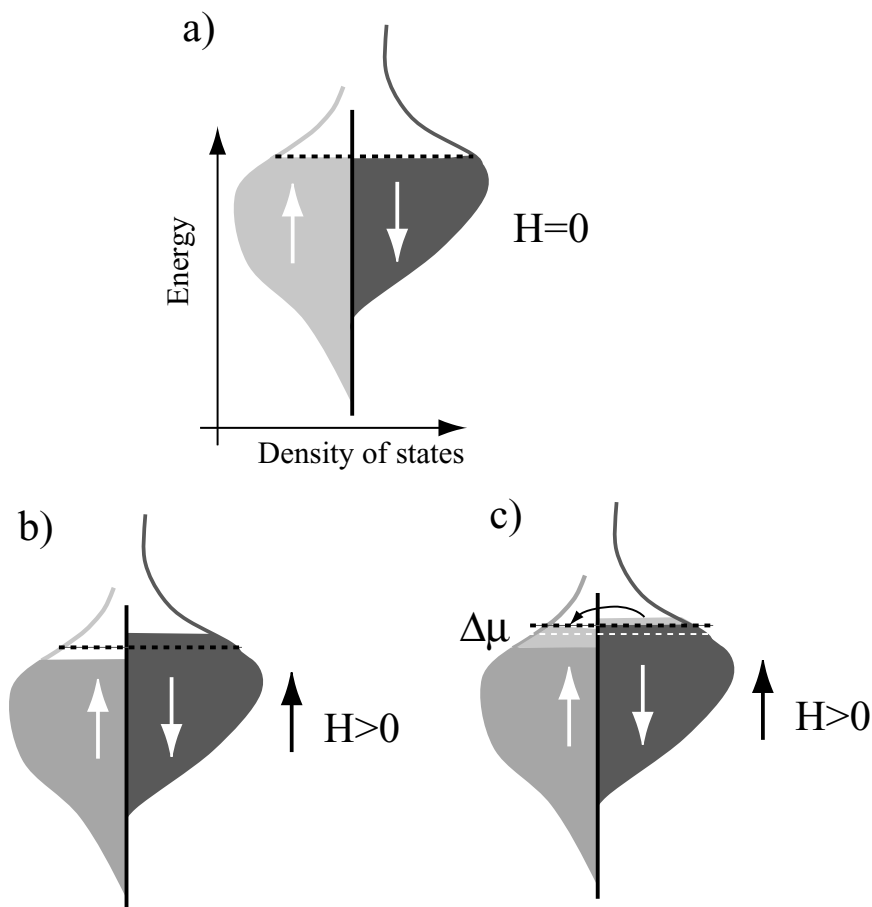


Figure 5.5: a) Cartoon showing the density of states for a ferromagnet using the two spin bands. b) Shift in the energy of the states due to a non-zero magnetic field assuming that the electrons are momentarily frozen in their previous states. The black dotted line indicates the position of the Fermi energy before the magnetic field is applied. c) Thermalization of the electrons leads to transfer of spins from the spin-down band to the spin-up band. A “thinner” slice of spin-down states is needed to fill up a “thicker” slice of spin-up states due to unequal density of states at the Fermi energy. The black dashed line indicates the position of the Fermi energy after the application of the magnetic field and the white dashed line indicates the position of the Fermi energy before the magnetic field is applied.

It should be pointed out that this change in chemical potential does not take exchange into account. A different and more rigorous approach to defining the chemical potential change has been followed by Allan MacDonald [16]. In his approach the exchange interaction has been taken into account. He calculates,

$$\Delta\mu = \frac{1}{2}g\mu_B H \frac{(D_\uparrow(E_F))^{-1} - (D_\downarrow(E_F))^{-1}}{(D_\uparrow(E_F))^{-1} + (D_\downarrow(E_F))^{-1} - 4I}. \quad (5.8)$$

We can rewrite this equation in a form similar to Equation 5.6 as

$$\Delta\mu = -\frac{1}{2}g\mu_B H P_\mu, \quad (5.9)$$

where,

$$P_\mu = \frac{(D_\uparrow(E_F) - D_\downarrow(E_F))}{(D_\uparrow(E_F) + D_\downarrow(E_F) - 4I) D_\uparrow(E_F) D_\downarrow(E_F)}. \quad (5.10)$$

Here the only new parameter is the exchange integral I , a phenomenological material property which is characteristic of the ferromagnet. We can now rewrite P_μ in terms of P_{DOS} in the following manner

$$P_\mu = \frac{P_{DOS}}{1 - 2ID^{HM}}, \quad (5.11)$$

where $(D^{HM})^{-1} = (D_\downarrow^{-1} + D_\uparrow^{-1})/2$. The denominator in the above expression has the form of a Stoner factor. The effect of this factor is that $|P_{DOS}| < |P_\mu|$ when I is positive. As a result ideally measuring the change in chemical potential allows us to probe thermodynamic quantities related to the magnetic system.

Now consider the case that a single electron transistor (SET) has a ferromagnetic lead and the SET is part of a measurement circuit, like the one shown in Figure 5.4(a). The net result of the presence of a magnetic electrode is that the electrochemical potential of the ferromagnetic electrode (μ_F) will depend linearly as a function of both the bias voltage (V_{bias}) and the magnetic field. Figure 5.6(a) shows the position of the Fermi levels of the right and the left lead together with

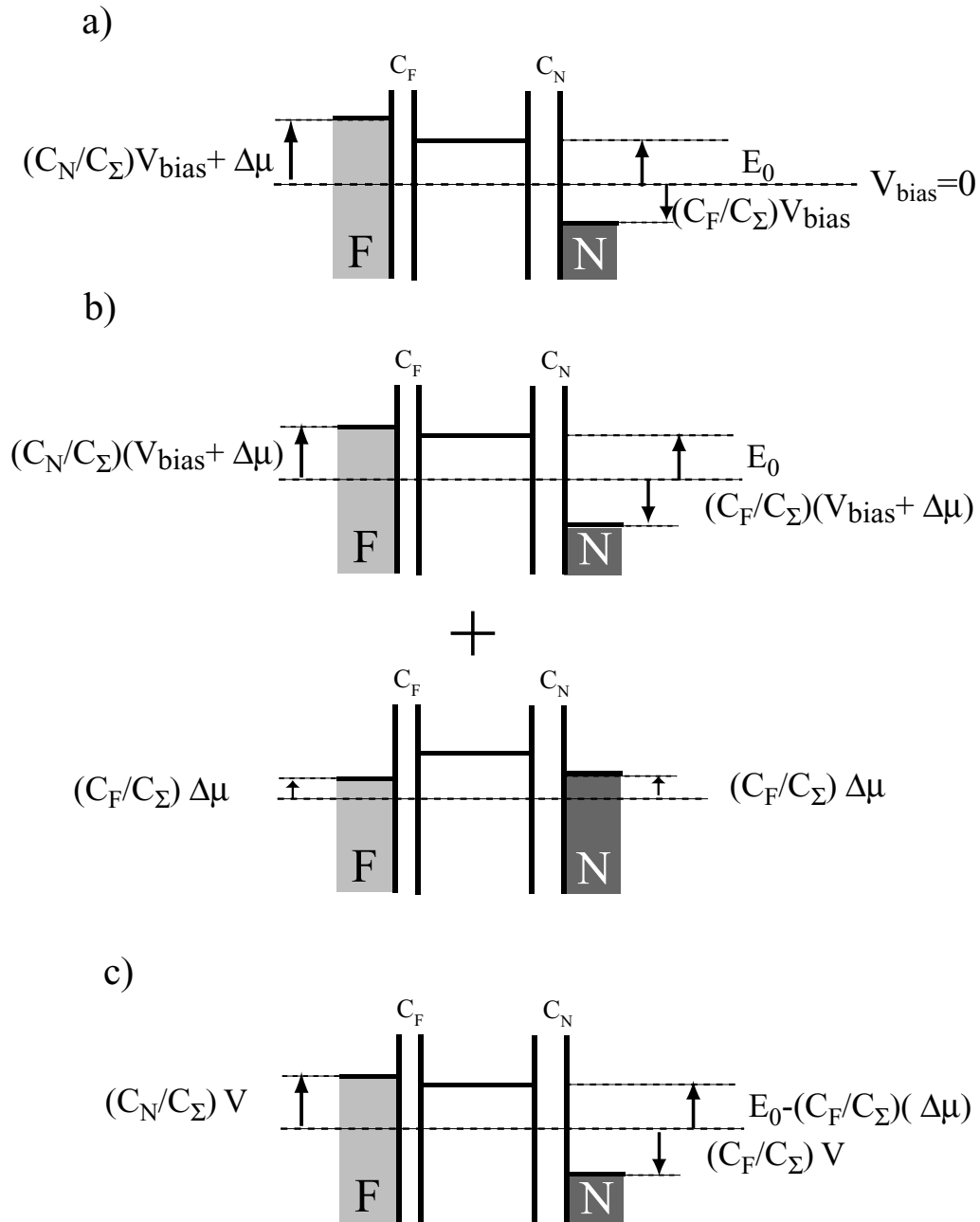


Figure 5.6: a) Schematic diagram showing the position of Fermi energies for the two leads and the position of the first threshold for tunneling to begin. C_N and C_F are the capacitances associated with the two tunnel barriers; with $C_\Sigma = C_N + C_F$. All the energies are measured with respect to the position of Fermi energy of the lead at zero bias ($V_{bias} = 0$). b) Linear superposition of two energy level diagrams equivalent to the diagram shown in (a). c) The net effect of $\Delta\mu$ is to shift the energy level spectrum within the nanoparticle, just like the effect of a gate voltage. Here V is the voltage measured by the voltage amplifier in the four probe setup.

the first level for the threshold tunneling step. It should be emphasized that the voltage measured by the voltage amplifier is not V_{bias} , but $V = V_{bias} + \frac{\Delta\mu}{e}$.⁵ Figure 5.6(b) shows the position of various levels as a linear combination of the two positions shown. This can be done since all the effects are linear to the leading order. The advantage of this linear superposition being that now all the energies are shown as a function of an experimentally measured quantities, V and $\Delta\mu$. It is only the relative shift between the Fermi energy of the leads and the energy level within the nanoparticle that is important. It is immaterial whether the energy levels move towards the Fermi levels or vice versa. Consequently, one can view the result of the shift of the chemical potential in the magnet as effectively shifting of the energy levels within the dot by an amount $\frac{-\Delta\mu C_F}{C_N + C_F}$; this can be schematically seen in Figure 5.6(c). The advantage of this approach is that we can now view the change in chemical potential of the ferromagnetic lead as a function of the magnetic field as an “effective” gate voltage proportional to $\Delta\mu$.⁶ Using such an approach allows us to account consistently for the effect of the magnetic field in a variety of scenarios.

In addition to the change in chemical potential due to the magnetic field there is another effect of the magnetic field – Zeeman splitting of the energy levels within the nanoparticle – which is due to the lifting of the degeneracy between the spin-up and spin-down states in the quantum dot. Now we have two linear effects of the magnetic field: the Zeeman effect, and the shifting of the all energy levels due to the magnetic lead (this is illustrated in the energy diagram shown in Figure 5.7(a)). The net effect is that the splitting of the spin-up and spin-down states, as a function of the magnetic field, is asymmetric, as can be seen clearly in Figure 5.7(b). The degree

⁵Note the symbol V used in this chapter has a different meaning. In this chapter it takes into account the effect of the bias voltage, as well as the change in the chemical potential of the electrode due to the magnetic field. In experiments with non-magnetic electrodes it has the same connotation as bias voltage.

⁶This effective gate-like effect does not need a physical gate to be present.

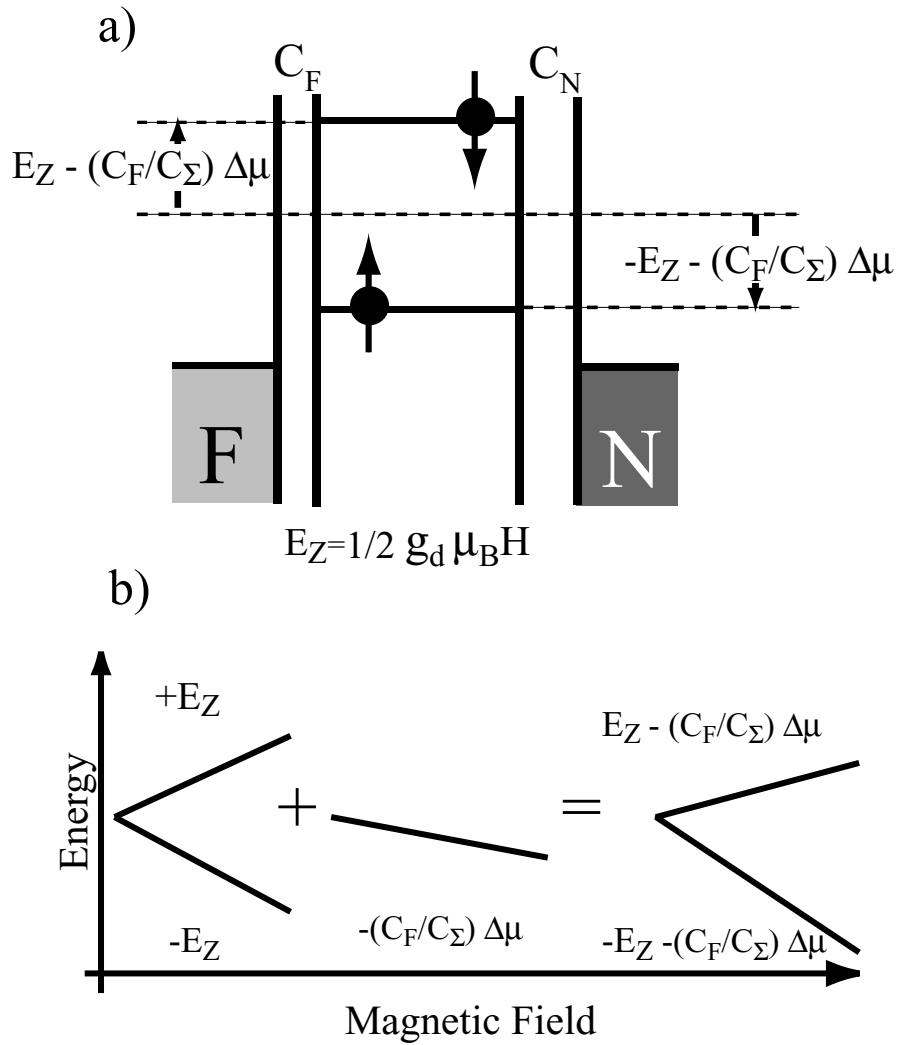


Figure 5.7: a) Energy-level diagram showing two effects of magnetic field: Zeeman splitting and the effect of the chemical potential shift for the ferromagnetic lead. F and N indicate the ferromagnetic and normal electrodes respectively. C_N and C_F are the capacitances associated with the normal and ferromagnetic electrode, and C_Σ is the sum of the two capacitances. The Zeeman energy is $E_Z = -g_d \mu_B \vec{s} \cdot \vec{H}$, where \vec{s} is the spin of the electron and \vec{H} is the magnetic field, and g_d is the g-factor associated with an energy level in the quantum dot. b) Cartoon for the evolution of the spin-split energy levels as a function of magnetic field. The asymmetric splitting is a consequence of the magnetic lead.

of the asymmetry is directly proportional to the electrochemical potential shift of the ferromagnet. It is important to note that there is an inherent assumption in taking the algebraic difference of the energies of the spin-up and spin-down levels, namely that the g-factors (g_d) for the spin-up and spin-down states are the same. I think that this assumption is justified since the g-factor is same for one orbital state. We find that the apparent g-factors of the spin states can change in the ranges of magnetic field where one state undergoes an avoided crossing with a neighboring state. In regions away from the avoided crossings we can calculate $\Delta\mu$ reliably.

Until this point our analysis assumes that the change in the chemical potential is the only effect that leads to the observed asymmetry. However, as it will become clear in the next section, there are other effects that contribute to the observed asymmetry in the splitting of spin-up and spin-down levels. As a result, the quantity we measure is not P_{DOS} . In order to compare the experiments with Equation 5.6, we express the experimentally determined change in chemical potential as,

$$\Delta\mu = -\frac{1}{2}g\mu_B H\Pi. \quad (5.12)$$

Here Π reflects the experimentally measured shift in the chemical potential of the ferromagnetic lead relative to the energy levels in the nanoparticle. We will discuss the experimental results in terms of the quantity Π which is a dimensionless measure of the asymmetric Zeeman splitting of the energy levels. So far Π does not have a physical significance, and it has been used to parameterize experiments.

Having discussed the physics behind our experimental measurements we consider the data next.

5.3.2 Measuring the change in chemical potential

Figure 5.8(a) shows the evolution of energy levels as a function of the magnetic field for a device with an aluminum nanoparticle contacted by one aluminum lead and one cobalt lead. The asymmetry in the spin-split states is evident. From the differential conductance plot near zero field we can find out that the threshold transition is a *tunneling in* transition, meaning that the electron tunnels onto the nanoparticle before it tunnels off. Determining the exact type of transition is impossible to determine in a two terminal device with drain-source electrodes fabricated from the same material. However we can determine the type of transition in this case, where we have one lead fabricated using aluminum (a superconductor) and the other using cobalt. This can be done either by looking for shifts in the position of peaks due to the superconducting gap, or by looking at the shape of the conductance peaks for either sign of bias voltage, or both. Details regarding this can be found in Chuck Black's thesis [17].

Once the type of transition is determined we can easily visualize various transitions using the energy diagram shown in Figure 5.8(b) and (c). Using these diagrams we can write down the following equation for the slope of lines tracing the position of peaks for positive V ,

$$\begin{aligned} \frac{dV_{\pm}}{dH} &= \frac{C_{\Sigma}}{C_N} \left(-\pm \frac{1}{2} g_d \mu_B H - \frac{C_F}{C_{\Sigma}} \Delta\mu \right), \\ &= \mp \frac{1}{2} g_d \mu_B H \frac{C_{\Sigma}}{C_N} - \frac{C_F}{C_N} \Delta\mu, \end{aligned} \quad (5.13)$$

where \pm corresponds to spin-up and spin-down states respectively, g_d is the g-factor associated with a particular energy level, H is the magnitude of the magnetic field, and μ_B is the Bohr magneton. Using a similar idea we can write down the expected

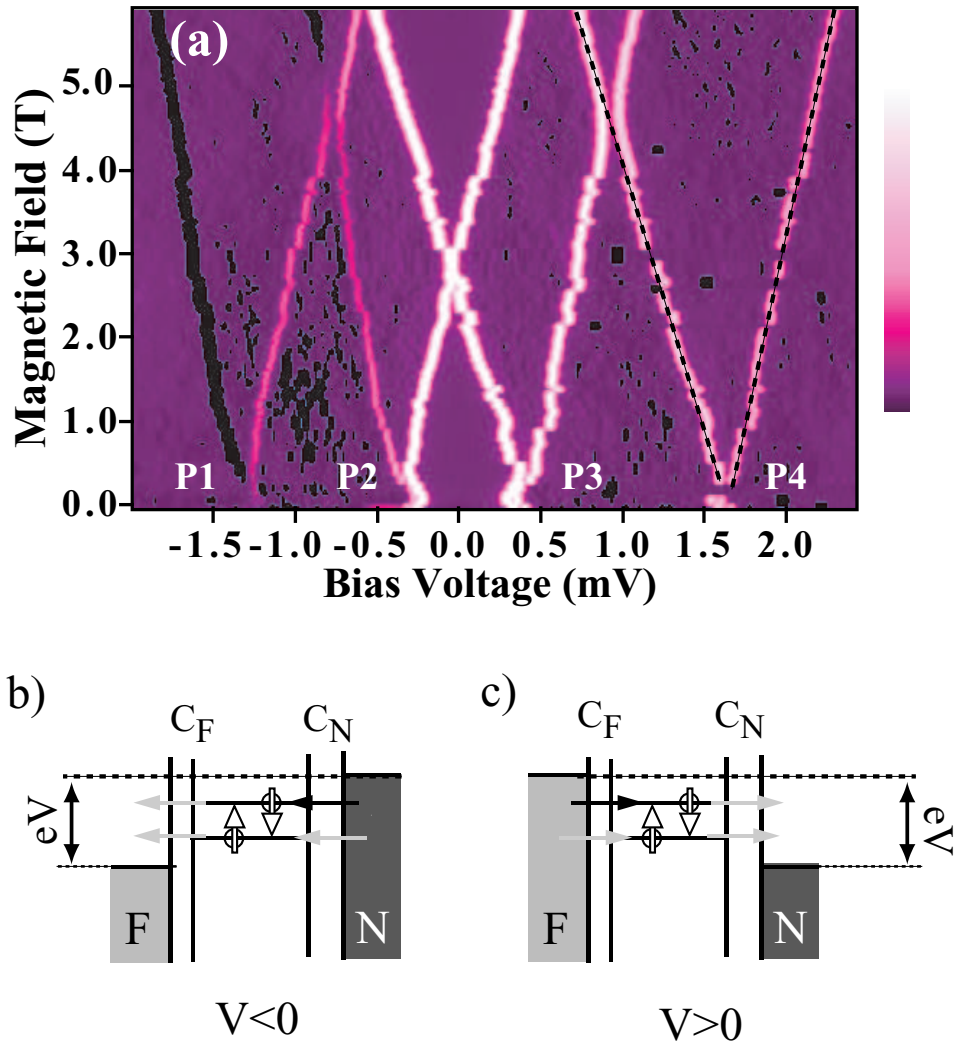


Figure 5.8: a) Colorscale conductance plot of a device – with one lead fabricated from cobalt – as a function of the magnetic field. Conductance peaks marked P1, P2, P3 and P4 split into two peaks corresponding to spin-up and spin-down states. The asymmetry in the splitting is clearly seen. The dashed line marks the position of the spin-split pair in P4. Conductance peaks P2 (P1) and P3 (P4) are due to tunneling via the same orbital level, but for different signs of $V = V_{bias} + \Delta\mu$. The sample shown here has some glitches because of the charging of a neighboring island. This, however, does not affect the physics under discussion. b) Energy level diagram for the first threshold for negative V . The threshold event being the *tunneling in* of an electron ($n_0 \rightarrow n_0 + 1$, n_0 is even), marked by a black arrow, followed by various transitions marked by grey arrows which indicate all the subsequent possible transitions. This set of transitions gives rise to the spin-split peaks P2. c) Energy level diagram for the threshold event for positive V . This gives rise to the spin-split peaks P3.

slopes for negative V ,

$$\begin{aligned}\frac{dV_{\pm}}{dH} &= -\frac{C_{\Sigma}}{C_F} \left(-\pm \frac{1}{2} g_d \mu_B H - \frac{C_F}{C_{\Sigma}} \Delta\mu \right), \\ &= \pm \frac{1}{2} g_d \mu_B H \frac{C_{\Sigma}}{C_F} + \Delta\mu.\end{aligned}\tag{5.14}$$

In Equation 5.14 we see that the average of the slopes directly gives bare $\Delta\mu$ – with no device specific parameters – together with the appropriate sign.⁷ Using Equations 5.13 and 5.14 we can calculate $\Delta\mu$ for this particular sample by using the slopes of pairs of energy levels as a function of the magnetic field. Table 5.1 shows the calculated values of $\Delta\mu/H$, Π and g_d , as defined by Equations 5.13, 5.14 and 5.12, for the pairs of energy levels indicated in Figure 5.8(a). The average value of Π for this sample is -0.37 ± 0.05 , where the standard deviation is the same as the typical error associated with the measurement of Π from each of the levels. We performed similar measurements on two more devices with one cobalt electrode where we measure the Π to be -0.7 ± 0.1 and -0.1 ± 0.1 .

Similar experiments were done for devices with one of the leads fabricated using nickel. The results of tunneling spectroscopy as a function of magnetic field are shown in Figures 5.9(a) and 5.10(a). One can notice clearly the asymmetry due to the chemical potential shift. For this particular device, the threshold transitions are associated with the tunneling off of an electron from the nanoparticle ($n_0 \rightarrow n_0 - 1$, where n_0 is even⁸). The energy level diagram for such transitions is shown in Figures 5.9(b) and 5.10(b). Using the ideas discussed earlier we can write down the expected slopes of energy levels as a function of magnetic field for this case. For a

⁷I want to emphasize that the sign of $\Delta\mu$ is not imposed but is calculated from the measurement. We do not make any *a priori* assumption about the band-structure of the ferromagnet.

⁸The parity of the quantum dot can be determined by checking if the first energy level – after the Coulomb blockade is overcome – splits into two energy levels or not. If a splitting is observed, then the quantum dot has even parity, and if the energy level just shifts to higher bias voltages without exhibiting any Zeeman splitting, then in that case the parity is odd [17].

Table 5.1: $\Delta\mu/H$, Π , and g_d calculated for cobalt using four different pairs of energy levels shown in Figure 5.8(a).

Pair number	$\frac{\Delta\mu}{H}$ (eV T ⁻¹)	Π	g_d
P1	$(2.14 \pm 0.06) \times 10^{-5}$	-0.37 ± 0.01	2.05 ± 0.06
P2	$(1.97 \pm 0.06) \times 10^{-5}$	-0.34 ± 0.01	1.99 ± 0.06
P3	$(2.13 \pm 0.13) \times 10^{-5}$	-0.37 ± 0.02	1.98 ± 0.07
P4	$(2.30 \pm 0.14) \times 10^{-5}$	-0.40 ± 0.02	2.04 ± 0.07

positive bias we can write the expression for the slopes of energy levels as a function of magnetic field as

$$\begin{aligned}\frac{dV_{\pm}}{dH} &= -\frac{C_{\Sigma}}{C_F} \left(-\pm \frac{1}{2} g_d \mu_B H - \frac{C_F}{C_{\Sigma}} \Delta\mu \right), \\ &= \pm \frac{1}{2} g_d \mu_B H \frac{C_{\Sigma}}{C_F} + \Delta\mu.\end{aligned}\tag{5.15}$$

Similarly the slopes for the negative bias can be written as

$$\begin{aligned}\frac{dV_{\pm}}{dH} &= \frac{C_{\Sigma}}{C_N} \left(-\pm \frac{1}{2} g_d \mu_B H - \frac{C_F}{C_{\Sigma}} \Delta\mu \right), \\ &= \mp \frac{1}{2} g_d \mu_B H \frac{C_{\Sigma}}{C_N} - \frac{C_F}{C_N} \Delta\mu.\end{aligned}\tag{5.16}$$

Using these equations together with Equations 5.12, 5.15 and 5.16 we can calculate Π for Ni using the seven energy levels marked in Figures 5.9(a) and 5.10(a). Calculated values are tabulated in Table 5.2. Using the slopes of pairs of Zeeman-split energy levels we calculate $\Pi = -0.45 \pm 0.05$ for this nickel sample. We also measured two more samples with nickel electrode, and calculated Π to be -0.15 ± 0.1 and -0.2 ± 0.1 .

Notice that the sign of Π is negative; the same sign for Π was also measured by Ono *et al.* [8] using a SET⁹ with ferromagnetic leads. A negative sign implies that there are more states corresponding to the minority spins at the Fermi energy, as one would expect for a typical ferromagnet as shown in Figure 5.1.

The observation of differences in the magnitude of Π between samples made from the same material is surprising since, from all the arguments we have discussed so far [8, 16], one would expect the value of Π to be a bulk property of a ferromagnetic material, so that it would not change from sample to sample. We think that

⁹In their measurements Ono *et al.* used the charging energy of the SET instead of the discrete energy levels of the quantum dot. The charging energy of their devices was comparable to the change in chemical potential of the ferromagnetic lead as a function of the magnetic field. As a result they could observe Coulomb oscillations as a function of magnetic field; this allowed them to measure the quantity we refer to as Π .

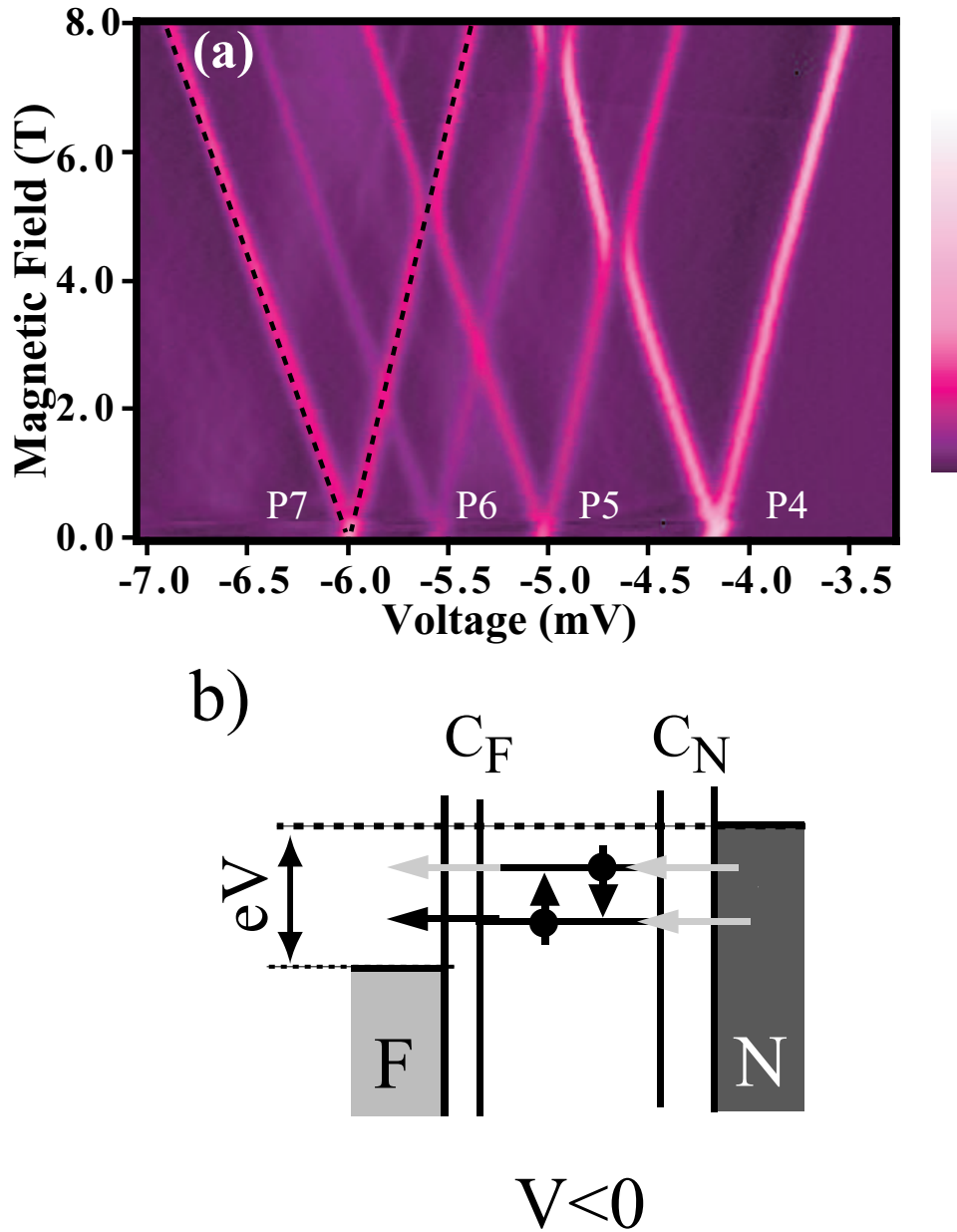


Figure 5.9: a) Colorscale conductance plot of a device – with one lead fabricated from nickel – as a function of the magnetic field. The dashed line marks the position of a spin-split pair. b) Energy level diagram for the first threshold for negative V . The threshold event being the *tunneling off* of an electron ($n_0 \rightarrow n_0 - 1$, where n_0 is even), marked by black arrow, followed by various transitions marked by grey arrows.

this sample to sample variation is due to the rearrangement of the charges at the ferromagnet-tunnel barrier interface. Ono *et al.* had also measured similar variation in their measurements, however, they attributed this to the uncertainty in measuring the charging energy for their SETs. We will consider the possible consequences of charge rearrangements a little later in greater detail (Section 5.3.3). The rearrangement of charges as a function of magnetic field has not been considered previously, and has important consequences for understanding operation of magnetic devices with multiple tunnel junctions.

In the next section we compare the values of Π that we measure and the numbers we would expect from the theory.

5.3.3 Comparison of measurements and theory

There are two aspects of the our measured values of Π – for both Ni and Co – that need a closer look: 1) the magnitude of Π , and 2) the variation in magnitude from sample-to sample.

Let us first consider the magnitude of Π . Our measured numbers $\Pi = -0.37 \pm 0.05$, -0.7 ± 0.1 , -0.1 ± 0.1 for Co and $\Pi = -0.45 \pm 0.05$, -0.15 ± 0.1 , -0.2 ± 0.1 for Ni are generally lower in magnitude than the numbers from band structure calculations [21], which find $P_{DOS} = -0.60$ for Co and $P_{DOS} = -0.80$ for Ni. This difference between the measured values of Π and P_{DOS} is further enlarged if one takes into account the exchange interactions in the ferromagnet – an approach followed by Allan MacDonald [16].

Dan Ralph proposed that the explanation for both the sample-to-sample variation in the measured values of Π and also the smaller than expected values is that a magnetic field may produce rearrangements in the charge distribution inside a mag-

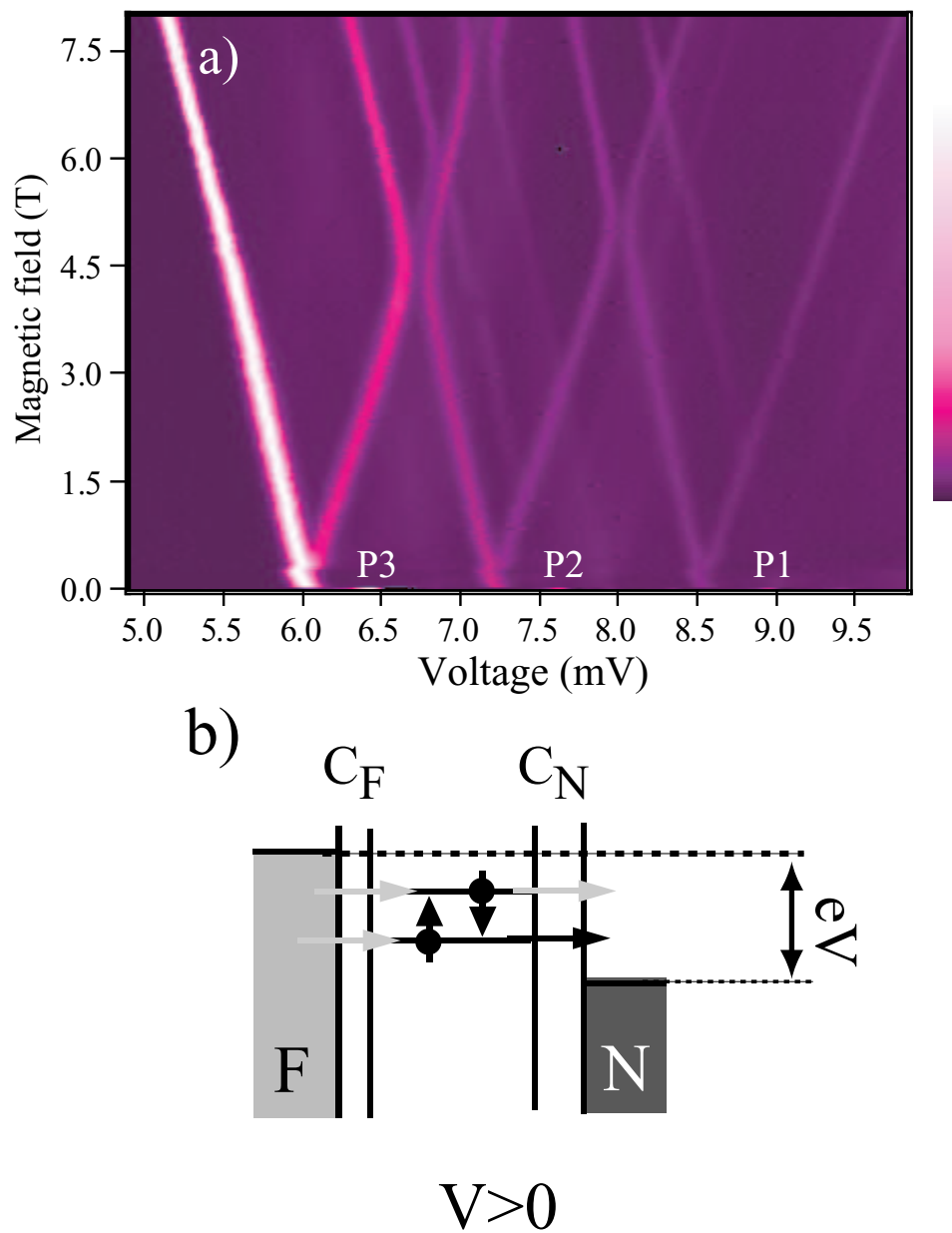


Figure 5.10: a) Colorscale conductance plot of a device – with one lead fabricated from nickel– as a function of the magnetic field. b) Energy level diagram for the first threshold for positive V . The threshold event being the *tunneling off* of an electron, marked by black arrow, followed by various transitions marked by grey arrows.

Table 5.2: $\Delta\mu/H$, Π and g_d calculated for nickel using seven different pairs of energy levels shown in Figures 5.9(a) and 5.10(a).

Pair number	$\frac{\Delta\mu}{H}$ (eV T ⁻¹)	Π	g_d
P1	$(2.64 \pm 0.08) \times 10^{-5}$	-0.46 ± 0.01	1.87 ± 0.06
P2	$(2.85 \pm 0.16) \times 10^{-5}$	-0.49 ± 0.03	1.83 ± 0.05
P3	$(2.36 \pm 0.14) \times 10^{-5}$	-0.41 ± 0.02	1.84 ± 0.05
P4	$(2.21 \pm 0.14) \times 10^{-5}$	-0.38 ± 0.02	1.83 ± 0.05
P5	$(2.80 \pm 0.20) \times 10^{-5}$	-0.48 ± 0.04	1.86 ± 0.06
P6	$(2.66 \pm 0.10) \times 10^{-5}$	-0.46 ± 0.02	1.89 ± 0.06
P7	$(2.64 \pm 0.10) \times 10^{-5}$	-0.46 ± 0.02	1.90 ± 0.07

netic tunnel junction that will produce an additional change in the energy levels of the nanoparticle as a function of H , with different strengths in each device. Such an effect is reasonable within the same picture of wavefunctions that explains why the tunneling polarization is positive while the overall density-of-states polarization at the Fermi level is negative. The predominantly d-band character of the minority electrons in Co or Ni causes their wavefunctions to decay over a short distance as they penetrate into the tunnel barrier. The majority electrons, with predominantly sp-band character, will have longer decay lengths [24, 25]. Therefore, as an applied magnetic field transfers electrons from minority to majority states, some charge density at the surface of the magnet may shift slightly into the barrier region [20]. Spin-dependent surface states could produce the same effect. This charge movement has the right sign to explain our results, in that it will generally increase the measured values of Π for Ni and Co electrodes.¹⁰ We can estimate the magnitude of the effect of surface charge by calculating the work that the moving charge density does on an electron in the nanoparticle. Within a simple picture that ignores the contribution of exchange interactions to the electrochemical potential shift in the ferromagnet [16], and making a rough approximation that the spin-dependent densities at the magnet's surface are similar to the bulk, the charge density per unit area – which changes spin – at the last monolayer of the magnet is

$$\sigma \approx e a g \mu_B \mu_0 H \frac{\rho_{\uparrow} \rho_{\downarrow}}{(\rho_{\uparrow} + \rho_{\downarrow})}, \quad (5.17)$$

where a is the lattice constant, ρ_{\uparrow} and ρ_{\downarrow} are the densities of state at Fermi energy for spin-up and spin-down electrons. If the average position for charges in the minority and majority states differs by Δx at the surface layer of the magnet, then the work done by charge movement should lead to a change in the value of the measured

¹⁰The rearrangement of charges due magnetic field will tend to decrease the magnitude of $|\Pi|$.

electrochemical shift

$$\Delta\Pi \approx \frac{-e^2}{\epsilon_0} g a(\Delta x) \frac{\rho_{\uparrow}\rho_{\downarrow}}{\rho_{\uparrow} + \rho_{\downarrow}} \quad (5.18)$$

$$\approx -12\Delta x/\text{\AA} \quad (5.19)$$

for either a Co or Ni electrode. Variations in the average value of Δx by less than 0.05 \AA are, therefore, sufficient to explain the sample-to-sample differences that we observe.

Next we consider how we can probe the polarization of tunneling electrons in our experiments.

5.4 Tunneling polarization

Tunneling polarization measures the relative spin asymmetry in the electrons that tunnel from a ferromagnet, and it is the relevant quantity for all devices based on tunnel magnetoresistance (TMR) effect [11]. The tunneling polarization can be defined as

$$P_{tunnel} = \frac{\gamma_{\uparrow} - \gamma_{\downarrow}}{\gamma_{\uparrow} + \gamma_{\downarrow}}. \quad (5.20)$$

Here γ_{\uparrow} and γ_{\downarrow} are the tunneling rates for the spin-up and spin-down electrons respectively. We can measure tunneling polarization when our devices are in the regime where only one spin degenerate energy level is involved in the current transport.¹¹ This could be done easily if one has the transistor geometry with one lead fabricated from a ferromagnet.¹² However, even after several attempts, I was unable to measure such a device with a working gate. Fortunately, I was able to measure

¹¹Theoretically one could measure this quantity with many energy levels involved in the current transport. However, solving the rate equations for these situations is very difficult.

¹²In Section 4.2 we discuss the data where the gate electrode is used to tune current flow via one energy level. Those devices were fabricated using aluminum for all the electrodes and the nanoparticle.

a device with a very small blockade voltage where the current flows via only one energy level. I will discuss the measurements done with that one sample.

5.4.1 Measuring the current via a single spin-degenerate energy level

Figure 5.8 shows the colorscale conductance plot for a device with one lead fabricated using cobalt. We have already analyzed the asymmetric splitting of the spin-up and spin-down levels in this device. One aspect of data that we have not used yet is the magnitude of the current, and this allows us to measure the polarization of the tunnel current. Figure 5.4(b) shows the current steps and the conductance peaks corresponding to the pairs of spin-split levels P2 and P3. Measuring the height of current steps allows us to calculate all the tunneling rates, and the tunneling rates can then be used to calculate P_{tunnel} .

Note that the rate of tunneling onto a discrete energy level can be estimated using Fermi's Golden rule [22, 23] and is simply

$$\gamma = \frac{4\pi}{\hbar} \rho_l |T|^2, \quad (5.21)$$

where ρ_l is the density of states for the leads from which the electron is tunneling, and T is the tunneling matrix element for the lead-energy level system. So, the quantity we measure is not simply the density of states polarization but the tunneling polarization which takes into account the relevant matrix elements.

Figure 5.11 shows the current through the device as a function of V (the voltage measured across the device). Consider first the current for positive bias. As V is gradually increased, the first energy level that allows current to flow is the spin-up level, followed by the spin-down level. For positive V electrons tunnel from the

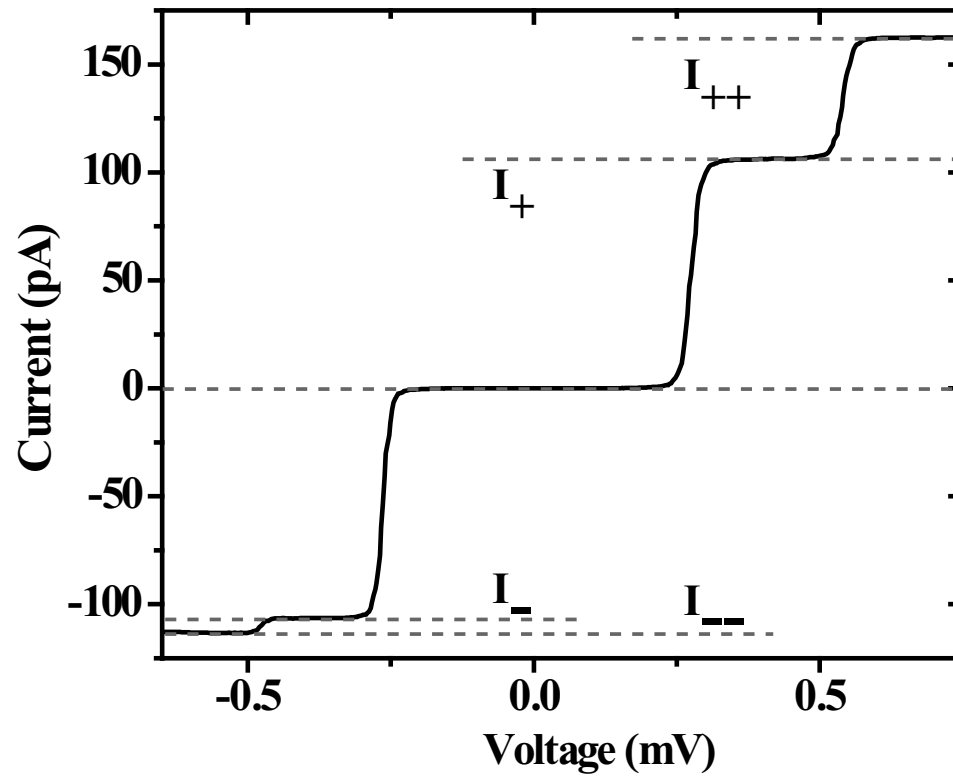


Figure 5.11: Plot of current as a function of the voltage V . The four different steps (I_{++} , I_+ , I_- and I_{--}) corresponds to the threshold of tunneling via the spin-split energy levels.

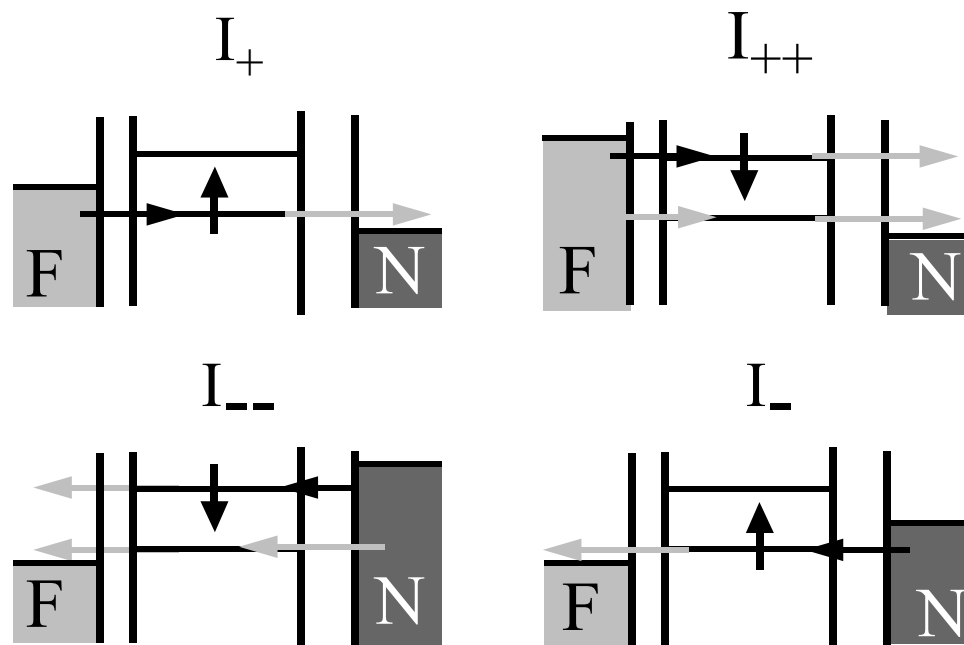


Figure 5.12: Energy diagrams corresponding to the four threshold steps in the measured current. The steps can be clearly seen in Figure 5.11. The black arrows indicate the threshold transition and the grey arrows indicate all the possible subsequent transitions.

ferromagnet onto the nanoparticle and then onto the aluminum electrode. The two steps, I_+ and I_{++} , in the current for positive V correspond to these two thresholds. This can be seen in the energy diagrams shown in Figure 5.12. Similar steps in the current can be seen for negative V , but now the electrons tunnel from the aluminum electrode onto the nanoparticle and then off it.

Using the rate equation approach developed in Chapter 3, we can calculate the current for these four current steps in terms of three tunneling rates: γ_\uparrow , the tunneling rate for spin-up electrons into or from the ferromagnetic lead, γ_\downarrow , the tunneling rate for spin-down electron into or from the ferromagnet, and γ_0 the tunneling rate for electrons, of either kind, into or from the non-magnetic electrode. The tunneling rates associated with spin-split levels are shown in Figure 5.13. We can then write down the current for the four steps:

$$\begin{aligned}
 I_{++} &= e \frac{\gamma_0(\gamma_\uparrow + \gamma_\downarrow)}{\gamma_0 + \gamma_\uparrow + \gamma_\downarrow}, \\
 I_+ &= e \frac{\gamma_0 \gamma_\uparrow}{\gamma_0 + \gamma_\uparrow}, \\
 I_- &= -e \frac{\gamma_0 \gamma_\uparrow}{\gamma_0 + \gamma_\uparrow}, \\
 I_{--} &= -e \frac{2\gamma_0 \gamma_\uparrow \gamma_\downarrow}{\gamma_\uparrow \gamma_\downarrow + \gamma_0 \gamma_\uparrow + \gamma_0 \gamma_\downarrow}.
 \end{aligned} \tag{5.22}$$

Note that the magnitude of the current for the current steps I_- and I_+ is the same, because single electron tunneling occurs via the same single non-spin-degenerate level in these cases. As a result, the system of Equations 5.22 reduces to a system with three unknowns and three equations which can be solved to get the values of three variables γ_0 , γ_\uparrow and γ_\downarrow from the measured values of I_+ , I_{++} , and I_{--} . We then calculate the tunneling polarization using Equation 5.20. We have calculated the tunnel polarization as a function of magnetic field, and for that we used I-V curves, like the one shown in Figure 5.11, at different strengths of magnetic field.

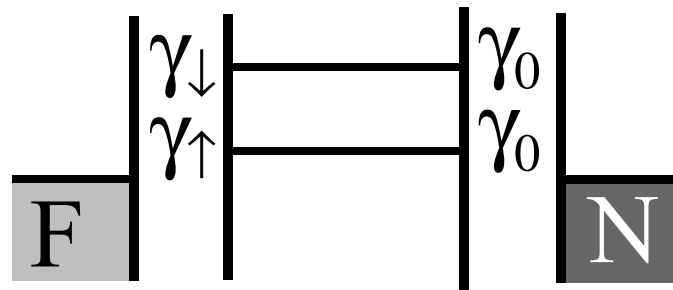


Figure 5.13: Energy level diagram showing the spin-split levels and the tunneling rates associated with each of them. F denotes the ferromagnetic electrode and N denotes the non-magnetic electrode.

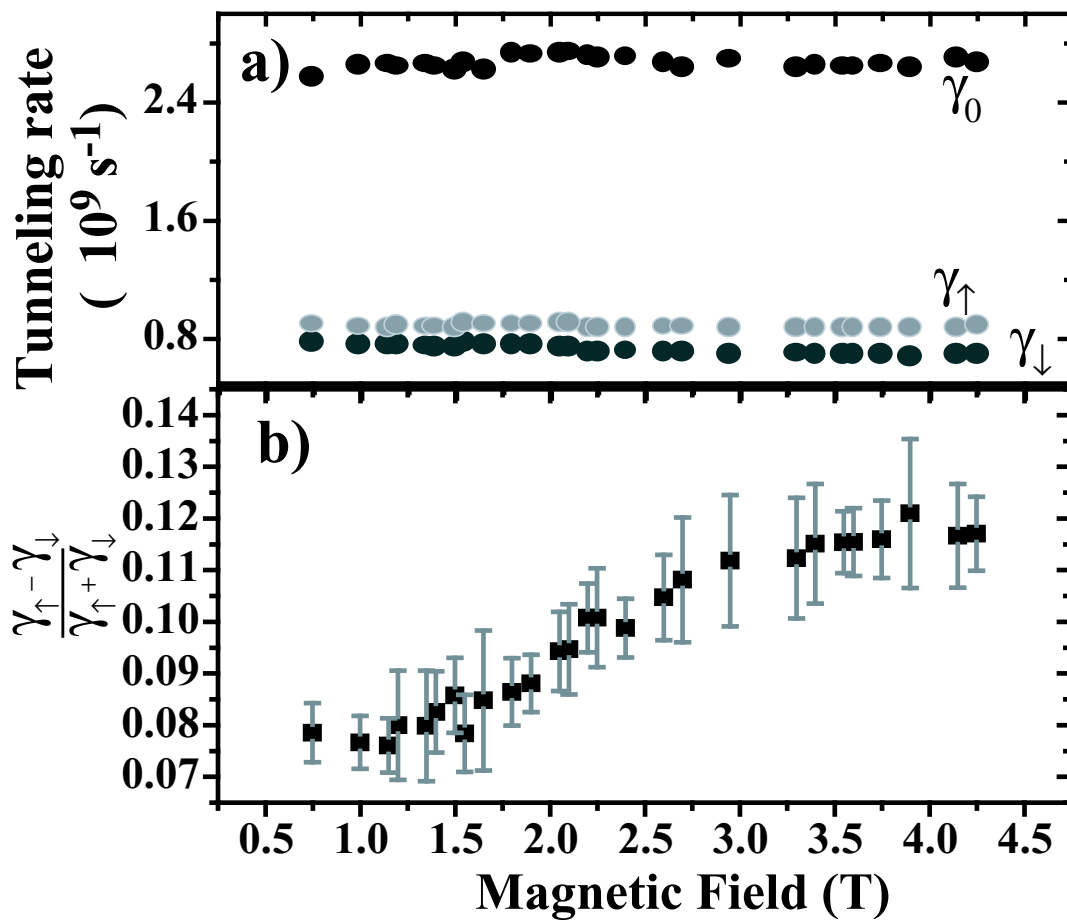


Figure 5.14: a) Plot of the tunneling rates for a device with cobalt electrode as a function of the magnetic field. The tunneling rates were calculated by analyzing the data using the rate equation approach described in Section 5.4.1. b) Tunneling polarization as a function of the magnetic field, for a device with Co electrode, calculated from the tunneling rates shown in Figure 5.14(a).

Figure 5.14(a) shows tunneling rates associated with our device, and Figure 5.14(b) shows the polarization as a function of the magnetic field. The first notable aspect of this measurement is that we can determine the sign of polarization as well as the magnitude, and we find the polarization to be positive, which means that the rate of tunneling for spin-up electrons is larger than that of spin-down electrons. Meservey and Tedrow measured the tunnel polarization of cobalt to be positive as well. Π measured for *this sample* (as discussed in Section 5.3.2) is found to be negative.

The tunnel-polarization and Π are different quantities. As mentioned earlier, the tunneling polarization measures the asymmetry in the tunneling rates for the two spins. Equation 5.21 points to the crucial role played by the matrix element for tunneling between the nanoparticle and the lead. Theoretical calculations indicate that *s*-electrons are primarily involved in the tunneling [10], whereas it is the *d*-electrons, which contribute predominantly to the density of states at the Fermi energy, whose probability density decays rapidly [24, 25]. The *s*-electrons have a density of states very similar to that shown in the cartoon in Figure 5.2, and the majority spin electrons have larger density of states at the Fermi energy, which results in a positive polarization.

Now we turn to the magnitude and magnetic field dependence of P_{tunnel} . The magnitude we measure is smaller than measurements done by Meservey and Tedrow, who found P_{tunnel} for cobalt to be $+35 \pm 3\%$. This is, however, not very surprising since the conditions for the fabrication of the tunnel barrier are very crucial in determining what P_{tunnel} is measured. In their initial measurements Meservey and Tedrow also observed lower values of polarization which they attributed to the “bad” quality tunnel barriers. It is evident from the definition of tunnel polarization that the role of tunnel barrier is a crucial one. The difference between our measurement

and other measurements is probably due to the different properties (for example oxidation conditions [26] or the thickness) of the tunnel barrier. The magnetic field dependence that we observe is something that others have not observed in the past. The exact mechanism for the increase in the polarization is not clear, but its origin must be related to the modification of the magnetic properties at the surface of the electrode rather than the bulk. The magnetic properties of a bulk ferromagnet should not vary over the energy range corresponding to the magnetic field within which we observe the variation in tunnel polarization.

5.4.2 Current flow via excited states

We can also measure the tunnel polarization using the excited states of the device. It becomes increasingly complicated to calculate tunnel polarization from the excited states, however, in this case we can use the rate-equation approach to calculate polarization using the first excited state. The asymmetry of the tunneling rates can be observed qualitatively by looking at the conductance plot. Figure 5.8(a) shows the colorscale conductance plot for the device with cobalt leads. We have discussed the physics associated with the spin-split levels P2 and P3. Note that the peak P1 also undergoes Zeeman splitting, but with one resonance giving positive conductance and the other negative. This can be clearly seen in Figure 5.15, where the peak corresponding to spin-down level in P1 has a negative dip. In itself a negative differential conductance is not surprising. It can arise from a variation in the tunneling rates for different energy levels. For instance, if an excited-state tunneling threshold has a smaller rate of tunneling compared to the low-energy tunneling states, the current through the device may decrease since the system may get stuck in the excited state. This is a qualitative picture, but it depends on the

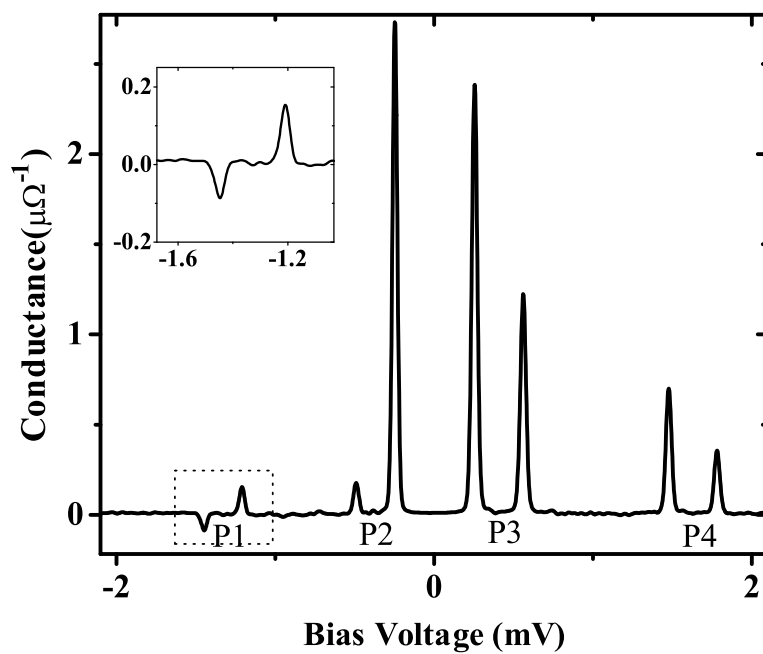


Figure 5.15: Differential conductance plotted as a function of the measured voltage. The inset shows a zoomed in view of peak P1 with the spin-split peaks having positive and negative amplitudes.

tunneling-in and tunneling-out rates. What is noteworthy about the data shown in Figure 5.15 is that the spin-split peak corresponding to the spin-down level has a negative weight. We saw in Section 3.2.4 how the weight of spin-split peaks can vary depending on the ratio of tunneling rates, but the negative peak for just the spin-down states is not possible within a model where the tunneling rates are the same for both spins. A negative conductance peak for a spin-split peak can occur only when the tunneling rates for the two types of spins are different, as is the case for this device geometry. This is a clear signature of polarized current flowing through the device. We have used the rate-equation formalism again for this second level to calculate the tunneling polarization. We find the polarization to be $\sim +0.15 \pm 0.05$.

5.5 Conclusions

The experiments in this chapter emphasize that tunneling spectroscopy can be used not only to probe energy level spectrum of a nanoparticle, but it can also be used to probe the bulk electrode. The measurement of the electrochemical potential, as a function of the magnetic field, suggest that the density of states at the Fermi energy for the minority spin (spin-down) is greater than that of majority spin. At the same time, the sample-to-sample variation suggests that charge rearrangement as a function of magnetic field should be taken into account, especially since Ono *et al.* [8] also observed such a variation, but they attributed it to the uncertainty in the charging energy. As far as the tunneling polarization measurements are concerned, the positive sign of polarization is in agreement with the measurements of Meservey and Tedrow [5]. What is different is the magnitude, and its variation with magnetic field. The origin of the variation in the magnitude of the tunnel

polarization is unclear. It should be emphasized that our measurements differ from other tunneling polarization measurements in that our measurements probe the polarization very locally, whereas other measurements are over a larger area.

Bibliography

- [1] S. A. Wolf *et al.*, Science 294, 1488 (2001).
- [2] G. A. Prinz, Physics Today, April 1995, p. 58.
- [3] J. M. Kikkawa and D. D. Awschalom, Phys. Rev. Lett. **80**, 4313 (1998).
- [4] W. H. Rippard and R. A. Buhrman, Phys. Rev. Lett. **84**, 971 (2000).
- [5] P. M. Tedrow and R. Meservey, Phys. Rev. Lett. **26**, 192 (1971); Phys. Rev. B **7**, 318 (1973).
- [6] S. F. Alvarado, Phys. Rev. Lett. **75**, 513 (1995).
- [7] S. K. Upadhyay, A. Palanisami, R. N. Louie, and R. A. Buhrman, Phys. Rev. Lett. **81**, 3247 (1998); R. J. Soulen *et al.*, Science **282**, 85 (1998).
- [8] K. Ono, H. Shimada, S. Kobayashi, Y. Ootuka, J. Phys. Soc. Jpn. **65**, 3449 (1996); J. Phys. Soc. Jpn. **66**, 1261 (1997); J. Phys. Soc. Jpn. **67**, 1359 (1998); J. Phys. Soc. Jpn. **67**, 2852 (1998).
- [9] R. Meservey and P. M. Tedrow, Phys. Rep. **238**, 173 (1994).
- [10] M. B. Stearns, Phys. Rev. B **8**, 4383 (1973); Phys. Rev. B **13** 1183 (1976); J. Magn. Magn. Mater. **5**, 167 (1977).
- [11] M. Julliere, Phys. Lett. **54A**, 225 (1975).
- [12] J. M. Teresa, A. Barthelemy, A. Fert, J. P. Contour, R. Lyonnet, F. Montaigne, P. Seneor, and A. Vaures, Phys. Rev. Lett. **82**, 4288 (1999).
- [13] M. Sharma, S. X. Wang, and J. Nickel, Phys. Rev. Lett. **82**, 616 (1999).
- [14] M. J. M. de Jong and C. W. J. Beenakker, Phys. Rev. Lett. **74**, 1657 (1995).
- [15] S. K. Upadhyay, Ph. D. thesis, Cornell University (1999).
- [16] A. H. MacDonald, in *Proceedings of the XVI Sitges Conference on Statistical Mechanics* (Springer-Verlag, Berlin, 2000), p. 21.

- [17] C. T. Black, Ph.D. thesis, Harvard University, 1996.
- [18] J. R. Petta and D. C. Ralph, Phys. Rev. Lett. **87**, 266801-1 (2002).
- [19] D. G. Salinas, S. Gueron, D. C. Ralph, C. T. Black, and M. Tinkham, Phys. Rev. B. **60**, 6137 (1999).
- [20] S. Zhang, Phys. Rev. Lett. **83**, 640 (1999).
- [21] D. A. Papaconstantopolous, *Handbook of the band structure of Elemental Solids* (Plenum, New York, 1986).
- [22] D. V. Averin and A. N. Korotkov, J. Low. Temp. Phys. **80**, 183 (1990).
- [23] D. V. Averin, A. N. Korotkov, and K. K. Likharev, Phys. Rev. B **44**, 6199 (1991).
- [24] E. Yu. Tsymbal and D. G. Pettifor, J. Phys. Cond. Mat. **9**, L411 (1997).
- [25] J. M. MacLaren, X.-G. Zhang, W. H. Butler, and X. Wang, Phys. Rev. B **59**, 5470 (1999).
- [26] L. Seve *et al.*, Europhys. Lett. **55**, 439 (2001).

Chapter 6

Tunneling spectroscopy of ferromagnetic nanoparticles

We saw in the previous chapter (Chapter 5) that several experiments have been used to characterize the spin polarization near the Fermi level in bulk ferromagnets [1, 2, 3, 4, 5], but different techniques give different results. Part of the difficulty is that these experiments measure different physical quantities; in essence they average over large numbers of states in determining the spin polarization, and different types of experiments effectively take differently weighted averages. As a result, it has been difficult to reach an adequate understanding of electronic states within ferromagnetic devices. In this chapter we follow a different approach to probing ferromagnets compared to the one followed in the previous chapter. Here, we will probe the electrons-in-a-box states *within* a ferromagnetic nanoparticle. This is in contrast to measurements in the previous chapter, where we used the well resolved electrons-in-a-box states, in a non-magnetic nanoparticle, to probe the properties of a bulk ferromagnet. The primary motivation for the current experiments is to better understand interactions within a ferromagnet. We saw in Chapter 4 how tunneling

spectroscopy allows us to probe the electronic interactions within the aluminum nanoparticle, in a unique way. In the present experiment we use this technique to probe magnetism at the nanometer scale. Most of the contents of this chapter have been adapted from a paper we wrote based on our experimental results [6].

Sophie Guéron started the measurements [7] involving the tunneling spectroscopy of ferromagnetic nanoparticles. These measurements helped motivate new descriptions of ferromagnetism that go beyond mean-field Stoner models [8, 9]. However, the first experiments left many open questions, particularly concerning the proper description of anisotropy energies, and whether the tunneling spectrum reflects the true electronic density of states or whether it is modified by non-equilibrium effects. The experiments described in this chapter improve upon earlier measurements done by Sophie Guéron. Prominent improvements being: fabrication of low noise tunnel barriers, a better data acquisition system,¹ and fabrication of devices with a gate electrode. These improvements have allowed observation of the energy levels with greater detail, allowing us to make comparisons with the existing models [8, 9].

The experimental procedure is similar to that discussed in previous chapters, but with significant modifications. In the next section we describe the fabrication procedure.

6.1 Sample fabrication

Devices measured in the current experiment contain a Co nanoparticle, separated from aluminum electrodes by aluminum oxide tunnel barriers, inside a tunnel junction with a nano-scale area small enough to allow individual particles to be contacted. (See device schematic, Figure 6.1.) The fabrication starts by making a

¹Thanks to the efforts of Abhay Pasupathy and Edgar Bonet.

nano-hole in a silicon nitride membrane using a series of steps including e-beam lithography and reactive ion etching (details described in Chapter 2). The gated device is fabricated by depositing 18.5 nm of Al to make the gate electrode on the lower side of the device as shown in Figure 6.1, and then isolating this gate by anodizing in an oxygen plasma to 3.5 V bias and depositing 8.5 nm of SiO_x . This is followed by depositing the first electrode by evaporating 150 nm of aluminum in the bowl-shaped hole, and oxidizing it at 50 mTorr for 3 minutes to form the first tunnel barrier. Nanoparticles are fabricated by depositing 0.5 nm of Co at room temperature, which makes particles – due to surface tension – in the range of 1–4 nm diameter. After this, 1.1 nm of aluminum oxide is deposited using e-beam evaporation to form the second tunnel barrier. The final step involves the deposition of a second aluminum electrode. For the case of non-gated devices, the procedure is similar to the one described here, with the omission of the gate fabrication steps. Details of the fabrication process are described in Chapter 2. The important difference between the fabrication of devices that will be discussed in this chapter and the ones described in Chapters 4 and 5 is that the second tunnel barrier is fabricated differently. In the two previous chapters the nanoparticles were made of aluminum, allowing us to fabricate the second tunnel barrier by oxidizing the surface of nanoparticles. However, for the case of the cobalt nanoparticle this is not feasible since oxidation leads to formation of cobalt oxide, an antiferromagnet, which causes spin-flip scattering during the tunneling process. We would like to avoid forming this for our experiments; since it is quite difficult to carry out the analysis with the spin of the tunneling electron being an ill-defined quantity. As a result, the second tunnel barrier is fabricated by depositing aluminum oxide di-

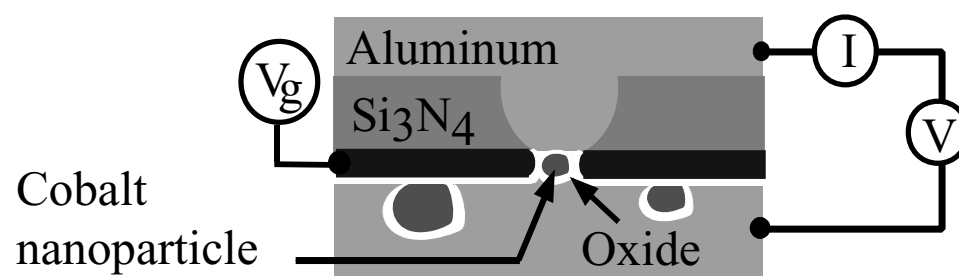


Figure 6.1: Device schematic showing a device with a cobalt nanoparticle and two non-magnetic leads.

rectly.² Following the fabrication, these devices are measured at 4.2 K to determine if they exhibit Coulomb blockade, and if they do, they are cooled down in a dilution refrigerator for detailed measurements (details described in Chapter 2).

6.2 Tunneling spectroscopy of a cobalt nanoparticle

When cooled to dilution refrigerator temperatures, the tunneling conductance dI/dV as a function of source-drain voltage V consists of individual peaks, as shown in Figure 6.2, associated with transitions between discrete electronic states in the nanoparticle. The V -spacings of resonances can be converted to energy, $\Delta E = e\Delta VC_2/(C_1 + C_2)$, in this way correcting for capacitive division across the two junctions. The capacitance ratio can be determined by comparing peak positions at positive and negative V (see Chapter 2 and ref. [10]). Performing tunneling spectroscopy as a function of magnetic field allows us to probe a magnetic system in a unique way. Features in different ranges of magnetic field allows us to isolate the effect of different interactions within a magnetic system. First, we look at the tunneling spectroscopy carried out in the low magnetic field range (~ 1 T). Here, magnetic anisotropy plays the dominant role.

6.2.1 Low-field magnetic field data

In Figure 6.3 (a) and (b), we plot the energies of tunneling resonances for a Co nanoparticle in a non-gated device as a function of magnetic field, H . The ca-

²Sophie Guéron tried fabricating the second tunnel barrier by depositing aluminum over the cobalt nanoparticle, and oxidizing it to form aluminum oxide. This method is risky since one can end up partially oxidizing the aluminum, leaving multiple nanoparticles electrically connected to each other.

capacitance ratios used to convert the bias voltage into energy are $C_1/(C_1 + C_2) = 0.70 \pm 0.04$ and 0.57 ± 0.03 respectively for the data shown in Figure 6.3(a) and (b) respectively. As H is swept from positive values toward zero, the levels first undergo significant continuous shifts. The discontinuity near $H = 0$ is an artifact of the Al leads going superconducting and then being driven normal by a negative field. This causes the resonance energies to jump by Δ , the superconducting gap [16], but the energies of the states within the nanoparticle evolve continuously.

Near $\mu_0 H_{sw} = -0.120$ T, for data shown in Figure 6.3(a), all the levels exhibit another large discontinuity, which can be identified with magnetic switching of the nanoparticle. If H is swept from negative to positive values, the field value for this transition is hysteretic, and the conductance spectrum is identical to that shown, but reflected about $H=0$. Similar hysteretic features were observed by Sophie Guéron as well [7]. So, by measuring the differential conductance of the device as a function of magnetic field we can probe the switching of a nanometer-scale magnet. This technique is complementary to switching measurements done by Wernsdorfer *et al.* using the SQUID microbridge techniques [17].³ The magnitude of the switching field (H_{sw}) we measure is in good agreement with measurements of Wernsdorfer *et al.* [17].

For the data shown in Figure 6.3(b), we observe continuous evolution of energy levels as the magnetic field is swept from positive to negative values. The energy levels in this device also exhibit the shift near 0 T due to the superconductivity of the leads. However, as the field is increased to more negative values, we observe two

³Measurements performed by Wernsdorfer *et al.* [17] look at the ground state properties of a magnetic system, whereas, in our experiments we can look at properties of a nanomagnet when it is not necessarily in the ground state – this is likely to happen in systems when electrons are flowing through it. The biggest advantage of their technique is the ability to characterize the switching properties of a nanomagnet – made from insulating or itinerant ferromagnets – in unprecedented detail. Our technique, in turn, allows to probe the magnetism of itinerant ferromagnets by changing the number of electrons on the nanomagnet.

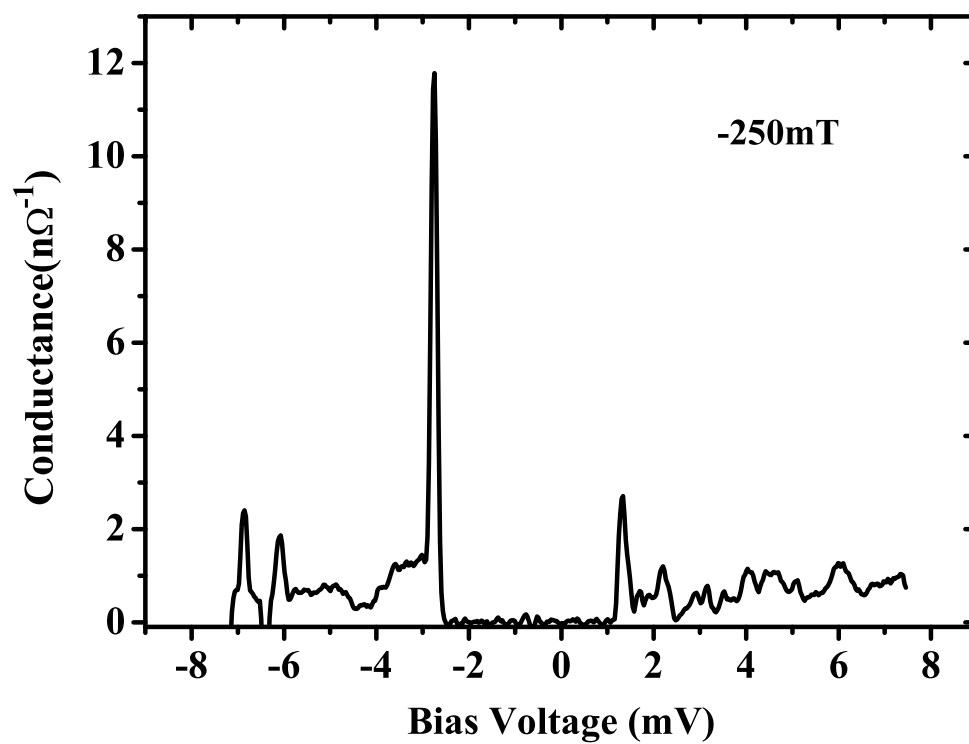


Figure 6.2: Differential conductance plot for a device with cobalt nanoparticle and non-magnetic leads.

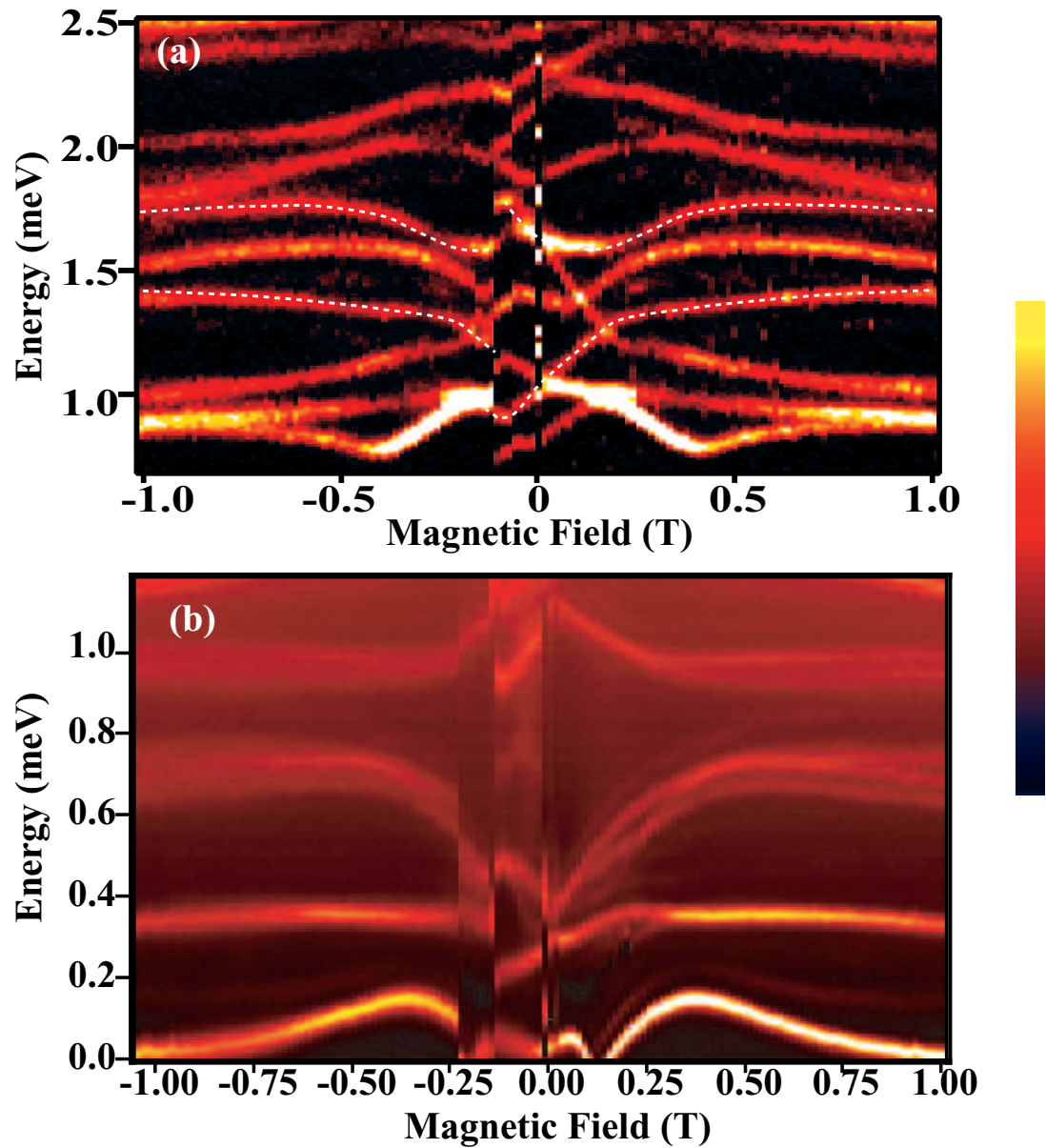


Figure 6.3: Colorscale differential conductance plot for two devices with a cobalt nanoparticle and aluminum electrodes. (a) The maximum conductance is $3 \times 10^{-9} \Omega^{-1}$. The field is being swept from positive to negative direction. (b) The maximum conductance is $1 \times 10^{-7} \Omega^{-1}$. The field is being swept from positive to negative direction.

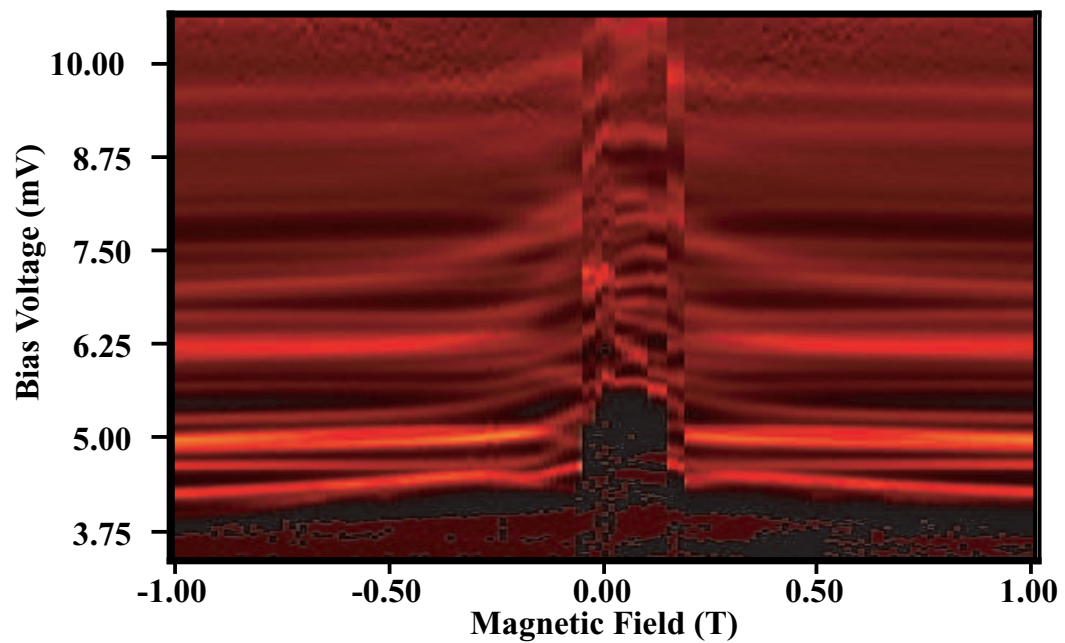


Figure 6.4: Colorscale differential conductance plot for a device – with a cobalt nanoparticle and aluminum electrodes – showing complex hysteric features, probably due to the dipolar field of neighboring nanoparticles. The maximum conductance is $8 \times 10^{-8} \Omega^{-1}$. The field is being swept from negative field direction to positive.

jumps in the energy levels at -0.14 T and -0.24 T – a behavior quite different from the data shown in Figure 6.3(a) – followed by continuous evolution of energy levels. We attribute one of the jumps to the magnetic switching of the nanoparticle via which the current flows. The second jump could be due to the magnetic switching of a neighboring nanoparticle which is coupled – via dipolar interactions – with the nanoparticle that participates in current transport. We have also observed complicated hysteretic features in other devices which suggest that the effect of neighboring particles is not negligible near the switching field. One example of the complex hysteretic features that we have measured is shown in Figure 6.4, which is likely to be due to dipolar coupling between neighboring nanoparticles.⁴ As a result, the jump seen in Figure 6.3(b) at -0.24 T could occur when the effective field felt by the nanoparticle being probed changes as a result of a magnetic switching event in a neighboring nanoparticle. Recently, there was a suggestion by Carlo Canali and Allan MacDonald that these multiple switching events may be characteristic features of switching in a *single* nanoparticle [18] subject to complex anisotropy forces. This is an issue that needs further investigation.

Two other features that I want to point out are, firstly, the non-monotonic evolution of energy levels as a function of magnetic field, and secondly, that all energy levels evolve quite differently from each other, at times crossing each other instead of exhibiting an avoided crossing. We will discuss these features again, once we have developed a framework for a semiclassical model to understand the experimental results.

At higher magnetic fields, the dominant contribution to the energy of the system

⁴The presence of neighboring nanoparticles is an undesirable feature of this technique. In our group Jason Petta has lead the efforts to fabricate devices so that only one nanoparticle could be attached to the leads using chemical means.

is from the Zeeman energy, and this can be seen easily at magnetic fields greater than ~ 1 T. Next we consider the data from the higher magnetic field range.

6.2.2 High-field magnetic field data

As the magnetic field is increased beyond ~ 1 T the energy levels eventually shift in a monotonic manner. The high magnetic field data in these samples differs significantly from the data for non-magnetic samples. Here we observe an absence of Zeeman splitting between the spin-up and spin-down electronic states, which was observed for non-magnetic samples, and we observe that all the energy levels have almost the same sign of slope. The absence of Zeeman splitting is something that is expected since there is no degeneracy between the spin-up and spin-down states for a ferromagnet. However, the similar sign of slopes for most of the energy levels,⁵ is difficult to reconcile with the simple picture of a ferromagnet which has both up and down spins near the Fermi level, albeit in different numbers. At larger values of $|H|$ (Figure 6.5(a) and (b)), all energy levels in a device move up (Figure 6.5(a)), or move down (Figure 6.5(b)) in energy, with slopes that correspond to effective g -factors ranging from 0.06 to 1.1. The fact that the g -factors are reduced below 2 indicates that the resonances are not purely spin-up or spin-down, but are mixed by spin-orbit scattering [19].

Another interesting aspect of the data is the observed density of states. We find the average level spacing to be about 0.2 meV in all of our samples.⁶ The range of particle sizes in a typical device can be estimated by imaging⁷ (using a scanning

⁵One energy level in each of the two samples for which we show data in Figure 6.5 seems to have almost zero slope.

⁶We measured 9 devices from which we could determine level spacing. This number includes measurements done by Sophie Guéron.

⁷Measuring the size of the nanoparticle in a particular device is impossible, at least for this technique. In the case of aluminum nanoparticles, it was possible to estimate the size of nanopar-

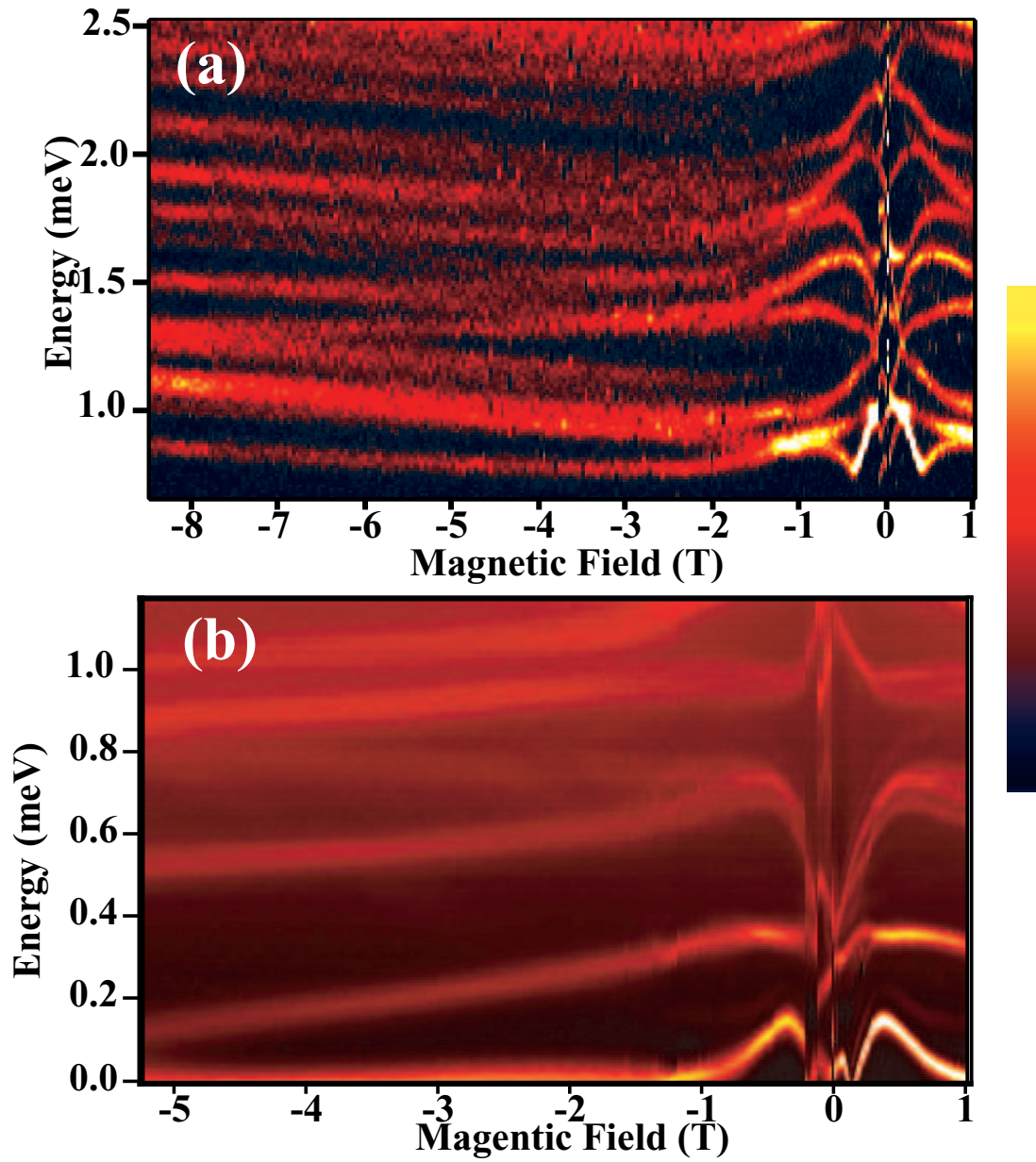


Figure 6.5: Colorscale differential conductance plot for two devices for higher field compared to the data shown in Figure 6.3(a) and (b). (a) The maximum conductance is $3 \times 10^{-9} \Omega^{-1}$. The data shown here is for the same device as the data shown in Figure 6.3(a). (b) The maximum conductance is $1 \times 10^{-7} \Omega^{-1}$. The data shown here is for the same device as the data shown in Figure 6.3(b).

transmission electron microscope (STEM)) particles formed by evaporating the same quantity of cobalt (5 Å) on a thin oxidized aluminum film [7]. The distribution of particle size is found to be 1-4 nm (diameter). The average level spacing predicted for simple noninteracting electrons should be between 0.75 and 40 meV, if one uses the calculated density of states in Co of $0.88 \text{ eV}^{-1} \text{ atom}^{-1}$ [12]. This estimate includes all the states with both *sp* and *d* bands.⁸ This discrepancy between the measured and expected level spacing is an important characteristic of this system, and we will see later in the chapter how this might be explained.

Having discussed the experimental data, we list the main observations, and then in the later sections we try to understand how each of the features can be explained.

Summary of the prominent features of our experimental data

1. In the small field range ($\mu_0 H < 0.25 \text{ T}$), discontinuous hysteretic switching in the energies of the discrete states occurs at a certain switching field $\mu_0 H_{sw}$ (typically 0.1-0.2 T), due to a sudden change in the direction of the magnetic moment. This indicates a strong coupling between the energy levels and the direction of magnetic moment. Resonances jump either up or down in energy at the switching fields, and both kinds of jumps can be seen in the same sample. At higher magnetic fields ($\mu_0 H < 1 \text{ T}$), we notice that there is pronounced non-monotonic behavior of the energy levels as a function of the magnetic field, with each energy level evolving quite differently from the others.

2. In the large-field regime ($|H| \gg |H_{sw}|$), the evolution of the energy levels is

ticle from the junction capacitance, by assuming a hemispherical geometry and a known dielectric constant (Chapter 4). However, for deposited aluminum oxide, as is the case here, it is difficult to estimate the size.

⁸One other possibility, although unlikely, is that somehow our fabrication process is selective, and automatically selects particles of larger size. There is no obvious reason for this selection to occur.

linear, with the sign of the slope being the same for almost all levels in a given sample. This is in marked contrast with the Zeeman-splitting of the spin-up and spin-down energy levels seen for non-magnetic nanoparticles.

3. We observe many more energy levels than expected. The expected density of states was based on the band-structure calculations that do not take into account the spin excitations [12].

Having listed the main features of our data, we next consider a semiclassical model to understand some of the experimental features.

6.3 Understanding the low-field data

The experimental data discussed in the previous section points to the richness of physics in this system. How does one begin to understand all the observed features? There are four minimal ingredients that one needs to model a magnetic system; they are orbital energy, exchange energy, Zeeman energy, and magnetic anisotropy energy (this is shown in a cartoon in Figure 6.6). Detailed theoretical descriptions using these four contributions to the energy are well described in the literature [8, 9, 11, 18]. Here, we will restrict the discussion to a simple semiclassical model to understand the behavior of the system at low magnetic fields. Of the four contributions to the energy of a magnetic system shown in Figure 6.6, the contributions that are relevant for modelling the response to a magnetic field are Zeeman energy and anisotropy energy. The inherent assumption in considering only anisotropy energy and the Zeeman energy is that they are sufficiently weak compared to the exchange energy splitting between different spin multiplets; this ensures that we can perform our

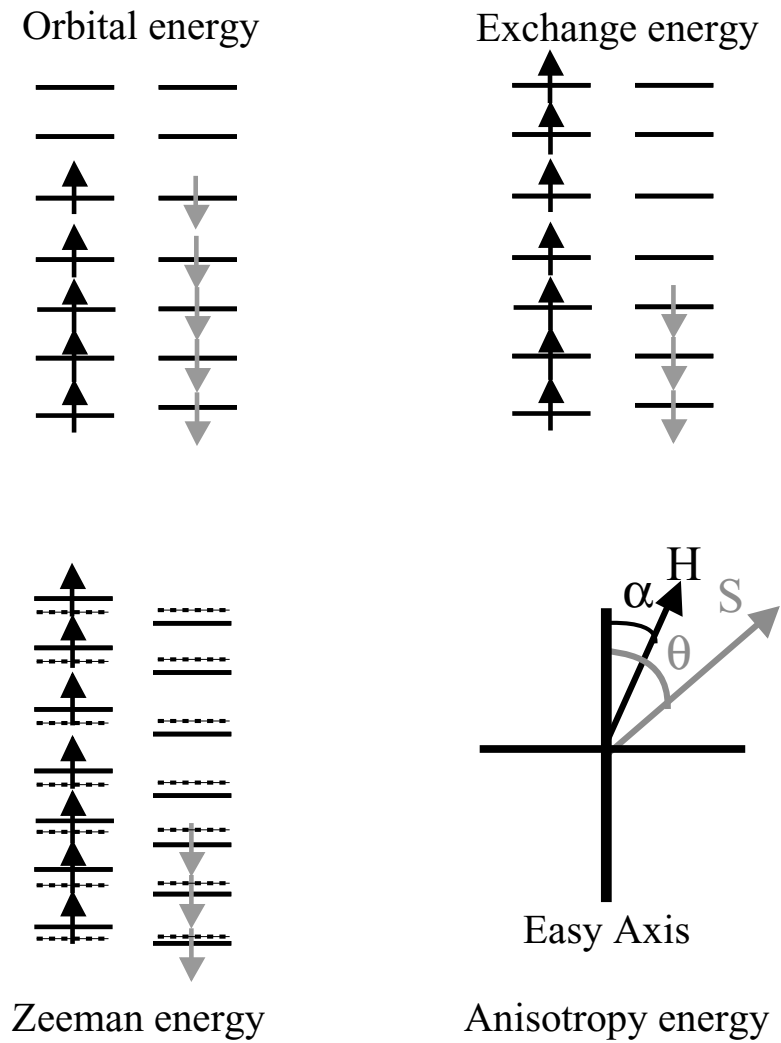


Figure 6.6: Minimal ingredients for describing a magnetic system. This is only a cartoon to pictorially depict different contributions to the energy of a magnetic system.

calculations in one spin multiplet.⁹ This allows us to assume that the exchange energy does not vary as a function of the magnetic field.

6.3.1 Phenomenological model to understand how magnetic switching affects the energy levels

Magnetic switching is due to the competition between the Zeeman energy, the tendency of the magnetic moment of the system to align along the direction of the magnetic field, and the anisotropy energy, which tends to align the moment along a direction preferred by the magnetic system. The magnetic moment occupies the local minima of the complex energy landscape described by the sum of Zeeman energy and anisotropy energy. As the magnetic field is swept past the switching field, one of the local minima in which the magnetic moment resides disappears, and the magnetic moment jumps to a new local minima. Among the two contributions – Zeeman energy and the anisotropy energy – the anisotropy energy is more complex in origin.

Anisotropy energy

Anisotropy energy, as the name suggests, varies over different spatial directions, and suggests a coupling between the spatial and spin degrees of freedom for a magnetic system. Prominent among the sources of anisotropy is magnetocrystalline anisotropy, which originates from spin-orbit interaction. The symmetry of the crystal lattice dictates the exact form of magnetocrystalline anisotropy. For instance, bulk cobalt has a hexagonal crystal structure, but in small clusters it is sometimes

⁹Simple toy-model calculations done by Canali *et al.* [8] and Kleff *et al.* [9] indicate that this is a valid assumption, and the energy separation between different spin-multiplets is much higher than the energy scales that we experimentally probe.

found to be in FCC orientation [13], consequently the form of the anisotropy is different. Shape anisotropy and surface anisotropy are two other contributions to the anisotropy energy. Shape anisotropy energy arises from magnetic dipole interactions, and depends on the particular shape of the ferromagnetic particle. In our experiments, the shape of nanoparticles is irregular [7], and estimates indicate that shape anisotropy's contribution is of the same order of magnitude as the magnetocrystalline anisotropy [14]. In their measurements, Jamet *et al.* [13] find that in cobalt clusters, ~ 3 nm diameter, the contribution of surface anisotropy is significant. Surface anisotropy arises due to the lack of spatial symmetry for the atoms at the surface. In our devices, a determination of the exact contributions of different sources of anisotropy is difficult. Extensive three dimensional switching measurements are needed to find out the contributions of various anisotropies [13]. Therefore, to begin, we will assume the simplest form of anisotropy – uniaxial anisotropy – to model our experiments. We have performed calculations using more complex forms of anisotropy, but we do not observe significant differences in the qualitative physics of the addition energy, the quantity we measure experimentally.

Calculating addition energy

Now, using a simple model consisting of the Zeeman and anisotropy energies allows us to calculate the quantities that we experimentally measure. The energy that we measure in our experiments is the addition energy (ΔE_{fi}) – the energy required to change the electron number on the nanoparticle by one. We begin by writing the Hamiltonian for a magnetic system as,

$$\mathcal{H} = -g_{\text{eff}}\mu_B\mu_0\vec{H} \cdot \vec{S} - k_N(\vec{S} \cdot \hat{n})^2/S_0. \quad (6.1)$$

Here $\hbar\vec{S}$ is the total spin with ground-state magnitude $\hbar S_0$ for N electrons, \hat{n} is a

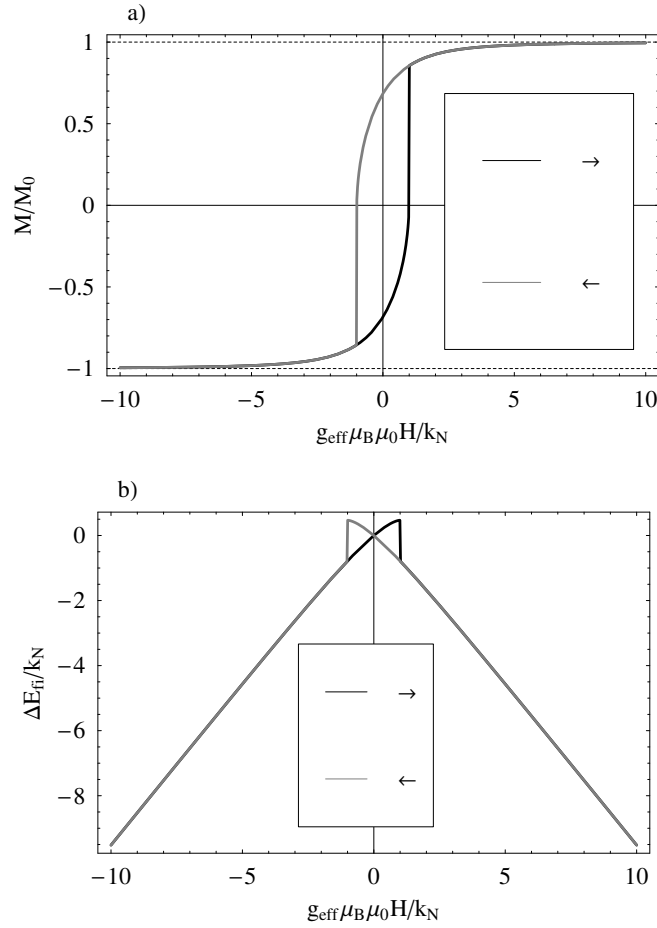


Figure 6.7: (a) Plot of magnetization projected along the direction of the magnetic field for the model with uniaxial anisotropy. (b) Plot of the addition energy as a function of the applied magnetic field for the case of spin-increasing transition due to the tunneling of an electron onto the nanoparticle. The relative angle between the easy axis and magnetic field is 45° . Here we assume that k_N and k_{N+1} are the same.

unit vector in an easy-axis direction, and the (uniaxial) anisotropy energy prefactor k_N is an intensive quantity and sets the energy scale in the system.¹⁰ Initially we will assume that k_N takes the same value for all electron numbers N . Later we will extend the model to the more general case. First, we solve for the ground state energy of the system for the case of N electrons and $N+1$ electrons semiclassically (corresponding to the situations before and after the tunneling of electron onto the nanoparticle).¹¹ Figure 6.7(a) shows that the model produces hysteretic switching in the magnitude of the moment projected along the direction of the magnetic field for two directions of the field sweep. Figure 6.7(b) shows the plot of addition energy as a function of the magnetic field for the case when the spin of the system increases. The jump in energy occurs at the value of magnetic field where the magnetic moment switches direction. A similar, but quantum-mechanical calculation – using exact diagonalization – was done by Sophie Guéron [7]. The semiclassical and quantum-mechanical calculations give similar results in the case of large spin, as expected.

There are a couple of aspects of this calculation that are noteworthy: 1) the addition energy does not depend on the total spin of the system, as one would expect, because the Hamiltonian scales with the total spin; consequently the addition energy just depends on the change in the spin of the system, 2) the exact magnitude of the switching field depends on the relative angle between the applied magnetic field and easy axis of the system [15], and 3) every transition should have identical addition energy, as a function of magnetic field, in a given nanoparticle. A similar calculation can be done for the case of spin-decreasing transition; in that case the addition energy is of a similar form. However, the energy scale is inverted. Now, we

¹⁰ k_N is the anisotropy energy per unit spin for the system, and sets the scale for the switching field.

¹¹ \vec{S} is treated as a classical number in our calculations.

compare the results of this simple model and the experimentally observed spectra shown in Figure 6.3. We notice that the main difference between the results of the model and the data is that the data exhibit non-monotonic evolution of energy levels after magnetic switching; this is absent in the results of our model. Another related feature is that in the experimental data, the energy levels jump up and down, but their eventual evolution at high fields is similar; this is not the case for the calculated addition energy, where the direction of the jump is the same as the evolution at higher fields (for *e.g.* in Figure 6.7(b) ΔE_{fi} undergoes a jump to lower energy (decreases) at the switching field, and at higher magnetic field ΔE_{fi} decreases). In many ways the qualitative features of our calculated data differ significantly from the experimental data. However, one feature that the model captures is the abrupt jump in addition energy at the switching field. This brings us to one more puzzling aspect of the data – the magnitude of the switching field. The switching field in our measurements is ~ 0.2 T, and this corresponds to $k_N \sim 0.01$ meV, whereas if one were to use values of bulk anisotropy energy density of 10^5 J/m³ [14] and the typical volume estimated for our particles, we would expect this energy scale ~ 0.1 meV. This discrepancy is still an open question, and has also been observed in experiments done by other techniques [13]. The possible answers lie in understanding the role of different sources of anisotropy.¹²

The model described above assumed a uniaxial anisotropy, but we have confirmed that the same behaviors hold for more complicated forms which include terms of 2nd and 4th-order in the spin-components [15], as long as one assumes that the same anisotropy function applies to all electronic states.

¹²At nanometer length-scale the number of atoms at the surface becomes increasingly comparable to the atoms in the bulk, and as a result extrapolating the energy-scale of magnetic switching from the bulk values may no longer be valid.

The difference between the data and results of our simple model, together with the fact that all the energy levels in one sample evolve differently as a function of magnetic field suggest that our initial assumption regarding the anisotropy energy might not be accurate: is it correct to assume that k_N is independent of N ?¹³ We now modify this simple model to include variations in the anisotropy due the change in the electron number.

Addition energy with variation of anisotropy

The fact that all the tunneling resonances undergo different energy variations, as a function of H , in the low- H range where the magnetic moment is being reoriented indicates directly that all the electronic states of the particle cannot be described by the same anisotropy-energy function. We have explored whether such variations in anisotropy energy may also affect the form for the H -dependence of the energies as described above, and we find that they provide a natural explanation for the complicated non-monotonic behavior as a function of H . We start by considering a single resonance associated with a transition between two states with N and $N+1$ electrons. We extend the N -electron Hamiltonian described in Equation 6.1 in the simplest way to incorporate variations in anisotropy energy. Now, the (uniaxial) anisotropy energy prefactor k_N is allowed to vary between the N - and $(N+1)$ -electron states. For simplicity, we assume that the easy axis is the same for all states. We have solved for the ground state energies for N and $N + 1$ electrons semiclassically as a function of H by finding the spin orientation that gives the local minimum in Equation 6.1, assuming that S_0 does not vary with H ,¹⁴ and then we calculate the

¹³An equivalent approach is to allow variation in the orientation of the easy axis. Here, we just model the variation in the magnitude.

¹⁴The analysis done by Carlo Canali and Allan MacDonald [8] indicates the energy scale for change in the ground state spin, S_0 , is very large compared to the energy range over which we perform our measurements.

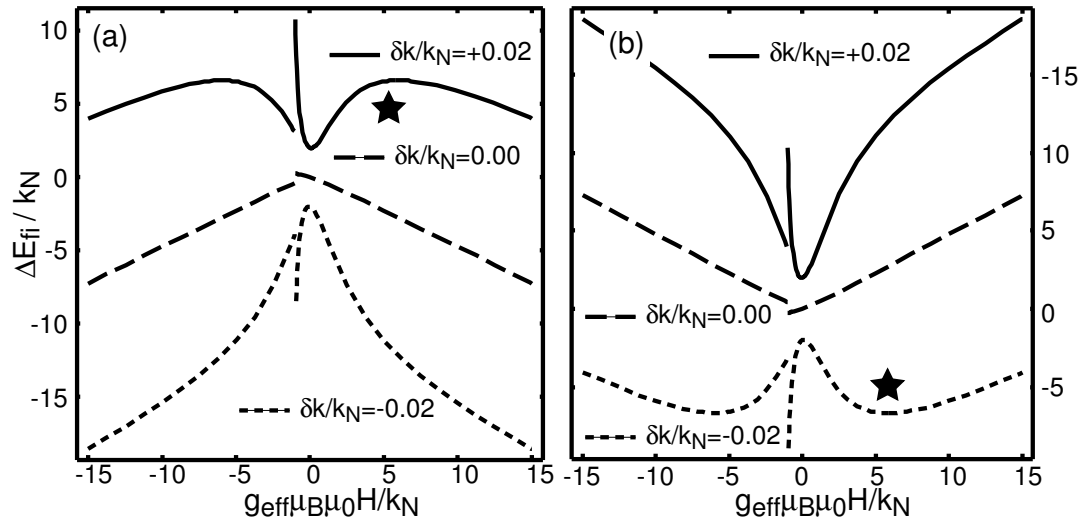


Figure 6.8: Tunneling energy ΔE_{fi} calculated using the semiclassical model discussed in the text, with H at 45° from the easy axis, for various values of the anisotropy-energy difference $\delta k = k_{N+1} - k_N$. In (a) the total spin is increasing; in (b) it is decreasing. The curves are offset for clarity. \star indicates the position of the extremum for the addition energy.

form of the tunneling transition energies as $E(N+1, H) - E(N, H)$. The results are shown in Figure 6.8. Assuming $S_0 \sim 1000$ (appropriate to a 4 nm Co particle), and an average value of $\langle k_N \rangle \approx 0.01$ meV in accord with the switching field [9], fluctuations in k_N , as a function of N , of order 1-3% (*i.e.* $\delta k/k_N = (k_{N+1} - k_N)/k_N = 0.03$) are sufficient to explain both the size and form of the non-monotonocities.¹⁵ Similar conclusions can also be reached in a more rigorous quantum-mechanical picture [9]. The results of the model show qualitative features that are similar to the experimental data.

By plotting the non-monotonic addition energy as a function of the spin S_0 and δk , we observe that when the addition energy exhibits an extremum (*e.g.* marked by \star in Figure 6.8), the value of the magnetic field at the extremum increases if either S_0 or δk is increased. Although this dependence is not linear, it is clear that the second energy scale in the system, other than k_N , is set by $\delta k S_0$.

Although fluctuations in the properties of eigenstates are not often considered in the context of ferromagnets, they are not surprising. In non-magnetic particles, the g -factors for Zeeman splitting fluctuate from energy level to energy level [19], and the statistics of these fluctuations have been investigated in random-matrix treatments of the spin-orbit interaction [20, 21]. Anisotropy in magnetic particles also arises from spin-orbit interactions. Therefore, it should not be surprising that different quantum states might have different anisotropy energy. An additional physical consequence of anisotropy-energy fluctuations should be that the value of H_{sw} will vary by 1-3%¹⁶ depending on the occupation of excited electronic states.

¹⁵The estimate $\langle k_N \rangle \sim 0.1$ meV in [7] based on the size of energy-level jumps at H_{sw} is inaccurate because it neglects effects of k_N -fluctuations [9].

¹⁶In the simple picture of magnetic switching $H_{\text{sw}} \propto k_N$ [15], and the proportionality constant depends on the relative orientation of the magnetic field and the easy axis. As a result, a variation of 1-3% in the magnitude of k_N translates to a proportional change in the magnitude of the switching field (H_{sw}).

This has yet to be investigated.

Our phenomenological model does not capture all the features of our experimental data. Some of the energy levels in Figure 6.3 show more than one region of non-monotonic behavior. This needs to be investigated further since our phenomenological model has no explanation for that.

Recent calculations done by Cehovin, Canali and MacDonald [18] suggest that the variation in anisotropy with electron number can be explained using a microscopic description of our system. Their finding supports our phenomenological picture.

Having discussed the low field magnetic behavior, and the possible origin of the magnetic field dependence of the tunneling energies, we next need to ask a very fundamental question – what are these resonances? A satisfactory explanation for the other experimental features cannot be provided without answering this very pertinent question.

6.4 What is the origin of the observed resonances?

In Chapters 3 and 4 we have seen how the resonances corresponded to transitions via electronic states in the metal nanoparticle. The question that arises is – should one expect similar electron-hole excitations to be the dominant contribution for resonances observed for ferromagnetic nanoparticles? Carlo Canali and Allan MacDonald [8], and Silvia Kleff and Jan von Delft [9] have proposed models of a nanometer-scale magnetic system which have similar predictions. Their model consists of two spin bands for the majority and minority spin together with the exchange interaction, Zeeman energy and anisotropy energy. They then consider the properties of the true many-body electronic states of the magnetic system, in contrast with

older models which attempted single-electron descriptions. A “cartoon” picture of their Hamiltonian can be seen in Figure 6.6. Their calculations indicate that the resonances we observe cannot be simple particle-hole excitations since the typical level-spacing for the majority (δ_{maj}) and minority (δ_{min}) electrons is much larger than what we experimentally measure. Within their model $\delta_{maj} = 5.55 \text{ eV}/N_A$ and $\delta_{min} = 1.43 \text{ eV}/N_A$, where N_A is the number of atoms in the magnetic nanoparticle. For our samples $N_A \sim 1000$, this implies that the level spacing we see is about two orders of magnitude smaller than the electron-hole excitations expected for this system. This suggests that the resonances have more to them than simple electron-hole excitations. Since our system is magnetic it is possible that the resonances that we observe are excitations involving the magnetic degree of freedom. The simplest kind of magnetic excitation is a spin-wave excitation. More complex excitations are possible when one begins to consider non-equilibrium processes. In each of these two scenarios we will check if other experimental features can be satisfactorily explained.¹⁷

6.4.1 Spin-wave excitations within the magnetic nanoparticle

It was suggested by Sophie Guéron [7] that the tunneling electrons could excite a spin-wave mode of the lowest order (uniform rotation) within the magnetic nanoparticle. Inelastic tunneling with emission of spin-wave excitations could then generate the extra density of states that we observe. Detailed analysis done by Silvia Kleff and Jan von Delft [9, 11] suggests that the observed resonances cannot be due only

¹⁷The main features that cannot be explained on the basis of the semiclassical model discussed in the previous section are: 1) the sign of slope for the high energy levels is the same for most energy levels, and 2) the average level spacing of $\sim 0.2 \text{ meV}$ or less in different samples.

to inelastic emission of spin waves. The typical energy of uniform-rotation spin-waves is $k_N \sim 0.01$ meV. This is much smaller than the spacing between the states that we experimentally observe. As a result, a simple emission of spin waves during inelastic tunneling cannot explain our experimental observations. Next we consider the possible role of non-equilibrium processes.

6.4.2 Non-equilibrium transport via a magnetic nanoparticle

Since neither the electron-hole excitations nor the simple inelastic tunneling with spin-wave emission explain the observed experimental features, it was proposed [7, 9, 11] that non-equilibrium excitations involving the spin could play an important role. In Chapters 3 and 4, we explained that non-equilibrium electron-hole excitations in Al nanoparticle can lead to broadening of tunneling resonances or (in very small particles) to the appearance of new resonances with energies different from the ground-state tunneling transitions [23]. This work motivated the idea that similar non-equilibrium excitations involving the spin of the nanoparticle may produce additional tunneling features for the case of ferromagnetic nanoparticles.

The basic idea of electron-hole non-equilibrium is shown in a cartoon in Figure 6.9.¹⁸ At bias voltages much larger than the typical level spacing a number of energy levels are involved in the current transport through the nanoparticle (as discussed in Chapter 3). As a result the tunneling events can lead the system to an excited state, and this can affect the tunneling energy of the next electron if it does not relax before the next electron tunnels in. Under such circumstances an ensemble of non-equilibrium states can be realized by the system.

¹⁸This figure here is shown for the case of particle-hole excitations, however, similar processes

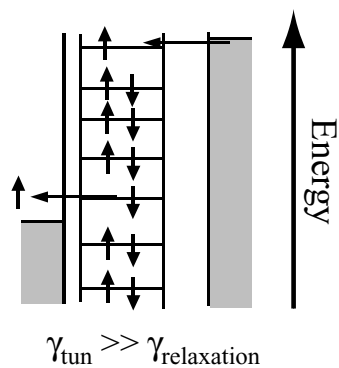


Figure 6.9: A cartoon diagram depicting tunneling events which can cause the system to be in an ensemble of non-equilibrium states when the rate of relaxation is much smaller than the rate of tunneling ($\gamma_{\text{relaxation}} \ll \gamma_{\text{tun}}$).

The consequences of spin non-equilibrium have been extensively investigated by Kleff *et al.* [9, 11], and we will briefly summarize the qualitative results of their study. They find that in a ferromagnetic nanoparticle, non-equilibrium spin excitations are also possible in addition to the non-equilibrium single-electron states. This can happen when the spin-flip rate Γ_{sf} is smaller than the tunneling rate Γ_{tun} . Under such circumstances a ladder of transitions will occur between states of different total spin, so that there is finite occupation probability of having states with spin other than the ground state spin. A rate equation calculation under such conditions predicts that the resonance spacing is determined primarily by the transitions involving the minority electrons and the model can predict the resonance spacings that we observe. Inclusion of spin-wave excitations within this non-equilibrium picture also explains the same sign of slope that we observe in our experiments, *i.e.* that all the transitions correspond to the same change in S_z . The absence of Zeeman-splitting of resonances is due to the fact that the tunneling weight corresponding to one transition in the Zeeman-split pair is smaller than the other by a factor of $1/s_0$ (the Clebsch-Gordan coefficient connecting the initial and the final states is $\propto 1/\sqrt{s_0}$), where s_0 is the ground state spin. This makes one of the resonances immeasurably small.¹⁹ As a result one observes the same sign of slope.

One of the ways of putting the non-equilibrium picture for the tunneling resonances to a test is to carry out tunneling spectroscopy with a device having a gate electrode. As seen in Chapters 2 and 4, the gate electrode changes the threshold voltage needed for the single electron tunneling to begin, consequently changing the extent of non-equilibrium.

can take place with the spin degree of freedom.

¹⁹Similar qualitative arguments were made by Sophie Guéron [7] to explain the absence of Zeeman-splitting.

6.5 Experimental results using the gate electrode

6.5.1 Testing the non-equilibrium picture

We now turn to data from a gated tunneling device, with the primary motivation being to test whether the larger-than-anticipated density of tunneling resonances observed at low energy is due to non-equilibrium effects [9, 5]. As explained earlier in Section 6.4.2,²⁰ the idea of the non-equilibrium mechanism is that the energy of tunneling transitions can be described as the energy differences of states in the nanoparticle with N and $N \pm 1$ electrons: $\Delta E_{fi}^{\pm} \equiv E_f^{N \pm 1} - E_i^N$. If under conditions of current flow, E_i^N can assume an ensemble of different values, for instance due to low-energy spin excitations or electron-hole excitations within the particle, then the number of observed tunneling resonances can increase above the number that originate only from a single equilibrium ground state. We can test this with a gate voltage because the energy of a tunneling transition can be tuned from high values down close to zero where tunneling can be initiated by small V . For sufficiently small V , the tunneling electrons may have insufficient energy to excite non-equilibrium states. Therefore, a test of whether tunneling resonances are associated with non-equilibrium initial states is whether some transitions disappear when they are tuned to small V . This disappearance is exactly what is observed for the lowest-energy transitions at $H=0$ (Figure 6.10(a)), when the electrodes are superconducting. We have not observed well-resolved transitions in non-magnetic particles to disappear completely as V_g is varied, whereas at least the first 5 lowest-energy states in the Co particle lose conductance. Non-equilibrium effects, therefore, appear to be much stronger in Co, perhaps due to larger fluctuations in electron-electron interactions for

²⁰We have discussed non-equilibrium in the context of electron-hole excitation in Sections 3.4 and 4.7. Here we consider the non-equilibrium involving the spin.

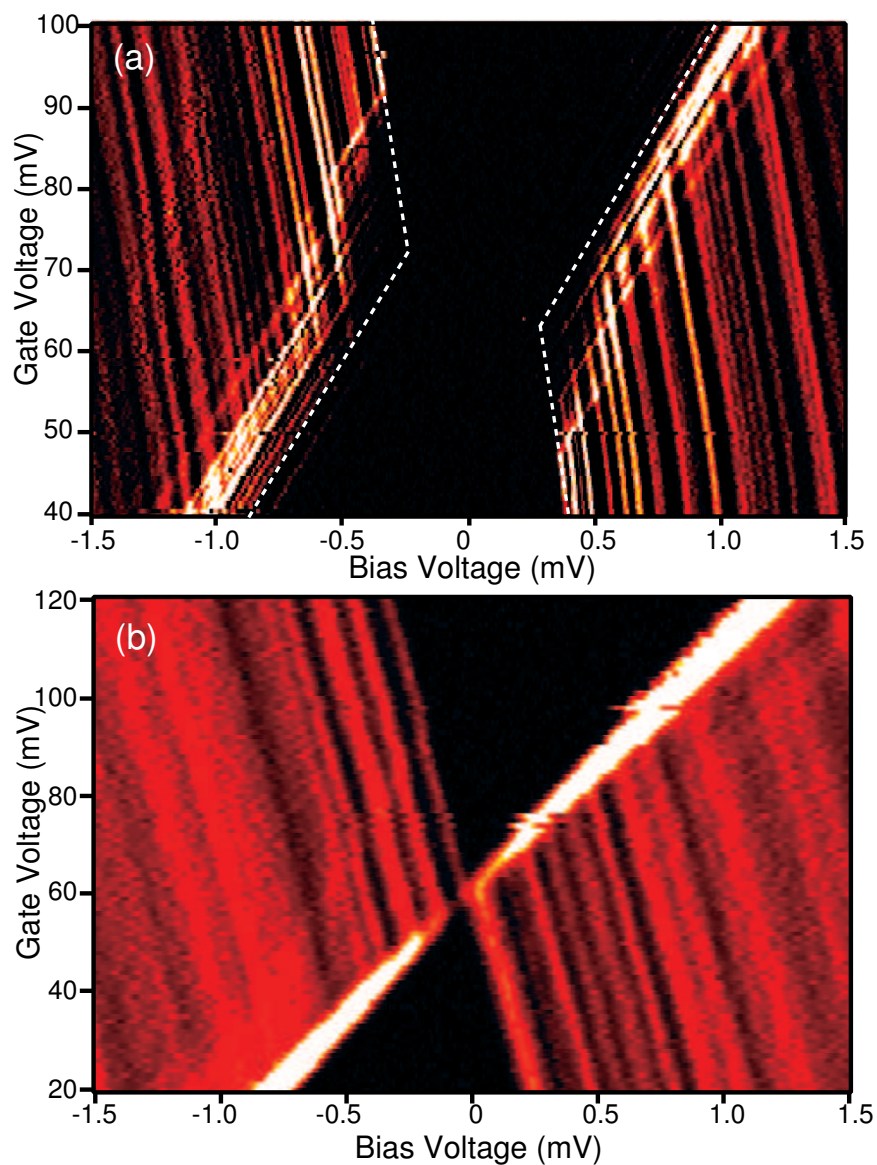


Figure 6.10: Colorscale conductance plot of a gated Co nanoparticle as a function of V_g and V . (a) Superconducting leads ($H=0$). (b) Normal-state leads (0.07 Tesla). The dashed lines in (a) indicate the expected evolution of the threshold peaks if the resonances did not involve non-equilibrium processes. The voltage resolution is better at $H=0$ because of the superconducting singularity in the electrode density of states. The electron $T \approx 90$ mK.

an ensemble of many-body states realized during non-equilibrium tunneling and/or a large multiplicity of low-energy collective spin excitations (in addition to the particle-hole excitations that were considered previously [5]). Since the relaxation rate of non-equilibrium excitations must be slower than the tunneling rate for the spectrum to be affected, the relaxation rate is of the order of or slower than ~ 1 MHz.

The presence of level crossings (instead of avoided crossings), noted in Figure 6.3 provides independent new evidence supporting the non-equilibrium scenario. In non-magnetic particles, when spin-orbit scattering reduces the large- H g-factors to less than 1.7, tunneling transitions originating from the same initial state exhibit clear level repulsion [19]. In contrast, under non-equilibrium conditions, tunneling resonances occurring at similar values of V can result from different pairs of eigenstates $(E_i^N, E_f^{N\pm 1})$, none of which are nearly degenerate, so an avoided crossing would not be expected.

Despite these two lines of evidence for the importance of non-equilibrium transitions, our observations are not in full agreement with the simplest phenomenological scenario that includes non-equilibrium effects [9]. Ref.[9] proposes that non-equilibrium spin-accumulation may occur by a sequence of transitions up a ladder of energy states having different total spin S , with the sequence terminating when the next step up the ladder requires more energy than that provided by the source-drain bias, eV . Within this scenario, a fraction of both the low-energy and high-energy tunneling resonances should disappear as V_g tunes the transitions to lower voltages. In Figure 6.10(a), only the lowest-energy transitions experience a loss of tunneling amplitude.

Another unanticipated observation is that the disappearance of tunneling resonances as a function of V_g occurs only when the electrodes are superconducting,

and not when they are normal (Figure 6.10(b)). Scans for normal-state electrode at 0.07, 1, 3, 5, and 8.5 T are all qualitatively similar. Perhaps, because of the singularity in the density of states for superconducting electrodes, the ensemble of non-equilibrium states may be populated differently by tunneling from normal and superconducting electrodes, with less non-equilibrium at low V in the superconducting case. One important difference between the cases for superconducting and normal electrodes is the existence of thermally-excited electrons in the normal case, which might play an important role in initiating non-equilibrium excitations in the nanoparticle. However, I think that there is at least one more piece of the puzzle missing before we can have complete understanding of the system.

A gated device can also be used to change the number of electrons in the magnetic nanoparticle, allowing us to answer the question – how does the magnetic moment change if the number of electrons on a nanomagnet is changed? We try to answer this question next.

6.5.2 Determining the spin type of resonances

An additional simple benefit of having a gate electrode is that it allows a determination of whether the tunneling resonances correspond predominantly to the motion of majority or minority electrons. Consider the data shown in Figures 6.10 and 6.11. At $V_g = 20$ mV the low-energy tunneling thresholds correspond to the addition of an electron to the nanoparticle ($N \rightarrow N+1$), and at large magnetic fields (Figure 6.11(a)) the tunneling energies increase, meaning that the tunneling states have lower $\langle S_z \rangle$. It follows that the transitions correspond predominantly to minority-electron tunneling. Similarly, at $V_g = 125$ mV (Figure 6.11(b)), the tunneling thresholds are $N+1 \rightarrow N$ processes in which the spin increases, so a minority electron is tunneling

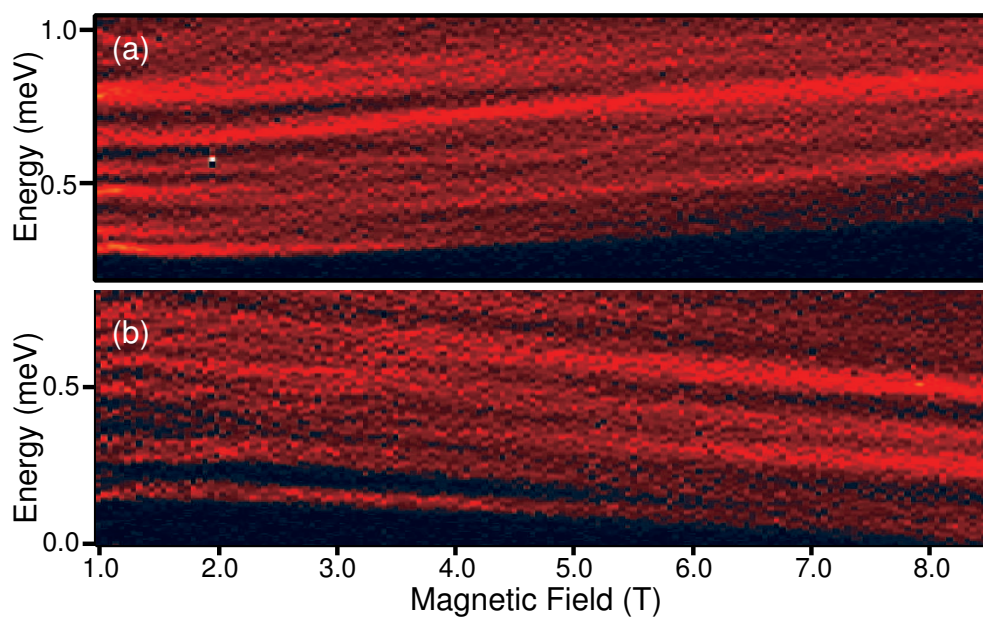


Figure 6.11: The data shown here is for the same sample as the one shown in Figure 6.10. High-field conductance spectra for the sample at (a) $V_g = 20$ mV and (b) $V_g = 125$ mV. The maximum conductance is $3.5 \times 10^{-9} \Omega^{-1}$.

off the nanoparticle. These results from one sample are in agreement with predictions [8, 9] that the total spin should almost always decrease when electrons are added, due to both a large minority density of states and strong exchange interactions. Of course, because of spin-orbit coupling, the transitions are not purely of minority-electron character.

6.5.3 Evolution of the degeneracy point as a function of the magnetic field

Figure 6.12 shows data from a gated cobalt nanoparticle for a sequence of magnetic fields.²¹ First we look at the qualitative features of the data, before diving into more quantitative information. The upper half in each of the gate scans, corresponds to a region where the transition is of the type $N + 1 \rightarrow N$, and the lower half corresponds to a region where the transitions are of the $N \rightarrow N + 1$. The degeneracy point corresponds to the gate voltage, V_{deg} , where the two charge states are degenerate. Note that as the magnetic field is increased the gate voltage at which the degeneracy point occurs increases. Using the idea that V_{deg} defines a point with a fixed number of electrons even as magnetic field is varied we can write an implicit relation between magnetic field B and V_{deg} ; this relationship can be used to compare the experimental results and the predictions of a model used to describe our system.

Canali and MacDonald predict [8], if the electron number is fixed, that

$$\frac{\Delta\mu_{gate}}{\Delta(\mu_B B)} = g \ 0.46, \quad (6.2)$$

where $\Delta\mu_{gate} = eC_g V_g / C_\Sigma$ is the change in chemical potential of the nanoparticle due to the gate voltage at a fixed magnetic field, and g is the g-factor.²² Figure 6.13

²¹This data is from the same device as the data shown in Figures 6.10(a) and (b).

²² $\frac{\Delta\mu_{gate}}{\Delta(\mu_B B)}$ depends on the charging energy of the device and in their calculation Canali *et al.*

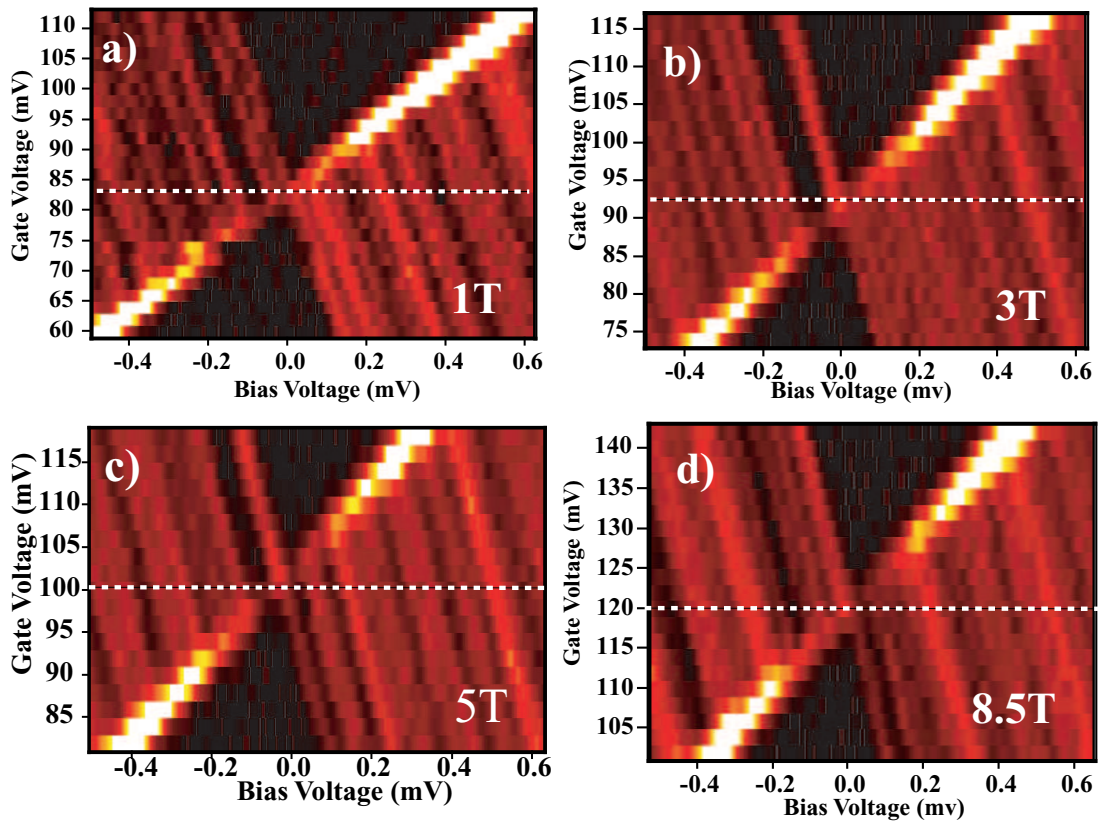


Figure 6.12: Conductance for a device with cobalt nanoparticle as a function of gate voltage and source-drain voltages for a sequence of magnetic fields. The dashed lines indicate the gate voltage corresponding to the charge degeneracy point (V_{deg}).

shows the plot of degeneracy voltage (V_{deg}) as a function of the magnetic field. Correcting for the capacitance division at the gate electrode we find

$$\frac{\Delta\mu_{gate}}{\Delta(\mu_B B)} = 0.38 \pm 0.04. \quad (6.3)$$

The g-factor corresponding to the first state that initiates the current flow in the lower half of Figure 6.12(a-d) is 0.77 ± 0.08 . As a result the calculation of Canali and MacDonald [8] predicts $\frac{\Delta\mu_{gate}}{\Delta\mu_B B} = 0.35 \pm 0.04$ (using Equation 6.2). This indicates a good agreement between the measured and predicted values (Equation 6.2 and 6.3).

Although there is good agreement between the results of the simple model developed by Canali *et al.* [8] and our experiments, this agreement should be examined carefully since the prediction of the model assumes a specific number of atoms (N_A). Nevertheless, this provides an interesting way to analyze data from the experiments and compare with the predictions of the model.

Until now we have discussed data in this chapter that involves analyzing the energy of the spectrum. We have not considered the amplitude of the resonances. The current amplitude provides interesting information about the system that is complementary to the data we get from measuring the energies of the resonances. We have previously used information from the amplitude of the current in non-magnetic particles to calculate the tunneling rates in Chapter 4, and in Chapter 5 we used that information to calculate tunneling polarization. In the next section we revisit some of the data discussed earlier in this chapter, but now the emphasis will be to measure the strength of resonances.

assume $E_C = 30$ meV and that the number of atoms in the nanoparticle (N_A) is 1500. For the device whose data is shown in Figure 6.12 we find $E_C = 26 \pm 3$ meV and $C_g/C_\Sigma = 0.0043$.

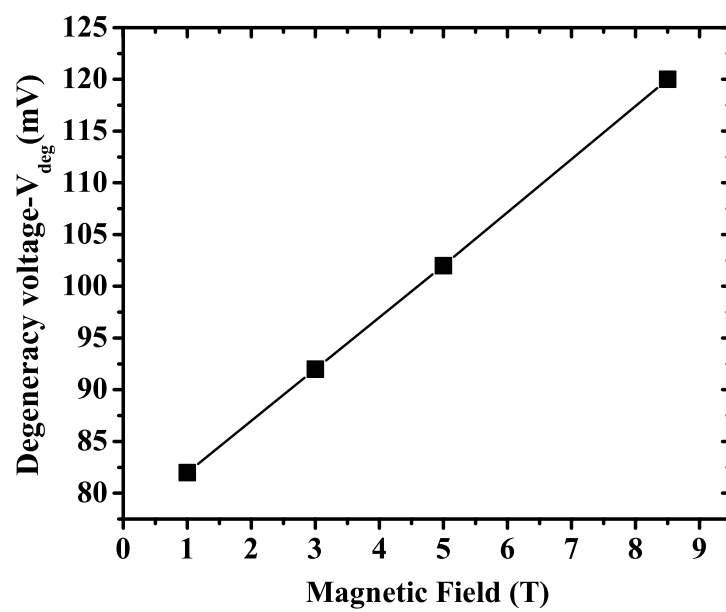


Figure 6.13: Plot of the degeneracy point (V_{deg}) as a function of the magnetic field.

6.6 Amplitude of the resonances

In this section we will look at the variation in the current amplitude as a function of magnetic field and gate voltage. In the last part we will briefly consider data where we see some structure in the Coulomb blockade regime, which may suggest the role of cotunneling. But first, we turn to the amplitude of the resonances as a function of magnetic field.

6.6.1 Low magnetic field data

We saw in Section 6.2.1 how the quantum levels exhibit an abrupt jump in their energies as one sweeps through the switching field (H_{sw}). In this section we will try to examine if the amplitude of the current carried by a resonance changes as a function of the magnetic field. Before we look at the current carried by resonances as a function of magnetic field I want to point out that the models that have been discussed until now do not provide any information about current – they are geared towards understanding the energies of resonances.

In Figure 6.14(a) we show the colorscale conductance plot for the data shown in Figure 6.3(b), except that we now plot the conductance for both signs of the bias voltage. The data shown in Figure 6.14(a) is used to extract information about the current carried by peaks 1 and 2. In Figure 6.14(b) we plot the current carried by peaks 1 and 2 as a function of magnetic field. This was obtained by fitting the conductance peak with the derivative of the Fermi function to extract the amplitude of the current. The reason we choose the peaks on the negative side of the bias is that they do not intersect each other and are well separated in energy to allow fitting.

We observe that the currents carried by peaks 1 and 2 change as a function of the

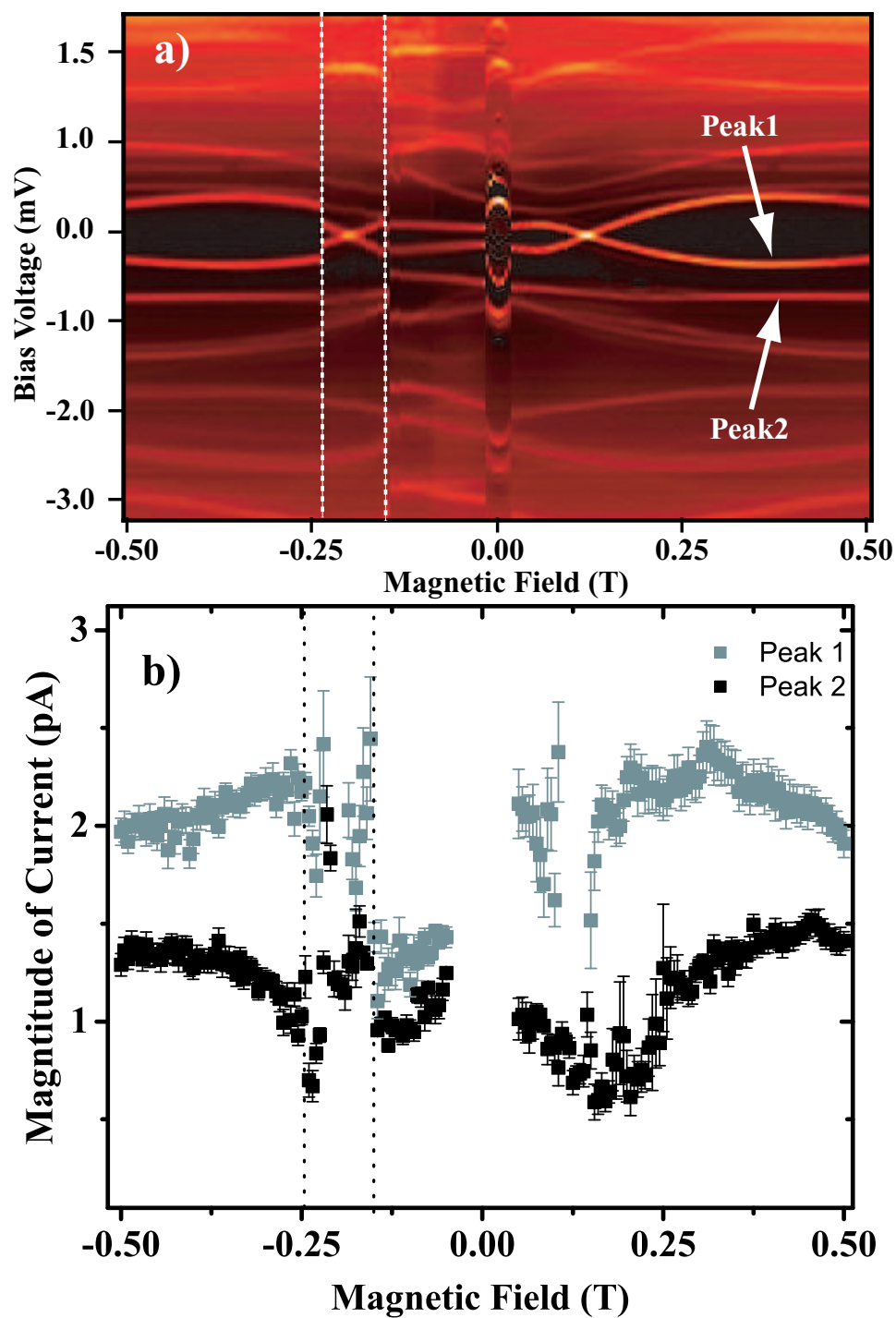


Figure 6.14: a) Color scale conductance plot for a device with cobalt nanoparticle and aluminum leads. b) Plot of current carried by for peak 1 and 2 as a function of the magnetic field. The direction of sweep is from positive magnetic field to negative. Two abrupt jumps of the energy levels are marked by two dashed lines. The data shown here is from the same device as in Figure 6.3(b).

magnetic field, and the variation is different for each of the two peaks. Data around 0 T is not shown since the aluminum leads turn superconducting and the resonances reflect the BCS density of states. Around the switching field (~ -0.15 T) we see abrupt jumps in the amplitude of the current. One other noticeable feature is the non-monotonic variation in the strength of the current.²³

As of now I do not have a model with which to compare this variation. However, there are two contributions that need to be taken into account when interpreting the variation in the amplitude of current as a function of the magnetic field; this effect could either be due to the presence of a magnetic oxide near the nanoparticle, or it may be an effect of the variation in the wavefunction of the state being probed. Strong variations in the addition energy as a function of magnetic field suggests that variation in the wavefunction of a state is possible resulting in the change of tunneling rates, and this could lead to the observed variation in the amplitude of the current. This is an aspect that needs further thought.

Next we consider the amplitude of the resonances as a function of gate voltage, V_g .

6.6.2 Data from gated devices at high magnetic fields

As seen in Chapter 4, the gate electrode allows us to change the threshold voltage required for tunneling. Using this feature we can access a regime where only one energy level is involved in the current transport. In this section we will examine data from a gated device at high magnetic fields with particular attention to the amplitude of the resonances.

²³It is difficult to fit in the region where peak 1 crosses the first peak for positive bias. This gives rise to some scatter in our data for peak 1 around the magnetic field ($\sim +0.12$ T and ~ -0.20 T) where the two peaks cross. This effect is not related to the magnetic switching of the nanoparticle.

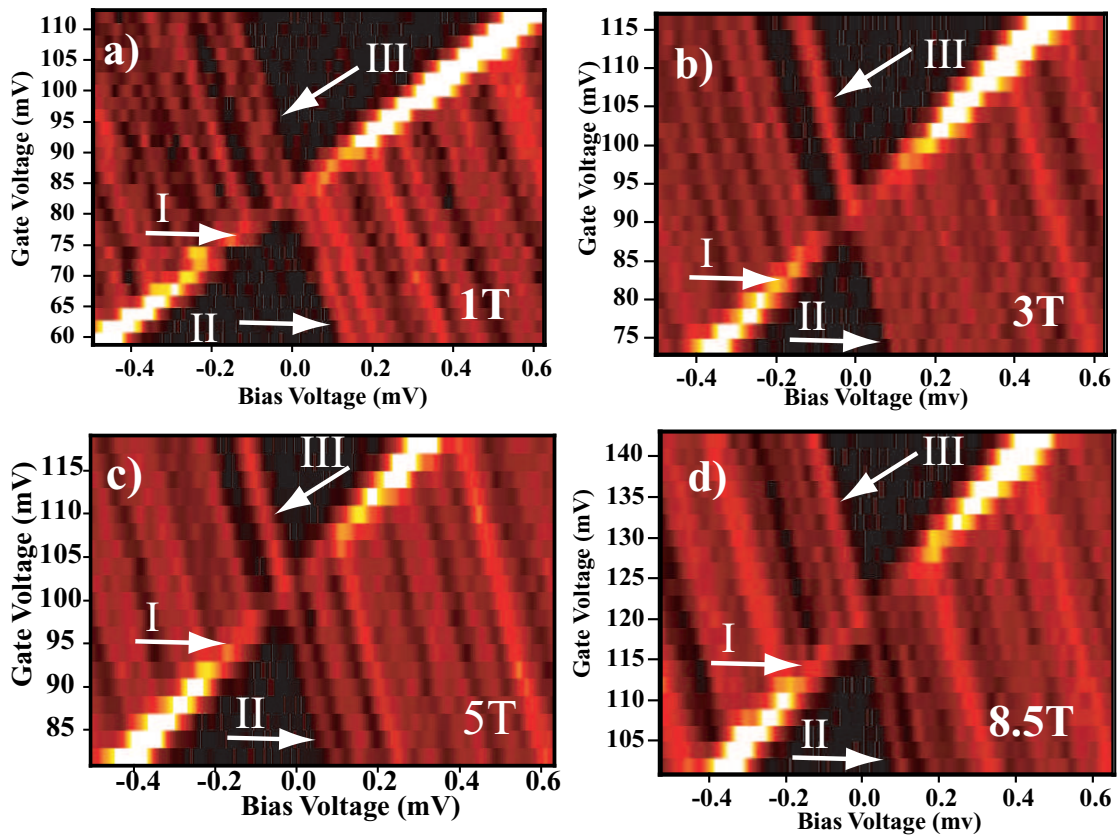


Figure 6.15: Conductance for a device with cobalt nanoparticle as a function of the gate voltage and bias voltage for a sequence of magnetic fields.

Figure 6.15 shows data from a gated device for different gate voltages.²⁴ As mentioned earlier, the threshold event for the upper half of the plot, in each of the gate scans, corresponds to a region where the transition is of the type $N+1 \rightarrow N$, and the threshold event for the lower half corresponds to a region where the transitions are of the $N \rightarrow N+1$ type. All the levels seen in Figure 6.15 with negative slope as a function V_g correspond to threshold transition across the high resistance barrier L. Only line I corresponds to transition across the low resistance barrier R. Since we observe no other levels corresponding to transitions across the low resistance barrier (R), we can conclude that the tunneling rates associated with the two barriers are very asymmetric $\gamma_R \gg \gamma_L$.

Before we look at the data shown in Figure 6.15 in greater detail, consider the cartoon – shown in Figure 6.16 – of the one of the panels in Figure 6.15. The dotted area corresponds to the region with Coulomb blockade. The black lines correspond to thresholds across the thick barrier and the grey lines are due to thresholds across the thin barrier. The black arrows “ \longleftrightarrow ” mark paths along which one can measure a current step for which only one energy level is involved in the transport. For any nanoparticle we expect the current steps across line I,II, and III (marked by \longleftrightarrow) to have the same magnitudes when all degeneracies are lifted (*i.e.* at high fields).²⁵ In this situation, the current steps across I and II should be the same due to time reversal symmetry. The currents via I and III along the sections marked with \longleftrightarrow are the same because they correspond to the same final current. The current step along I and III therefore should be the same in any system, whenever electrons are tunneling via only a non-degenerate ground state.²⁶ Now, we look at the data to

²⁴This data is from the same device as the data shown in Figures 6.10(a) and (b).

²⁵All the current steps considered in this discussion are measured before the first excited states are involved in the current transport.

²⁶The current step along I and III should be the same in all systems when the energy levels are

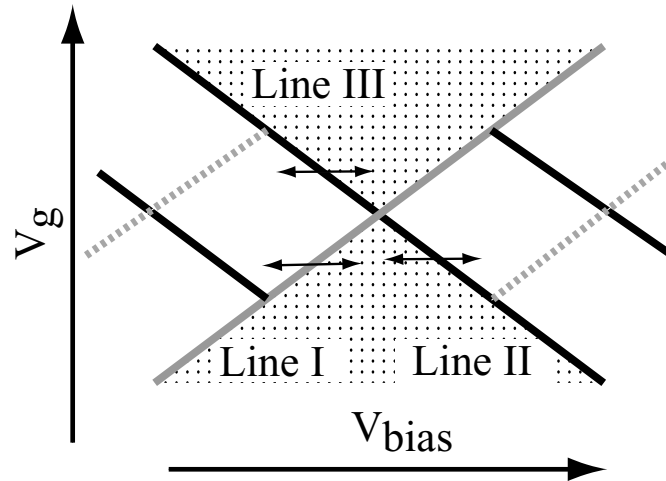


Figure 6.16: Cartoon showing the region near the charge degeneracy point. The dotted area corresponds to the region with zero conductance due to Coulomb blockade. The black lines correspond to the transition across the thick barrier L , and the grey lines correspond to transition across the thin barrier R ($\gamma_R \gg \gamma_L$). The grey dotted lines correspond to transitions across the thin barrier R , and have almost zero weight since $\gamma_R \gg \gamma_L$; these threshold do not result in an increment in the magnitude of the current. The \longleftrightarrow indicates the current steps along lines I,II and III.

see if the magnitudes of the current steps across the lines II and III are indeed the same for the magnetic system.

For the case of the magnetic nanoparticle, whose data we show in Figure 6.15, we observe that the ratio of the amplitude of currents for the two signs of bias (I_+ is current step across line II, and I_- is current step across line III) $I_+/I_- = 0.53 \pm 0.10$ at 5 T, and $I_+/I_- = 0.58 \pm 0.20$ at 8.5 T.²⁷

As mentioned earlier the current step for line I and II has to be the same when simple ground state tunneling occurs via a non-degenerate energy level. In our system the degeneracies are lifted due to the magnetic field, so the asymmetry in the measured current for the two signs of the bias requires an explanation. It may be due to the presence of non-equilibrium excitations in the magnetic particle even at very small bias voltages, when the electrodes are in the normal state (not superconducting). The non-equilibrium occupation of states might take place due to thermal excitations in the electrodes even at dilution fridge temperatures. This means that the single electron tunneling via magnetic nanoparticles would always be a non-equilibrium process as long as the electrodes are normal. Recall that in Section 6.5.1 we saw that non-equilibrium tunneling could be tuned off by tuning the gate voltage when the source and drain are superconducting. In a superconductor, thermal excitations are exponentially suppressed.

Next we discuss the possible origin of structure in the Coulomb blockade region that is seen in the case of devices fabricated using cobalt nanoparticles.

non-degenerate and the transition is due to equilibrium tunneling.

²⁷At other magnetic fields it is difficult to extract the ratio of currents since it is difficult to resolve the first resonance from the other higher energy resonances. In calculating these ratios we have used the fact that current across lines I and III are the same since it is difficult to measure the current along I in a very small range of V_g .

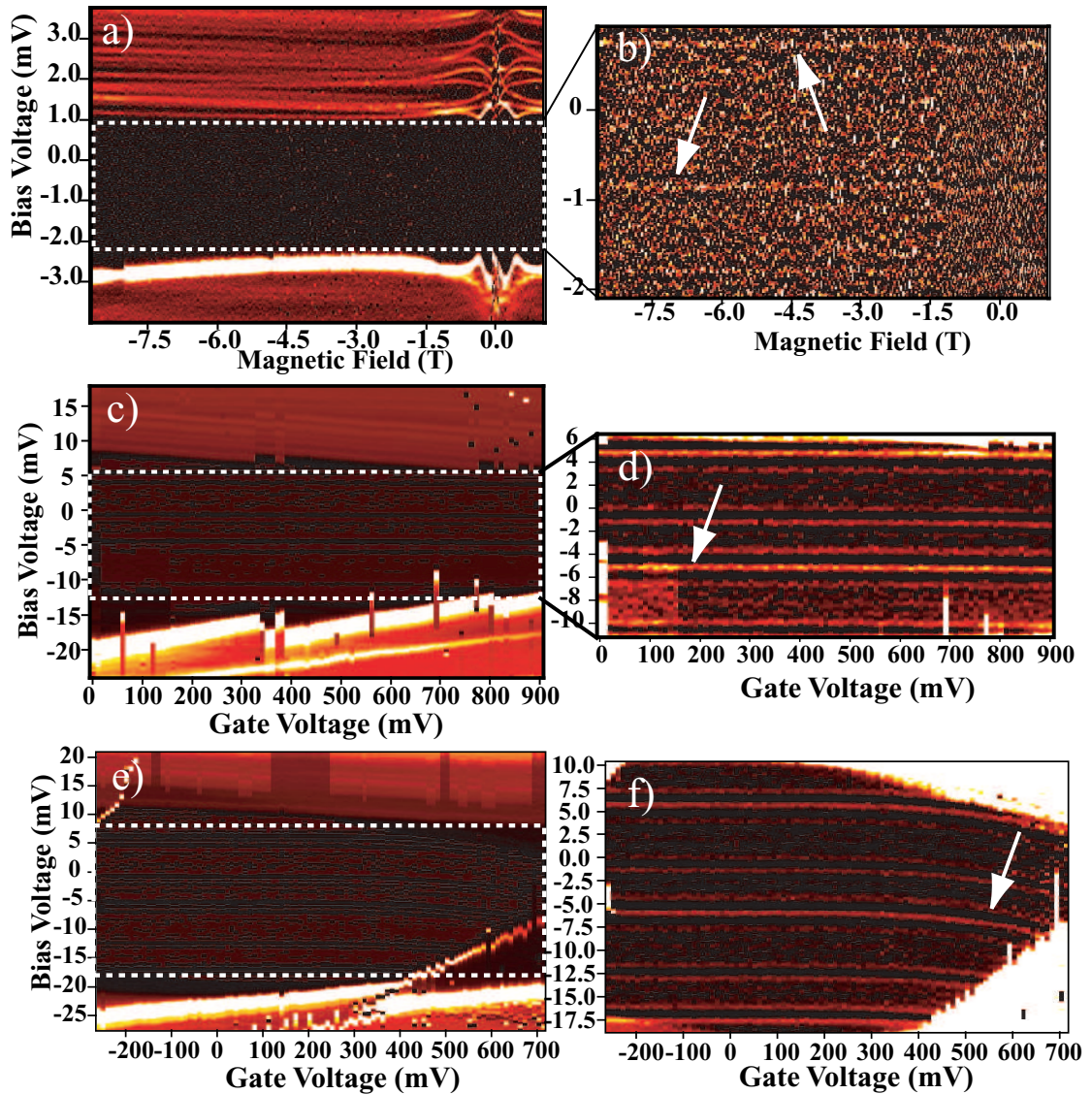


Figure 6.17: Colorscale conductance plot for three different devices with a cobalt nanoparticle and aluminum leads, with the plots on right showing the structure in the Coulomb blockade regime. Structures within the blockade are marked by arrows. a) & b) Conductance plot as a function of magnetic field (same sample as the one shown in Figure 6.5(a)). The maximum of the conductance-scale is 2×10^{-9} S for a) and 2×10^{-10} S for b). c) & d) Conductance plot as a function of the gate voltage. The maximum of the conductance-scale is 2×10^{-8} S for c) and 2×10^{-10} S for d). e) & f) Conductance plot as a function of the gate voltage. The maximum of the conductance-scale is 1×10^{-8} S for e) and 4×10^{-10} S for f).

6.6.3 Cotunneling ?

After discussing the amplitude of resonances due to single electron tunneling we next turn to features that we observe in the Coulomb blockade region, where one does not expect resonances because of the cost of charging energy. However, higher order tunneling events are energetically allowed in this region. These are commonly known as cotunneling events since they involve the simultaneous tunneling of two or more electrons [25]. Signatures of cotunneling events have been observed in a variety of experiments using quantum dots [26] and nanotubes [27]. Figure 6.17 shows colorscale conductance plots of devices with a cobalt nanoparticle. We observe that there is a regular structure in the Coulomb blockade regime which shows no dependence on the gate voltage (Figure 6.17 (d) & (f)), and magnetic field (Figure 6.17 (b)). The average spacing between the structure in the Coulomb blockade regime is ~ 0.5 meV which is much larger than the energy of spin-wave excitations $\sim k_N = 0.01$ meV. These features in the Coulomb blockade regime might be a signature of inelastic cotunneling events [25, 26]. However, there are several reasons why I am skeptical about this. These structures in the blockade could be due to another nanoparticle conducting in parallel to the nanoparticle whose features we prominently observe. The way we fabricate our devices makes me think that we cannot completely rule this out. Also, the tunneling rates associated with cotunneling events, which are second order processes, should be related to the resistances of the devices in the following way [25],

$$\Gamma_{cotun} \approx \Gamma_{se} \frac{R_K}{R_t}, \quad (6.4)$$

where Γ_{cotun} is the rate associated with cotunneling events, Γ_{se} is tunneling rate associated with single electron tunneling events, R_K is quantum of resistance, and R_t is the resistance of the rate limiting tunnel barrier in the device. For our devices

$R_t \geq 10 \text{ M}\Omega$, this results in $\frac{R_K}{R_t} \leq 10^{-3}$. (The quantum of resistance R_K is $25.8 \text{ K}\Omega$.) As a result one would expect the amplitude of the structure in the Coulomb blockade to be smaller than what we measure. In our experiments we find that the amplitude for the structure in the Coulomb blockade region is a factor of 0.1 to 0.01 smaller than the amplitude of the transitions due to single electron tunneling. As a result the experimentally observed amplitude of the structure in the Coulomb blockade region is a factor of ~ 10 larger than the very simple estimate. Most of the work in the literature deals with non-magnetic systems (low-spin); further theoretical work is needed to check if the cotunneling signal could be enhanced in magnetic systems because presence of spin excitations.

6.7 Summary and open questions

Our measurements of the H -dependence of the tunneling-resonance energies in cobalt nanoparticles exhibit level-to-level differences and non-monotonic variations that can both be explained qualitatively by variations of 1-3% in the magnetic anisotropy energy between different states. Recent microscopic calculations by Cehovin *et al.* [18] support our phenomenological model. The observation of level crossings and the disappearance of resonances as a function of V_g indicate that the majority of low-energy resonances are associated with tunneling transitions from non-equilibrium initial states. The strength of non-equilibrium effects appears to depend on whether the electrodes are normal or superconducting. The fact that we observe asymmetry in the magnitude of current flow for different signs of bias when current flow occurs via one energy level is puzzling.

It is possible that in our experiments non-equilibrium occupation exists for very small bias voltages due to the effects of thermally excited electrons in the electrodes;

this is suggested by the asymmetry in the magnitude of current for different signs of bias. When the leads of our device are superconducting, the non-equilibrium population of states in the nanoparticle – due to the thermal excitations in the lead – is exponentially suppressed. However, the non-equilibrium population of states within the nanoparticle is gradually turned on as the bias voltage is increased. This would explain the difference between the data as a function of gate voltage for the cases when the electrodes are superconducting and when they are normal.

There are several open questions that need further thought, and I list them here in the hope that someone else will also think more about them.

- If these resonances are due to non-equilibrium processes then what are the ingredients that need to be included to arrive at a complete description? Is this non-equilibrium only due to spin degree of freedom, or do the electron-hole excitations also contribute to it, if so then in what way are they coupled? Is there any other description of the physics we have explored?²⁸
- Why do we see a discrepancy between the values of k_N , anisotropy energy per unit spin, for bulk (0.1 meV) and nanometer scale magnets (0.01 meV)?
- Are cotunneling amplitudes enhanced in high-spin system? This would need to be answered before we can start thinking of the structure in Coulomb-blockade region of our samples as a signature of cotunneling.

²⁸Recent calculations done by Cehovin *et al.* [18] suggest that non-monotonic features, and same sign of high field slope for resonances can be explained without non-equilibrium processes. In their picture, they still do not observe high density of resonances we experimentally observe and it is not clear if their model can explain the asymmetry in the current for the two signs of bias. This aspect needs further thought.

Bibliography

- [1] R. Meservey and P. M. Tedrow, Phys. Rep. **238**, 173 (1994).
- [2] K. Ono, H. Shimada, and Y. Ootuka, J. Phys. Soc. Jpn. **66**, 1261 (1997); **67** 2852 (1998).
- [3] S. K. Upadhyay, A. Palanisami, R. N. Louie, and R. A. Buhrman, Phys. Rev. Lett. **81**, 3247 (1998).
- [4] R. J. Soulen *et al.*, Science **282**, 85 (1999).
- [5] J. M. De Teresa *et al.*, Phys. Rev. Lett. **82**, 4288 (1999).
- [6] M. M. Deshmukh, S. Kleff, S. Guéron, E. Bonet, A. N. Pasupathy, J. von Delft, and D. C. Ralph, Phys. Rev. Lett. **87**, 226801-1 (2001).
- [7] S. Guéron, M. M. Deshmukh, E. B. Myers, and D. C. Ralph, Phys. Rev. Lett. **83**, 4148 (1999).
- [8] C. M. Canali and A. H. MacDonald, Phys. Rev. Lett. **85**, 5623 (2000).
- [9] S. Kleff, J. von Delft, M. M. Deshmukh, and D. C. Ralph, Phys. Rev. B **64**, 220401(R) (2001).
- [10] C. T. Black, Ph.D. thesis, Harvard University, 1996.
- [11] S. Kleff and Jan von Delft, Phys. Rev. B **65**, 214421 (2002).
- [12] D. A. Papaconstantopolous, *Handbook of the band structure of Elemental Solids* (Plenum, New York, 1986).
- [13] M. Jamet *et al.*, Phys. Rev. Lett. **86**, 4676 (2001).
- [14] B. D. Cullity, *Introduction to Magnetic Materials*, (Addison-Wesley, Reading, 1972).
- [15] A. Thiaville, Phys. Rev. B **61**, 12221 (2000).
- [16] D. C. Ralph, C. T. Black, and M. Tinkham, Phys. Rev. Lett. **74**, 3241 (1995).

- [17] W. Wernsdorfer *et al.*, Phys. Rev. Lett. **78**, 1791 (1997).
- [18] A. Cehovin, C. M. Canali, and A. H. MacDonald, preprint.
- [19] D. G. Salinas *et al.*, Phys. Rev. B **60**, 6137 (1999).
- [20] K. A. Matveev, L. I. Glazman, and A. I. Larkin, Phys. Rev. Lett. **85**, 2789 (2000).
- [21] P. W. Brouwer, X. Waintal, and B. I. Halperin, Phys. Rev. Lett. **85**, 369 (2000).
- [22] S. Zhang, P. M. Levy, A. C. Marley, and S. S. P. Parkin Phys. Rev. Lett. **79**, 3744 (1997).
- [23] O. Agam *et al.*, Phys. Rev. Lett. **78**, 1956 (1997).
- [24] M. M. Deshmukh, E. Bonet, A. N. Pasupathy, and D. C. Ralph, Phys. Rev. B **65**, 073301 (2002).
- [25] D. V. Averin and Yu. V. Nazarov, in *Single Charge Tunneling: Coulomb Blockade in Nanostructures*, edited by H. Grabert and M. H. Devoret (Plenum Press and NATO Scientific Affairs Divison, New York, 1992), p217.
- [26] S. De. Franceschi *et al.*, Phys. Rev. Lett. **86**, 878 (2001).
- [27] W. Liang, M. Bockrath, and H. Park, Phys. Rev. Lett. **88**, 126801-1 (2002).

Chapter 7

Tunneling spectroscopy of a nanomagnet using a ferromagnetic electrode

In the previous chapter, we used tunneling spectroscopy to probe a ferromagnetic nanoparticle using nonmagnetic electrodes. In this chapter, we perform tunneling spectroscopy on a ferromagnetic nanoparticle (cobalt) by using one lead fabricated from a ferromagnetic metal (cobalt) and the other from a non-magnetic metal (aluminum). The motivation is to understand the interplay of spin and charging, in ways different from what was considered in Chapter 5 and Chapter 6. I will be discussing qualitative features of the data, since I have not been able to analyze these data in detail. I hope to complete the analysis sometime soon.

7.1 Introduction

There have been several recent studies [1, 2, 3, 4] which suggest that making components of single electron transistors (SETs) with ferromagnetic elements allows access to regimes where the interplay of spin and charge can be observed in the conductance of the device. These studies [1, 2, 3, 4] have motivated the present set of experiments. Most of the theoretical [1, 2] and experimental work [5] has focused on regimes where the ferromagnetic island has a continuum of states, whereas our technique allows us to measure a discrete electronic spectrum. Measurement of the conductance via discrete energy levels should allow us to measure the tunnel magnetoresistance (TMR) effect for conductance via *single* energy level.

7.2 Fabrication

The fabrication procedure for devices described in this chapter is very similar to the process described in the earlier chapters. Figure 7.1 shows the schematic of our device. The process starts by fabricating a nano-hole in a freely suspended silicon nitride membrane by using a combination of e-beam lithography and reactive ion etching (RIE).¹ After this, the first electrode is formed by depositing 150 nm of aluminum; this is followed by controlled oxidation at 50 mTorr for 3 min to form the first tunnel barrier. Following this, the nanoparticles are fabricated by depositing 0.5 nm of cobalt using e-beam evaporation. The second tunnel barrier is formed by depositing 11-12 Å of aluminum oxide. The second electrode is then deposited by evaporating 80 nm of cobalt using e-beam evaporation. Deposition of cobalt completes the fabrication procedure, following which the devices are checked

¹Fabrication of the nano-hole is described in detail in Section 2.4.1.

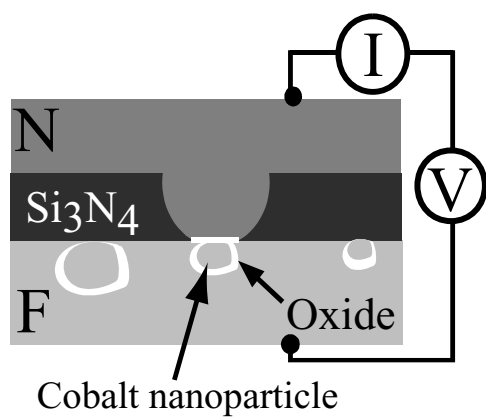


Figure 7.1: Schematic of a device with a cobalt electrode (F), a cobalt nanoparticle and an aluminum lead (N).

at 4.2 K to see if they exhibit Coulomb blockade – a sign that a single nanoparticle is formed between the two leads. Good devices are then cooled in a dilution refrigerator to measure the discrete conductance spectra.

7.3 Experimental data

Figure 7.2(a) shows a colorscale conductance plot as a function of the magnetic field; with the field being swept from positive to negative values. One can notice that each of the energy levels shift continuously as a function of the magnetic field, and some energy levels undergo a shift to higher bias voltages near 0 mT. This shift near 0 mT, observed for some energy levels, is due to the superconductivity of the aluminum lead. Notice that the first resonance for positive bias does not undergo the shift due to the superconductivity; this means that the threshold step for positive bias is tunneling in of an electron from the ferromagnet.² Using one superconducting lead and one ferromagnetic lead has an advantage that we can identify which energy level corresponds to the threshold across the ferromagnetic electrode. After the superconductivity of the aluminum electrode is suppressed due to the magnetic field, we notice that all energy levels undergo an abrupt shift at -0.04 T. We associate this shift with the switching of the ferromagnetic electrode. This shift arises because the electrochemical potential of the electrode undergoes a change when the magnetic moment of the electrode undergoes magnetic switching. The switching field of cobalt films ~ 100 nm thick is expected to be around ~ 5 mT. However, this can be enhanced in disordered films [6]. At fields more negative than -0.04 T we see a continuous variation of energies for different levels. At ~ -0.25 T we observe another small shift for all the energy levels. We associate this with the

²This transition has been referred to as the transition of $n + 1 \rightarrow n$ kind.

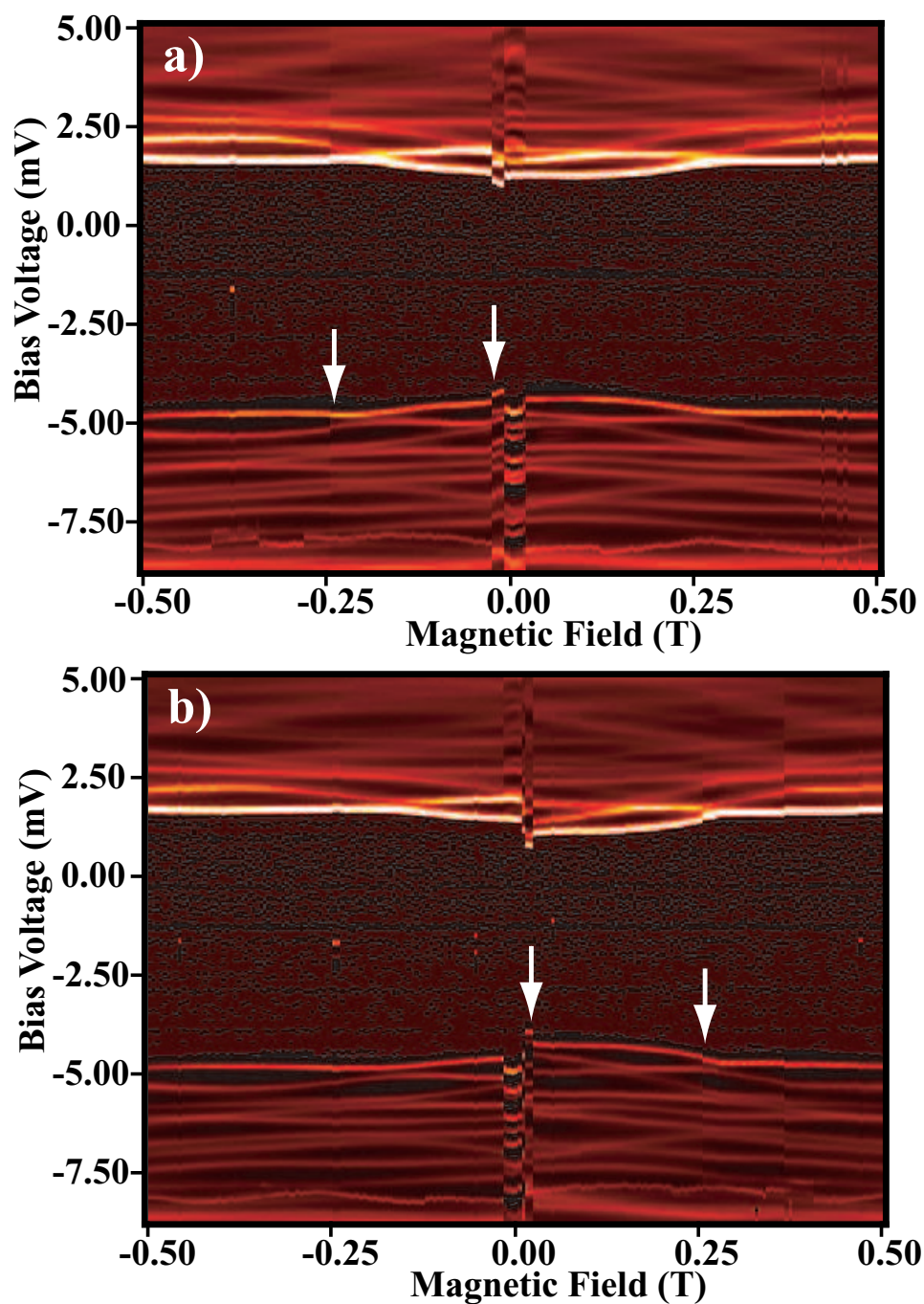


Figure 7.2: Colorscale conductance plot of a device with a cobalt lead, a cobalt nanoparticle and an aluminum lead. a) Data taken while the magnetic field is swept from positive to negative values. b) Data taken while the magnetic field is swept from negative to positive values. The arrows indicate the two switching events: one ~ 40 mT and the second ~ 250 mT.

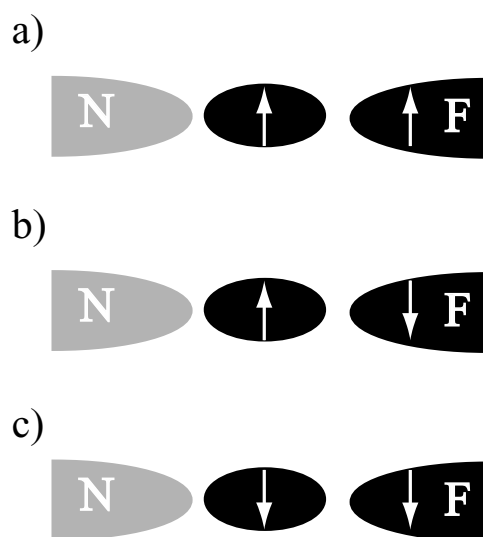


Figure 7.3: Cartoon showing the relative orientation of the direction of magnetization for the nanoparticle and ferromagnetic lead. This sequence of cartoons is for the case of sweeping the field from “ \uparrow ” to “ \downarrow ” direction. These cartoons illustrate that ideally we can measure the tunnel magnetoresistance (TMR) effect for the case of transport via *single* energy level. This can be easily achieved for the case of device with a gate electrode.

reversal of nanoparticle's magnetic moment. The switching field measured here is larger than the switching field for cobalt nanoparticles measured in the previous chapter. This could be due to dipolar coupling of the ferromagnetic lead and the nanoparticle. As the magnetic field is increased further, there are continuous shifts for the energy levels. Figure 7.2 (b) shows a similar plot of the conductance as a function of magnetic field with the difference that magnetic field is now swept from negative values to positive values. We observe similar features for the two directions of magnetic field sweep; the difference being that they are reflected about 0 mT. The fact that the nanoparticle and ferromagnetic particle have different switching fields allows us to study the device when the two are aligned parallel to each other, and then antiparallel to each other.³ Three different cases for the orientation of magnetic moments relative to each other is shown in Figure 7.3. Ideally, this device geometry allows us to measure the tunnel magnetoresistance (TMR) effect for the case when transport occurs via a *single* energy level. Unfortunately for this device, we cannot observe such an effect since it has a large threshold voltage for the initiation of tunneling. This makes it difficult to deconvolve the effect of one level. We observe only a $\sim 10\%$ variation in the peak conductance of the first level at positive bias for parallel and anti-parallel orientation. It is difficult to conclude that this is due to the TMR effect. However, with a gated device one could make direct conclusions.

Figure 7.4 shows the conductance plot for a field sweep from positive to negative values for a larger range of magnetic fields. The important aspect of this plot is that there is symmetrical behavior for positive and negative values of the magnetic field if one omits the region between -250 mT and $+250$ mT.⁴ This supports the

³This is a very simplistic view point. It is possible that the moments of the nanoparticle and the electrode are not collinear.

⁴The extra glitch seen at ~ 350 mT is due to a sudden change in the offset charge.

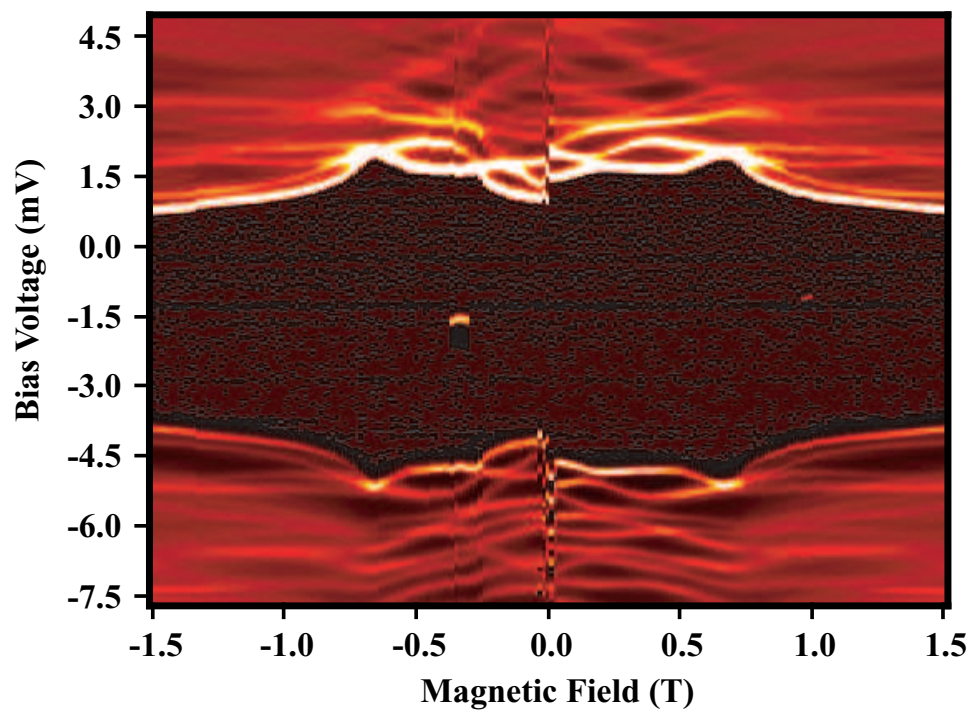


Figure 7.4: Colorscale conductance plot as a function of magnetic field. The sweep direction is from positive to negative values. Note the symmetry for the position of the energy levels outside the -250 mT to +250 mT region.

picture that the shift at -250 mT is due to magnetic switching of the nanoparticle. Figure 7.4 also shows complex evolution of different energy levels as a function of applied magnetic field, similar to the data discussed in previous chapter. However, in this case there are two different effects that contribute to the shifting of energy levels at high fields – the shift in energy of the individual levels within the nanoparticle, and the shift due to chemical potential change for the ferromagnetic lead.

7.4 Outlook

Unfortunately, I have not carried out a detailed analysis of the data now, but I hope to do it soon. This system has interesting physics associated and needs to be pursued further. It would make a very interesting project.

Bibliography

- [1] J. Barnaś and A. Fert, Europhys. Lett. **44**, 85 (1998).
- [2] J. Barnaś and A. Fert, Phys. Rev. Lett. **80**, 1058 (1998).
- [3] G. Usaj and H. Baranger, Phys. Rev. B **63**, 184418-1 (2001).
- [4] L. F. Schelp *et al.*, Phys. Rev. B **56**, R5747 (1997).
- [5] K. Ono, H. Shimada, and Y. Ootuka, J. Phys. Soc. Jpn. **66**, 1261 (1997); **67** 2852 (1998).
- [6] E. B. Myers, personal communication.

Chapter 8

Nanofabrication using a stencil mask

In the previous chapters, we considered the transport properties via quantum dots fabricated using different metals. In this chapter, we consider a stencil fabrication technique that I worked on during my first year in the group. This chapter has been adapted from a paper we wrote [1]. The tests described here are results from preliminary work, with the motivation being to demonstrate that the stencil based fabrication technique can make structures in the ~ 15 nm range. Since then, this technique has been extensively developed by Alex Champagne and Aaron Couture. Now, Alex can fabricate structures on the tip of an atomic force microscope (AFM) controllably.

8.1 Introduction

The usual procedures for fabricating nm-scale devices, using electron-beam, x-ray, or other forms of lithography, involve exposing a pattern in a polymer-resist layer

applied directly to a sample substrate. However, there exist several circumstances in which it would be convenient to do away with the resist on the sample; instead completing the pattern-formation process separately to make a free-standing stencil, which is later used to deposit patterned material onto the substrate. By this means, lithography could be performed on substrate materials which would be damaged by the chemical or thermal stresses encountered during resist application and baking. Another application is for the fabrication of nanostructures on surfaces in ultrahigh vacuum, for experiments such as studies of atomic diffusion, or the fabrication of electrodes to contact self-assembled nanostructures. It would also be possible to make devices on unusual substrates for which it is not possible to achieve the uniform coating of resist necessary for ordinary processing. We have in mind the desire to write nm-scale devices directly on the tips of scanning probe microscopes, for the purpose of creating new types of scanning sensors [2].

In this chapter, we describe a process for fabricating nanostructures by evaporating metal through holes in a suspended silicon nitride membrane. In doing this work, we follow many groups who have used stencil techniques to make structures $\geq 0.1 \mu\text{m}$ in scale [3, 4, 5]. We are able to write metal dots 15 nm in diameter and lines 15-20 nm wide. We have also tested the rate at which nm-scale holes in the stencil clog during the deposition process, and the extent to which the ultimate resolution of this technique is limited by the divergence angle of the deposition beam and diffusion of atoms on the sample surface.

8.2 Fabrication of stencil and nanostructures

The stencil masks are made by adapting a procedure used previously for fabricating metal point-contacts [6] and tunneling devices [7]. Details of the fabrication

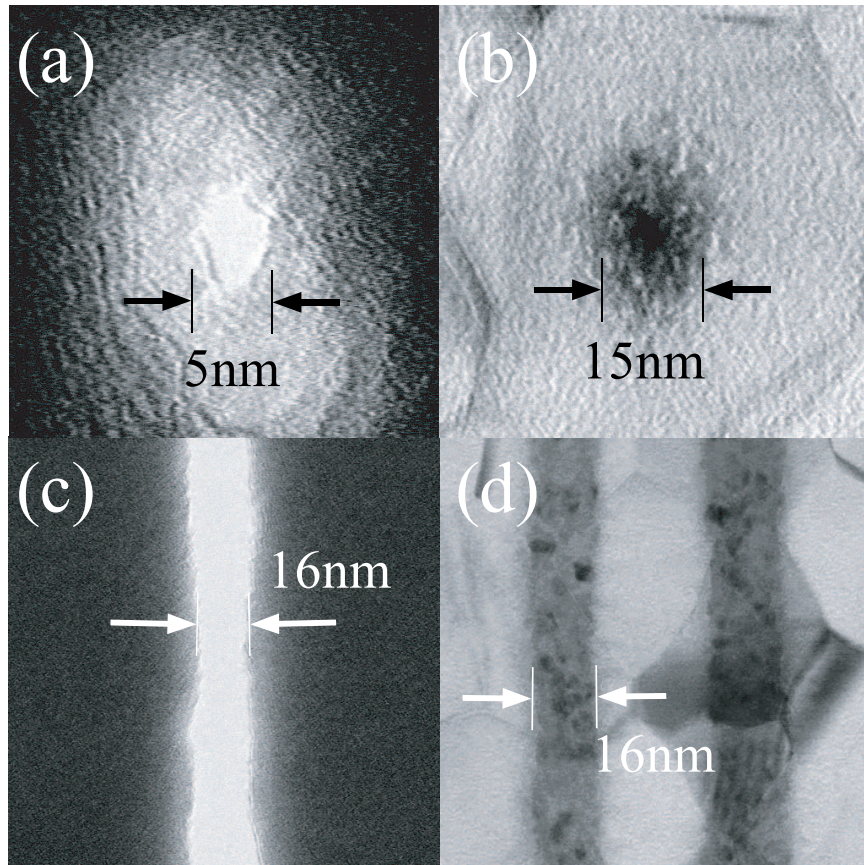


Figure 8.1: Bright-field scanning transmission electron microscope (STEM) images. (a) A hole 5 nm in diameter etched through a silicon nitride membrane. (b) A metal dot made by evaporating 10 nm of Er through an orifice 5-10 nm in diameter onto an oxidized aluminum film held at room temperature. (c) Section of a $4\ \mu\text{m}$ -long \times 15-20 nm-wide line etched through a silicon nitride membrane. (d) Sections of 10 nm-thick Er lines, which are deposited through an orifice similar to the one shown in (c), at room temperature onto an oxidized Al film. The two lines, 19 nm and 16 nm wide, were made by separate depositions of Er, from different angles, through the same linear hole.

steps are described in Chapter 2, but here we describe the process briefly. First, low-stress silicon nitride is deposited on both sides of a $\langle 100 \rangle$ double-side-polished silicon wafer. Photolithography and etching in an aqueous KOH solution are used to remove selected regions of the silicon to leave square suspended membranes of silicon nitride 50 nm thick and 60-80 μm on a side. Electron-beam lithography is then performed to write an array of holes on the membrane, using the Leica VB6 operating at 100 keV. After development, the holes are etched through the silicon nitride membrane using a CHF_3/O_2 plasma. The etching conditions are such that the hole is bowl-shaped, and the final orifice is smaller than the original pattern formed by lithography [6]. Figure 8.1(a) displays a STEM (Scanning Transmission Electron Microscope) bright-field image of a single 5-nm-diameter hole in an array, looking through the membrane. The gradual darkening in the region surrounding the hole is due to the taper on the sides of the bowl-shaped hole. In our tests we have used holes ranging up to 50 nm in diameter, and also larger orifices for contact pads and other test structures.

The geometry for deposition through the stencil mask is shown in Figure 8.2. For simple single-step metal depositions, the mask can be clamped directly to a substrate. However, we find that the mask-substrate spacing in this case varies, due to small particulates or surface irregularities, typically being in the range of 1 μm . A predictable spacing is necessary for alignment of multiple-angle evaporations and for tests of the ultimate size resolution of the technique, so we introduce 1.6- μm -diameter silica spheres [8] as spacers between the stencil and substrate before clamping. The sample/stencil assembly is attached to a stepper-motor controlled tilting stage within an evaporator, so that the angle of evaporation can be varied. The mask-substrate spacing with the microspheres is generally reproducible to ± 0.1

μm , and is checked by evaporating metal through a nano-hole from two known angles, measuring the distance between the resulting dots on the substrate by scanning electron microscopy (SEM) or atomic force microscopy (AFM), and using triangulation. The sample and stencil are baked in vacuum to remove adsorbed water before the evaporation (one exception will be noted).

In order to produce nm-scale features by deposition through a stencil more than $1 \mu\text{m}$ from the substrate, the incoming beam of metal atoms must be collimated. This is achieved by using a resistive-heating source containing a pinhole of width $w_{\text{source}} = 1 \text{ mm}$ through which metal is evaporated [10]. From the geometry shown in Figure 8.2, assuming no diffusion of atoms on the surface, the width of a deposited dot should be $w_{\text{dot}} \approx w_{\text{hole}} + (d/L)w_{\text{source}}$, where w_{hole} is the width of the orifice in the stencil, d is the stencil-substrate spacing, and $L = 30 \text{ cm}$ is the source-stencil spacing [9]. The broadening $(d/L)w_{\text{source}}$ is, therefore, expected to be approximately 5 nm .

Figure 8.1(a) shows a bright-field plan-view STEM image of one example from an array of metal dots made by depositing 10 nm of erbium (Er) through an orifice $5\text{-}10 \text{ nm}$ in diameter onto a room temperature substrate. The deposited dot is $\sim 15 \text{ nm}$ in diameter. The substrate in Figure 8.1(b) (and also Figure 8.1(d)) is an oxidized Al film, 30 nm thick, deposited on a photoresist layer on top of a Si wafer. This geometry allows the Al film to be lifted off for STEM examination of the Er structures. Because of the photoresist layer, the samples in Figure 8.1 were not baked prior to the deposition. The images were taken looking through the Al film, whose grains are visible on the $40\text{-}50 \text{ nm}$ scale. We choose Er for depositions tests due to its sticking properties, good visibility in electron microscopes (atomic number = 68), and convenient melting temperature. Chromium and aluminum have also

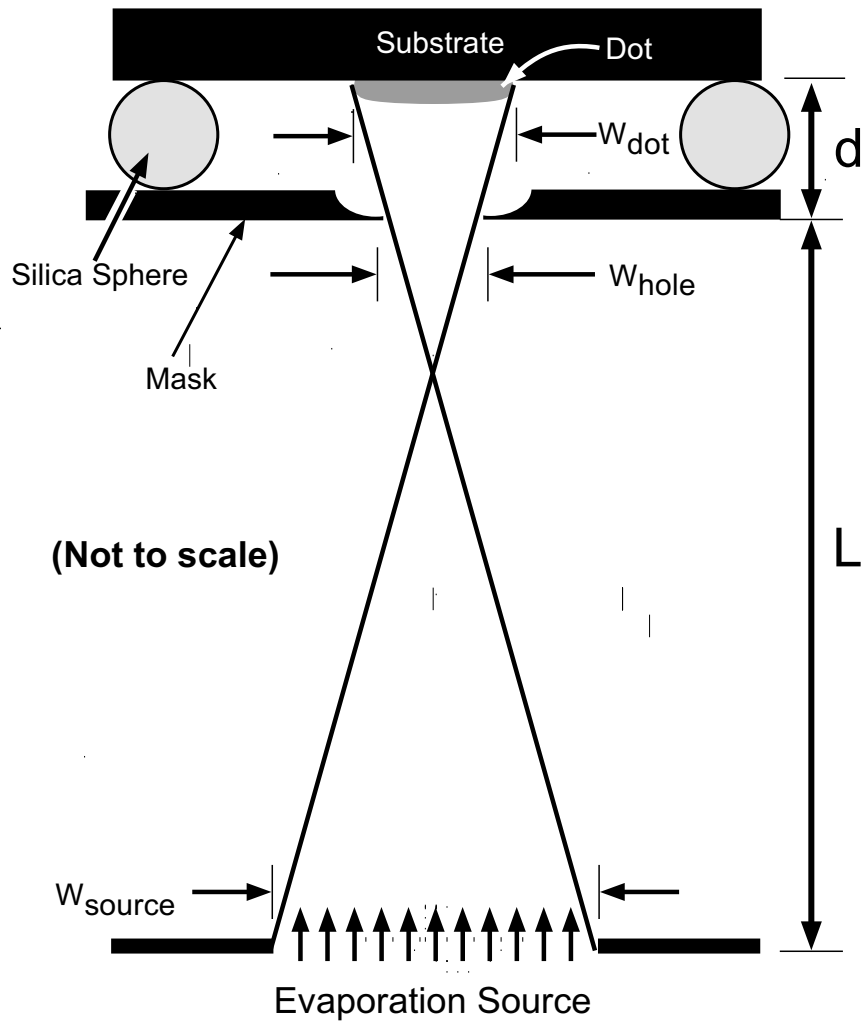


Figure 8.2: Diagram of deposition through the stencil mask using a pinhole evaporation source. (Not to scale.)

been deposited successfully. We have verified that the dots are Er, using electron energy-loss spectroscopy.

In Figure 8.1(c), we show a section of a 4 μm -long line-shaped orifice in a stencil membrane, and in Figure 8.1(d) images of two 10-nm-thick Er lines deposited through such a hole. Both the deposited lines and the stencil orifice have widths 15-20 nm. The grain size of the deposited Er is visible in Figure 8.1(d), 2-5 nm.

The results described above show that this technique is capable of fabricating nanometer scale patterns. However, it is essential to determine how much metal can be deposited through the holes in order to determine the usefulness of the technique. Next, we describe a test to quantify the clogging of the holes as metal is deposited through them.

8.2.1 Clogging of holes

We have investigated how much material may be deposited through the nm-scale holes before they become clogged. This test is done by slowly tilting the stencil/substrate assembly, using a stepper motor, while Er is evaporated at a constant rate so as to draw a line of material on the substrate. In one test, with a 1.8- μm stencil-substrate spacing, we deposited 200 nm of Er over the course of a 20 degree rotation, which in the absence of hole-clogging would give a 660 nm line. The deposited structures (*e.g.*, Figure 8.3(a,b)) have an angular shape, thinning as the evaporation proceeds, indicating that the holes close gradually. From the length of the lines, we can estimate that for a hole of approximately 40 nm diameter, 65 nm of evaporated Er clogs the hole, while for 20-nm-diameter holes, 30 nm of Er is the limit. Somewhat greater thicknesses of gold can be deposited without clogging the stencil, approximately 3 times the hole diameter; however gold produces broader

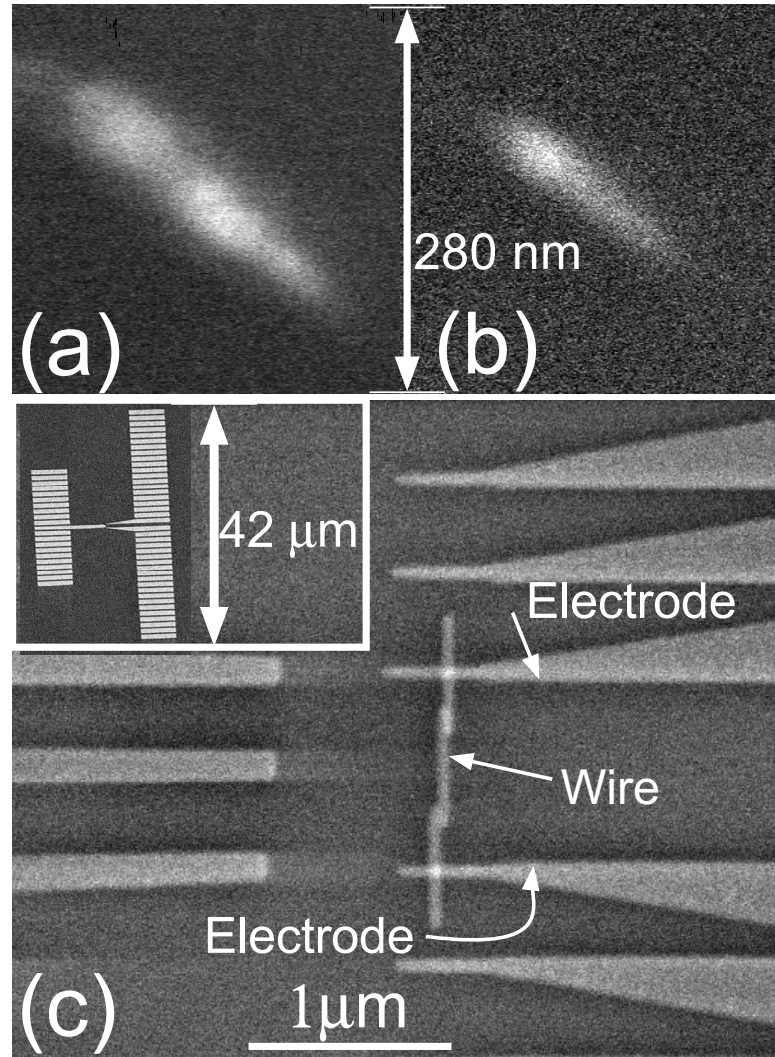


Figure 8.3: (a,b) Clogging tests: SEM images of Er deposited through 40 and 20-nm-diameter orifices onto oxidized Si, as the substrate was gradually tilted so as to scan the deposition spot. The hole clogs after the deposition of 65 nm and 30 nm of material respectively. (c) 25-nm-wide, 10-nm-thick Er line connected to macroscopic electrodes using multiple-angle evaporations. The inset shows the pattern of the stencil mask used to fabricate the device.

deposited features than Er, due to increased surface diffusion.

The next test determines the effect of surface diffusion on the dimensions of the deposited structures.

8.2.2 Role of surface diffusion

As a test of the extent to which the divergence of the incident atom beam and also surface diffusion of Er limit the resolution of the stencil technique, we have used an AFM to compare the heights of Er dots with different diameters, deposited simultaneously at fixed angle onto oxidized silicon through holes in one stencil membrane. The heights are listed in Table 8.1 as averages over tens of dots made in arrays of similar diameters. The total deposited thickness of Er is determined by measuring the thickness of very large ($0.5\text{-}\mu\text{m}$ -wide) features in the test array. Smaller-diameter dots are progressively shorter, as would be expected due to spreading of the deposited metal. In order to obtain an approximate measure of this spreading, we can model the deposited features as pillars (slightly tapered to take into account hole-clogging) convolved with a Gaussian spreading function. This is not accurate in all cases, since some dots are observed with thicknesses greater than the deposited film, due to clustering of the metal. However, the average dot heights indicate a full-width at half maximum (FWHM) for the spreading function of approximately 18 ± 5 nm. For a substrate cooled to liquid nitrogen temperature during the evaporation, this is reduced to 10 ± 4 nm, so we can conclude that thermal diffusion of Er contributes to the spreading at room temperature.

Table 8.1: AFM study of the thicknesses of Er dots deposited through orifices of varying diameter, in order to measure the spreading of the deposited Er. Room-temperature and 77 K depositions were performed through the same sets of holes, from different angles. The smaller hole sizes listed for the 77 K deposition reflect partial hole clogging. The uncertainties are standard deviations for dots deposited through different holes of similar size in the same array. Diameters are accurate to ± 3 nm.

Hole diameter(nm)	500	47	31	25
Height for RT (nm)	10.8 ± 0.1	10.4 ± 0.3	8.5 ± 0.1	6.6 ± 0.3
Hole diameter (nm)	500	41	25	19
Height for 77K (nm)	10.1 ± 0.1	10.9 ± 0.3	10.4 ± 0.4	7.3 ± 0.2

8.2.3 Fabrication of micrometer-scale structures

In order to make use of nm-scale structures as electrical devices, it is necessary to connect them to macroscopic leads. We have accomplished this by making a stencil pattern which contains both a line on the 25-nm scale and electrodes on the 10's-of- μm scale. Then we have connected the wire and the electrodes using a series of three 10-nm-thick Er evaporations from different angles (Figure 8.3(c)). The electrodes are large enough to be convenient for wire-bonding. The room-temperature resistance of the wire + electrodes shown in Figure 8.3(c) is $\sim 1000 \Omega$.

8.3 Conclusion

We have demonstrated that the stencil based fabrication has the potential to fabricate structures with sizes as small as approximately 15-20 nm. Structures can be made by evaporating metal at multiple fixed angles, or they can be drawn continuously by tilting the stencil and thus scanning the substrate relative to the stencil orifice. The technique is useful for performing lithography on substrates for which it is not possible to apply resist.

Since the time of this preliminary work, Alex Champagne and Aaron Couture have developed this technique further, and it has reached a stage where structures can be fabricated controllably on a tip of an atomic force microscope (AFM). This opens up a whole new way of making “smart” surface probes like a high resolution magnetic force microscope (MFM) tip, near field antennas [11], and charge sensors based on single electron transistors fabricated on the tip of an AFM [2]. The ability of the stencil based technique to fabricate structures in ultra high vacuum (UHV) has already been exploited in the Buhrman group; they fabricated magnetic structures \sim

100 nm in size on semiconductor surfaces in an ultra-high vacuum environment, and probed the magnetic properties of the fabricated structures using ballistic electron magnetic microscopy (BEMM) [12].

Bibliography

- [1] M. M. Deshmukh, D. C. Ralph, M. Thomas, and J. Silcox, *Appl. Phys. Lett.* **75**, 1631 (1999).
- [2] M. J. Yoo, T. A. Fulton, H. F. Hess, R. L. Willett, L. N. Dunkleberger, R. J. Chichester, L. N. Pfeiffer and K. W. West, *Science* **276**, 579 (1997).
- [3] K. Ono, H. Shimada, S. Kobayashi, and Y. Ootuka, *Jpn. J. Appl. Phys.* **35**, 2369 (1996).
- [4] J. N. Ullom, P. A. Fisher, and M. Nahum, *Phys. Rev. B* **58**, 8225 (1998).
- [5] C. Stamm, F. Marty, A. Vaterlaus, V. Weich, S. Egger, U. Maier, U. Ramsperger, H. Fuhrmann and D. Pescia, *Science* **282**, 449 (1998).
- [6] K. S. Ralls, R. A. Buhrman, and R. C. Tiberio, *Appl. Phys. Lett.* **55**, 2459 (1989).
- [7] D. C. Ralph, C. T. Black, and M. Tinkham, *Phys. Rev. Lett.* **74**, 3241 (1995).
- [8] Duke Scientific Corp., Palo Alto, CA 94303.
- [9] C. T. Black, Ph.D. thesis, Harvard University, 1996.
- [10] R. D. Mathis Company, Long Beach, CA 90806.
- [11] R. D. Grober, R. J. Schoelkopf, and D. E. Prober, *Appl. Phys. Lett.* **70**, 1354 (1999).
- [12] W. H. Rippard *et al.*, *Appl. Phys. Lett.* **77**, 1357 (2000).

Chapter 9

Conclusion

In this work, I have described how tunneling spectroscopy, using metallic quantum dots, can be used to explore physics associated with magnetic and non-magnetic metals. The basic principle of all these experiments was to measure the discrete energy spectrum of a nanometer-scale metallic particle; the measured spectrum reflects the forces at work in the quantum dot and its electrodes. We were able to probe electronic interactions in non-magnetic systems, and the interplay of spin and charge for the case of a ferromagnet. The versatility our fabrication technique allowed us to study the flow of polarized currents from a ferromagnet in a unique way, and our results confirm the crucial role played by interfaces in magnetic systems. The technique can be used further to study spin transport in greater detail. The physics explored in this work has wider applicability in the burgeoning fields of molecular electronics and spintronics.

Appendix A

Stripline cryogenic filters

The cryogenic electrical filters described here were designed to reduce the electron temperature for tunneling spectroscopy measurements. As discussed in Section 2.3.2, the resolution in energy is improved with lower electron temperature, and proper filtering of the electrical lines connecting a room-temperature apparatus to an electronic device at cryogenic temperature is essential. Anchoring¹ the electrical lines helps to reduce the noise that is generated in them. However, it does not attenuate the noise travelling down from equipment at room temperature. The problem of electrical noise is further complicated by the fact that the electron-phonon coupling decreases rapidly as one reduces the temperature below the Debye temperature (Θ_D). The electron-phonon scattering rate $\propto T^3$ [1]; so at low temperatures the rate of heat flow from electrons to phonons is slow, and the electrons are easily heated above the temperature of the lattice. The result of this decoupling is that the electron temperature (T_e) is always higher than the base temperature of the refrigerator.

¹Attaching the electrical lines near the 1 K pot and the mixing chamber of the refrigerator helps to anchor them.

There have been several schemes for the design of cryogenic electrical filters: copper powder filters [2], miniature electrical filters [3], waveguide filters [4], and thermocoax cables as filters [5]. However, we have used only the first two types of filters on our refrigerator since they are compact, and can be attached easily on our refrigerator. I am not going to discuss the details of fabrication of the copper powder filter since their recipes can be easily found in the literature [2]. Most of the data that is discussed in this thesis was taken with only the copper-powder filters acting to reduce the noise; the lowest electron temperature T_e was measured to be ~ 70 mK. It was only in the fall of 2001 that the miniature electrical filters were fabricated with help of Kirill Bolotin, Abhay Pasupathy, Edgar Bonet, Eric Smith and Alex Corwin. The data shown in Chapter 5 were taken after these filters were installed.

A.1 Fabrication of miniature electronic filters

These filters were fabricated by adapting the design of Saclay group [3]. We have adapted this design with changes, so that 16 filters can be attached to the mixing chamber of the refrigerator. On the basis of the results, we can say that the operation of the filters has not been compromised by the design changes. Figure A.1 shows the diagram of a single filter and its cross-section. The filtering element is a meander line which acts like a RLC filter [3]. The microfabrication is done using photolithography since the minimum feature size is $10\mu\text{m}$. The steps are:

- A silicon wafer coated with 500 nm of silicon oxide is used as a starting substrate. Then 200 nm of gold is deposited to form a ground plane. It is important to use a 15 nm of chrome as a sticking layer since the gold tends to peel

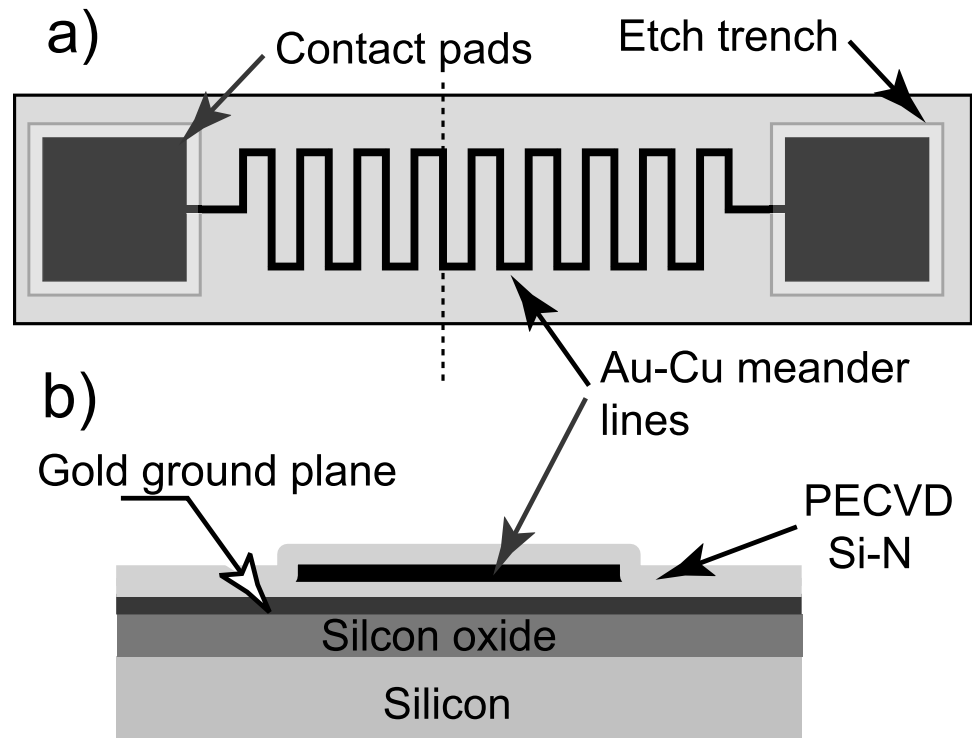


Figure A.1: a) Top view shows the design of a microfabricated meander line filter, which serves as a RLC filter, with exposed contact pads. b) Cross-section of filter shows various layers: the oxide layer is 500 nm thick, the gold ground plane is 200 nm thick, the meander line made of Cu-Au alloy is 200 nm thick, and both the silicon nitride layers are $1\mu\text{m}$ thick.

off at later stages due to internal stress from three more layers of deposition.

- Following the gold deposition $1\mu\text{m}$ of silicon nitride is grown using plasma enhanced chemical vapor deposition (PECVD). The PECVD process was carried out with a substrate temperature of 300°C .
- The meander line is patterned on a $2\mu\text{m}$ thick photoresist using the 5X-stepper. A 2 minute descum is done to get rid of any photoresist sticking on the substrate. This is important since any photoresist remaining will degas and the layers to be deposited next will peel off.
- 200 nm of a copper-gold alloy is thermally evaporated to form the meander lines. The composition of the Au-Cu alloy is 85% copper and 15% gold by weight. The composition of the alloy is critical, since the resistivity of the binary system varies significantly [6]. This binary system's resistivity, $7.5 \times 10^{-8}\ \Omega\text{m}$ at 4 K, is an order of magnitude larger than that of gold or copper. The higher resistivity ensures that the meander line has enough resistance at cryogenic temperatures to function as RLC filter. The resistance of the meander lines is typically $\sim 4.5\ \text{k}\Omega$.
- The meander line is then insulated by deposition of $1\mu\text{m}$ PECVD silicon nitride. The square contact pads are exposed by a patterned trench etch, as shown in Figure A.1 (a).

The microfabricated meander lines are then cleaved into individual pieces, so that they can be inserted into a “pillbox” designed to shield the filters electromagnetically. The schematic of the design is depicted in Figure A.2. Each of the filters is placed in a compartment of the pillbox, and the ground plane is contacted with the ground of the system (the dilution refrigerator support), by using dense silver epoxy

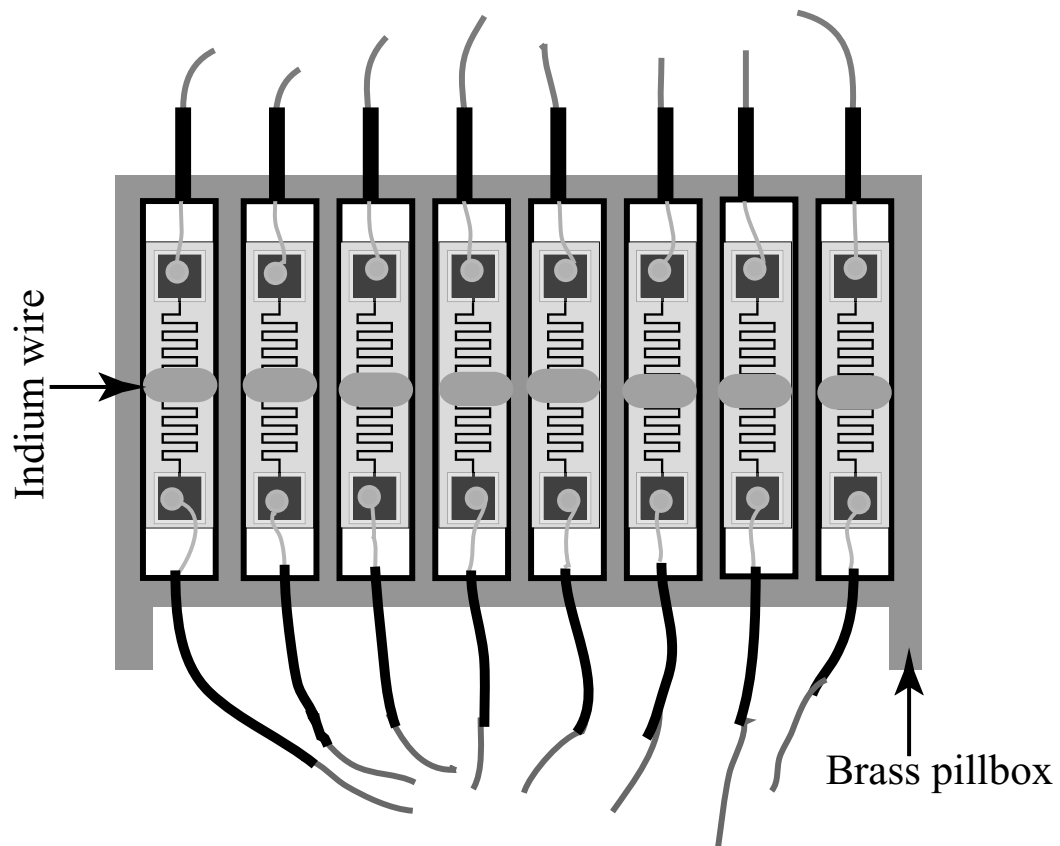


Figure A.2: Placement of each of the individual filters in a brass “pillbox” for electromagnetic shielding. The filters are soldered to wires using indium. The indium wire in the center of the box is used to fill the gap between the individual filters and the cover of this “pillbox”. (Not to scale.)

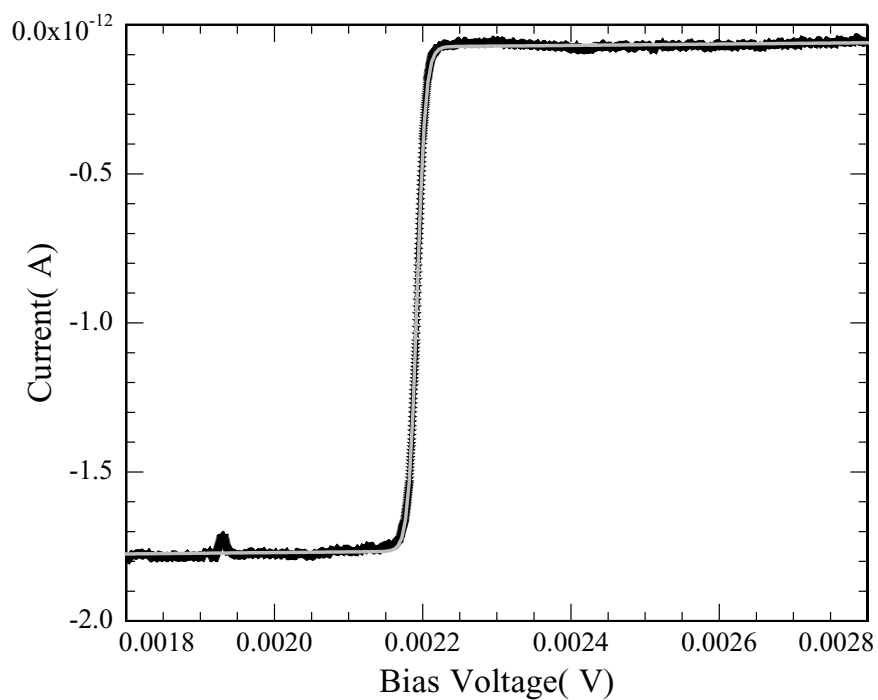


Figure A.3: Result of fitting for a current step using a Fermi function. The black stars show the experimental data and the grey solid line is the result of fitting. The electron temperature calculated from this fit is 38 ± 3 mK.

at one point on the edge of the chip. This provides a good way to contact the ground plane and the pillbox without resorting to a couple more layers of lithography. The leads from each of the lines are soldered onto the pads using indium wire. Care should be taken to wash away any flux used during soldering, since it provides a parasitic path to ground. A small piece of indium is then used to bridge the gap between the chip and the lid of the pillbox. I should point out that I have used thin braided coax to connect the samples lines and the filters, so as to minimize coupling with noise from the unfiltered lines. I have used these filters for several (~ 10) cool-downs and have found that they withstand the thermal cycling well. During these cool-downs I have had to replace filters on two lines due to leakage to ground.²

A.2 Result of using these filters

The improvement in the electron temperature due to the addition of the filter can be measured by fitting one of the current steps in the I-V characteristics with a Fermi function. The temperature extracted from the width, after correcting for the capacitive division, is a measure of the electronic temperature. Figure A.3 shows the result of such a fitting. The temperature extracted from this measurement is 38 ± 3 mK; the uncertainty arises from the measurement of the capacitance ratios, and from the fitting procedure. One other way to benchmark the filter is also to measure the width of a current step as a function of the temperature of the dilution refrigerator. This can be done easily in a stable manner by heating the mixing chamber using a heater with feedback. Figure A.4 shows the result from such an

²I have made several spare filters that are with Kirill Bolotin and they can be used to replace the bad ones.

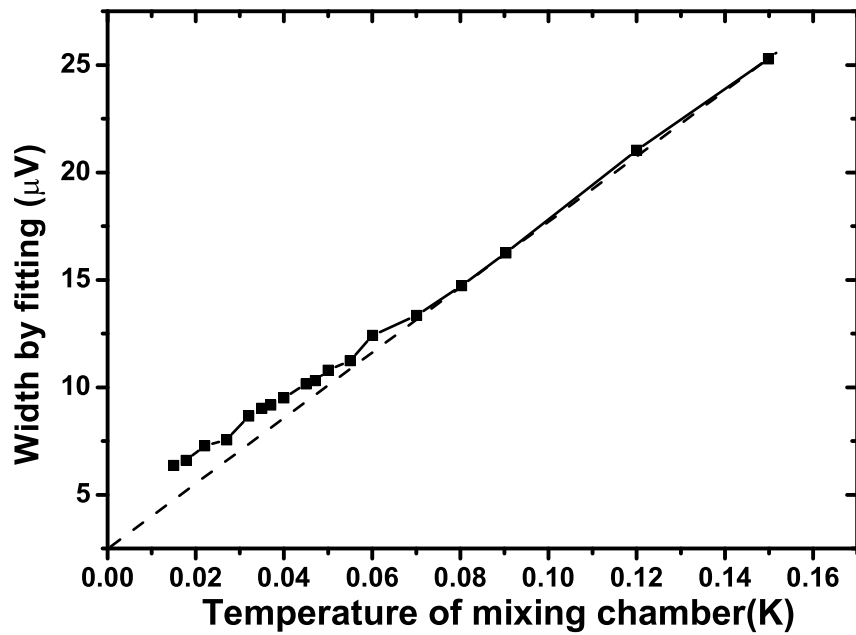


Figure A.4: This plot shows the measured width of a Fermi function, a measure of the electron temperature T_e , fitted to a current step, as a function of the temperature of the mixing chamber temperature. The dashed line is a guide to the eye, and shows the deviation of the measured width from a linear dependence on mixing chamber temperature.

experiment. We notice that the electron temperature follows the temperature of the refrigerator at higher temperatures, however, at lower temperatures there is a departure from this linear behavior (as indicated by the dashed line which is a guide to the eye). This sort of departure is expected if the noise level starts dominating. What is interesting is that this departure from linearity is not abrupt, but gradual. There are several effects that could contribute to this: the samples had not really reached the temperature indicated by the thermometer on the mixing chamber, or the temperature calibration of the thermometer on the refrigerator is not accurate. I haven't looked into this carefully, and this may be a good short project for a starting graduate student who can do a careful calibration with a gated device. It is clear that we can attain electron temperatures of ~ 40 mK. This electron temperature may not be the lowest attained,³ but it is one of the lower temperatures.

³The Saclay group has measured an electronic temperature of 30 mK in their experiments [3].

Bibliography

- [1] N. W. Ashcroft, and N. D. Mermin, in *Solid State Physics* (W.P. Saunders Company), Chapter 26.
- [2] J. M. Martinis, M. H. Devoret, and J. Clarke, *Phys. Rev. B* **35**, 4682, (1987).
- [3] D. Vion, P. F. Orfila, P. Joyez, D. Esteve, and M. H. Devoret, *J. Appl. Phys.* **77**, 2519, (1995).
- [4] H. Courtois, O. Buisson, J. Chaussy, and B. Pannetier, *Rev. Sci. Instrum.* **66**, 3465, (1995).
- [5] A. B. Zorin, *Rev. Sci. Instrum.* **66**, 4296, (1995).
- [6] *J. Phys. Chem. Ref. Data* **12**, 215 - 225, (1983).